Optical self-switching effects in Mach-Zehnder interferometers

Please check the document version of this publication:

• A submitted manuscript is the version of the article upon submission and before peer-review. There can be important differences between the submitted version and the official published version of record. People interested in the research are advised to contact the author for the final version of the publication, or visit the DOI to the publisher's website.
• The final author version and the galley proof are versions of the publication after peer review.
• The final published version features the final layout of the paper including the volume, issue and page numbers.

Link to publication

Optical Self-Switching Effects in Mach-Zehnder Interferometers

Optical Self-Switching Effects in Mach-Zehnder Interferometers

PROEFSCHRIFT

TER VERKRIJGING VAN DE GRAAD VAN DOCTOR

AAN DE TECHNISCHE UNIVERSITEIT EINDHOVEN,

OP GEZAG VAN DE RECTOR MAGNIFICUS, PROF.DR.IR. C.J. VAN DUIJN,

VOOR EEN COMMISSIE AANGEWEZEN DOOR HET COLLEGE VOOR PROMOTIES

IN HET OPENBAAR TE VERDEDIGEN OP

MAANDAG 19 DECEMBER 2005 OM 16.00 UUR

DOOR

Evgeni Arkad'evich Patent

geboren te Minsk, Wit-Rusland

Dit proefschrift is goedgekeurd door de promotoren:

prof.dr.ir. M.K. Smit
en
prof.dr. D. Lenstra

Copromotor:
dr. J.J.G.M. van der Tol

aan mijn ouders

Contents

Contents

Contents

x

Chapter 1

Introduction

This chapter gives an overview of different switching techniques commonly used for Mach-Zehnder interferometer (MZI) based switches. The self-switching concept in MZIs is introduced and a number of applications are discussed: the pattern effect compensator, the 2R-regenerator and the low-loss optical combiner.

1.1 Introduction

The use of light for communication purposes dates back to ancient times. A complete overview of the fiber optics history tracing its transformation throughout the centuries is given by Hecht in [1]. The ancestors of the modern optical communication systems are fire and smoke signals to transmit a single piece of information. In the 18th century this idea was extended to the so-called "optical telegraph", invented by the French engineer Claude Chappe. This system was transmitting mechanically coded messages through a sequence of relay stations maintained on towers. The function of light in such a system was simply to visualize the coded signal on one tower, so that it could be caught on the following one. The relay stations were acting as signal regenerators or repeaters. The transmission medium of the optical telegraph was open air. Another optical system, known as the Photophone, was patented by Alexander Graham Bell in 1880. In this system optical signals were also sent through the air. But because the atmosphere did not transmit light signals as reliable as wires transmit electricity, it did not get any future. Both the optical telegraph and the Photophone were replaced by their electrical analogues. Years of intense research work and a number of inventions followed before optical communication systems became an inherent part of our present life.

As stated above, optical signals could not be reliably transmitted through open air. The approach to transmit light within a certain medium is based on the phenomenon of total internal reflection: light can be confined in a material surrounded by other materials with lower refractive index, such as glass in air. The first experiments on light confinement were shown in a flowing jet of water in the 1840s. In a way, this experiment was so successful that it can still be observed in some famous fountains all over the world. The first fibers were essentially transparent rods of glass or plastic, which were stretched, so they were long and flexible. A real breakthrough in fiber optics was achieved by the Dutch scientist Abraham van Heel of the Technical University of Delft and by Harold H. Hopkins and Narinder Kapany of Imperial College in London. In contrast to the first experiments, where reflections at glass-air interface were used, their fibers of glass or plastic were covered by a transparent cladding with lower refractive index. This protected the total internal reflection interface from contaminations and reduced the crosstalk between fibers. The next important step was development of glass-clad fibers by Lawrence Curtiss. These first fibers were too lossy for communication systems. Attenuation of 1 decibel per meter was fine for some medical applications (like for example looking inside the body), but communications operated over much longer distances and required losses to be not more than 10 or 20 decibels per kilometer (dB/km). In 1960s, Charles K. Kao succeeds to achieve propagation losses in a glass fiber as low as 20 dB/km. This opened new perspectives to transmit optical signals over fairly large distances.

Other important breakthroughs in optical communications are related to the invention of the ruby laser by Theodore Maiman in 1960, and a continuous-wave helium-neon laser, shown later in the same year. Ten years later the first continuous-wave room-temperature semiconductor laser was invented. The semiconductor heterojunction lasers were made by the group of Zhores Alferov at the Ioffe Institute in Leningrad (now St. Petersburg). This last invention can undeniably be considered as the birth of what is today called semiconductor integrated optics.

Development of modern optical fiber networks is caused by the availability of compact optical sources and low-loss optical fibers on one hand, and by the ever increasing demand for data transmission capacity on the other hand. The continuously increasing number of customers requires specific data management techniques. The rapidly growing need for high capacities can be satisfied by using optical multiplexing techniques: Wavelength-Division Multiplexing (WDM) and Optical Time-Division Multiplexing (OTDM). That puts an increasing demand on the optical hardware used in fiber networks. All-optical signal processing components enable the highest switching rates and allow all-optical regeneration of pulse streams. This enables data transmission without converting the optical signal into electrical current, except at the final

destination. One of the key building blocks of various optical circuits is the Mach-Zehnder Interferometer (MZI). The history of the Mach-Zehnder interferometer starts over one hundred years ago in the world of free-space optics and it is generally used for optical measurements. In a MZI [2], light from a single source is split into two beams which travel along different optical paths after which they are recombined. The resulting interference pattern can be used to detect changes in the optical path length in one of the two arms. The Mach-Zehnder interferometer can be used for example to determine the phase shift caused by a small sample which is placed in one of two beams from a coherent light source. In the following sections, the use of MZIs as switches will be explained.

1.2   Switching in Mach-Zehnder interferometers

In integrated optics Mach-Zehnder interferometers have also found various applications. One of the wavelength converters with the best overall performance is the MZI-based all-optical wavelength converter, demonstrated in [3, 4, 5]. It is schematically depicted in Fig. 1.1. It performs well on stability, bitrate, chirp and conversion efficiency [3].
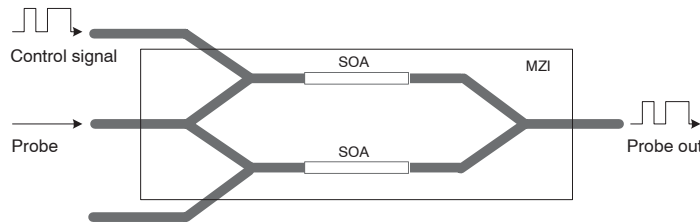
Figure 1.1: Schematic of a MZI-based wavelength converter.

Mach-Zehnder interferometer based optical switches are also widely used in Photonic Integrated Circuits (PIC). This type of switch usually consists of an optical splitter and an optical combiner, connected with each other by two interferometer arms, as schematically depicted in Fig. 1.2.

An optical signal injected in one of the input ports, is equally distributed over the interferometer arms of the MZI switch by the 2×2 optical splitter[1], as can be seen from Fig. 1.2. The two signals at the output of the 2×2 splitter have a (constant)

---

[1]Usually optical splitters and combiners have a coupling ratio of 0.5/0.5. Since half of an optical signal in terms of decibels is -3 dB, they are often referred to as 3-dB splitters and 3-dB combiners.
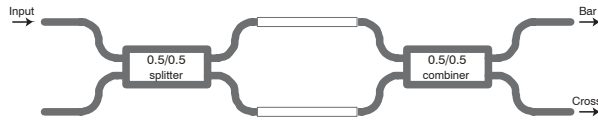
Figure 1.2: Schematic of a 2×2 MZI-based switch.

phase difference of $\pi/2$ rad. If the two arms are equal, the 3-dB combiner will cause a destructive interference at the bar-output port, and a constructive interference at the cross-output port. By introducing a phase shift of π in one of the interferometer arms, the signal can be switched from the cross-output port to the bar-output port. The required phase shift is related to the change in the refractive index. A relatively small refractive index change in the interferometer can be sufficient for the switching. Several physical effects can provide the required phase shifting. These are summarized below.

Electro-optic effect

The application of an electric field to many semiconductor materials leads directly to a change in the real and imaginary refractive indices [6]. The shift in real refractive index with electric filed, Δn, is known as electrorefraction, and the shift in the imaginary component, $\Delta \alpha$, is known as electroabsorption. Numerous phenomena may be employed for generation of field-induced index changes [7, 8].

The Pockels and Kerr effects are also known as the linear and quadratic electro-optical effects, respectively. The Pockels effect causes a shift in real refractive index and appears in semiconductor materials with noncentrosymmetric crystal structures. The quadratic dependence on electric field (shown by the Kerr effect) is relatively small in III-V semiconductor materials.

The Franz-Keldysh effect [9] causes both electrorefraction and electroabsorption. Here, an externally applied electric field gives rise to a shift of the absorption spectrum and results in the absorption of photons with lower energies than in absence of the applied field. Such a shift in absorption also implies a change of the refractive index, because of fundamental reasons (see section 2.2).

To enhance the electroabsorption and electrorefraction, Quantum Well (QW) structures can be used. The effects employed in quantum wells are the Quantum Confined Stark Effect (QCSE) and the bandfilling effect [10]. The Quantum Confined Stark effect causes a red shift of the interband transition with applied field [11]. Bandfilling of a quantum well at zero applied field introduces a blockade of the absorption

near the bandgap [12]. Carrier depletion at an applied field removes this blockade, resulting in an effective red shift of the absorption spectrum. Therefore, this effective red shift of the absorption spectrum adds up to the QCSE. This yields a red shift of the bandgap with increasing external field.

Opto-optic effect

If refractive index or absorption depend on optical power, it is possible to switch Mach-Zehnder interferometer with optical signals. This requires thus a nonlinear element. A Semiconductor Optical Amplifier (SOA) can be used in the interferometer arms as such a nonlinear element. The nonlinear behavior of the SOA originates from the carrier depletion at high optical input powers. This changes both the gain and the refractive index, which results in a phase shift of the optical signal in the SOA (more on the nonlinear operation of SOAs can be found in section 5.2). The operation of the MZI-based wavelength converter with two SOAs in the interferometer arms is based on cross modulation of two optical signals in a SOA, as illustrated in Fig. 1.1. In the SOA-based switches, an optical control signal can be introduced onto one arm of the MZI to deplete the carriers in the corresponding amplifier. Thus, in SOA-based switches when the control signal is on, the data signal is switched from the cross- to the bar-output port. The required refractive index change is obtained by all-optical switching: here the electronic control signal is replaced by an optical one.

Thermo-optic effect

In thermo-optic switches, a change of the refractive index is obtained by variation in temperature. Raising the temperature of the material directly decreases the bandgap energy E_g, which causes a refractive index change of the material. The temperature dependence of the bandgap energy can be written as [13]:

$$E_g(T) = E_g(0) - \alpha \frac{T^2}{\beta + T}, \tag{1.1}$$

where $E_g(0)$ is the bandgap at 0 K, α and β are coefficients independent of the composition of $In_{1-x}Ga_xAs_yP_{1-y}$, which values are 0.49 meV/K and 327 K, respectively [14]. The change in the refractive index induced by the change in temperature can be calculated as:

$$\Delta n = -\alpha \frac{\lambda}{hc} \left(\frac{2\beta T + T^2}{(\beta + T)^2} \right) \Delta T. \tag{1.2}$$

The temperature change of the interferometer arm might locally be induced by heaters. A disadvantage of such devices is the long switching time.

5

1.3 Mach-Zehnder Interferometers based on self-switching

The switching techniques described in the previous section require a control signal: an electrical control signal is employed directly in electro-optical switches, or for changing the temperature of either of two interferometer arms, and, finally, an optical control signal is required for opto-optic switching. That complicates the circuitry and operation due to the fact that synchronization is needed between the switch and the optical signals.

A new switching technique in Mach-Zehnder interferometers has been suggested in [15]. This is a technique in which the incoming optical signal itself determines the path through the switch, without involving an external control mechanism. Unlike in the MZI structures mentioned above, in this switching technique the input signal is distributed unequally over the interferometer arms, as schematically depicted in Fig. 1.3.

Such a Mach-Zehnder interferometer consists of the following components:

- An input $2{\times}2$ optical coupler with asymmetric coupling ratio $(1 - X)/X$. This coupler distributes the input signal unequally over the interferometer arms.

- An output $2{\times}2$ or $2{\times}1$ optical combiner. In this coupler the two signals from the interferometer arms are recombined. The coupling ratio of the output coupler should not necessarily be symmetric. Its choice is determined by the application and will be treated in the following chapters.

- Nonlinear phase shifters. The phase shifter sections provide an intensity depended change in the refractive index and, therefore, a phase difference between the signals from the interferometer arms.

When light is injected in one of the input ports (e.g. port 1, as shown in Fig. 1.3), the optical power is distributed unequally over the two interferometer arms (with X < 0.5 and input port 1, the high-power arm is the upper one). In the high-power arm, an intensity dependent phase shift can be induced due to Self-Phase Modulation (SPM), while in the low-power arm almost no intensity dependent phase shift
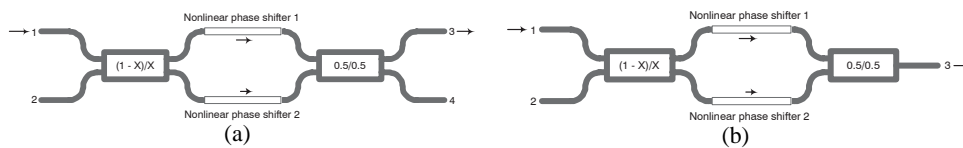
Figure 1.3: Schematic of the MZI based on self-switching. (a) $2{\times}2$ configuration and (b) $2{\times}1$ configuration.

is induced. Therefore, between two optical signals of unequal intensities a nonlinear phase shift $\Delta\phi_{\mathrm{NL}}$ can be induced. However, at low input power levels, the nonlinear phase shift is negligible. At higher input power levels, the phase in the high-power arm changes, and maximum output power (at port 3) can be reached if the nonlinear phase shift compensates the phase differences caused by both couplers. The phase difference between two optical signals at the 2×2 coupler outputs is $\pi/2$ rad. The two signals from the interferometer arms are then in phase, constructively interfering at the output port. An optimum recombination of the two signals is then observed. The result of this is the self-switching: the optical signals from either of the two input ports are guided to an output port depending on their signal strength, without any control mechanism in the interferometer. For the structure shown in Fig. 1.3(a), due to the phase differences induced by both 2×2 couplers, the required nonlinear phase shift is π. In case of the structure shown in Fig. 1.3(b), the required nonlinear phase shift is $\pi/2$, since the 2×1 output coupler does not induce an additional phase difference between the two signals.

The nonlinear phase shifter should provide an intensity dependent change in the refractive index and, therefore, a nonlinear phase shift $\Delta\phi_{\mathrm{NL}}$. There are several mechanisms of the refractive index change, which can be classified by the need of an external source:

- **Active phase shifters** requiring an external source (e.g. current source). Active phase shifters that can provide an intensity dependent change in the refractive index are usually based on semiconductor optical amplifiers. For optimal use of the SOAs in nonlinear applications, high values of the phase change should accompany low changes in gain. However, the gain itself should of course be as high as possible.

- **Passive phase shifters** showing refractive index changes without external powering.

In this thesis, devices based on both types of nonlinear phase shifters are reported.

1.4 Applications of the MZIs based on self-switching

A number of applications for optical fiber networks can be realized with a Mach-Zehnder interferometer based on self-switching. In this thesis, three novel applications are described and analyzed: the pattern effect compensator, the 2R-regenerator and the low-loss optical combiner. Below a short description of these devices is presented.

1.4.1   Optical signal regeneration

Already in the first prototype of optical communication systems, the optical telegraph, described in section 1.1, a sequence of relay stations was placed for regeneration of the optical signal. Regeneration in modern communication systems is a somewhat more complicated procedure. There are three levels of signal regeneration commonly used in todays optical networks: 1R-regeneration includes only re-amplification, 2R-regeneration includes both re-amplification and re-shaping, and 3R-regeneration is a combination of 2R-regeneration and re-timing. The latter, 3R-regeneration, will remain outside of the scope of this thesis.

In optical links due to fiber losses and limited power budgets there is a need to use amplifiers for increasing the scalability of optical networks. Traditionally, the amplification is achieved by converting the optical signal into an electric one, and amplification takes place in the electric domain. Subsequently, the signal is converted back into the optical form (this is also known as a Optical-Electrical-Optical (O-E-O) conversion).

Alternatively, an optical amplifier can be used, avoiding the O-E-O conversions. Optical amplification can cause a number of problems in optical networks. If the amplifier does not provide approximately the same gain for all the data bits, patterning effects occur and the quality of the optical data signal is degraded. Furthermore, optical amplifiers add ASE noise to the signal, and signal degradation accumulates over multiple amplification stages [16]. This results in bit errors. Both these sources of signal degradation can be countered with the self-switching circuits described below.

Pattern effect compensator

A serious restriction on the linear operation of semiconductor optical amplifiers is caused by the gain saturation effect. At high optical powers, carrier depletion takes place, which consequently reduces the optical gain. In optical networks this can lead to pulse form distortion, commonly referred to as the pattern effect [17]. The gain becomes dependent on the bit pattern. At longer bit times it shows up as a higher gain on the leading edge of a pulse. In this thesis we propose a novel integrated device that reduces the unwanted pulse form distortion. Furthermore, because the compensation counteracts the effect of saturation, it can also be used as a pattern-free optical amplifier providing a gain that is at least comparable to a single SOA, and with an extended input power dynamic range.

The 2×2 Mach-Zehnder interferometer based on self-switching with SOA phase shifters (SOA-MZI) can be used for the suppression of the unwanted pulse form distortions (the pattern effect). The device is schematically depicted in Fig. 1.4.
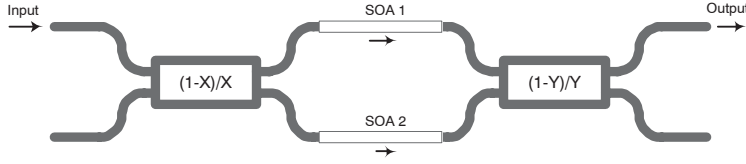
Figure 1.4: Schematic of the proposed pattern effect compensator.

The unequal distribution of the input optical signal can be achieved by using e.g. a 2×2 MultiMode Interference (MMI, see subsection 2.3.2) coupler with the coupling coefficient $X = 0.15$. The output coupler used in the circuit is a 2×2 MMI coupler with the coupling coefficient $Y = 0.5$ (the output coupler choice is discussed in chapters 5 and 6). The optical signal injected into the input port is distributed unequally over the interferometer arms. Furthermore, a phase difference of $\pi/2$ is induced between the two signals by the input MMI coupler. Ideally, SOA 2 is working in the unsaturated regime and does not induce a nonlinear phase shift. Therefore, the leading part of the optical pulse entering SOA 1 is amplified with unsaturated gain. Thus, the total phase difference across the leading part at the output equals π since also the output MMI coupler induces an additional phase difference of $\pi/2$. As a result, destructive interference for the output signal is obtained.

After the amplification of the leading part of the pulse, SOA 1 enters the saturation regime. Therefore, the pulse form distortion and a nonlinear phase shift caused by change in the refractive index in SOA 1 will take place simultaneously. If the induced nonlinear phase shift is equal to π, the two signals from the interferometric arms corresponding to the trailing part of the pulse will constructively interfere in the output coupler.

The net effect is as follows. The leading part of the distorted pulse experiences a lower transmittance, since no nonlinear phase shift is induced. However the destructive interference is incomplete because the power levels at the output coupler are unequal and some signal is still present at the output port of the interferometer. The trailing part of the pulse experiences a higher transmittance, since a nonlinear phase shift π is induced due to the carrier depletion, resulting in constructive interference. In this way, the pulse distortion is compensated.

9

2R-regenerator

Propagating through an optical network optical signals pass through several amplification cascades and splitters. The accumulation of Amplified Spontaneous Emission will deteriorate the signal-to-noise ratio and limit the transmission distance. Therefore regenerators will be needed at regular intervals in long distance links. The 2×2 SOA-MZI can be used for this, supplying an all-optical 2R-regeneration function.

Basically, our 2R-regenerator has the same structure as the aforementioned pattern effect compensator. The regeneration is based on the fact that the structure shown in Fig. 1.4 (or similar to it) has a nonlinear transfer function. This results in the redistribution of the logic signal levels and the suppression of noise added to the signal. Consequently, the accumulation of bit errors can be limited.

1.4.2   The low-loss optical combiner

An essential function in optical fiber networks is the combination of optical signals. Traditionally, the combiner is a passive function, obtained with fused fiber couplers or planar Y-junctions. For passive combination of two optical signals in photonic integrated circuits, directional couplers, Y-junctions or MMI couplers can be used. An important disadvantage of these components for combining signals is an inherent loss of at least half of the optical power, or in terms of decibels 3 dB loss (see section 7.1). This can be avoided with optical switches, but then control functions are needed to synchronize the switch with the optical signals.

In this thesis we propose a novel interferometric solution based on self-switching in Mach-Zehnder interferometers: the low-loss optical combiner. The low-loss optical combiner is aimed to reduce the unwanted 3 dB loss without using any control signals. The device is a 2×1 Mach-Zehnder interferometer, which is schematically depicted in Fig. 1.5.

For the low-loss optical combiner presented in Fig. 1.5, assuming unit input power, the expression of the output power (at port 3) can be written as:

$$P_{\text{out}} = 0.5 + \sqrt{X(1-X)} \sin(\Delta\phi_{\text{NL}}). \tag{1.3}$$

The second term of the expression describes an extra output power obtained with respect to a passive 3 dB combiner. This suggests a maximum output power can be reached if the nonlinear phase shift $\Delta\phi_{\text{NL}} = \pi/2$, which compensates the coupler-induced phase difference. The two signals from the interferometer arms are then in phase, constructively interfering at the output port, yielding a optimum recombination of two signals:

$$P_{\text{out}} = 0.5 + \sqrt{X(1-X)}. \tag{1.4}$$
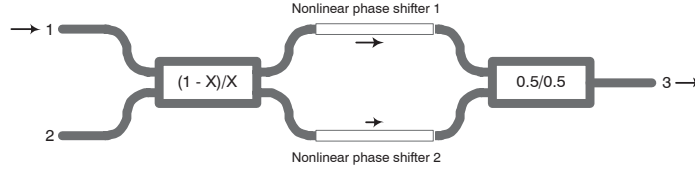
Figure 1.5: Schematic of the proposed low-loss optical combiner.

From the Eq. 1.4 it can be seen that the maximum output power can be obtained if $X = 0.5$. In that case, however, no $\Delta\phi_{NL}$ can be induced. So in practice the choice of X implies a compromise between efficient $\Delta\phi_{NL}$ and output power. Using port 2 instead of 1 mirrors the situation: both the coupler-induced phase difference and the nonlinear phase shift occur in the other arm, compensating each other.

Two realizations of the low-loss optical combiner circuits are presented in this thesis. One of them is based on semiconductor optical amplifiers, which are used as the nonlinear phase shifters. The second one is based on quantum dot material, which provides an intensity dependent phase shift in a fully passive way.

1.5   Structure of this thesis

This thesis describes and analyzes the realization of photonic integrated circuits, containing Mach-Zehnder interferometers based on self-switching, and their applications in optical networks. Chapter 2 introduces the InP-based material system, which is an integration platform for the MZIs. This chapter also explains principles of optical waveguiding and waveguide components used in these MZIs. The fabrication technology is discussed in chapter 3. The SOA-MZIs are realized in a layer stack, in which active and passive regions have been monolithically integrated. The passive MZIs are realized in a layer stack containing quantum dot structures. Chapter 4 describes the design and the characterization of the main components of the Mach-Zehnder interferometers. Chapter 5 is focussed on self-switching effects in the integrated MZIs. The active and passive phase shifting mechanisms are discussed in this chapter. The last two chapters deel with the applications of the MZIs based on self-switching. Chapter 6 presents two novel applications of SOA-MZIs, the pattern effect compensator and the 2R-regenerator. Chapter 7 presents two realizations of the low-loss optical combiner. The active combiner is based on all-optical switching in semiconductor optical amplifiers, whereas the passive one is based on the novel all-optical switching technique in quantum dot structures.

Chapter 2

Photonic integration on InP

This chapter describes the properties of the material system used for our photonic integrated circuits. The indium phosphide integration platform is well suitable for integration of the Mach-Zehnder interferometers based on self-switching. Further, special attention is given to the principles of optical waveguiding and of the waveguide components that are used in the Mach-Zehnder interferometers.

2.1   Introduction

In chapter 1 we have seen that all-optical signal processing in optical communication systems is a favorable technique to obtain the highest switching rates and all-optical regeneration of pulse streams, avoiding expensive optical-electrical-optical (O-E-O) conversions. It is possible to integrate various optical components together on one chip and connect them by means of optical waveguides. These chips are commonly known as Photonic Integrated Circuits (PIC). Photonic integration leads to a drastic reduction in dimensions and interconnection costs of complex optical circuits and devices. These compact units are less sensitive to the environmental changes than their counterparts constructed of stand-alone components. In Fig. 2.1(a), a Mach-Zehnder interferometer implemented with stand-alone fiber based components in a lab is shown. The circuit takes a large volume and is sensitive to environmental changes. In Fig. 2.1(b), a photonic integrated version of the same component is shown. The integrated version of this device takes an area less than 1 mm^2 and shows stable operation.

There is a number of material systems that allow integration of optical devices, a.o. silica-on-silicon [18], polymer materials [19], LiNbO$_3$ [20] and III-V semiconductors. The III-V semiconductor material system indium phosphide / indium gallium

(a)

~ 3 mm

(b)
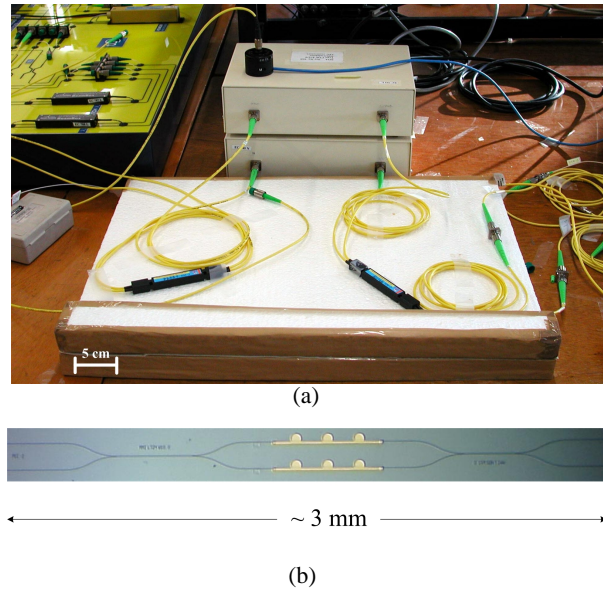
Figure 2.1: Reduction of volume through photonic integration. (a) MZI constructed of stand-alone components and (b) MZI photonic integrated on a chip.

arsenide phosphide (InP/In$_{1-x}$Ga$_x$As$_y$P$_{1-y}$) is suitable for the fabrication of a variety of optoelectronic devices for optical communication systems. It allows to fabricate devices operating in the low-loss and low-dispersion transmission windows of the glass fibers at wavelengths of 1.3 μm and 1.55 μm[1] [21]. This material system is also suitable for high speed electronics because of the high carrier mobility. That makes it possible to integrate photonic and electronic functions on one chip. In this material system fabrication of both transparent optical devices and optical amplifiers is possible. This material system is therefore chosen to realize the Mach-Zehnder interferometers based on self-switching, which are subject of this thesis.

2.2 InP-based material system

This section describes the indium phosphide / indium gallium arsenide phosphide material system and its relevant optical properties.

---

[1]The devices described in this thesis are operating in the 1.55 μm transmission window.
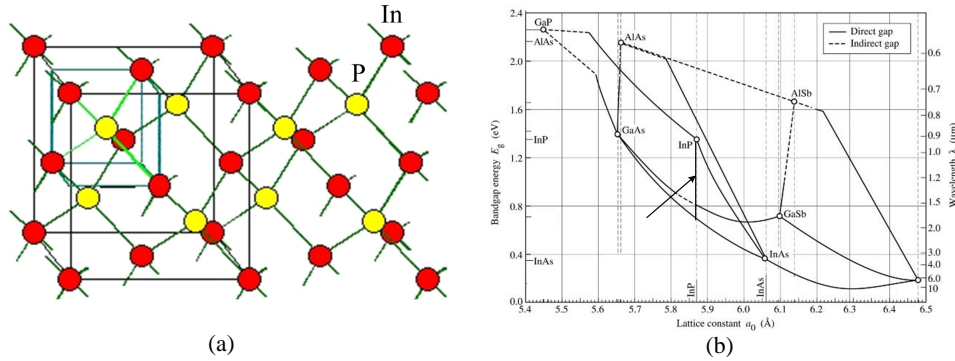
Figure 2.2: (a) Zincblende crystal structure of InP. (b) Energy bandgap vs lattice constant for the III-V semiconductors. The arrow points to the quaternary alloys lattice-matched to InP.

2.2.1 Material system possibilities

The binary compound InP forms an important integration platform for a variety of optoelectronic components. Indium phosphide has a zincblende lattice structure, which is similar to the diamond lattice (see Fig. 2.2(a)). The InP lattice consists of two intertwined sublattices, one with only indium atoms, and one with only phosphorus atoms. Indium phosphide is a direct bandgap semiconductor material, which implies that radiative transitions of electrons from the conduction band into the valence band are strong. Indium phosphide can be combined with a more complex alloy: indium gallium arsenide phosphide, or $In_{1-x}Ga_xAs_yP_{1-y}$. The bandgap energy and the refractive index of this quaternary alloy is dependent on the compositional fractions x and y. Therefore, variation of x and y provides additional flexibility in choosing a bandgap. $In_{1-x}Ga_xAs_yP_{1-y}$ can be grown on InP with high quality when there is lattice matching between the materials. The lattice matching is an essential requirement to allow growth of crystalline layers on top of each other. In Fig. 2.2(b), the relation between the lattice constant and the energy bandgap for III-V semiconductors can be seen.

The bandgap of the quaternary lattice-matched alloy $In_{1-x}Ga_xAs_yP_{1-y}$ can vary in the range of energies between 0.75 and 1.35 eV, corresponding to an absorption edge of 1.65 μm to 0.92 μm [21]. Therefore, it can be either transparent or absorbing at the wavelengths within the transmission window around 1.55 μm. This also means that transparent, amplifying (as it is a direct bandgap material) and absorbing devices can be fabricated on one chip, based on quaternary materials grown on InP.

The quaternary $In_{1-x}Ga_xAs_yP_{1-y}$ material can be considered as an alloy of four

binary materials: InP, InAs, GaAs and GaP. Its material properties can therefore be approximated by linear interpolation of the properties of these binaries. The lattice constant can in this way be calculated according to Vegard's law. Applying Vegard's law to $In_{1-x}Ga_xAs_yP_{1-y}$, the following relationship between the composition parameters is experimentally obtained for lattice-matching to InP [13]:

$$x = \frac{0.4526y}{1 - 0.031y}, (0 \le y \le 1).$$ (2.1)

The bandgap energy is found by S. Adachi as:

$$E_g[eV] = 1.35 - 0.72y + 0.12y^2.$$ (2.2)

In case of lattice matching, the quaternary alloy $In_{1-x}Ga_xAs_yP_{1-y}$ is often referred to as InGaAsP. In the literature, it is common to denote InGaAsP by its absorption edge wavelength (at room temperature). For example, Q(1.55) and Q(1.25) correspond to the absorption edge wavelength of 1.55 and 1.25 μm, respectively. We will refer to these film layer compositions often in this thesis, since in the wavelength range around 1.55 μm, Q(1.25) forms a transparent waveguiding layer, whereas Q(1.55) forms an absorbing layer suitable for an amplifier. Lattice-matched to InP Q(1.25) has a bandgap energy of 0.992 eV, and a composition $(x, y) = (0.252, 0.547)$ and Q(1.55) has a bandgap energy of 0.8 eV, and a composition $(x, y) = (0.418, 0.898)$.

2.2.2   Optical properties

Knowledge of the optical properties of the material system is very important in the design and analysis of photonic integrated devices. Below, the physical background of the optical properties of InGaAsP/InP heterostructures is reviewed.

Band structure

The behavior of electrons and holes in semiconductor materials can be described by the Schrödinger equation. By solving this equation, the relationship between the energy and momentum (wave vector **k**) of an electron can be found [22, 23]. For periodic lattices this results in a band structure. In general, such a band structure is rather complicated, but for small values of k, the parabolic band approximation can be sufficient to describe bulk materials. The energies of the states in the conduction and valence band, E_2 and E_1 can be written as:

$$E_2 = E_c + \frac{\hbar^2 k_2^2}{2m_e} \text{ and } E_1 = E_v - \frac{\hbar^2 k_1^2}{2m_h},$$ (2.3)

where E_c and E_v represent the band edge energies of the conduction band and the valence band, respectively, m_e and m_h are the effective masses of the electron and the hole, respectively, and k_2 and k_1 are the corresponding wave vectors. The effective masses depend on the material properties. The band structure of a direct bandgap semiconductor in the parabolic band approximation is schematically depicted in Fig. 2.3.
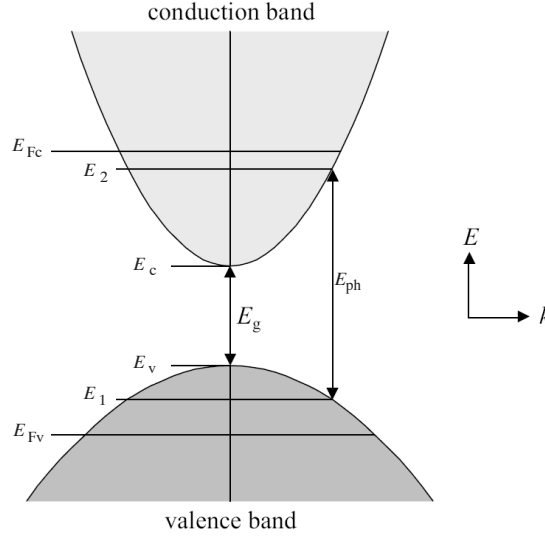
Figure 2.3: Direct bandgap semiconductor band structure in the parabolic band approximation.

The bandgap energy is the difference between the band edge energies of the conduction (the lowest empty allowed energy band) and the valence (the highest occupied band) bands: $E_g = E_c - E_v$. A transition from the conduction band to the valence band, or vice versa, is restricted by the conservation of both energy and momentum in accordance with:

$$E_{ph} = E_2 - E_1 \quad \text{and} \quad \Delta k = k_1 - k_2 = 0. \tag{2.4}$$

Therefore, the photon energy E_{ph} associated with such a transition can be written as:

$$E_{ph} = E_g + \frac{\hbar^2 k^2}{2m_r}, \tag{2.5}$$

17

$E_{ph}<E_g$
transparent
n-type

$E_{ph}\approx E_g$
active
undoped

$E_{ph}<E_g$
transparent
p-type

electrons

cond. band

$E_{QF,n}$

$e\cdot V_{bias}$

$E_{QF,p}$

holes

valence band
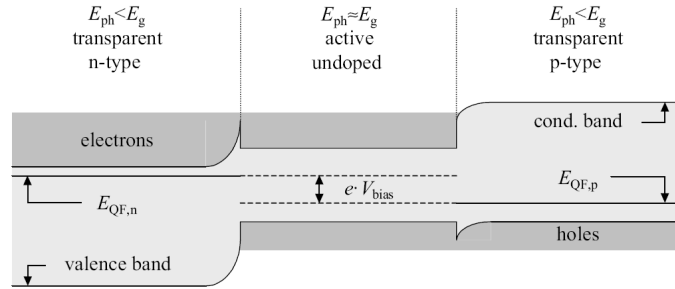
Figure 2.4: Band diagram of a double heterostructure [21].

where m_r is the reduced mass:

$$\frac{1}{m_r} = \frac{1}{m_e} + \frac{1}{m_h}. \tag{2.6}$$

Many semiconductor devices have a multilayer structure. When a layer of a low bandgap material (e.g. InGaAsP) is placed between two layers with larger bandgap (e.g. InP), such a structure is referred to as a double heterostructure. It is schematically depicted in Fig. 2.4. In double heterostructures carrier confinement can easily be created in the low bandgap layer. Furthermore, the low bandgap material of the inner layer has a higher refractive index than the outer layers. Therefore, light can be guided in this layer as well.

If the width of a low bandgap layer of a double heterostructure decreases to the order of the electron wavelength, the wave-like behavior of electrons and holes can not be neglected anymore. The electrical and optical behavior of such a structure is determined by quantum effects. The electrons and holes are confined in this thin layer and their energies can be defined by solving the quantum mechanical equations, which result in a number of discrete energy states within the quantum well. This particular kind of heterostructure, in which one thin well layer is surrounded by two barrier layers, is referred to as a Quantum Well (QW).

In bulk materials the density of states in energy $\rho(E)$ is dependent on the square root of the energy, i.e. $\rho(E) \propto \sqrt{E}$. Therefore, the optical absorption spectrum has a similar form, following directly from $\rho(E)$. This results in an absorption edge that rises as a square root of the energy. In QWs the increase of density of states is step-like. Since in quantum wells besides the momentum conservation rule, there is a selection rule, which allows transitions between states with the same quantum number in the
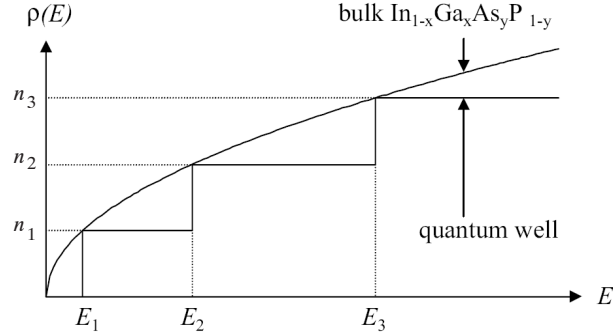
Figure 2.5: Density of states versus energy for bulk and quantum well materials. n_1, n_2 and n_3 denote discrete energy levels in a QW.

conduction and the valence bands [24], the optical absorption is a series of steps, with one step for each quantum number. Both cases, bulk and quantum well, are compared in Fig. 2.5.

The essential difference between quantum well and bulk active materials is that the energy levels of the quantum well depend on the well and barrier width. Therefore, quantum well material provides an additional degree of freedom in the design of optical (active) devices. Besides, due to relatively strong nonlinear properties, which are discussed in chapter 5, QW structures can be employed in compact electrorefractive and all-optical switches.

Quantum wells are one-dimensional quantum confined systems. The InP material system, however, also allows to grow three-dimensional confined systems, quantum dots (QDs). In QDs electrons and holes are confined in all three orthogonal directions [25]. These structures open new possibilities of bandgap engineering at the nanometer scale. Besides, these nanostructures are expected to provide strong all-optical nonlinearities, which will be exploited in Chapters 5 and 7 of this thesis.

Interaction with light

The effect of the material on an optical wave propagating through it is represented either by the refractive index n or by the dielectric constant ϵ ($\epsilon = n^2$). The refractive index is generally a complex number. The complex refractive index $n'(\omega)$ is given by

$$n' = n_R(\omega) + j n_I(\omega), \tag{2.7}$$

where $n_R(\omega)$ and $n_I(\omega)$ are the real and imaginary values of the refractive index, respectively. The real part of the refractive index corresponds to the polarizability of the material and determines velocity of an optical wave in a material. The imaginary part of the refractive index defines the absorption.

For the complex refractive index, the real and the imaginary parts are interrelated by the Kramers-Krönig relations [26]:

$$
\begin{aligned}
n_R(\omega) - 1 &= \frac{2}{\pi} P \int_0^\infty \frac{\omega' n_I(\omega')}{\omega'^2 - \omega^2} d\omega', \\
n_I(\omega) &= -\frac{2\omega}{\pi} P \int_0^\infty \frac{n_R(\omega')}{\omega'^2 - \omega^2} d\omega',
\end{aligned}
\tag{2.8}
$$

where P denotes the Cauchy principal part of the integral[2]. We will use these relations in the next chapters for describing the behavior of SOA-MZIs and QD-MZIs.

In practical cases, as we will see in chapter 5, it is useful to work with the absorption coefficient α rather than with the imaginary part of the refractive index. The absorption coefficient $\alpha(\omega)$ is related to the imaginary part of the refractive index as:

$$
\alpha(\omega) = \frac{4\pi}{\lambda} n_I(\omega),
\tag{2.9}
$$

where λ is the wavelength of light in the vacuum.

The propagation constant k in the medium is related to the propagation constant in the vacuum k_0 by means of a dielectric constant, and is a complex number as well:

$$
k = k_0 n' = k_0(n_R + j n_I).
\tag{2.10}
$$

Therefore, the magnitude, phase and time dependence of an electrical field propagating in the z-direction in a material is given [6]:

$$
E = E_0 \exp(-\frac{\alpha z}{2}) \exp(-j k_z z) \exp(j\omega t),
\tag{2.11}
$$

where E_0 is field amplitude, k_z is the propagation constant in the z-direction, with the absorption taking the form of exponential decay. If no absorption is taken into account, the refractive index is purely real. This is usually a case considering optical properties of waveguides.

---

[2]The Cauchy principle part of the integral $P \int_0^\infty \equiv \lim_{\delta \to 0} \left(\int_0^{\omega-\delta} + \int_{\omega+\delta}^\infty \right)$.

2.3   Waveguide components

In this section we will look at three main components that are needed to realize our devices. These components are: passive waveguides, optical couplers and semiconductor optical amplifiers. Here we will discuss physical principles, geometry and features of these components.

2.3.1   Passive waveguides

Waveguides are the basic components of photonic integrated circuits. They form a basis for a number of optoelectronic devices, like e.g. lasers, modulators, interferometers, etc. Without further processing, waveguides may also be used as passive elements executing different functions, like e.g. coupling or filtering.

The optical waveguiding is based on the confinement of light in the higher refractive index layer of a double heterostructure (InGaAsP-layer). This layer is commonly referred to as the film layer, whereas the surrounding lower refractive index layers are known as the cladding layers (InP-layers). The heterostructure provides an index contrast in the transversal direction and, therefore, light confinement in that direction. Without further structuring, such a configuration is also known as a slab waveguide. The lateral confinement of light can be obtained in a ridge structure, where the lateral index contrast is created by locally etching the waveguide material outside of the ridge. A three-dimensional schematic representation of a typical ridge waveguide and a Scanning Electron Microscope (SEM) picture of the fabricated one are shown in Fig. 2.6.
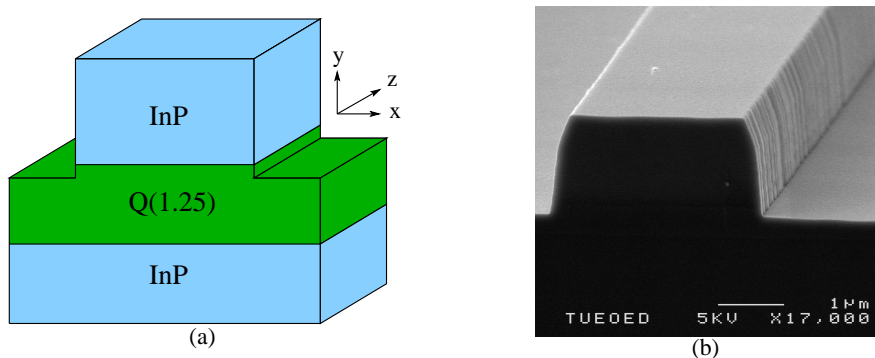
Figure 2.6: Ridge waveguide. (a) Schematic representation and (b) SEM picture of an etched structure.

According to Fiedler and Schlachetzki [27], the refractive indices of the film layer at a wavelength of 1.55 μm lie between $n = 3.22$ for Q(1.00) and $n = 3.39$ for Q(1.3), whereas the refractive index of InP is $n = 3.17$.

The function of the passive waveguides in photonic integrated circuits is transportation of optical signals between different locations in the circuit. Realization of our devices will require two types of passive waveguides: straight and curved waveguides. The ability to change the direction of the guided optical signal is essential, and this can be achieved in curved waveguides.

In a ridge waveguide only a discrete number of lateral field patterns can be supported. These patterns, waveguide modes, are stable and propagate along the waveguide with a characteristic propagation constant, phase velocity, and polarization. If an optical field $E(x)$ enters a waveguide, it excites a number of modes of the following form:

$$E_{l,m}(x, z) = E_{l,m}(x) \cdot \exp(-j\beta_{l,m}z), \qquad (2.12)$$

where l, m are the vertical and horizontal mode orders, $\beta_{l,m}$ denotes the propagation constant of the mode l, m (this is actually k_z of the mode, with z the propagation direction). With $l = 0$ and $m = 0$, the mode is referred to as the zero-order mode, or the fundamental mode. Each optical mode can be described by an effective refractive index, which is a weighted index that the mode experiences propagating through a waveguide. The effective index takes into account the refractive indices of waveguide layers and the confinement factor of each of these layers.

The effective refractive index $N_{l,m}$ of an optical mode l, m in terms of propagation constant can written as:

$$N_{l,m} = \frac{\beta_{l,m}}{k_0}, \qquad (2.13)$$

where k_0 is the wave number in the vacuum, defined as $k_0 = 2\pi/\lambda$.

Waveguides can either support only one mode (monomode waveguides), or a number of modes (multimode waveguides). This can be controlled by adjusting the design parameters: waveguide width, film layer thickness and the etching depth. In the vertical direction, usually only one mode is supported, and the index l is left out.

We distinguish modes of two polarizations: Transverse Electric (TE-) and Transverse Magnetic (TM-) modes. A TE-mode has its electric field component in the plane of incidence (x-direction in Fig. 2.6(a)). The TM-mode has its magnetic component in the plane of incidence.

A good optical propagation minimizes the insertion losses of the entire photonic integrated circuit, which results e.g. in reduction of the optical power needed for switching. Therefore, low propagation losses in passive waveguides is an important condition for the successful realization of the required optical functions.

22

Waveguide losses

Waveguides have propagation losses. The optical signal with the initial intensity I_0 propagating through a waveguide is exponentially attenuated with distance z:

$$I(z) = I_0 \exp(-\alpha z), \qquad (2.14)$$

where α is the loss factor[3], [cm^{-1}]. These losses can result from photon absorption and from scattering.

A number of absorption mechanisms can contribute to the losses. The interband absorption is inherent to semiconductors and increases rapidly as the energy of the propagating photon approaches the bandgap energy of the material. Based on the ideal band structure discussed earlier in this chapter, the photon absorption would abruptly start at the bandgap energy and increase with the density of available electron states for higher photon energies. In reality, the energy bands are not abrupt, but extend into the bandgap forming so-called band tails [6]. Therefore, absorption takes place even for wavelengths longer than the absorption edge. This photon absorption mechanism is known as the band tail absorption, and in accordance with the Urbach rule is exponentially dependent on $(E_g - h\nu)$. In addition, intraband transitions contribute to the losses. This effect is known as the free carrier absorption. Generally, the absorption due to free carriers increases with the wavelength and the carrier density.

Scattering losses are caused by the refractive index fluctuations at the waveguides borders, as a consequence of sidewall and interface roughness. The scattering losses can be described (see e.g. [28, 29]) as:

$$\alpha = C \frac{(\Delta n)^2 E^2}{P}, \qquad (2.15)$$

where Δn is the refractive index contrast at the sidewall, E is the field amplitude at the sidewall, P is the mode optical power, and C is a constant depending on the roughness (which can be determined empirically). As Eq. 2.15 suggests, the scattering losses are proportional to the square of the optical field amplitude and the index contrast at the sidewalls, normalized by the power. Therefore, it can be concluded that low contrast waveguides are beneficial to obtain low losses. Also, propagation losses can be reduced by using a wider waveguide, since then the field amplitude at the sidewall is smaller. However, the latter is achieved at the expense of an increasing number of supported optical modes.

The radii of the curved waveguides are usually in the range of several hundreds of microns to one millimeter. The need for a large radius is based on loss considerations:

---

[3]Losses are often expressed in dB/cm. In that case $\alpha_{dB} = 4.34\,\alpha$ and $I(z) = I_0 10^{(-\alpha_{dB} z/10)}$.
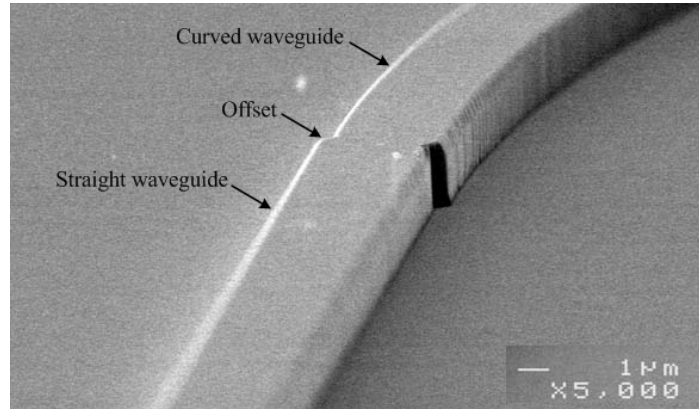
Figure 2.7: SEM picture of a straight and a curved waveguide with an offset between them.

as the waveguide changes direction, the mode is pulled outwards [29]. As a result, some of the optical field energy radiates out of the waveguide. Other losses are caused by coupling losses at the beginning and the end of the curved waveguide, and by scattering losses at the waveguide walls. Because the mode profile shifts, the field is stronger at the outer edge. The scattering losses are therefore higher (see Eq. 2.15) than in a straight waveguide. The waveguide should be made wide, so that at least the inner edge does not contribute to the losses. In a curved waveguide, the mode profile becomes narrower than in a straight one of the same width, and shifts outwards. The coupling losses between a curved and a straight waveguide can be minimized by introducing an offset between them and by making the straight waveguide narrower. In this case, the mode field profiles of the two waveguides overlap better. In Fig. 2.7, a SEM picture of a fabricated curved-straight waveguide junction is shown.

The offset between a straight and a curved waveguide can be calculated according to:

$$\Delta r \cong \frac{1}{R} \left[\frac{2N w_e^2}{\lambda_0} \right]^2 , \qquad (2.16)$$

where R is the radius of the curved waveguide, w_e is the effective width of the straight waveguide (the width plus the exponential tails of the mode in the cladding layers).

Design issues and optimization of the passive waveguides, their fabrication and characterization results will be discussed in chapter 4.

2.3.2 Optical couplers

Optical power couplers are used in our Mach-Zehnder interferometers for the unequal distribution of the input signal over the interferometer arms and for combining the two signals at the output. Different types of couplers are available. For devices investigated in this thesis, directional and MultiMode Interference (MMI) couplers are considered.

Directional couplers

The operation principle of a directional coupler is based on optical power exchange between two coupled waveguides. Coupled waveguides are two identical waveguides, which are placed in close physical proximity. In such a configuration, the evanescent field of a mode in one waveguide can excite an optical mode in the other one [6]. Through coupling of the evanescent fields, optical power may be transferred between the waveguides. This is illustrated in Fig. 2.8.

Consider two identical ridge waveguides a and b at the distance d from each other. They can propagate optical modes of the form:

$$
\begin{aligned}
E_a(z) &= e_a(z)\exp(-j\beta_a z), \\
E_b(z) &= e_b(z)\exp(-j\beta_b z),
\end{aligned}
\tag{2.17}
$$

with $\beta_a = \beta_b$, e_a and e_b are slowly changing complex functions in the z-direction according to:

$$
\begin{aligned}
e_a(z) &= \cos(cz), \\
e_b(z) &= j\sin(cz),
\end{aligned}
\tag{2.18}
$$
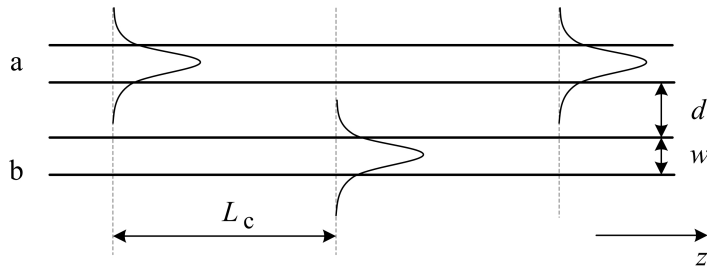
Figure 2.8: Coupling between two parallel waveguides.

where c denotes a coupling coefficient. The transfer of optical power from one waveguide to another one is periodic in the z direction:

$$
\begin{aligned}
P_a(z) &= \cos^2(cz), \\
P_b(z) &= \sin^2(cz).
\end{aligned}
\tag{2.19}
$$

The optical power transfers with a period given by the coupling length L_c for which the complete energy transfer from one waveguide to another takes place. It is called the coupling length of the device:

$$
L_c = \frac{\pi}{2c}.
\tag{2.20}
$$

Half of the energy will be transferred at half of this length. Splitting the optical energy equally between the two waveguides results in a structure known as a 3-dB coupler. By choosing an appropriate length, any coupling ratio can be obtained.

For the 100% coupling in the above mentioned example, it was assumed that the propagation constants in both waveguides are equal, which is equivalent to $\Delta\beta_{ab} = \beta_a - \beta_b = 0$. In this case the coupling is synchrone. However, if $\beta_a \neq \beta_b$, the coupling is asynchrone, and the expressions for e_a and e_b become more complicated. In [30], the following expressions for the asynchrone coupling are presented:

$$
\begin{aligned}
P_a(z) &= (1 - \rho^2 \cos^2(c'z)), \\
P_b(z) &= \rho^2 \sin^2(c'z),
\end{aligned}
\tag{2.21}
$$

where

$$
\begin{aligned}
\rho^2 &= \frac{c^2}{c^2 + (\Delta\beta_{ab})^2}, \\
c' &= \sqrt{c^2 + (\Delta\beta_{ab})^2}.
\end{aligned}
\tag{2.22}
$$

From Eq. 2.21 it can be seen that maximum only a fraction of optical power ρ is coupled into the other waveguide. The distance for maximum transfer of power is shorter than in the synchrone case.

In an effective index approximation [31, 32], a directional coupler can be defined as a five-layer waveguide structure with a low effective index in the middle layer. The coupling between the waveguides can then be described as an interference between a symmetric and an asymmetric system-modes, as illustrated in Fig. 2.9.

Consider light is injected into the upper waveguide. In the system-mode approach this is equivalent to excitation of two modes with equal amplitudes. In this
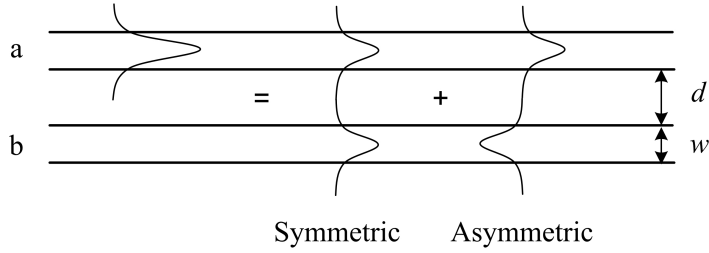
Figure 2.9: System-modes of two coupled waveguides.

case, at the starting point the modes are in phase (the phase difference $\Delta\phi = 0$), interfere constructively in the upper waveguide, and destructively in the lower waveguide. However, these modes have different propagation constants, and at a certain distance L_c they will be in antiphase ($\Delta\phi = \pi$). Therefore, constructive interference in the lower waveguide, and destructive interference in the upper waveguide is observed. The coupling length L_c and the coupling coefficient c can be defined, respectively, as:

$$L_\mathrm{c} = \frac{\pi}{\beta_0 - \beta_1} \tag{2.23}$$

and

$$c = \frac{1}{2}(\beta_0 - \beta_1), \tag{2.24}$$

where β_0 and β_1 are the propagation constants of the symmetric and asymmetric system-modes, respectively.

A real directional coupler consists of the coupled waveguides connected to in- and output waveguides. The in- and output waveguides should be uncoupled, e.g. by means of curved waveguides. At the end point of the directional coupler the power can be written as:

$$P_\mathrm{a} = \cos^2(\frac{1}{2}\Delta\phi) \ \text{ and } \ P_\mathrm{b} = \sin^2(\frac{1}{2}\Delta\phi). \tag{2.25}$$

It can be seen that with $\Delta\phi = \pi/2$, a coupling ratio of 0.5/0.5 is obtained.

It is noteworthy to mention, that this theory is only applicable for so-called adiabatic devices, where the changes in geometry are so slow, that there is no energy exchange between the two system-modes.

Directional couplers allow for any arbitrary coupling ratio. The insertion losses are low and not much dependent on the deviations of the geometry, while their coupling ratios are very sensitive to these deviations. Also, this type of couplers suffers

from polarization sensitivity, meaning that it is difficult to couple signals of different polarizations with the same coupling ratios.

MultiMode Interference couplers

The operation of MultiMode Interference (MMI) couplers is based on the self-imaging principle, which is described in [33] as: self-imaging is a property of multimode wave-guides by which an input field profile is reproduced in a single or in multiple images at periodic intervals along the propagation direction of the guide. MMI couplers are widely used in integrated optics, due to their large optical bandwidth [34], polarization insensitivity [35], compact design [36] and low insertion losses. They can provide cou-pling or splitting with a number of fixed ratios [33]. Here, theory of the MMI couplers that will be used in the MZIs is presented. The design issues and their applications will be treated in chapter 4.

A MMI coupler is based on a waveguide that can support a large number of modes. For coupling light into and out of the coupler, a number of access waveguides are used. We consider a general MMI coupler with N input and N output waveguides (coupler ports). By coupling light into the multimode waveguide through an input waveguide, the input field is decomposed into the modal field distributions of all the supported modes. A periodic interference pattern, observed along its length, can be described in terms of the beat length L_π. This is the coupling length between the two lowest order modes:

$$L_\pi = \frac{\pi}{\beta_0 - \beta_1} = \frac{\lambda}{2(N_0 - N_1)}, \tag{2.26}$$

which is similar to the coupling length of the directional coupler (see Eq. 2.23). In case no restrictions are put on the modal excitation, the direct and mirrored images are formed by general interference at distances $L = p(3L_\pi)$, with even p corresponding to the direct image, and odd p - to the mirrored image. Multi-fold images can be formed at specific intermediate positions. We can also put restrictions on the modal excitation such that only some of the guided modes at the multimode waveguide are excited by the input field. Then, short MMI couplers with "interesting" coupling ratios can be obtained [37]. The input and output access waveguides can be positioned in such a way, that interference occurs between overlapping self-images. Therefore, a new light distribution and a reduced number of overlapping images at the coupler output can be obtained. Positions, intensities, and phases of the obtained images can be calculated for purely symmetric and asymmetric input field distributions.

An MMI coupler can be defined by its length L, width W and the (effective) refractive index n at the operating wavelength λ. N self-images of equal intensities

28

$1/N$ are formed at the output of MMI couplers of length:

$$L_N^M = \frac{M}{N} 3 L_\pi, \tag{2.27}$$

where M is a multiple occurrence of the interfering N images at different device lengths. M and N do not have a common divisor [38].

Consider interference between two equal light distributions with intensity $1/N$ taking place at the output of an MMI coupler. The resulting image has an amplitude A and phase Φ, which can be represented in the following way:

$$A \exp(j\Phi) = \frac{1}{\sqrt{N}} \exp(j\phi_1) + \frac{1}{\sqrt{N}} \exp(j\phi_2). \tag{2.28}$$

where ϕ_1 and ϕ_2 are the phases of the interfering images. With phase difference $\Delta\phi = \phi_1 - \phi_2$ and mean phase $\overline{\phi} = (\phi_1 + \phi_2)/2$, Eq. 2.28 can be expressed as:

$$A \exp(j\Phi) = \frac{2}{\sqrt{N}} \cos\left(\frac{\Delta\phi}{2}\right) \exp(j\overline{\phi}). \tag{2.29}$$

An expression for intensity and phase for interference between two equally intense images has a form of:

$$
\begin{aligned}
A^2 &= \frac{4}{N} \cos^2\left(\frac{\Delta\phi}{2}\right), \\
\Phi &= \begin{cases} \overline{\phi} & \text{for } \cos\left(\frac{\Delta\phi}{2}\right) > 0 \\ \overline{\phi} + \pi & \text{for } \cos\left(\frac{\Delta\phi}{2}\right) < 0. \end{cases}
\end{aligned} \tag{2.30}
$$

Overlapping of the images at the output can be obtained when the input waveguide positions fulfill the following requirement:

$$x_i^{\text{in}} = i \frac{1}{N} W, \quad x_j^{\text{out}} = W - j \frac{1}{N} W, \tag{2.31}$$

with i and j are the input and output port numbers, respectively, and $i+j$ is an even number. Complete interference can be obtained for either symmetrical or antisymmetrical input field distributions. The number of self-images is reduced because two images interfere into one.
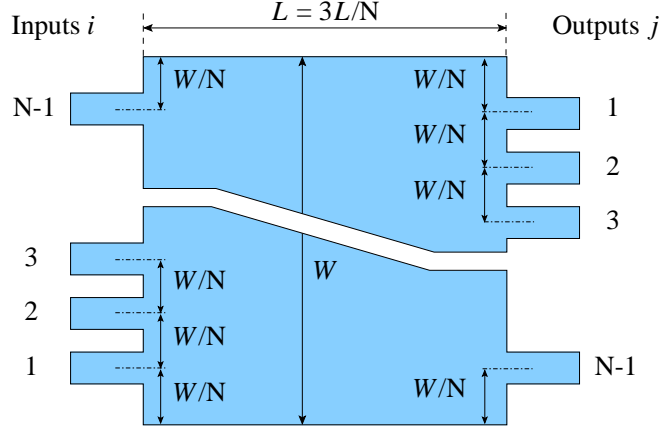
Figure 2.10: Definition of parameters of a MMI coupler.

Leaving out some derivations that can be found in [38], the intensities A_{ij}^2 and phases Φ_{ij} of the images based on Eq. 2.30 are derived:

$$A_{ij}^2 = \frac{4}{N} \cos^2\left((N-j)i\frac{1}{N}\frac{\pi}{2} - b\frac{\pi}{2}\right),$$

(2.32)

$$\Phi_{ij} = \begin{cases} -(i^2+j^2)\frac{\pi}{4N} + j\frac{\pi}{2} + b\frac{\pi}{2} & \text{for } \cos\left((N-j)i\frac{\pi}{2N} - b\frac{\pi}{2}\right) > 0 \\[2mm] -(i^2+j^2)\frac{\pi}{4N} + j\frac{\pi}{2} + b\frac{\pi}{2} + \pi & \text{for } \cos\left((N-j)i\frac{\pi}{2N} - b\frac{\pi}{2}\right) < 0. \end{cases}$$

(2.33)

Here, factor $b = 1$ for symmetrical and $b = 0$ for asymmetrical input field distributions. Fig. 2.10 shows an MMI coupler that satisfies the requirements of Eq. 2.31. Intensities and phases of the images in this coupler can be obtained from Eq. 2.33.

The theory explained above allows us to obtain MMI couplers with some fixed coupling ratios. We use the configuration shown in Fig. 2.10 with $N = 4$. It should be noticed, that though in general $N = 4$, the MMI coupler has a reduced number of used input and output ports (two input and two output ports), as shown in Fig. 2.11. Therefore, in the remaining of this thesis, this type of MMI coupler will be referred to as a 2×2 MMI coupler. Below, we will investigate the possibilities and motivate the choices.

The self-switching in Mach-Zehnder interferometers requires an unequal distribution of the input optical signal over the interferometer arms.

30
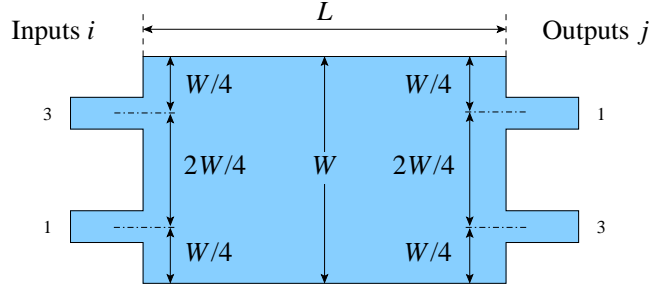
Figure 2.11: Schematic of a 2×2 MMI coupler.

With $b = 1$ (the zero-order mode entering the MMI is assumed) and $M = 1$, the MMI coupler has a length of $L = 3/4L_\pi$, and input and output ports placed at the positions $1/4W$ and $3/4W$, as shown in Fig. 2.11. Consider the case where the light signal is coupled into the input port $i = 3$. At the bar-output port ($j = 1$), the intensity A_{31}^2 calculated from Eq. 2.33 is equal to 0.146. At the cross-output port ($j = 3$), the intensity $A_{33}^2 = 0.854$. So, a coupling ratio of 0.15/0.85 is obtained. The phase difference between the two images at bar- and cross-ports can also be calculated from Eq. 2.33, and is equal to $\pi/2$ as it should be.

However, at the input of the interferometer, an inverted coupling ratio is required due to the sign of the refractive index change in the high power arm, which implies the maximum optical power could be coupled into the bar-port, resulting in the nonlinear phase shift in the upper arm of the interferometer. This coupling ratio can be obtained with $M = 3$. At a distance of $L = 9/4L_\pi$, a coupling ratio of 0.85/0.15 can be found. Indeed, from Eq. 2.33 at the bar-output port ($j = 1$), the intensity $A_{31}^2 = 0.854$. At the cross-output port ($j = 3$), the intensity $A_{33}^2 = 0.146$. The phase difference between the two images is again equal to $\pi/2$.

Another useful coupler, a 50/50-type MMI coupler, can be obtained with $M = 2$ at a distance of $L = 6/4L_\pi$. In this case, $A_{31}^2 = A_{33}^2 = 0.5$.

Finally, for the realization of a 2×1 MZI configuration (e.g. the low-loss optical combiner), a 2×1 50/50-type coupler will be needed. In this case, the intensities A_{ij}^2 for all allowed images should be constant with odd $i + j$. The 2×1 MMI coupler can be obtained by placing its output port at the center of the multimode waveguide, whereas the input port positions remain are as shown in Fig. 2.11. The length of such a MMI coupler is $L = 3/8L_\pi$.

2.3.3 Semiconductor optical amplifiers

Self-switching in active Mach-Zehnder interferometers is provided by semiconductor optical amplifiers, which are employed as nonlinear phase shifters. The phase shifting mechanism in the SOAs will be discussed in chapter 5. This section covers the fundamentals of SOAs. After a qualitative description, the gain characteristics will be treated.

Just like a passive waveguide, a semiconductor optical amplifier is a double heterostructure, but now containing an active layer, grown between two cladding layers, as shown in Fig. 2.12. The composition of the active layer is such, that its bandgap energy corresponds to the desired photon energy.

Operation principles

In an optical amplifier, the amplification process is based on transitions of free electrons between states of different energies, which result from the interaction between the incident photons and the excited electrons in the active layer. The fundamental interactions between electrons and optical waves are the transitions between two levels with different energies. These processes are spontaneous and stimulated emission, and absorption. In semiconductors the low and high levels are placed in the valence and conduction bands.

Optical emission results from the transition of electrons from the higher to the lower energy levels. The spontaneous emission is a random process, in which recombination of an electron in the conduction band with a hole in the valence band takes place.
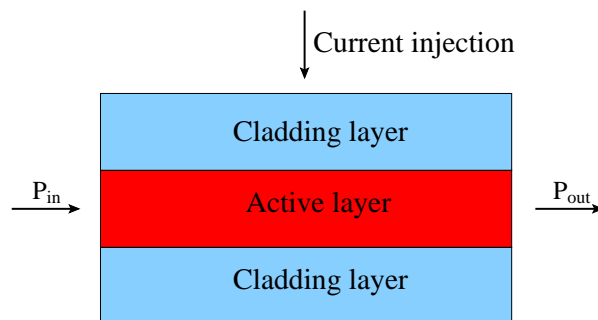
Figure 2.12: Schematic cross-section of a semiconductor optical amplifier.

In the presence of an optical field both absorption and stimulated emission processes can occur. Absorption is a generation process of electron-hole pairs in the presence of an optical field. In case of stimulated emission, an incident photon stimulates an electron-hole recombination process in the presence of an optical field, resulting in the generation of a photon with the same properties (energy, momentum and phase) as the first one. As a result of this process, photons of energy $E_{\text{ph}} = h\nu \geq E_{\text{g}}$ are emitted. Stimulated emission and absorption are two reciprocal processes.

Stimulated emission is the basic process for the operation of semiconductor lasers and semiconductor optical amplifiers. Dominance of stimulated emission can be obtained through population inversion (which is an excess population of electrons in the conduction band).

The intensity of the propagating optical field in z-direction in a gain medium is given by:

$$P(z) = P(0) \cdot e^{gz}, \tag{2.34}$$

where the factor g is the gain of the material, represented in $[\text{cm}^{-1}]$, which determines the proportional growth of the optical field:

$$g = \frac{1}{N_{\text{p}}} \frac{dN_{\text{p}}}{dz} = \frac{1}{v_{\text{g}}N_{\text{p}}} \frac{dN_{\text{p}}}{dt}, \tag{2.35}$$

where N_{p} is the photon density and v_{g} is the group velocity of the optical field. The term $\frac{dN_{\text{p}}}{dt}$ determines the net stimulated emission rate per unit volume, which can be defined as a difference between the stimulated emission and absorption rates. Here it is assumed, that the spontaneous emission is negligible. Stimulated emission requires an electron in the conduction band and a hole in the valence band. Conversely, a "hole" in the conduction band and an electron in the valence band are needed for absorption. The transition rates can be calculated knowing the number of possible transitions and the probability of their occurrence. The first depends on the density of states function in the conduction and the valence band (see subsection 2.2.2). The latter depends on the probability that a state is occupied, and on the overlap of the electron wavefunctions in the initial and final states under the electromagnetic perturbations due to the incoming photons (Fermi's Golden Rule) [3]. In thermal equilibrium, the probability that a state is occupied is described by the Fermi function. The conduction and the valence band

have their own Fermi function each, F_c and F_v, respectively:

$$F_c(E_2) = \frac{1}{\exp\left(\frac{E_2 - E_{F_c}}{k_B T}\right) + 1}, \qquad (2.36)$$

$$F_v(E_1) = \frac{1}{\exp\left(\frac{E_1 - E_{F_v}}{k_B T}\right) + 1}, \qquad (2.37)$$

where F_c and F_v is the Fermi energy in the conduction and the valence band, respectively, E_{F_c} and E_{F_v} is the quasi-Fermi levels in these bands, respectively, k_B is the Boltzmann's constant, and T is the temperature.

The gain of a semiconductor as a function of photon energy can be written as:

$$g(E_{ph}) = \frac{\pi e^2 \hbar}{\epsilon_0 n c m_0^2} \frac{1}{E_{ph}} |M|^2 \rho_r(E_{ph}) \cdot \left(F_c(E_{ph}) + F_v(E_{ph}) - 1\right). \qquad (2.38)$$

The first factor of Eq. 2.38 contains a number of constants, which are: e (the elementary charge), ϵ_0 (the dielectric constant in vacuum), n (the refractive index), m_0 (the free electron mass) and c (the speed of light in vacuum). The next two factors follow from Fermi's Golden Rule [39], with M defining the probability of the transition from a state in the conduction band to a state in the valence band. The term $\rho_r(E_{ph})$ describes the density of possible transitions with an energy E_{ph}. The Fermi functions $F_c(E_{ph})$ and $F_v(E_{ph})$ describe the probability to find an electron in the conduction band and a hole in the valence band, respectively, required for such transition.

For population inversion, efficient carrier injection combined with a good carrier confinement are required. This can be achieved in a double heterostructure. As we have seen earlier in this chapter, its inner layer provides both carrier confinement, and optical confinement. Therefore, population inversion can be created by applying an injection current across the heterostructure. If the photon energy is lower than the bandgap, the semiconductor is transparent. This property is used for choosing the composition of the film layer in passive waveguides, integrated together with the active ones. On the other hand, if the photon energy is larger than the quasi-Fermi spacing, the material is absorbing, because no stimulated transitions are possible in this case. And only if the optical field accomplishes the condition that its photon energy is larger than the bandgap, but does not exceed the quasi-Fermi spacing, the semiconductor can work as a gain medium.

This is illustrated in Fig. 2.13, where the gain is plotted as a function of the photon wavelength for different electron concentrations. Higher electron concentrations can be achieved by increasing the injection current. Above the transparency, gain becomes positive for an increasing wavelength range with the increasing electron concentration.
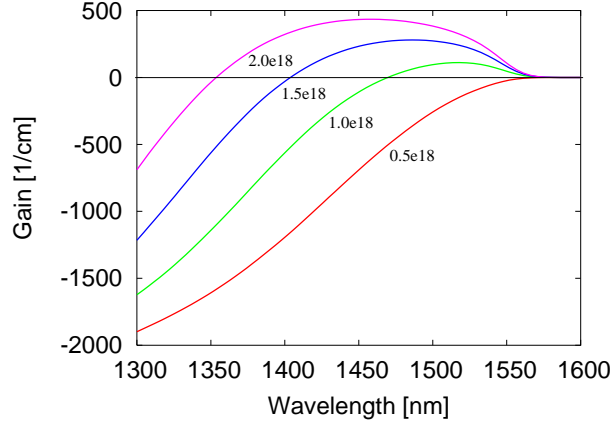
Figure 2.13: Gain as a function of photon wavelength calculated for different carrier concentrations, which are indicated in [cm^{-3}].

The carrier density, where the semiconductor neither absorbs nor amplifies, is typically referred to as the transparency density. The peak gain is linearly dependent on the inversion carrier concentration, and, therefore, increases linearly with the current:

$$g_{\text{peak}} = g_{\text{D}}(n - n_{\text{tr}}) \propto g_{\text{D}}(J - J_{\text{th}}), \tag{2.39}$$

where n_{tr} and J_{th} are the transparency carrier density and the threshold current density, respectively, g_{D} is the differential gain represented in [cm^2].

The recombination, while contributing to the optical amplification, results in carrier depletion. As a consequence, the gain starts to saturate as photon generation increases. The phase shifting in SOAs is based on this property, and will be discussed in detail in chapter 5.

Extended cavity lasers and extended waveguide SOAs

The semiconductor optical amplifiers used in this thesis are integrated together with passive waveguides at both sides. The as-cleaved facets of an amplifier have a power reflection coefficient of 0.33, and the device operates basically as a so-called extended cavity laser (ECL). Anti-reflection (AR) coatings on the end facets reduce the reflection coefficient to prevent laser action, and then the structure operates as an extended waveguide SOA. Since it is easier to characterize a laser, SOA structures are first investigated as lasers. Therefore, this paragraph introduces a number of parameters that will be used for this characterization [3].

35

The optical gain in a SOA is provided by the active layer, which has a material gain g_m [cm^{-1}]. However, only a fraction Γ of the optical mode propagates through the active layer and gets amplified. The fraction is also known as the confinement factor. In addition to amplification, the mode experiences a loss α_{act}. The net modal gain coefficient is:

$$g = \Gamma g_m - \alpha_{act}. \tag{2.40}$$

Modal gain g is a relative increase per unit length in the optical power P as the mode propagates in the z direction through the gain medium:

$$g = \frac{1}{P}\frac{dP}{dz}. \tag{2.41}$$

Here, the modal gain g is assumed to be constant along the amplifier length. The single pass SOA gain G can be defined as $G = P(L_{act})/P(0)$. Integrating Eq. 2.41, the following expression for the SOA gain can be derived:

$$G = e^{g L_{act}} = e^{(\Gamma g_m - \alpha_{act})L_{act}}. \tag{2.42}$$

Consider an amplifier with length L, gain G and mirror reflection coefficients R_1 and R_2. When the gain exceeds the mirror loss, the roundtrip gain $G_{rt} = R_1 R_2 G^2$ becomes larger than 1, and a small amount of noise will be amplified to infinite output power. However, the increasing output power saturates the amplifier decreasing the gain such, that G_{rt} is again equal to 1, and the device operates as a laser. The laser condition for an extended cavity laser can be written as:

$$\Gamma g_m = \alpha_{act} + \frac{1}{2L_{act}}\ln\left(\frac{1}{R_1 R_2}\right) + \frac{1}{L_{act}}\ln\left(\frac{1}{f}\right), \tag{2.43}$$

where α_{act} is the internal cavity loss, $\frac{1}{2L_{act}}\ln\left(\frac{1}{R_1 R_2}\right)$ is the distributed mirror loss, and $\frac{1}{L_{act}}\ln\left(\frac{1}{f}\right)$ is the distributed passive cavity loss. This formula is valid if a 100% coupling is assumed between the active and the passive waveguides.

The lowest current at which the roundtrip gain compensates for the roundtrip loss is the threshold current. At this current, the transparency condition $\Gamma g_m = \alpha_{act}$ is satisfied. For sub-threshold bias currents, the ECL output is mainly determined by spontaneous emission. The transition to lasing is quite abrupt and takes place at an injection current equal to the threshold current, I_{th}. Above the threshold, the laser condition (Eq. 2.43) is satisfied, and the output is determined by stimulated emission.

The output power plotted as a function of the injection current is called an LI-curve. An illustration of a typical LI-curve is presented in Fig. 2.14. The laser output power above the threshold is described by the following expression:
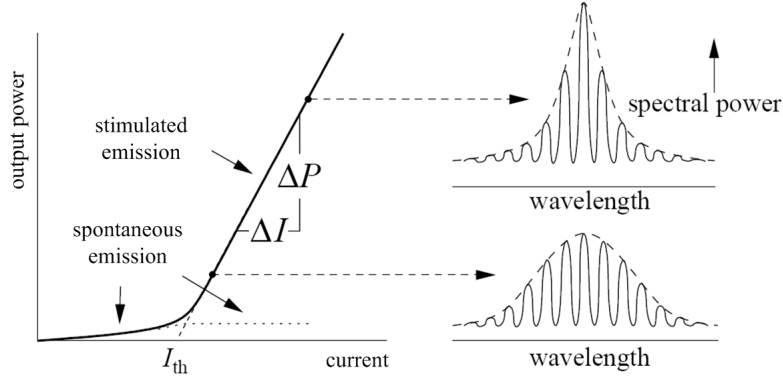
Figure 2.14: A typical LI-curve and its spectra at different injection currents.

$$P = h\nu\eta_{\mathrm{i}} \frac{I - I_{\mathrm{th}}}{e} \frac{\Gamma g - \alpha_{\mathrm{int}}}{\Gamma g}, \tag{2.44}$$

with η_{i} the internal quantum efficiency and α_{int} the internal loss contribution in both active and passive parts of the cavity, and e the elementary charge. The butt-joint loss is here assumed to be negligibly small, which is usually true for a good integration scheme.

The slope of the LI-curve ($\Delta P/\Delta I$) is proportional to the differential quantum efficiency, which determines the additional number of photons in the laser output per additionally injected electron into the SOA.

Inside a Fabry-Perot laser as the ECL, the light experiences multiple reflections between the mirrors, before it is transmitted. The cavity between the mirrors acts as a resonator and supports only longitudinal modes for which a round trip in the cavity equals an integer number of wavelengths [3]. A laser spectrum is schematically shown on the right hand side of Fig. 2.14. The envelope of the modes is determined by the net gain in the laser as a function of the wavelength. If the injection current is increased, then the mode near the gain peak becomes dominant.

With anti-reflection coatings applied to the end facets, the distributed mirror loss becomes high (see Eq. 2.43). Therefore, increasing the injection current, while the gain g increases, the roundtrip gain G_{rt} remains below 1, preventing laser action. This is beneficial for both the one-pass gain and the nonlinear behavior of the SOA. Consequently, the threshold current becomes very high, allowing to operate the SOA at high currents without the lasing action. In this case, spontaneous emission is the dominant

process in a SOA. If an emitted photon couples to a waveguide mode, it travels through the SOA to the output facet and is amplified on the way. Therefore, at the output this radiation is referred to as an amplified spontaneous emission (ASE). The ASE output spectrum can be fitted to a Gaussian function (or a parabolic function, if the power is measured in dBm) [3].

Measured LI-curves and output power spectra of the SOAs can be used to extract some useful information. The threshold current obtained from the LI-curves determines a proper range of injection currents to operate the SOA-based phase shifters. Furthermore, the slope of the LI-curves can be used to evaluate the material quality, and the quality of the fabricated SOA-waveguides. Measured output power spectra determine the gain peak wavelength and, therefore, a range of suitable wavelengths.

2.4 Conclusions

In this chapter a suitable material system for the integration of the Mach-Zehnder interferometers is presented. The indium phosphide integration platform has been chosen for realization of the photonic integrated devices since it allows integration of optical devices operating in the low-loss and low-dispersion transmission window of the glass fibers. Relevant material properties (band structure, optical properties and interaction with light) are discussed. The components needed to realize our devices (passive waveguides, optical couplers and semiconductor optical amplifiers) are introduced. Low propagation losses in passive waveguides can be obtained in wide shallowly etched waveguides, which is however achieved at the expense of an increasing number of propagating modes. Curved waveguides need also be wide, and have a radius in the range of several hundreds micrometers in order to reduce the radiation losses. Couplers of two different types were discussed: directional couplers and MultiMode Interference couplers. Whereas directional couplers allow for any arbitrary coupling ratio, they can be rather long and their coupling ratio is sensitive to fabrication tolerances and polarization. The MMI couplers allow for only a limited number of coupling ratios, e.g.: 0.15/0.85, 0.5/0.5 and 0.85/0.15. This type of coupler has a compact design and polarization insensitive operation. In active Mach-Zehnder interferometers, the phase shifting is based on semiconductor optical amplifiers. The fundamentals of these devices, such as the optical gain mechanism, are explained. In the devices investigated in this thesis, the SOAs are integrated together with passive waveguide components. Since it is easier to characterize a laser, SOA structures are first investigated as extended cavity lasers. A number of parameters that will be used for this characterization are introduced.

Chapter 3

Fabrication technology for the MZIs

This chapter describes the fabrication technology of Mach-Zehnder interferometer structures. Two realizations of the MZIs are described. The first employs semiconductor optical amplifiers as nonlinear phase shifters, the second one uses quantum dot based phase shifters. After describing the epitaxial growth for both realizations, the main chip processing steps are explained. Finally, the complete chip processing is given for the realization of, respectively, SOA-based and QD-based Mach-Zehnder interferometers.

3.1   Introduction

Fabrication of photonic integrated circuits begins with growth of a InGaAsP/InP wafer with a specific layer structure (layer stack). The SOA-MZIs require integration of active and passive waveguides in the InGaAsP/InP material system. For that, the low pressure Metal Organic Vapor Phase Epitaxy (MOVPE) technique using butt-joint coupled active and passive waveguides is used. Fully passive MZIs, also investigated in this thesis, are fabricated in the quantum dot based material, grown by the Chemical Beam Epitaxy (CBE) technique. After a discussion of the growth techniques and the chosen layer stacks, the chip fabrication steps will be explained, including lithography, waveguide etching and metalization. Finally, the complete processing schemes are given.

3.2   Epitaxial growth

3.2.1   Active-passive integration technique

Realization of Mach-Zehnder interferometers with semiconductor optical amplifiers requires integration of waveguides for passive (interconnection waveguides, couplers) and active elements (SOAs) on one chip. An overview of the available integration techniques can be found in [40, 41, 42, 43]. The active-passive integration technique used in this thesis is based on low pressure (LP) MOVPE using butt-joint coupled active and passive waveguides. This approach has a number of advantages. First, it offers flexibility for the design of layer stacks for both active and passive circuit elements. In this way, different requirements can independently be fulfilled for active and passive components. Second, positions and dimensions of the active areas can be adjusted with respect to the complexity and the requirements of the circuit. And third, it demonstrates low losses at butt joints [3, 44]. This integration scheme is described in detail in [3], and is briefly discussed here using Fig. 3.1.

The epitaxial growth on a 2" InP substrate was performed by JDS Uniphase[1]. First, an all-active layer stack is grown on a n-type substrate. The first growth includes a 500-nm-thick InP-buffer layer, a bulk active layer, consisting of a 120-nm-thick Q(1.55) embedded between two 190-nm-thick Q(1.25) layers, and a 200-nm-thick first part of the p-InP top cladding. These layers are shown on the left side of Fig. 3.1 below the dashed-double-dotted line. Subsequently, the active areas are defined with a special mask, the layout of which is shown in Fig. 3.2(a) and 3.2(b) (the active-passive layouts shown in Fig. 3.2 are corresponding to a quarter of the 2" wafer. The complete mask consists of 4 equal layouts).

The active areas are rectangular blocks, with a width of 20 μm (Fig. 3.2(a) for the first circuits realization) and a width of 30 μm (Fig. 3.2(b) for the second circuits realization). The width of the active blocks is limited in this technology to 50 μm. This is to avoid an unwanted deposition on the masking material (SiO$_2$), when the active blocks are too broad. The length of the active blocks that corresponds to the needed SOA length is not technologically limited. The InP cladding and partly the film layer are selectively etched as indicated in Fig. 3.1 by a dashed-dotted line in the "PASSIVE" part of the scheme. During the second growth, an approximately 360-nm-thick layer of Q(1.25) and 200-nm-thick InP cladding layer are regrown. These layers are non-intentionally doped (n.i.d.)[2], as required for low propagation losses in passive waveguide structures. In the final growth step, after removing the SiO$_2$ mask, a p-InP

---

[1]JDS Uniphase, Eindhoven, The Netherlands.
[2]The non-intentional doping concentration is n $= 1 \times 10^{15}$ cm^{-3}.
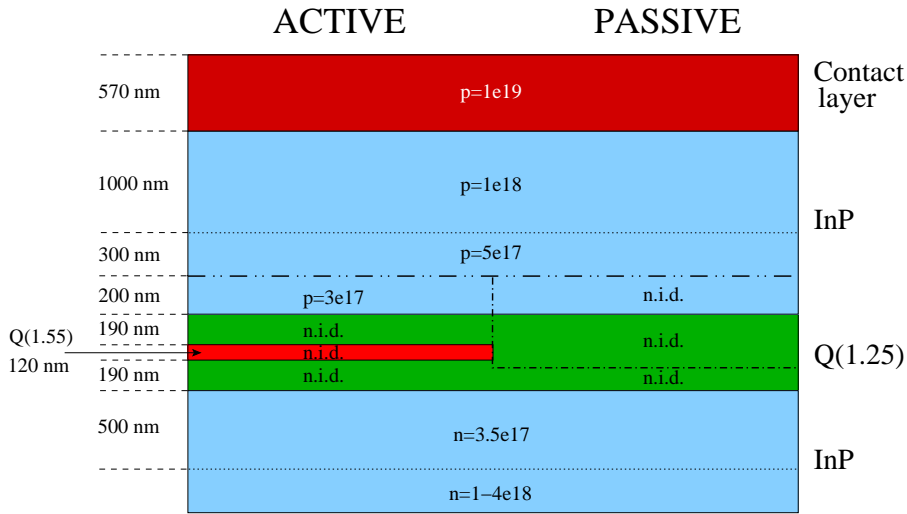
ACTIVE   PASSIVE

Figure 3.1: Schematic cross-section of the regrown active-passive wafer with indication of layer compositions, thicknesses and doping profiles.

cladding layer and a 570-nm-thick contact layer stack with InGaAs are grown.

The doping concentration in the p-InP cladding layer determines the series resistance through the SOA, and at the same time the optical absorption in the ridge. In the first circuit realization for improved electrical behavior of the SOAs the cladding was a highly doped 1300-nm-thick InP ($p = 10^{18}$ cm^{-3}). In order to reduce the propagation losses in the second circuit realization, the p-InP cladding layer was split into two parts: a lower layer of 300-nm-thick InP with $p = 5 \times 10^{17}$ cm^{-3} and on top of that a 1000-nm-thick InP layer with $p = 10^{18}$ cm^{-3}. The electrical resistance, as follows from the IV-curves presented in section 4.4, has not suffered significantly from this change in doping profile.

The contact layer, needed for making an electrical contact on the SOAs, shows a high optical absorption. The 1500-nm-thick p-InP top cladding is intended to minimize the coupling of the guided modes to this layer, and thus the loss. As shown further in this chapter, during the processing the contact layer is totally removed in the passive part of the wafer.

(a)

(b)
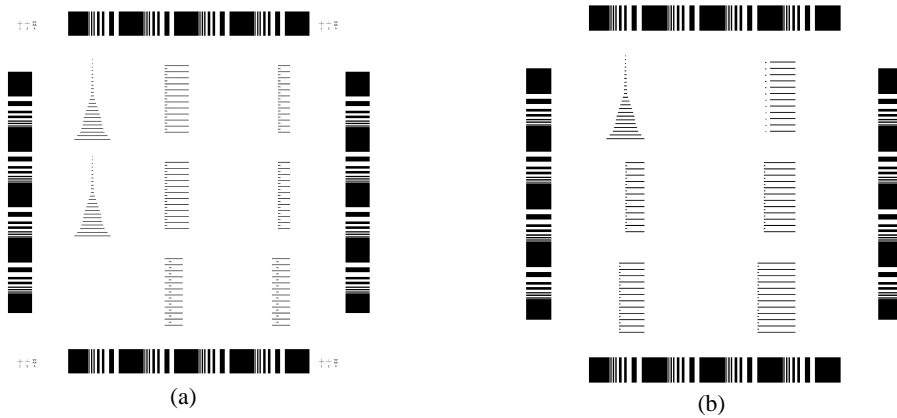
Figure 3.2: Mask layout defining the active regions (black stripes) for the active-passive integration technique. (a) Mask layout for the first circuits realization. (b) Mask layout for the second circuits realization. The bars surrounding the pattern are for coarse alignment purposes.

3.2.2   Quantum dots growth on InP

For realization of the passive all-optical switching in MZIs, nonlinear waveguides are needed. Unlike the active-passive integration technique, where the phase shifting elements (SOAs) and passive waveguide components (waveguides, couplers) are fabricated in different layer stacks on one wafer, all the components in the present realization of the passive MZIs are made in a quantum dot based material. In the future, the regrowth technique can also be applied to the quantum dot wafers, reducing the overall losses of such a chip.

The growth technique for the quantum dot sample is based on the Chemical Beam Epitaxy (CBE). The epitaxial growth on the (100) oriented InP substrate was performed by the Semiconductor Physics group[3]. The quantum dots were prepared with the Stranski Krastanow method by depositing 4.3 monolayers of InAs at 500°C on top of a lattice matched InGaAsP layer (Q(1.29)). A thin GaAs layer was inserted underneath the quantum dots allowing reproducible tuning of the emission wavelength in the 1.55 μm range [45]. Atomic Force Microscopy (AFM) shows a quantum dot density of 1.4×10^{10} cm^2. The single quantum dot layer is embedded in a 500-nm-thick Q(1.29) film layer, which is covered with an InP cladding of 1300 nm. The layer stack is shown in Fig. 3.3. The film and the cladding layers are non-intentionally doped.

---

[3]Semiconductor Physics group, COBRA Research Institute, Technische Universiteit Eindhoven.
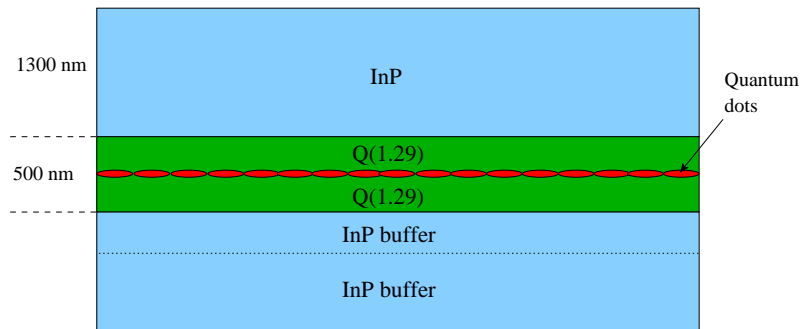
Figure 3.3: Schematic cross-section of the double heterostructure with quantum dots grown in the middle of the film layer, with indication of layer compositions and thicknesses.

The AFM image of the InAs/InP self-assembled quantum dots is shown in Fig. 3.4. The room temperature photoluminescence (PL) spectrum of the InAs quantum dots is presented in Fig. 3.5. The PL emission peak around 1290 nm corresponds to the emission of the Q(1.29) film layer. The second peak, centered at 1520 nm, corresponds to the emission from the quantum dots. The broad peak of the PL of the quantum dots reflects variations in dot size, and not the behavior of individual dots. The latter show a very sharp peak, which will be discussed in subsection 5.3.3.

3.3 Processing technology

Each processing run starts with the layer thicknesses verification. This is because the grown layers can deviate from the designed ones, and therefore the exact etching depth should be adjusted. The procedure includes a series of local masking and etching of the semiconductor material in suitable selective wet etchants, and subsequently measuring the step height.

3.3.1 Patterning

The processing of the Mach-Zehnder interferometers starts with the definition of all waveguide structures. As masking material a layer of silicon nitride (SiN_x) of a certain thickness (the thickness will be specified later in this section) is deposited in the Plasma Enhanced Chemical Vapor Deposition (PECVD) reactor. The layer of SiN_x will be used to transfer the pattern from the mask to the wafer. First, the pattern from the
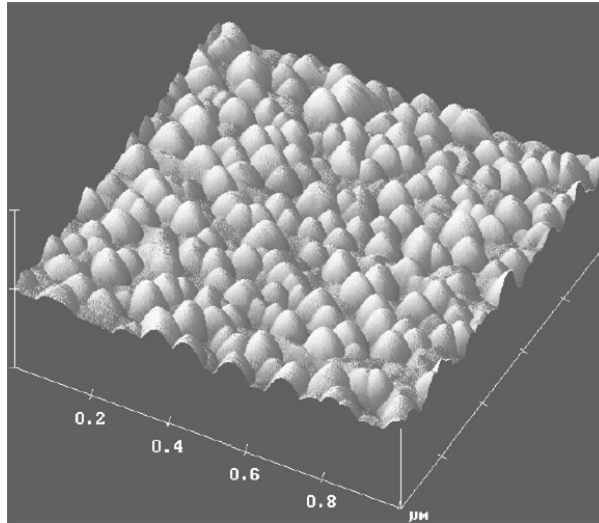
Figure 3.4: AFM of the InAs/InP self-assembled quantum dots [46].
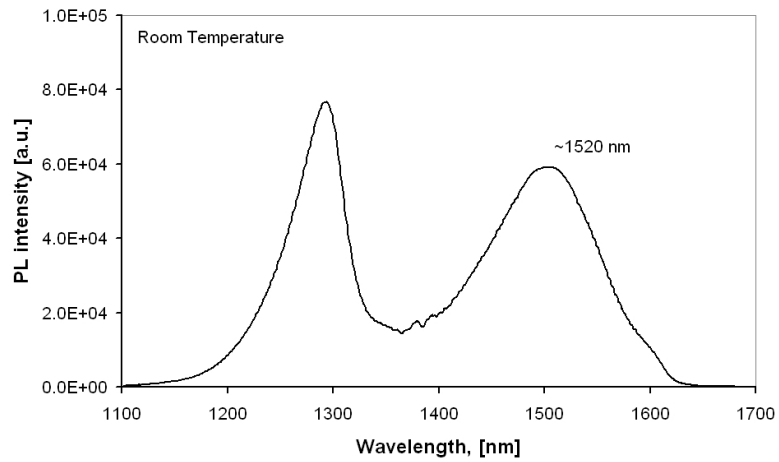
Figure 3.5: PL spectrum of the QD sample at room temperature. The PL peak around 1290 nm corresponds to the emission of the Q(1.29) film layer, the PL peak around 1520 nm corresponds to the emission from the quantum dots.

mask glass plate is transferred into a photoresist layer. A positive type of photoresist is used. Second, the SiN_x layer is etched selectively by Reactive Ion Etching (RIE) using a CHF_3 process. The photoresist residues are subsequently removed by a 5 min oxygen (O_2) plasma at 300 W and a dip in a 1% HF solution. The obtained SiN_x mask is then usable for etching the semiconductor material.

Definition of the waveguides is a critical step, as sidewall roughness and deviation of the dimensions can influence the overall performance of the device, and in particular increase the propagation losses.

3.3.2 Dry etching techniques for low-loss waveguides

To transfer the pattern from the SiN_x layer into the semiconductor material, in order to etch the ridge waveguides, dry etching techniques are used. Dry etching allows a good control over the etch shape. Proper selection of the dry etch parameters can yield smooth sidewalls, and anisotropic and vertical profiles, which are required for optical waveguides. That is why this is one of the key processes in fabrication of waveguide components of photonic integrated circuits [47]. Here, two dry etching techniques, used in this thesis for fabrication of the chips, are presented. These are RIE and Electron-Cyclotron Resonance (ECR) RIE. The latter is nowadays replaced by the Inductively Coupled Plasma (ICP) etching technique. However, the ICP was not used in this thesis.

Reactive ion etching technique for low-loss waveguides

The pioneers in etching InP/InGaAsP-based materials in a reactive ion etching reactor employing a CH_4/H_2 plasma are Niggebrügge *et al.* [48]. CH_4/H_2-based RIE process and its modifications are widely used in fabrication of photonic components.

The main advantage of using the CH_4-chemistry is the high etch selectivity between masking materials (SiN_x, photoresist, or titanium) and a semiconductor, due to deposition of hydrocarbon polymers on the mask. However, the deposition on the edge is not homogeneous, therefore the roughness of the sidewalls increases during etching. This results in vertical striations [49, 50], which strongly increase the waveguide losses by scattering. In order to achieve low loss, the amount of polymer deposition should be controlled. Therefore, the etching procedure involves a sequence of InP-etching (CH_4/H_2-RIE) processes, and descum (O_2-RIE) processes for removing the polymer depositions [47].

Reactive ion etching is a combination of chemical and physical processes. Chemical reactions cause the formation of volatile residual etching products and polymers,

whereas physical sputtering by accelerated ions removes the material. The basic chemical reaction on the InP surface in contact with the CH_4/H_2 plasma is:

$$InP + 3H^+ + 3CH_3^+ + 6e^- \rightarrow In(CH_3)_3 + PH_3. \tag{3.1}$$
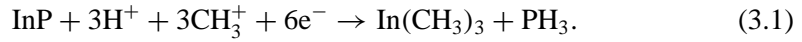
Phosphorus reacts with the hydrogen forming PH_3, a very toxic and volatile material. Indium reacts with the methane forming $In(CH_3)_3$. During the CH_4/H_2 etching process there are more polymers formed than could be removed by the positive ions sputtering. On one hand, the polymers deposited on the masking material yield a high selectivity of the etch due to protection of the masking material. On the other hand, the deposition of polymers on the side of the mask and on the etched sidewalls creates extra roughness.

After a certain period of etching accompanied with polymer deposition, the etching process is interrupted for a descum process. During the descum process, polymers are removed in an oxygen plasma. The oxygen does not create any volatile formations with InP or with the masking material (SiN_x). However, the masking material can be eroded by physical sputtering if the protective layer of polymers is completely removed from the mask. For the accelerated ions it is difficult to remove the polymer depositions from the strictly vertical sidewalls. Hence an additional (incidental) advantage of the mask erosion is that slightly reducing mask width causes a sidewall slope, which might be less affected by polymer depositions. By optimizing the parameters of the CH_4/H_2 and O_2-descum processes, the sidewall roughness can be reduced. Thickness of the masking material, flow rate, pressure, power, and the duration of the processes are the most important parameters that are optimized to obtain smooth sidewalls for reducing the propagation losses of etched waveguides.

The reaction limiting the etching rate is the one of indium with methane [47]. Below the optimal concentration of CH_4, the etched surface is rough due to the reactivity of hydrogen that preferentially removes phosphorus. Above the optimal concentration, the roughness increases due to the formation of polymers. We have found that the optimized RIE process for InP employs the gas flow ratio $CH_4:H_2 = 20:80$ sccm.

Influence of the descum process duration on the sidewall roughness can be seen from the SEM picture in Fig. 3.6. In Fig. 3.6(a), horizontal stripes indicate borders formed by an etching cycle (i.e. one InP etch and one descum process). In this case, each descum process removes all polymers from the mask, yielding a mask width reduction. In Fig. 3.6(b), instead, the descum time is not sufficiently long to remove all the polymers, yielding sidewall roughness. In the optimized CH_4/H_2-RIE process, the InP etching process duration is 120 seconds at RF power of 220W. The O_2-descum process duration is 12 seconds at RF power of 200W. The resulting etching rates for

(a)   (b)
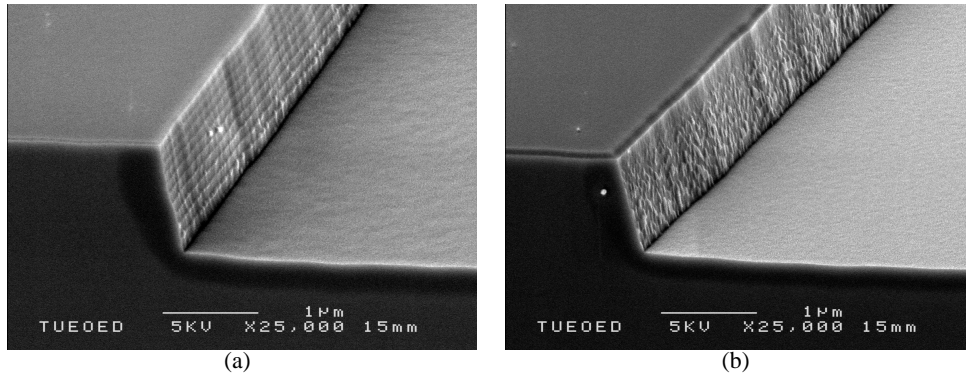
Figure 3.6: Waveguides etched by the CH_4/H_2-RIE process with two different O_2-descum times: (a) 30 sec and (b) 20 sec.

InP and InGaAsP are approximately 50 ± 5 nm/min and 30 nm/min, respectively. The etching rate depends on material composition, doping profile, and the ratio of etched surface to the masked one.

When gas flow ratio and etching duration are optimized, the masking material thickness becomes an important issue. Fig. 3.7 shows the influence of the SiN_x mask thickness on the sidewall roughness. If the thickness of the SiN_x layer is 100 nm, during the first few etching cycles the mask does not change (no-erosion case), the sidewalls are strictly vertical and polymer depositions are not well removed (this can be concluded from observing the lower part of the ridge). After a certain number of cycles, the mask starts to erode, which consequently leads to the sidewall slope. The polymer depositions are then removed more efficiently and the rest of the etch is sufficiently smooth. If the SiN_x layer thickness is reduced to 50 nm, the mask start to erode very quickly, and the whole etch profile is smooth.

As a result, the waveguide sidewalls are not perfectly vertical, but at an angle varying between 7 and 8°. This does not cause problems for the waveguide structures used in this thesis. However, this parameter should be taken into account in the design of the structures, as it affects the resulting width of the etched waveguides.

For increasing the homogeneity of the etching across the sample (which is usually a quarter of a 2" wafer), a full 2" InP substrate is placed underneath [51]. In order to etch the waveguides to the required depth, loading effects should also be taken into account: the areas closer to the waveguide ridges are etched less deep. Smaller open areas are etched slower, which becomes an issue e.g. for the directional couplers.

47
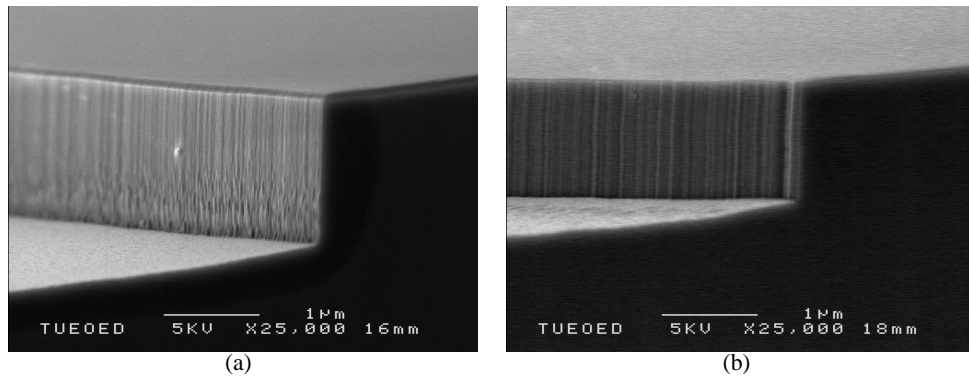
Figure 3.7: Waveguides etched by the CH_4/H_2-RIE and O_2-descum process. The thickness of the SiN_x mask is: (a) 100 nm and (b) 50 nm .

Electron-cyclotron resonance reactive ion etching

An alternative dry etching technique is Electron Cyclotron Resonance RIE (ECR-RIE) [52]. ECR plasmas provide a high degree of ionization at low pressures and the discharge is generated separately and independent from the substrate stage. In that case the substrate should not suffer from excessive ion bombardment, since it is possible to work with low DC biases. However, it is known [52] to be difficult to obtain smooth surfaces with CH_4/H_2-ECR plasmas. This is because high ECR powers lead to a preferential etching of phosphorus resulting in the formation of indium droplets, and thus increased surface roughness. Smooth surface and reasonably vertical sidewalls are obtained with a significantly lower ECR power of 150 W.

The ECR reactor was used in the earlier phase of the research and was later substituted by the RIE. Experiments related to the optimization of the couplers (presented in section 4.3) were carried out using this technique. Here, a brief overview of the ECR-RIE technique is given.

For dry etching, a gas mixture of $CH_4/H_2/Ar$ is used in the proportion 10:8:8 [53]. The use of argon is explained by the need to (partly) remove polymers, that are heavily deposited on the etched surface. Polymer deposition is an issue, as the machine does not allow for alternating the $CH_4/H_2/Ar$ process with an O_2-descum process in one chamber. As a result, waveguides with rough sidewalls are obtained (Fig. 3.8(a)). This can be improved by taking the sample out of the etching chamber, and apply an O_2-descum process in another one. The resulting waveguide is shown in Fig. 3.8(b), which is a typical waveguide of the couplers optimization run. A relatively smooth waveguides are obtained. For the waveguide masking, a SiN_x layer with a thickness

48
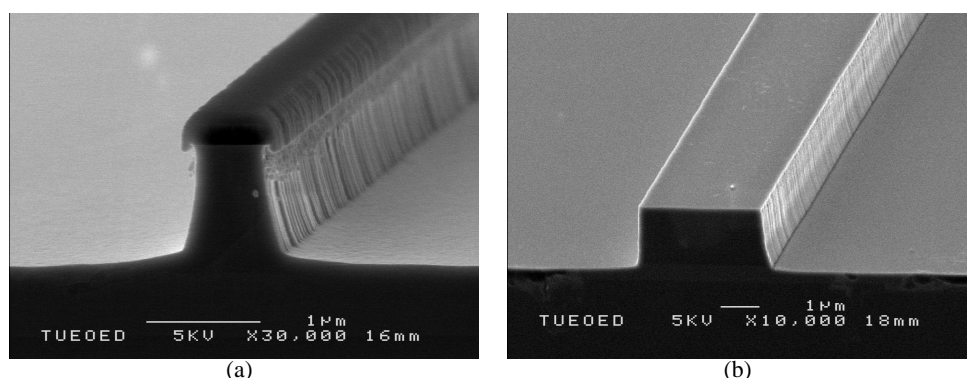
Figure 3.8: Results of the $CH_4/H_2/Ar$ ECR-RIE etched waveguides. (a) Continuous etch. Polymer depositions can be seen (the SiN_x mask is not removed). (b) The InP etch is alternated with the O_2-descum process.

of at least 100 nm is used. This is needed because of mask erosion by the argon.

3.3.3 Contact opening and metalization

The use of SOAs in Mach-Zehnder interferometers requires electrical contacts. In order to avoid high optical losses caused by a metal layer and for isolation purposes, a 300-nm-thick PECVD-SiN_x layer is deposited on the chip. For contacting an SOA, a contact opening in this layer is needed on top of the SOA ridge. A contact opening can be defined directly by using a contact lithography. In this way a narrow opening in resist is defined, and the SiN_x in the opening is subsequently etched away. An alternative way could be to use a self-alignment method, explained in [3].

For making a 1.5-μm-wide contact opening on top of the 2-μm-wide SOA ridge as used in the realized circuits, a contact-opening mask (dark field) in combination with positive photoresist is applicable. After exposure with UV light and development of the resist, the SiN_x layer is etched in two steps: the first 250 nm with the RIE, and the remaining part in buffered HF (BHF), slightly over-etching, to make sure that all the contact openings are opened. The two step etch prevents the contact layer surface from being damaged in the plasma. Subsequently, the resist is removed in acetone and isopropanol. Fig 3.9 shows a SEM picture of a typical SOA ridge with the contact opening.

A technique for creating the metal pattern of the contacts is lift-off. This requires a profile in photoresist, with a strong undercut (can be seen in Fig. 3.10(a)), so that a deposited metal does not cover the resist sidewalls. The lift-off profile is created
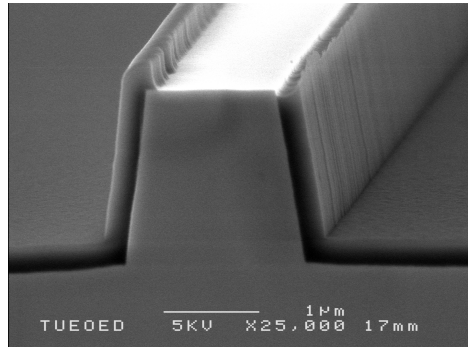
Figure 3.9: SEM picture of a SOA ridge with a contact opening in the SiN$_x$ layer.

in a thick layer of negative resist which is exposed through a light-field mask. By dissolving the resist in aceton, the metal on its surface is removed, leaving only metal in the exposed open regions (see Fig. 3.10(b)).

Metalization of the chip was carried out at JDS Uniphase. The p-metalization stack consists of Pt/Ta/Pt/Au, and the n-metalization on the bottom side of the chip consists of a AuGeNi(alloy)/Ni with a top layer of Mo/Au. The first Pt layer is the actual electrical p-contact, yielding a low contact resistance to the underlaying p-InGaAs layer. Ta serves as a barrier material, which prevents interdiffusion of group III and group V elements and Au from the uppermost layer. The annealing was done at 350°C for 30 seconds. More details on the metalization can be found in [3] and [51].

3.4 Process flows overview

3.4.1 Fabrication of the SOA-based circuits

In this section, the process flow for realization of the devices based on SOAs is presented. A contact top layer required for operation of an amplifier causes unwanted propagation losses in passive waveguides. Thus it must be selectively removed everywhere except for the active areas. This can be done in the following way. First, all the waveguides are etched partly to a certain depth (the first etch). Second, the SiN$_x$ mask is removed from the passive waveguides, uncovering the contact layer for the etch. Third, all waveguides are etched to their target depth of 100 nm depth into the film layer (the second etch). In this way the contact layer is automatically etched away

(a)   (b)
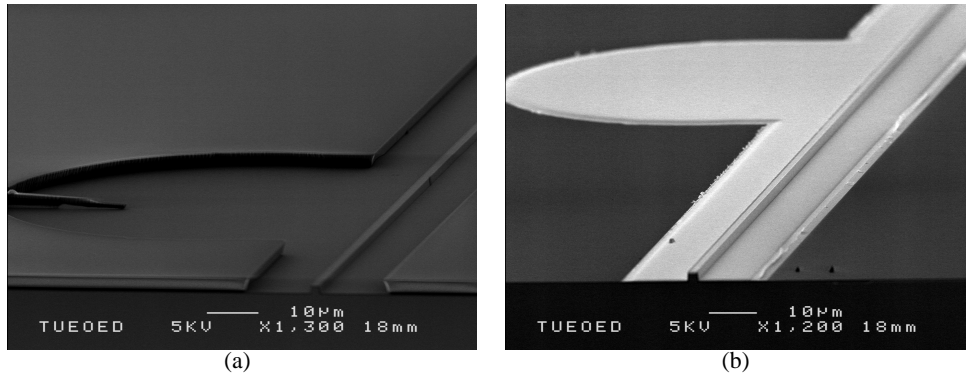
Figure 3.10: (a) Photoresist profile for the lift-off. (b) Metal pattern after the lift-off process.

from the passive waveguides. The etching stop point for the first etch can be calculated knowing the etching rates of InP, InGaAs and InGaAsP. The processing scheme is summarized in Fig. 3.11. The full processing use a total of 5 masks. It consists of the following steps (the capital letters of the list refer to the figure):

A. **Deposition of SiN$_x$.** A layer of PECVD-SiN$_x$ with a thickness of 50 nm is deposited.

B. **Definition of all waveguides.** A layer of positive resist HPR-504 is spun on top of the SiN$_x$ layer. Mask "GUIDES" is used to define all waveguides (passive elements and SOAs). The SiN$_x$ layer is etched in the RIE using the CHF$_3$ process. Then, the photoresist is removed.

C. **The first waveguide etch.** All waveguides are partly etched in the RIE, using an optimized CH$_4$/H$_2$ process alternated by the O$_2$-descum process, as explained in subsection 3.3.2.

D. **Removing the mask from the passive waveguides.** A layer of positive resist HPR504 is spun on top of the partly etched waveguides. The SiN$_x$ layer in active areas is protected by using mask "QTOP". Subsequently the SiN$_x$ layer is removed wet chemically from the passive part of the circuit, using BHF.

E. **The second waveguide etch.** All waveguides are etched to their target depth of 100 nm in the film layer using the RIE. At the same time, the contact layer

51
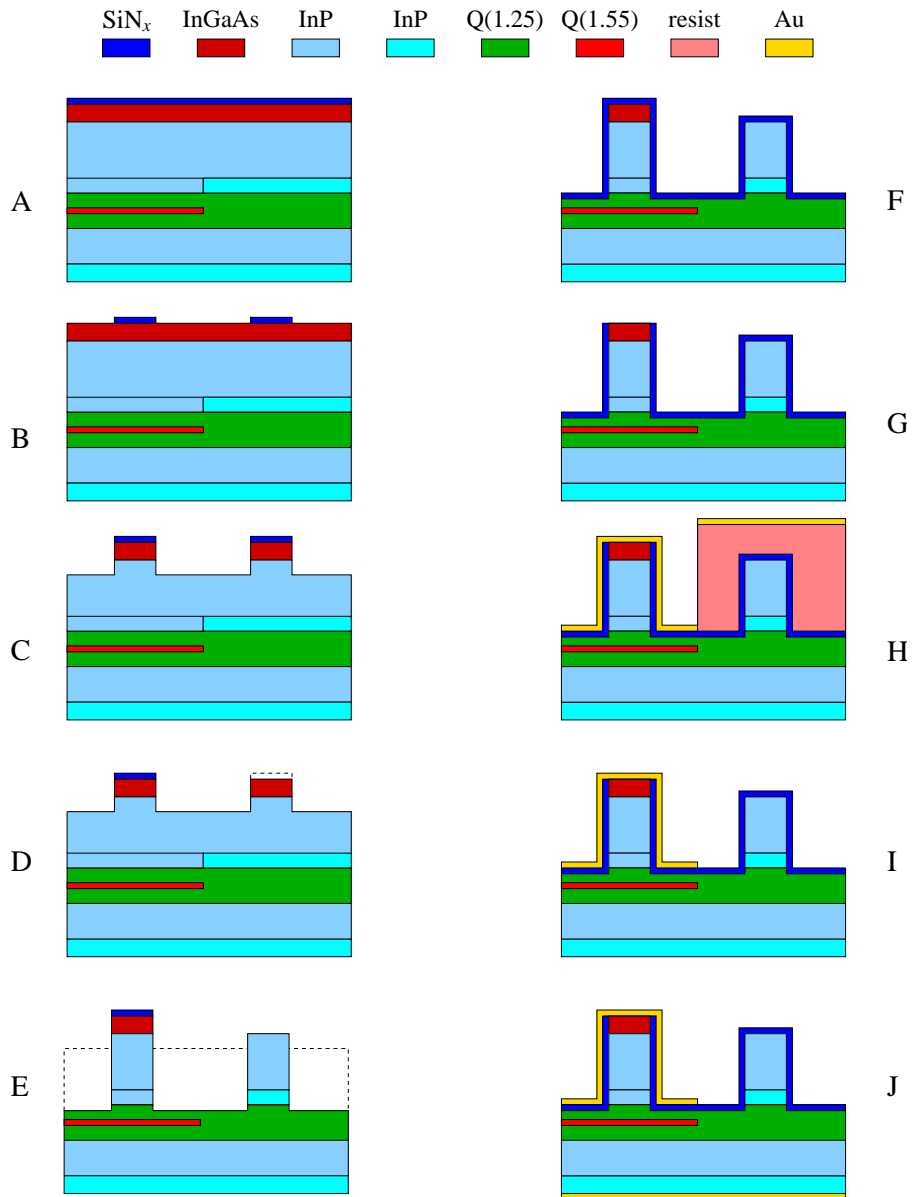
Figure 3.11: Illustration of the process steps that are used in the fabrication of integrated SOA-based Mach-Zehnder interferometers.

(a)   (b)
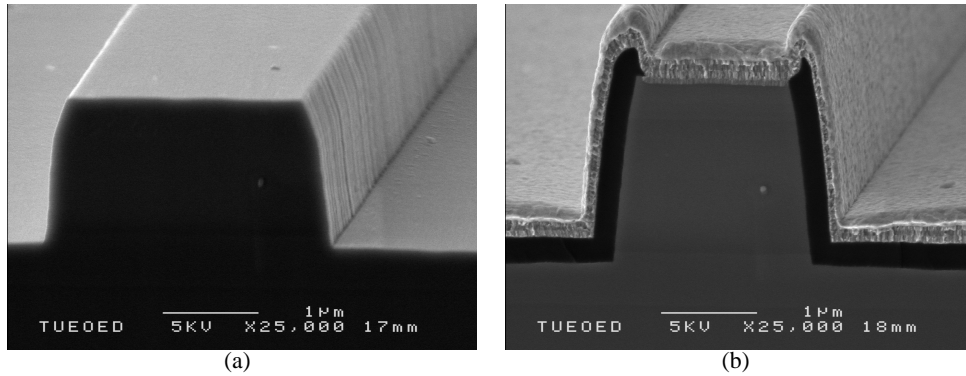
Figure 3.12: SEM pictures of the fabricated structures. (a) Passive waveguide, (b) SOA-waveguide.

is etched away from the passive waveguides. SEM picture in Fig. 3.12(a) illustrates the effect of etching a waveguide without a SiN_x mask layer: the top of the passive waveguide is rounded. All the waveguides are etched now. The remaining SiN_x mask layer is removed.

F. **Deposition of the isolation layer.** A 300-nm-thick PECVD-SiN_x for isolation is deposited. In this layer, the contact openings for the p-contact metalization are made.

G. **Contact openings.** A layer of positive resist HPR-504 is spun on top of the isolation layer. The contact openings on top of the SOA ridges are defined with the dark field mask "CONTACT OPENING". SiN_x is then etched in two steps: the first 250 nm with the RIE and the rest wet chemically in BHF.

H+I. **p-metalization.** A thick layer of negative resist MaN-440 is spun on top of the structures. Mask "METAL" is used to define the metal pattern. The metals are deposited using a sputtering process at JDS Uniphase. After the lift-off process, the contacts are annealed in order to reduce the contact resistance and make the contacts Ohmic. SEM picture of the fabricated SOA-waveguide is shown in Fig. 3.12(b).

J. **Back contact.** The back contact is deposited and annealed at JDS Uniphase. The nitride is removed everywhere except for the parts covered by the metal contact pads. The top metal contact serves as a mask to remove the SiN_x layer for stress-free cleaving. The sample is subsequently cleaved and AR-coated.

53

3.4.2   Fabrication of the QD-based circuits

In this section, the process flow for the first realization of the devices based on quantum dot material is presented. In the first realization of the MZIs, both nonlinear phase shifters and other circuit elements are fabricated in the same layer stack. For verification of the nonlinear switching in quantum dots in the present realization, all waveguides are defined by the mask "GUIDES", originally designed for the SOA-based devices.

The SiN_x masking layer is etched in the RIE using the CHF_3 process. All waveguides are shallowly etched in the RIE in one step, using an optimized CH_4/H_2 process alternated by the O_2-descum process, as previously described in this section. The sample is subsequently cleaved.

Chapter 4

Components for the Mach-Zehnder interferometers

This chapter discusses simulations, design and characterization of the components needed for the integration of the Mach-Zehnder interferometers. First, optimization issues of the passive waveguides are presented. Then, optical power couplers are discussed and optimal configurations are chosen. Finally, extended cavity lasers and semiconductor optical amplifiers are investigated.

4.1 Introduction

In chapter 2 we discussed the basic concepts of the main components that are needed to realize our Mach-Zehnder interferometers: passive waveguides, optical couplers and semiconductor optical amplifiers (in case of active switching in SOA-MZIs). The technology to integrate these structures we discussed in chapter 3. Simulations, design and experimental characterization of these components are the subject of this chapter.

Successful realization of the photonic integrated devices depends on the choices we make for different components. An important milestone is therefore the optimization of each of all these components.

4.2 Passive waveguides

The insertion losses of an entire photonic integrated circuit are to a large extent determined by the propagation losses in passive waveguides. Our goal is therefore to minimize the propagation losses. This can be achieved by optimizing the material structure

(layer stack, layer thicknesses, doping levels), improving the sidewall smoothness (optimizing the etching process), and optimizing the waveguide design (waveguide width and etching depth). Furthermore, radiation losses in the curved waveguides can be reduced by optimizing the radius and the curved waveguide parameters (waveguide width and etching depth).

Waveguide design and fabrication

Active-passive material.   The cross-section of a typical passive waveguide is schematically shown in Fig. 4.1. The film layer consists of Q(1.25) material, and has a thickness d_{film} of 500 nm. The composition of the film layer is chosen to minimize (and ultimately avoid) the absorption due to interband transitions and band tails in the wavelength range around 1550 nm. The thickness of the film layer determines the optical confinement in the film layer.

The absorption due to free carriers can be minimized by reducing the doping concentration. However, in case of the active-passive integration platform, the doping profile is a trade off between low optical absorption and low electrical resistance in the SOAs. As we have already mentioned in chapter 3, in the first circuit realization the top InP cladding layer consisted of a 200-nm-thick n.i.d. InP layer followed up by a 1300-nm-thick InP layer with doping concentration p = 10^{18} cm^{-3}. In order to reduce the absorption due to free carriers, the upper p-InP layer in the second circuit realization was further split into two parts: first a 300-nm-thick InP layer with doping concentration p = 5×10^{17} cm^{-3} and a 1000-nm-thick InP layer with doping concen-
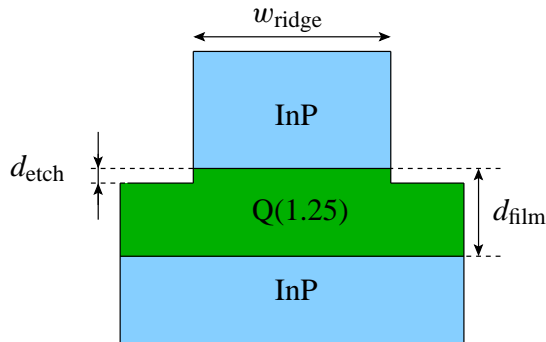
Figure 4.1: Schematic cross-section of a shallowly etched passive waveguide as fabricated in the active-passive material.

tration p $= 10^{18}$ cm^{-3}.

Scattering of the optical field at rough sidewalls forms a significant contribution to the propagation losses. In a waveguide only partly etched into the film layer, the sidewall surface is reduced. Such a waveguide is commonly referred to as a shallowly etched waveguide. An optical signal experiences lower scattering loss in such a waveguide, compared to a deeply etched one. The scattering losses can be further reduced by improving the sidewall smoothness through optimization of the etching process, which we presented in subsection 3.3.2. The scattering losses are according to Eq. 2.15 proportional to the square of the optical field amplitude at the sidewalls. The field strength at the sidewalls can be reduced by increasing the waveguide width w_{ridge}, leading to lower scattering. However, this increases the number of supported optical modes in such a waveguide.

In curved waveguides (also referred to as bends), radiation losses contribute to the losses. They can be reduced by increasing the lateral index contrast of the waveguide, and by increasing the radius of the curvature. The lateral contrast is created by etching the waveguide partly into the film layer. The radius of a bend is chosen in such a way that the bend introduces a negligible radiation loss. A trade off between the propagation losses and the radiation losses leads to an etching depth $d_{etch} = 100$ nm into the film layer. Since the optical field in a curved waveguide is pulled outwards, so that the field becomes stronger at the outer sidewall, the scattering losses are higher than in a straight waveguide. The curved waveguides should be wide enough, so that at least scattering from the inner sidewall does not contribute to the losses.

Based on the above mentioned loss considerations and experimental results presented in [3, 51], the waveguides that we will use in our SOA-based Mach-Zehnder interferometers are 3-μm-wide shallowly etched waveguides (for both straight and curved). The optimal radius for a 3-μm-wide curved waveguide is calculated[1] to be 500 μm.

The coupling losses between a curved and a straight waveguide can be minimized by introducing a lateral offset between them. This leads to a better overlap of the optical fields. In case of a 3-μm-wide shallowly etched curved waveguide with radius 500 μm, the required offset between a straight and a curved waveguide is calculated to be 0.29 μm.

Quantum dot material. The cross-section of a typical passive waveguide in quantum dot material is schematically shown in Fig. 4.2. A single quantum dot layer is

---

[1]Calculations are performed with the Microwave Design System (MDS) software, for which a set of simulation methods for optical applications has been developed [54].
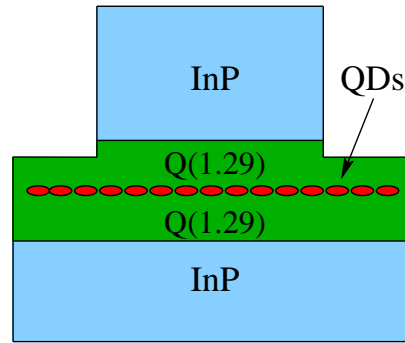
Figure 4.2: Schematic cross-section of a shallowly etched waveguide as fabricated in the quantum dot material.

embedded in a 500-nm-thick Q(1.29) film layer, which is covered with an n.i.d. 1300-nm-thick InP cladding layer.

Absorption in the quantum dot layer and scattering of the optical field at rough sidewalls form two major contribution to the propagation losses in the sample. Similarly to the active-passive integration, in order to reduce scattering losses in the waveguides, 3-μm-wide shallowly etched waveguides are chosen for our QD-based Mach-Zehnder interferometers (for both straight and curved configurations). The optimal radius for a 3-μm-wide curved waveguide is again 500 μm.

Usually, waveguides and other test structures are fabricated in the same processing run with the photonic integrated devices. Therefore, determination of losses in these waveguides supplies information of the quality of the devices themselves. Detailed description of the fabrication steps can be found in chapter 3.

Characterization

For characterization of the propagation losses in straight waveguides, the Fabry-Pérot (FP) technique can be used [6]. This technique employs the intensity modulation of the Fabry-Pérot resonances in the waveguide cavity. Between two mirrors (the cleaved facets of an optical chip), a waveguide forms a cavity. The transmission through this resonator is a function of the loss between the mirrors.

The FP technique involves tuning a wavelength of an external laser source in order to sweep the waveguide cavity through a few minima and maxima. In our experimental setup, a Distributed FeedBack (DFB) laser operating at a wavelength $\lambda = 1534.8$ nm is used as a light source. The wavelength is tuned by changing the laser

temperature. By analyzing the resonances in the transmitted light through a waveguide, a value of propagation losses in decibels per centimeter (dB/cm) can be calculated, if the reflection coefficients are known. These can be calculated with available software.

Below, a brief overview of the propagation losses for each realization is presented.

Active-passive material. In the first realization of the active devices (SOA-MZIs), the high p-doping started above the 200-nm-thick non-intentionally doped InP cladding layer. The same material was used for the realization of the optical couplers, presented later in this chapter. Measured TE and TM propagation losses for 3-μm-wide waveguides fabricated in this stack were between 4 and 8 dB/cm. These high losses can be attributed to insufficient smoothness of the sidewalls and to high p-doping concentration in the top InP cladding.

As mentioned before, in the second realization of the active devices (SOA-MZIs), the 1300-nm-thick p-InP layer is split into two parts with gradually increasing doping. As a result, the TE losses for 3-μm-wide waveguides are reduced down to 2.5 - 3.5 dB/cm and TM losses to 3 - 4 dB/cm. Measured TE losses for 2-μm-wide waveguides are somewhat higher, between 4 and 5 dB/cm. Measured TM losses for 2-μm-wide waveguides are between 5 and 6 dB/cm.

These numbers indicate that both TE and TM losses are still rather high. For waveguides with a smooth etching profile, one could expect losses around 1 - 2 dB/cm. Deviations in layer thicknesses and doping profiles, observed in the second realization of the SOA-MZIs, and possibly remaining roughness on the sidewalls could be the reasons for the high losses.

Characterization of the bends have shown negligible radiation losses.

Quantum dot material. Waveguides fabricated in quantum dot material are strongly polarization dependent. TE losses are very high due to strain created in quantum dots during growth, and due to their shape [45], which resulted in absorbing material for this polarization. Measured TM losses for 3-μm-wide waveguides are between 5.5 and 7 dB/cm. For 2-μm-wide waveguides they are between 6 and 9 dB/cm. Absorption in quantum dots contributes to the propagation losses in the quantum dot sample, since the used wavelength is close to the absorption peak of the quantum dots ($\sim$ 1520 nm), see the PL-spectrum in Fig. 3.5. However, experiments reported in chapters 5 and 7 were done at longer wavelengths ($\geq$ 1550 nm), where a lower loss is expected.

4.3 Optical couplers

Basically we need two types of couplers for the Mach-Zehnder interferometers, studied in this thesis: unbalanced couplers, and optical power combiners/splitters with a coupling ratio of 0.5/0.5.

In the first realization of the SOA-MZIs, MMI-type couplers were used. Their major design parameters are summarized in [55]. The unbalanced MMI couplers have shown rather high insertion losses. Optical power at the coupler high power output port should, however, be high enough to drive the SOA into saturation, and thus induce a nonlinear phase shift. For the initial design of the MMI couplers the refractive indices of InP and Q(1.25) material were used according to the Adachi-Weber model[2]: 3.181 and 3.369 respectively [57]. This results in a beatlength $L_\pi = 305$ μm. Since the MMI length is a defined fraction of L_π, an error in L_π is most severe for the 85/15-type MMI couplers, which have the largest length of all MMI couplers used: $L = 9/4L_\pi$. Deviations of the coupler length lead to high losses in these couplers. The first realization showed high losses for these couplers, implying large deviations in their length. Therefore, an experimental study into design parameters was needed.

We have designed a mask with a number of MMI couplers having variable design parameters. In this way, optimized design for low-excess-loss MMI couplers with well defined coupling ratio can be determined for use in the following generations of the devices. Furthermore, another type of couplers, a directional coupler, was included on the mask, especially because of its flexible coupling ratio. A number of directional couplers was designed in order to assess their applicability and reproducibility for the integrated Mach-Zehnder interferometers.

4.3.1 Directional couplers

Directional coupler design and fabrication

The directional coupler consists of two 2-μm-wide coupled waveguides. The gap between these waveguides should be small enough to provide sufficient coupling, and in the same time it should be possible to define it in the available processing technology. To achieve this, the distance between the two coupled waveguides is chosen to be 1.5 μm. The coupling length of the device, at which complete energy transfer from one waveguide to another one takes place, is calculated based on the system-mode approach, as explained in subsection 2.3.2. In accordance with Eq. 2.23, the calculated

---

[2]This model is implemented in the simulation software FIMMWAVE, based on the film mode matching method [56], which was used for the initial design of the MMI couplers.

(a)   (b)
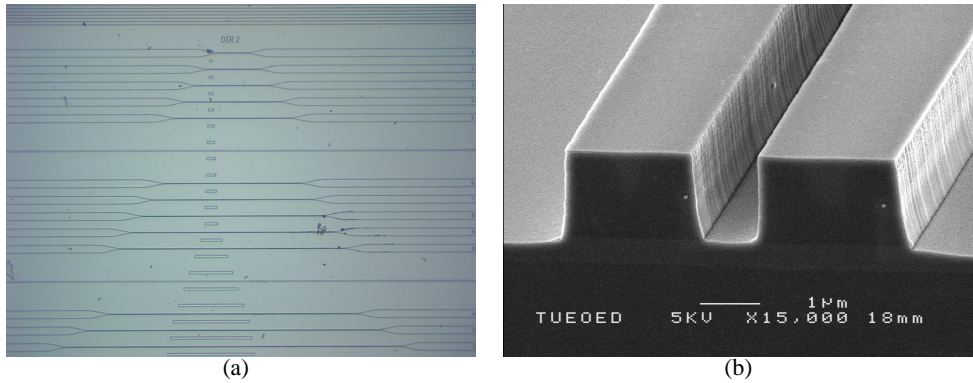
Figure 4.3: (a) Photograph of the fabricated directional couplers. (b) SEM picture of two coupled 2-μm-wide waveguides placed at a distance of 1.5 μm from each other.

coupling length $L_c = 2500$ μm.

In order to obtain various coupling ratios, a number of directional couplers with different lengths were designed and put on the mask. The length of the couplers is varied between 200 and 2200 μm, with a step of 200 μm. This step corresponds to a phase change between the system-modes of 0.08π. Furthermore, a 2600-μm-long and 3000-μm-long couplers were added. This will allow to investigate the coupling behavior over a wide range of lengths.

In order to get a reliable feedback from the experiments, the material used for fabrication of the couplers is a typical active-passive wafer, the same as used for the first realization of the SOA-MZIs. The wafer contains active regions, which is a restriction to the design of the mask layout since the waveguide components should not cross these [55]. For fabrication of the couplers, an optimized ECR-RIE process based on gas mixture $CH_4/H_2/Ar$ was used as described in subsection 3.3.2, alternated with short cycles (duration 2 min) of O_2 plasma for removing of polymers. A photograph of the fabricated directional couplers and a SEM picture of the coupled waveguides are shown in Fig. 4.3.

From Fig. 4.3(b) it can be seen, that the etching depth between the coupler waveguides is smaller due to the loading effect, explained in subsection 3.3.2. This will strongly influence the coupling length of the directional couplers.

Characterization

The experimental setup used for the characterization of the optical couplers is schematically depicted in Fig. 4.4(a). As a light source, an erbium-doped fiber amplifier in combination with a tunable bandpass filter at $\lambda = 1550$ nm is used. With this source, instability problems during measurements caused by the Fabry-Pérot resonances in the chip are avoided[3]. Such an input signal has a relatively broad linewidth (several nanometers). This allows neglecting the Fabry-Perot peaks which have a spacing of ~ 0.05 nm with a cavity length of ~ 5 mm (the length of the cleaved sample). The light is TE polarized. The optical chip is placed on a vacuum chuck. The light is coupled into and out of the waveguides with microscope objectives. These objectives were maintained on stages controlled by piezoelectric drivers. The stages and the chip mounted between the microscope objectives can be seen on the photograph in Fig. 4.4(b).

(a)

(b)
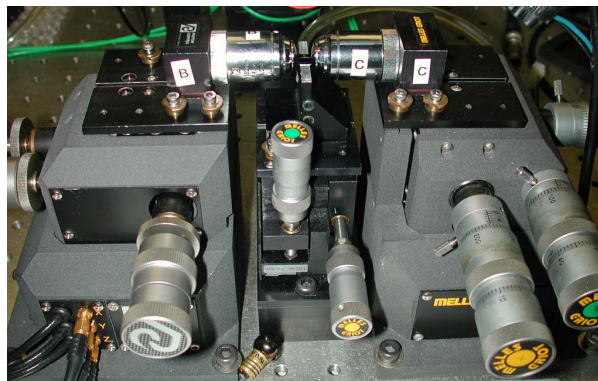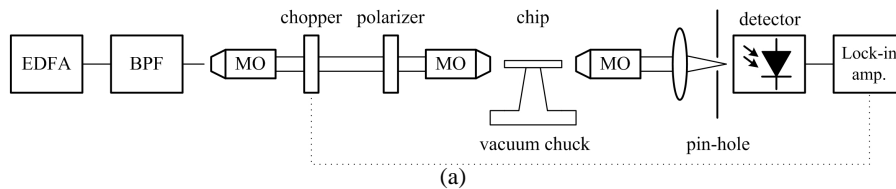
Figure 4.4: (a) Schematic of the measurement setup for characterization of the couplers without AR-coatings. EDFA: Erbium Doped-Fiber Amplifier, BPF: BandPass Filter, MO: Microscope Objective. (b) Photograph of the microscope objective stages and the chip on a vacuum chuck.

---

[3]The facets of the chip were not AR-coated.

The piezoelectric drivers allow positioning a microscope objective with a high degree of accuracy ($\sim 0.1~\mu$m). Both output ports can be visualized by an infrared camera.

The measurement results of the directional couplers are presented in Fig. 4.5, where they are compared with the simulation results. As can be seen from the graph, the measurement results do not meet the simulations: there is no complete power transfer from the bar-output to the cross-output port. This indicates a difference in propagation constants in the coupled waveguides, as was explained in subsection 2.3.2. Furthermore, from Fig. 4.3(b) it can be seen, that the coupled waveguides do not have the same width, which could be a result of some non-uniformities during the processing. The etching depth varies due to loading effects, also influencing the coupling length.

We can conclude that the directional couplers are less suitable to be used in MZIs. Also, they are polarization dependent, which is unfavorable for using them in both realizations: SOA-based and QD-based, which use TE- and TM-polarized optical signals, respectively.
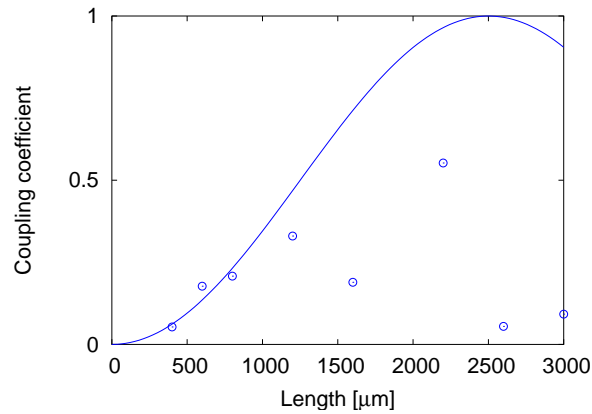
Figure 4.5: Simulated (solid line) and measured (opened circles) coupling coefficient of the directional couplers as a function of the coupler length.

4.3.2 MMI couplers

MMI coupler design and fabrication

We consider MMI couplers with three different coupling ratios: unbalanced 85/15 and 15/85-type couplers and two configurations of balanced 50/50-type couplers, namely 2×1 and 2×2. The schematic layouts and important design parameters of the MMI couplers are presented in Fig. 4.6. The performance and dimensions of the couplers depend on the width of the interference region w_{mmi}. In general, increasing w_{mmi} reduces the crosstalk between the ports, due to the increasing gap between them. However, the couplers become large in that case, as the length L_{mmi} depends on the square of the width [58]. This becomes especially an issue for the long 85/15-type couplers. In order to keep the circuit design sufficiently compact, the width is chosen to be 10 μm.

Table 4.1 summarizes the major design parameters of the MMI couplers. The effective refractive indices of the zero order mode N_0 and the first order mode N_1 in the multimode waveguide were calculated using the Fiedler-Schlachetzki model [27]. In this model, the refractive indices of InP and Q(1.25) are 3.169 and 3.365, respectively. This yields the beatlength $L_\pi = 324$ μm. In order to define experimentally the correct design parameters, and study the tolerances, a number of couplers with varying lengths were put on the mask. The length is varied with a step of 5 μm. This variation of the length will help to link the measurement results to the simulation results. For simulations of the MMI couplers, the MDS software was used.

The offset d_{off} as it appears in table 4.1, is not equal to $1/4W$, which was indicated in subsection 2.3.2. This is because the MMI waveguide is shallowly etched, causing lateral penetration of the modes. This is taken into account in the calculations.

The MMI couplers were fabricated together with the directional couplers, as described earlier in this section.
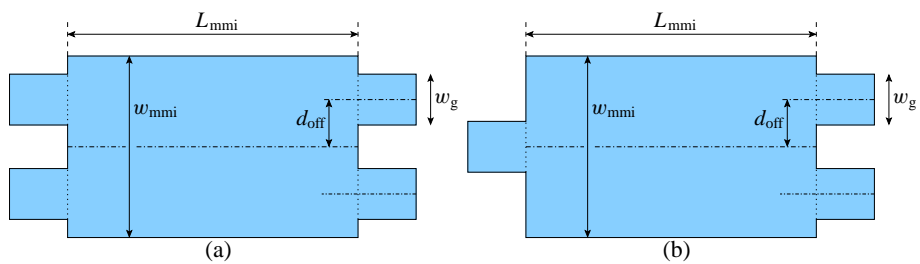
Figure 4.6: Schematics of the designed MMI couplers. (a) 2×2 MMI coupler, (b) 2×1 MMI coupler.

Table 4.1: Design parameters for MMI couplers with different coupling ratios.

	w_{mmi} μm	w_{g} μm	d_{off} μm	L_π μm	L_{mmi} μm	L_{calcul} μm	L_{mmi} var μm
MMI 8515	10	3	2.69	324	729	734	709-739
MMI 1585	10	3	2.69	324	244	244	229-249
MMI 5050	10	3	2.69	324	122	122	110-125

Characterization

The experimental setup used for the characterization of the MMI couplers is schematically depicted in Fig. 4.4(a). The complete description of the setup can be found in earlier in this section. The alignment of the input and output microscope objectives with respect to the access waveguides of the MMI couplers was optimized in the following way. Injecting an optical signal into the input port of a coupler, the positions of the microscope objectives had to be such, that the power detected at the output port had a maximum value. For a straight waveguide that would imply excitation of the zero-order mode only, as that mode has the highest confinement, and thus the lowest propagation loss. The input objective is then positioned in the middle of the waveguide (no-displacement case). However, in the experiments with couplers it appeared, that this seemed to be a correct procedure only when the position of the input microscope objective was optimized in combination with the detection of the optical power at the high-power output port (85%) of the unbalanced coupler. When optical power was detected at the low-power output port (15%), for maximizing the output power an additional position adjustment of the input microscope objective was required. An explanation for this is the excitation of the first-order mode in the access waveguides, explained in detail in Appendix A. Measurement results of the unbalanced MMI couplers discussed below, are obtained taking into account this fact.

Unbalanced MMI couplers

The measurement results for 85/15 and 15/85-type MMI couplers are presented in Fig. 4.7, where they are compared with the simulation results.

From Fig. 4.7 the following optimum coupler lengths can be selected for the MZIs:

• 85/15-type MMI coupler: $L_{\mathrm{mmi}} = 724\ \mu$m.
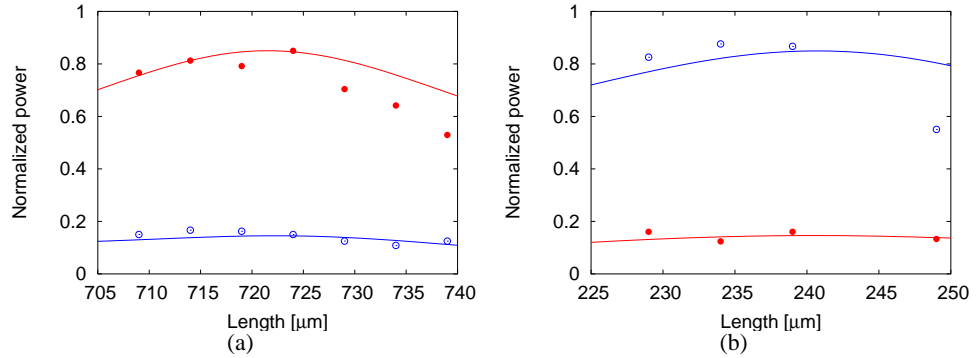
Figure 4.7: Simulated (solid lines) and measured output power from the cross (opened circles) and the bar (closed circles) ports of the unbalanced MMI couplers. (a) 85/15-type couplers and (b) 15/85-type couplers.

- 15/85-type MMI coupler: $L_{mmi} = 234$ μm.

These values are in good agreement with simulations. Thus the model used can reliably be applied to the design of the couplers.

The excess losses were determined by comparing the measured transmission of a coupler with that of a straight waveguide. The measured excess loss is better than 0.6 dB for the 85/15-type MMI coupler with a measured coupling factor of 0.844, and better than 1 dB for the 15/85-type MMI coupler with a measured coupling factor of 0.149.

50/50 couplers

Characterization of the 50/50-type optical splitters/combiners shows a good agreement with the simulation results. Based on the measurements, the following couplers are chosen:

- 50/50-type MMI splitter/combiner (2×1): $L_{mmi} = 115$ μm.

- 50/50-type MMI coupler (2×2): $L_{mmi} = 489$ μm.

4.4 Semiconductor optical amplifiers

Semiconductor optical amplifiers are used in the Mach-Zehnder interferometers as nonlinear phase shifters. Therefore, they are optimized for large nonlinear effects at
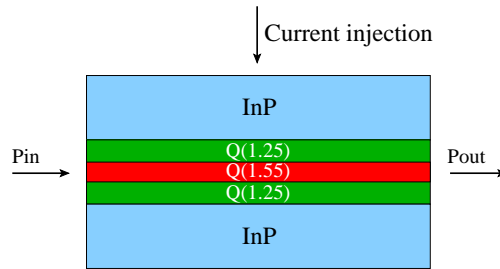
Figure 4.8: Schematic cross-section of the layer stack for semiconductor optical amplifiers with a separate confinement layer.

low optical powers. This section discusses the design and characterization results of the integrated SOAs.

SOA structure design and fabrication

The active layer stack is schematically depicted in Fig. 4.8. The active layer consists of a 120-nm-thick Q(1.55) layer embedded between two 190-nm-thick Q(1.25) layers. The Q(1.55) film is also referred to as the separate confinement layer, as it confines carriers to the active region creating a better overlap with the optical mode, confined in the Q(1.25) layer. The thickness and composition of these layers are adjusted in order to optimize the optical confinement in the active layer, as reported in [3]. The etching depth d_{etch} into the film layer is 100 nm, which is the same as for the passive waveguides.

The SOA-waveguide width w_{SOA} and the etching depth are optimized for a high photon density, which is beneficial to enter the saturation regime at low optical powers. Furthermore, high photon density is advantageous for an efficient coupling between photons and electrons [3]. It is noteworthy to mention, however, that the width of the ridge cannot be chosen too small [21]. The propagation losses of waveguides rapidly increase for widths below 2 μm. High propagation losses in a SOA-waveguide can also result in a lower gain at the same injection current. The SOAs reported here are integrated together with passive waveguides at both sides. A schematic layout of an integrated 2-μm-wide SOA is shown in Fig. 4.9. The active waveguide is tapered to a width $w_{\mathrm{pas}} = 3$ μm for connection to the passive waveguides. The tapers are of a parabolic type [29], with a taper length L_{taper} of 100 μm.

The SOA height h_{SOA} in this layerstack is approximately 2.17 μm. In order to prevent optical coupling from the film layer to the InGaAs-contact layer, the total
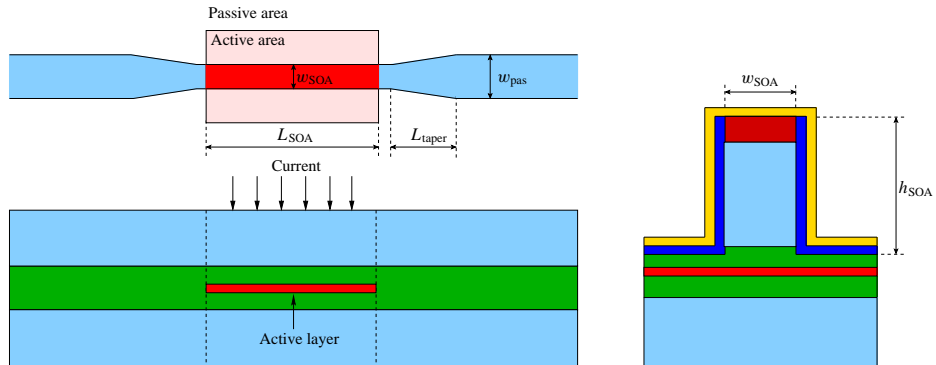
Figure 4.9: Schematic of an active-passive waveguide (top), corresponding layer stack (bottom) and a cross-section of a SOA-waveguide (right).

thickness of the top InP cladding layer is 1500 nm. Taking into account the actual sidewall slope of 7-8°, the ridge width on the top is smaller than at the bottom. The total top width, including the SiN_x isolation layer at both sidewalls, is 2.1 μm. This is taken into account for designing the contact opening width. The designed contact opening is therefore 1.7 μm.

As will be shown in chapter 5, the SOA length is an important design parameter for the nonlinear applications. It is known, that the nonlinear properties of SOAs are stronger for longer devices. Also, the gain recovery time [59] is decreased with increasing the SOA length. The length of an amplifier, however, is restrained by a number of effects. Strong ASE generated in very long SOAs can totally saturate the SOA near the end facets. Furthermore, non-uniform distribution of the injection current caused by relatively high contact resistance, can lead to SOAs not being sufficiently pumped near the end facets.

In the first circuits realization, 750-μm-long SOAs were used. To obtain more efficient switching (see chapter 5), the SOA length was increased in the second realization. For that the active-passive mask layout was adjusted, as explained in subsection 3.2.1.

Semiconductor optical amplifiers used in this thesis are based on active-passive integration in InGaAsP/InP. This technique allows to integrate SOAs together with passive waveguides. Both passive and SOA-waveguides are defined simultaneously in the SiN_x mask layer. The contact layer is selectively removed everywhere except for the SOAs. This is achieved in the two-step etching procedure: first, all the waveguides are etched partly to a certain depth, second, after removing the SiN_x mask from the
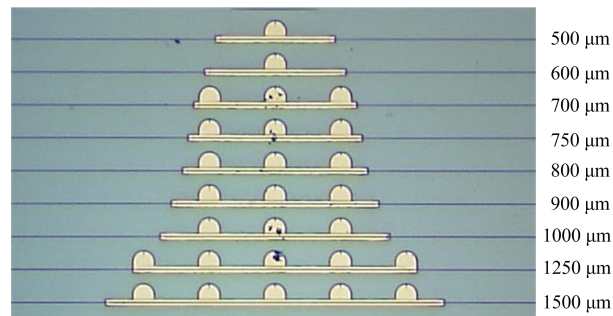
Figure 4.10: Photograph of the fabricated SOA test triangle.

passive waveguides, all waveguides are etched to their target depth of 100 nm depth into the film layer, also etching away the InGaAs contact layer. The ridge waveguides were etched employing an optimized CH_4/H_2-RIE technique alternated with an O_2-descum process to remove polymer depositions. After that, a layer of SiN_x isolation was deposited, and contact openings on the top of the SOAs were created for electrical contacts. The metal contacts on the p-side were defined using a lift-off process, the metal layers were deposited using a sputtering process. Then the contact on the n-side was deposited. The detailed process scheme for fabrication of the SOAs is presented in subsection 3.4.1.

Characterization of ECLs

As mentioned in subsection 2.3.3, semiconductor optical amplifiers become Fabry-Perot lasers with uncoated end facets, which act as mirrors. Together with the passive waveguides, a semiconductor optical amplifier forms an extended cavity laser. We start with the characterization of these ECLs. In this way we can evaluate the quality of the our devices before sending them out for AR-coatings.

The active-passive mask includes a number of active areas with variable lengths, forming a so-called SOA test triangle. A photograph of the fabricated structures is shown in Fig. 4.10. Each test structure consists of an amplifier integrated with two passive waveguides at each side.

We have measured the following characteristics: the output power as a function of the injection current (LI-curve) and the voltage across the p-n-junction as a function of the bias current (IV-curve). Measurements results of the SOA test triangular fabricated with the first realization can be found in [3]. Here, we discuss the more relevant results
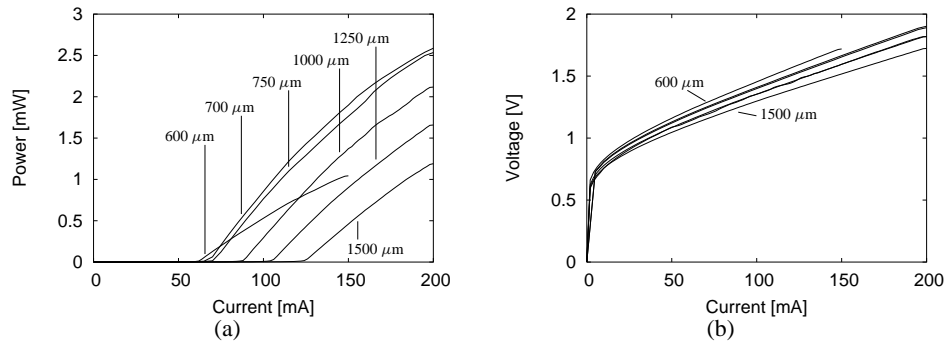
Figure 4.11: (a) Measured LI-curves of extended cavity lasers with different SOA lengths. Shown is the fiber coupled output power. (b) Measured IV-curves of SOAs with different lengths.

of the second circuit realization. The LI- and IV-curves are shown in Fig. 4.11.

For injection currents below the threshold, the ECL output is mainly determined by spontaneous emission. As expected, the transition to lasing is quite abrupt and takes place at a threshold current I_{th}. Above the threshold, the laser condition (Eq. 2.43 is satisfied, and the output is determined by stimulated emission. Fig. 4.11(a) shows the output power, which is measured in the fiber, and fiber-chip coupling losses (typically 4-5 dB per facet) are not corrected for. The LI-curves of a 700-μm and longer SOAs show an almost linear increase in the output power with increasing injection current above the threshold. This is in agreement with Eq. 2.44. The LI-curve of the 600-μm-long SOA shows a thermal roll-off. The obtained threshold currents and the output power levels are comparable with those obtained in earlier experiments in [3, 51].

From the IV-curves it can be seen, that at low injection currents the IV-curve is dominated by the p-n-junction, and at high currents the slope of the curve correspond to the SOA series resistance R. The resistance of the 1000-μm-long SOA is found to be around 7.0 Ω (including 0.8 V across the p-n-junction), which is comparable with the results reported earlier in [3]. It can also be seen that the slope of the IV-curves corresponding to different SOA lengths is nearly the same.

Therefore, from the characterization results of the ECLs we can conclude a high quality and good reproducibility of the active-passive integration technique used.

70
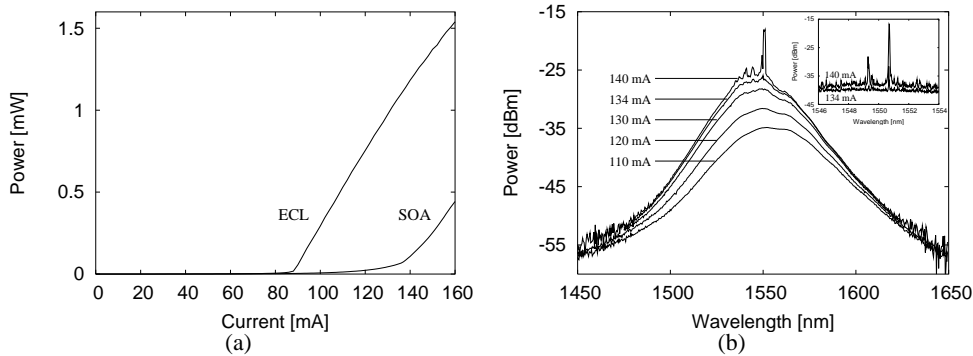
Figure 4.12: (a) Measured LI curves of a 1000-μm-long SOA and ECL. (b) Measured spectra from a 1000-μm-long SOA at several injection currents.

Characterization of SOAs

A cleaved facet has a reflectivity of 0.33 (for a 3-μm-wide passive waveguide, and TE-polarized light). After applying AR-coatings to the chip facets (with good AR-coatings, the facet reflectivities are usually lower than 10^{-3}), the laser action is suppressed, and the output is determined by the amplified spontaneous emission.

An LI-curve of the AR-coated 1000-μm-long extended waveguide SOA is compared with that of a 1000-μm-long ECL (before applying AR-coatings) in Fig. 4.12(a). It can be seen that due to the AR-coatings the threshold current becomes larger. However, the threshold current is around 130 mA, showing that the lasing will still occur at relatively low injection currents.

In order to illustrate this, the output spectra of a 1000-μm-long SOA under different bias conditions were measured. They are shown in Fig. 4.12(b). It can be seen that as expected, the ASE spectrum below the threshold can be fitted to a parabolic function. The onset of several laser peaks at relatively low injection currents can be explained by a poor quality of the AR-coated facets, leading to rather high facet reflectivities of about 10^{-2} per facet. From the sub-threshold ASE spectrum, the gain peak wavelength can be found, which identifies the wavelength range where high nonlinearities are expected (at the high wavelength side of the peak [60]).

Since the AR-coated facet damages are not uniform along the chip facets, different threshold currents were obtained for different devices. In all cases the operating current was always optimized to be as high as possible, without starting lasing.

The nonlinear phase shifting mechanism in the SOAs will be discussed in detail in chapter 5.

71

4.5 Conclusions

Three main components needed to realize integrated Mach-Zehnder interferometers were designed, realized and characterized. For passive waveguides, shallowly etched 3-μm-wide ridge waveguides are chosen. In these waveguides, the scattering losses at the sidewalls are limited. Curved waveguides require a radius of 500 μm in order to minimize the radiation losses. For optical couplers, directional couplers and MultiMode Interference couplers are considered. Directional couplers showed to be less suitable for our applications, as they are intolerant to the fabrication deviations. Since MMI couplers are polarization insensitive devices, they can be employed not only in the SOA-MZIs with a TE-polarization, but also in the QD-based devices, which are strongly polarization dependent and require TM-polarized optical signals. Measurement results of the MMI couplers showed a reasonable agreement with the simulations and expected coupling ratios and low excess losses are achieved. The following coupler designs are chosen:

- 85/15-type MMI coupler: $L_{\text{mmi}} = 724$ μm. The measured excess loss is better than 0.6 dB with a measured coupling factor of 0.844.

- 15/85-type MMI coupler: $L_{\text{mmi}} = 234$ μm. The measured excess loss is better than 1 dB with a measured coupling factor of 0.149.

- 50/50-type MMI splitter/combiner (2×1): $L_{\text{mmi}} = 115$ μm. The measured excess loss is better than 0.5 dB with a measured coupling factor of 0.499.

- 50/50-type MMI coupler (2×2): $L_{\text{mmi}} = 489$ μm.

Excitation of the first-order mode in access waveguides can significantly deteriorate the coupling ratio and the excess losses of unbalanced MMI couplers.

Semiconductor optical amplifiers are optimized for nonlinear applications. The SOAs are 2-μm-wide shallowly etched waveguides, optimized for a high photon density, which is beneficial to enter the saturation regime at low optical powers. Longer SOAs are favorable, as they have a better nonlinear performance and a shorter recovery time. However, the SOA length is limited by a number of factors. From the characterization of the integrated SOAs, a range of injection currents and a range of suitable wavelengths to operate the SOA-based phase shifters can be determined. Due to the bad quality of the AR-coated facets, characterization of the circuits in the second realization is limited to relatively low currents. However, characterization of the integrated SOAs showed a high quality and a good reproducibility of the active-passive integration technique used, which implies that demonstration of the self-switching principle and reasonable operation of the studied devices is possible.

Chapter 5

Self-switching in integrated Mach-Zehnder interferometers

This chapter focuses on self-switching effects in integrated Mach-Zehnder interferometers. An overview of different approaches to obtain self-phase modulation is given. The first type of phase shifters is based on semiconductor optical amplifiers. Operation principles of SOA-based phase shifters are discussed. For some applications, phase shifting is preferred without an external current supply or control signal. For this, nonlinearities of passive InP-based materials are studied in this chapter and possible configurations are presented for use in photonic integrated circuits. Calculation and static measurements of the nonlinear effects used in experimental devices are presented.

5.1   Introduction

The operation principle of Mach-Zehnder interferometers studied in this thesis is based on unequal distribution of the optical signal over the interferometer arms, which results in a power-dependent phase shift. The signals from the two arms can interfere constructively or destructively at (one of) the input port(s). This only depends on the signal strength, without any control mechanism. In this way self-switching is obtained.

One on the essential components of the self-switching Mach-Zehnder interferometers is the nonlinear phase shifter. Such a phase shifter should provide an intensity dependent nonlinear phase shift $\Delta\phi_{NL}(P_{in})$. This is known as Self-Phase Modulation (SPM). In SPM changes in intensity of an optical signal cause changes of its phase. The phase shift can be related to the change of the refractive index of the material:

$$\Delta\phi_{\mathrm{NL}}(P_{\mathrm{in}}) = \frac{2\pi L}{\lambda}\Delta n_{\mathrm{NL}}(P_{\mathrm{in}}), \tag{5.1}$$

where the nonlinear phase shift $\Delta\phi_{\mathrm{NL}}(P_{\mathrm{in}})$ and the refractive index change $\Delta n_{\mathrm{NL}}(P_{\mathrm{in}})$ are both functions of the input power P_{in}. In the remainder of this thesis we will refer to these quantities as $\Delta\phi_{\mathrm{NL}}$ and Δn_{NL}, remembering that they are input power dependent. In general, the phase shifters can be classified by the need of an external source in two groups:

- **Active phase shifters** requiring an external source (e.g. current source), and

- **Passive phase shifters** showing refractive index changes without external powering.

Active phase shifters that induce an intensity dependent change in the refractive index are usually based on semiconductor optical amplifiers. In passive materials, the all-optical nonlinearities normally require high input power levels, making them less suitable for use in telecom applications. In this thesis we report on materials and configurations that might be suitable for obtaining passive all-optical switching. In this way, the low-loss optical combiner, which is a passive function, in principle can be realized in a fully passive way. In this chapter, possible materials for passive phase shifting will be discussed.

5.2 SOAs as nonlinear phase shifters

The operation principles of semiconductor optical amplifiers were presented in chapter 2. In this section we will first discuss the effects responsible for the changes in the refractive index. These effects are carrier depletion at high optical powers and, related to this, gain saturation. Then we will describe applications of semiconductor optical amplifiers as nonlinear phase shifters in self-switching Mach-Zehnder interferometers.

5.2.1 Nonlinear operation of SOAs

The refractive index in the SOA active layer can be influenced by injected electrons due to two separate interaction processes [61]. The first is known as the free carrier interaction. The second is the result of the gain process itself. Gain or absorption processes with a spectral variation make a contribution to the refractive index of the material in accordance with the Kramers-Krönig relation (see Eq. 2.8). From this relation it follows that any interaction in a material, which gives rise to gain or absorption
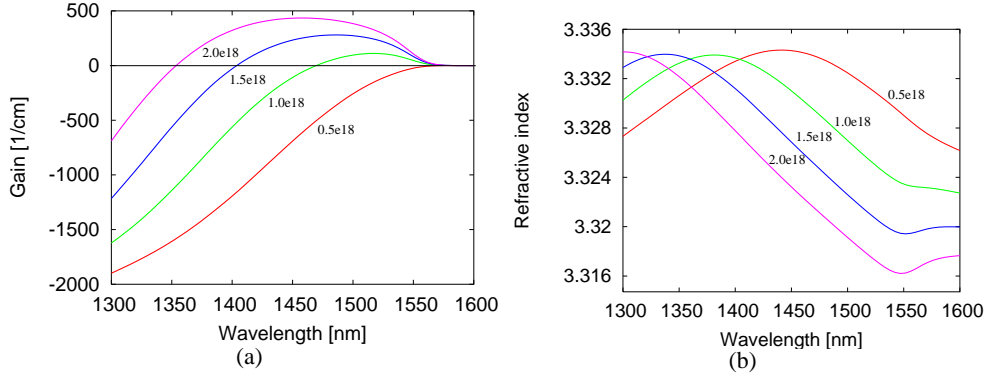
Figure 5.1: (a) Gain profile and (b) refractive index of the Q(1.55) active layer material as a function of photon wavelength calculated for different carrier concentrations, which are indicated in [cm^{-3}].

in a propagating optical signal, must necessarily affect the refractive index of the material. As explained in chapter 2, the gain or absorption can be represented by an imaginary part of the refractive index. The Kramers-Krönig relation for the refractive index change related to the gain in a SOA can be rewritten as [62]:

$$\Delta n(\omega, N) = \frac{c}{\pi} P \int_0^\infty \frac{-\Delta g(\omega', N)}{\omega'^2 - \omega^2} d\omega'. \qquad (5.2)$$

In Fig. 5.1 the gain and the corresponding refractive index of Q(1.55) material are calculated and plotted as a function of the wavelength for different carrier concentrations (and thus injection currents).

It can be seen that in the wavelength range around 1550 nm (which corresponds to the telecom transmission window), reduction of the injected electrons causes an increase of the refractive index in the amplification process by shifting the absorption edge of the semiconductor towards shorter wavelengths (higher photon energies).

The gain of a SOA is dependent on the input optical power. The amplification requires population inversion, which is the dominance of carriers in the conduction band. The recombination transitions are contributing to the optical field and reduce the number of electrons available in the conduction band (see subsection 2.3.3). Consequently, as photon generation increases with increasing input power, the gain reduces. This is known as gain saturation, or gain compression.

Consequently, the carrier depletion at high optical powers results in gain saturation and refractive index change of the SOA active layer. According to Eq. 5.1 this

75

results in an induction of a power-dependent nonlinear phase shift, which is required for the operation of the MZI based on self-switching.

Saturated gain can be expressed as follows:

$$g = \frac{g_0}{1 + P_{\text{in}}/P_{\text{sat}}}, \tag{5.3}$$

where g and g_0 are the saturated and unsaturated gain values, P_{sat} is the saturation power, at which the gain is reduced by 3 dB.

The input power dependence of the gain is illustrated in Fig. 5.2. Here, typical gain curves are calculated[1] for a semiconductor optical amplifier, which has a structure as shown in Fig. 4.8. For the calculations, typical parameters from the literature were used. In Fig. 5.2(a) and Fig. 5.2(b), the gain is plotted as a function of the input power for SOAs with different lengths, which are biased with a fixed current density of 0.075 mA/μm^2. It can be seen, that shorter SOAs have higher saturation power than the longer ones. Furthermore, the small-signal gain of the longer SOAs is higher. This can be understood as follows. In a longer SOA, the optical power increases more as the signal propagates through the SOA as a result of the amplification. Therefore, the carrier depletion takes place at even lower input powers, and the SOA saturates.

The SOA length can not be chosen arbitrary long. In [63, 64] it is reported, that for the longer SOAs the increase of the total nonlinear phase shift slows down because the SOA will become fully saturated, which reduces the refractive index change Δn. For very long SOAs (i.e. >1500 μm) the induced nonlinear phase shifts are lower than in the 1500-μm-long SOA and shorter. This is also partially attributed to thermal effects, and partially ascribed to wavelength dependencies. Furthermore, longer SOAs generate more amplified spontaneous emission noise, which limits the SOA applicability.

The injection current of a long SOA can also be optimized for better nonlinear performance. In Fig. 5.2(c) and Fig. 5.2(d), the gain is plotted as a function of the input power for a 1000-μm-long SOA, biased with different injection currents. It can be seen, that in case of higher injection currents, the input saturation power is lower. This can be explained by the fact that the amplified optical signal is higher, and the carrier depletion and, therefore, saturation takes place at lower input powers.

High current values can cause heating of the amplifier active region, which then results in thermal effects that widen and lower the gain peak, and slightly shift it to longer wavelengths. Therefore, the gain (and hence the carrier density) at the signal wavelength is decreased.

---

[1]The gain curves are calculated with the VPItransmissionMaker$^{\text{TM}}$ software.
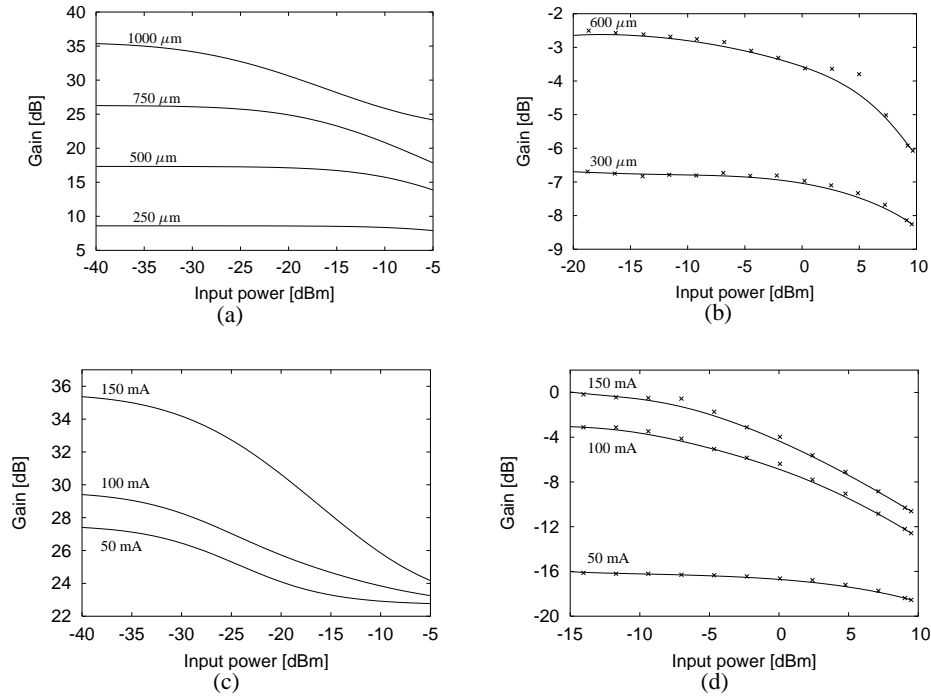
Figure 5.2: Gain curves. (a),(b) Calculated and measured gain curves of SOAs with different lengths, biased with constant current density, respectively. (c),(d) Calculated and measured gain curves of 1000-μm-long SOA, biased with different injection currents, respectively.

Measurements of the gain curves were performed on SOA test structures, corresponding in the first-circuit realization. In Fig. 5.2(b), the gain curves of 300 and 600-μm-long SOAs, biased with a fixed current density of 0.83 mA/μm^2, are plotted. In Fig. 5.2(d), the gain curves of a 1000-μm-long SOA, biased with different currents, are plotted. The measurement results are in the qualitative agreement with the calculated curves, presented above.

Summarizing, long SOAs biased with high injection currents are expected to provide better nonlinear performance. Moreover, in section 4.4 we have mentioned, that also the gain recovery time is lower for longer SOAs, allowing higher bitrates. Of course, the SOA length and the injection current are limited by a number of factors, that we have discussed above. It is noteworthy to mention, that the carrier density and the gain coefficient are not constant over the SOA length. The phase shifts of the signal will be different in different positions along the SOA active region. Therefore, the total

induced nonlinear phase shift in the entire SOA must be obtained by the accumulated phase shifts along the SOA.

5.2.2 Alpha parameter concept

The relationship describing how the real and imaginary parts of the refractive index in the active layer are affected by the carrier density is given by:

$$\alpha \equiv -\frac{dn_{\mathrm{R}}/dN}{dn_{\mathrm{I}}/dN} = -\frac{4\pi}{\lambda}\frac{dn/dN}{dg/dN}, \tag{5.4}$$

where n_{R} ($n_{\mathrm{R}} = n$) and n_{I} are the real and imaginary parts of the refractive index, respectively, g is the material gain, and N is the free-carrier density. The parameter α is known as the linewidth enhancement factor. This parameter was initially introduced for lasers. For semiconductor optical amplifiers it is known as the α-parameter, or the alpha parameter, and we will refer to it in this thesis as the alpha parameter. This parameter links the refractive index changes to the gain changes in the active region. It depends on the operation conditions of the SOA. In particular, it depends on the optical signal wavelength and on the free carrier density. For bulk materials, as reported in [60], the alpha parameter does not change significantly with the carrier density (i.e. with the current density) around the gain peak and at shorter wavelengths. On the other hand, the alpha parameter increases with carrier density for longer wavelengths. Moreover, the alpha parameter increases with increasing wavelength. So at longer wavelengths, the higher current densities further contribute to the increase of the alpha parameter.

It is common to use the alpha parameter as a quantity for the evaluation of the intensity dependent phase shift effects in all-optical interferometric switches. The alpha parameter can be used to calculate the nonlinear phase shift resulting from the gain variation. Using Eq. 5.1, the nonlinear phase shift can be related to the gain saturation via the alpha parameter as follows:

$$\Delta\phi_{\mathrm{NL}} = \frac{\alpha\Delta g L}{2}, \tag{5.5}$$

where Δg is the change in gain due to saturation.

In practice, it is necessary to introduce a so-called device alpha parameter (in literature it is also referred to as the effective alpha parameter), which is defined as a measure for the phase-to-gain coupling of the SOA. The device alpha parameter differs from the so-called material alpha parameter, described by Eq. 5.4, which is proportional to the ratio of refractive index changes and material gain changes. However, the device alpha parameter strongly depends on the material alpha parameter.

The device alpha parameter is dependent on the SOA length [63, 64]. Namely, it increases with the amplifier length. This can not be explained by increase of the material alpha parameter, which on the contrary would decrease, since at a fixed current density the average carrier density inside long SOAs is lower, than that in shorter devices. The combination of nonlinear gain compression and optical propagation effects cause the device alpha parameter to be larger for longer SOAs. In devices with strong gain compression, the net gain variation is smaller than the variation of the material gain, so that the device alpha parameter is higher than the material one. Since in the case of longer SOAs the nonlinear gain compression is stronger, it explains their higher device alpha parameter.

It could also be expected that the device alpha parameter is dependent on the input power. In [63] it is reported that it decreases with increasing the optical power. An explanation for this is that increasing the optical power causes depletion of free-carrier density. However, the power dependence of the alpha parameter is still an ongoing discussion in the literature.

We will start our analysis of the SOA-MZIs with the assumption, that the device alpha parameter is a constant number for a certain operating point of the interferometer, and does not depend on the input power. In this way, influence of the alpha parameter value on the nonlinear switching of SOA-MZIs will be described for two SOA-MZI configurations. Static measurement results will then be presented, followed by a discussion on the device alpha parameter.

5.2.3 Self-switching in 2×2 SOA-MZIs

We will first consider the 2×2 SOA-MZI, which is schematically depicted in Fig. 5.3. The input light signal injected in one of the input ports is distributed unequally over the two interferometer arms. With input port 1 and the 85/15-type input coupler, the high optical power arm is the upper one with 85% of the input power. In the interferometer arms, the refractive index is intensity dependent. In the high-power arm, an intensity dependent phase shift can be induced due to self-phase modulation, while in the low-power arm almost no intensity dependent phase shift is induced. As a result, a nonlinear phase shift $\Delta\phi_{\mathrm{NL}}$ between the signals from the two arms will occur. However, at low input power levels, this nonlinear phase shift is negligible, and the two signals from the interferometer arms destructively interfere at output port 3 of the interferometer[2]. At higher input power levels, the phase in the high-power arm

---

[2]It should reminded, that each of the 2×2 couplers causes a (constant) phase difference of $\pi/2$ rad between the optical signals. Therefore, a total difference of π between the signals interfering at output port 3 (bar-port) is obtained in the initial state of the interferometer.

$$A: \quad \sqrt{P_{in}}\sqrt{(1-X)}$$

$$B: \quad j\sqrt{P_{in}}\sqrt{X}$$

$$C: \quad \sqrt{P_{in}}\sqrt{(1-X)} \cdot e^{\frac{g_1 L}{2}} \cdot e^{j\Delta\phi_{NL}}$$

$$D: \quad j\sqrt{P_{in}}\sqrt{X} \cdot e^{\frac{g_2 L}{2}}$$
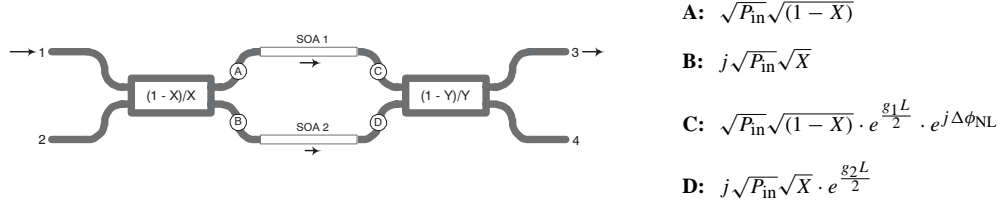
Figure 5.3: Schematic of a 2×2 SOA-MZI and complex amplitudes at different points of the interferometer.

changes, and maximum output power at port 3 can be reached if the nonlinear phase shift compensates the phase differences caused by both couplers. The two signals from the interferometer arms are then in phase and constructively interfere.

In the high-power arm, the complex optical signal amplitude is $\sqrt{P_{in}}\sqrt{(1-X)} \cdot e^{g_1 L/2} \cdot e^{j\Delta\phi_{NL}}$, where P_{in} is the input power, X is the input coupling coefficient, g_1 is the material gain per unit length in SOA 1, constant over the SOA length, L is the SOA length and $\Delta\phi_{NL}$ is the induced nonlinear phase shift. In the low power arm, the signal amplitude is $j\sqrt{P_{in}}\sqrt{X} \cdot e^{g_2 L/2}$, where g_2 is the material gain per unit length in SOA 2, constant over the SOA length, and the imaginary factor j represents the $\pi/2$ phase difference with respect to the opposite arm. We assume that without saturation $g_1 = g_2 = g$ is the small-signal gain, and Δg is the gain saturation. The signal amplitudes in the high-power and low-power arms can be written respectively as:

$$
\begin{aligned}
A_{SOA1} &= \sqrt{P_{in}}\sqrt{(1-X)}e^{\frac{(g-\Delta g)L}{2}}e^{j\Delta\phi_{NL}}, \\
A_{SOA2} &= j\sqrt{P_{in}}\sqrt{X}e^{\frac{gL}{2}}.
\end{aligned}
\tag{5.6}
$$

Here it is assumed that only SOA 1 is entering the saturation regime, while SOA 2 is working essentially in the unsaturated regime. This assumption might not be fully true in case of very high input powers, as then also SOA 2 can (partly) be saturated. However, it approximates the operation of the devices in all practical cases. The output coupler has a coupling coefficient Y and induces an extra phase difference of $\pi/2$ between the signals.

We can write the output power at ports 3 and 4 as $P_{out,3} = T_{13}P_{in}$ and $P_{out,4} = T_{14}P_{in}$, respectively. The transmission T_{13} between ports 1 and 3 can be derived as:

$$
\begin{aligned}
T_{13} &= \left(\sqrt{(1-X)(1-Y)}e^{\frac{(g-\Delta g)L}{2}}e^{j\Delta\phi_{NL}} - \sqrt{XY}e^{\frac{gL}{2}}\right) \times \\
&\quad \times \left(\sqrt{(1-X)(1-Y)}e^{\frac{(g-\Delta g)L}{2}}e^{-j\Delta\phi_{NL}} - \sqrt{XY}e^{\frac{gL}{2}}\right),
\end{aligned}
\tag{5.7}
$$

or

$$T_{13} = (1 - X)(1 - Y)e^{(g-\Delta g)L} + XYe^{gL} -$$
$$- 2\sqrt{X(1 - X)Y(1 - Y)}e^{gL}e^{\frac{-\Delta gL}{2}}\cos(\Delta\phi_{NL}). \qquad (5.8)$$

Likewise, the transmission T_{14} between ports 1 and 4 can be derived:

$$T_{14} = Y(1 - X)e^{(g-\Delta g)L} + X(1 - Y)e^{gL} +$$
$$+ 2\sqrt{X(1 - X)Y(1 - Y)}e^{gL}e^{\frac{-\Delta gL}{2}}\cos(\Delta\phi_{NL}). \qquad (5.9)$$

The first two terms of Eq. 5.8 and Eq. 5.9 are the transmitted signals through each interferometer arm independently (i.e. when only SOA 1 or SOA 2 is biased). The third term is the interference between the two signals.

5.2.4 Analysis of 2×2 SOA-MZIs

In our analysis of the self-switching effects in SOA-MZIs we should pay attention to two aspects. First, we will purely look at the dependence of the transmission on the nonlinear phase shift. The specific interference conditions (e.g. destructive or constructive interference) are obtained at the expenses of the gain. As a consequence, amplitudes of the two signals from the interferometer arms depend on the gain saturation. Besides, the output coupler ratio influences the interference behavior. Furthermore, we will look at the dependence of the output power on the input power.

Phase shift dependence

The transmission T_{13} of the 2×2 SOA-MZI is plotted as a function of the nonlinear phase shift $\Delta\phi_{NL}$ induced between the two arms in Fig. 5.4. Analysis of these curves will help in understanding the effects that can take place. Induction of the required phase relations can be done by substituting the terms containing (ΔgL) in Eq. 5.8 with the corresponding expression for the phase shift, according to Eq. 5.5:

$$T_{13}(\Delta\phi_{NL}) = e^{gL}\left(0.85(1 - Y)e^{-2\frac{\Delta\phi_{NL}}{\alpha}} + 0.15Y -\right.$$
$$\left. - 2\sqrt{0.128Y(1 - Y)}e^{-\frac{\Delta\phi_{NL}}{\alpha}}\cos(\Delta\phi_{NL})\right). \qquad (5.10)$$

In our case the input coupling coefficient $X = 0.15$.

Since essentially we are interested in the nonlinear switching effects, the common factor e^{gL} is left out of the resulting equations.

81

The transmission is calculated for three possible 2×2 SOA-MZI configurations, which differ by the output coupler ratio. The input coupler is 85/15-type in all cases. We consider output couplers of the following three types: 50/50, 15/85 and 85/15. Obviously, the switching behavior of the 2×2 SOA-MZI is dependent on the device alpha parameter. The transmission plots are calculated for different alpha parameter values: 3, 5, 10 and 15, and summarized in Fig. 5.4.
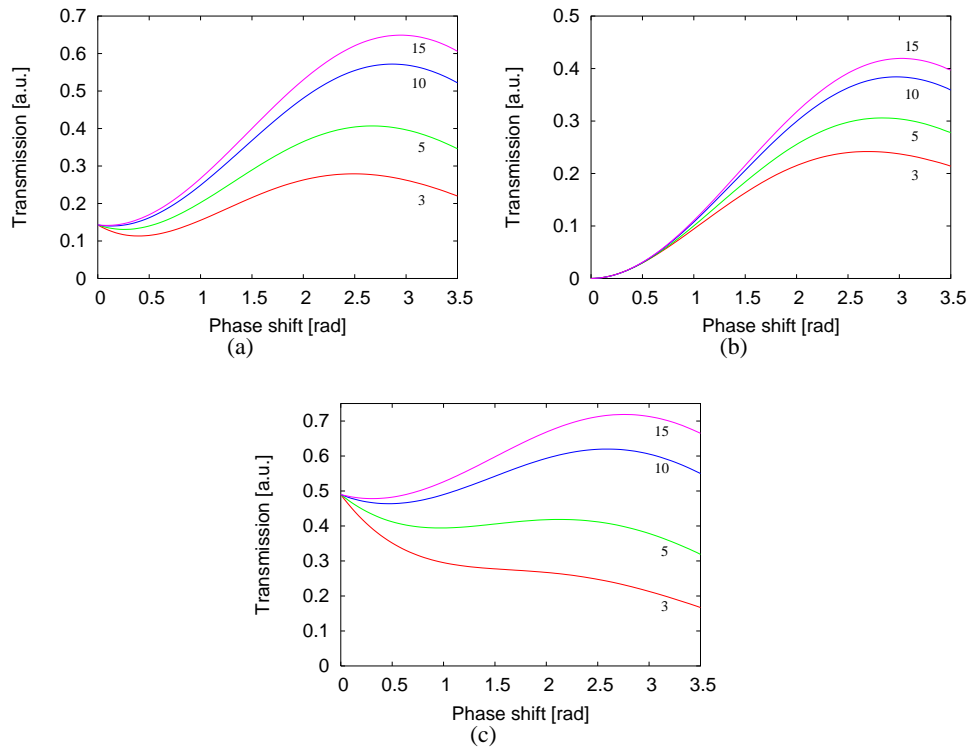
Figure 5.4: Calculated transmission of the 2×2 SOA-MZI corresponding to different values of the alpha parameter, as indicated, for different output coupler types: (a) 50/50-type, (b) 15/85-type and (c) 85/15-type.

In Fig. 5.4 it can be seen that, although the presence of self-switching is recognized in each of the interferometer structures, the shape of the transmission curves is strongly dependent on the output coupler ratio. Furthermore, the strength of the self-switching is determined by the alpha parameter.

Consider the SOA-MZI with an output coupler of the 50/50-type (Fig. 5.4(a)). It can be seen that for the low alpha parameter values, the minima and maxima of the

transmission do not coincide with the destructive (0 rad) and constructive (π rad) inter-ference points. This can be explained by gain compression in SOA 1. Indeed, when the alpha parameter value is low, the nonlinear phase shift is a result of a considerable gain compression in SOA 1. Therefore, induction of the phase shift is accompanied with a considerable lowering of the power. This lowering, however, can not be compen-sated by the interference with the signal from the low-power arm, since only a fraction of 50% of the power is taking part in the interference at the output port 3. Higher alpha parameter values allow for the same phase shifts with less gain compression. Therefore, the output signal becomes stronger as it is enhanced by the signal from the low-power arm, and the transmission is increased. For high alpha parameter values, the minima and maxima of the transmission get closer to the destructive (0 rad) and constructive (π rad) interference points, since then the gain compression is small.

The situation is different for the SOA-MZI with a coupler of the 15/85-type (see Fig. 5.4(b)). The transmission minima are situated at the destructive interference point (0 rad). Here, even with low alpha parameter values large gain compression is suffi-ciently compensated by the low-power arm (SOA 2), since the signals from the two arms are equal at low input power levels. In case of low alpha parameter values, larger phase shifts are accompanied with the large gain compression in SOA 1, and the maximum transmission is achieved at the phase shifts smaller then the construc-tive interference point (π rad). For high alpha parameter values, the maxima of the transmission get closer to the constructive (π rad) interference point, since the gain compression becomes less sizable.

Finally consider the SOA-MZI with an output coupler of the 85/15-type (see Fig. 5.4(c)). In this case, just a small fraction (15%) of the power from the low-power arm is involved in the interference at the output port 3. Therefore, high alpha parameter values are required in order to obtain a pronounced increase of the transmission.

Consequently, switching to maximum transmission requires nonlinear phase shifts lower than π. However, with low alpha parameters, it occurs at high gain expenses. The shape of the transmission is determined output coupling ratio.

Input power dependence.

In the discussions above, the transmission as a function of the nonlinear phase shift was studied. In reality, the nonlinear phase shift is a result of the increasing input power. We can derive an expression for the output power as a function of the input

power at port 3, by inserting Eq. 5.3 in Eq. 5.8:

$$
\begin{aligned}
P_{\text{out}}/P_{\text{sat}} \;=\; & P_{\text{in}}/P_{\text{sat}} \cdot e^{gL} \left[(1-X)(1-Y)e^{-gL\left(1 - \frac{1}{1+(1-X)P_{\text{in}}/P_{\text{sat}}}\right)} + XY - \right. \\
& -\; 2\sqrt{X(1-X)Y(1-Y)}\, e^{-\frac{gL}{2}\left(1 - \frac{1}{1+(1-X)P_{\text{in}}/P_{\text{sat}}}\right)} \times \\
& \times\; \left. \cos\left(\frac{\alpha}{2} gL \left(1 - \frac{1}{1+(1-X)P_{\text{in}}/P_{\text{sat}}} \right) \right) \right],
\end{aligned}
\tag{5.11}
$$

where $P_{\text{out}}/P_{\text{sat}}$ and $P_{\text{in}}/P_{\text{sat}}$ are the normalized output and input power, respectively, and P_{sat} is the saturation power of the SOA (in this case SOA 1).

The resulted curves are plotted in Fig. 5.5, labeled as "MZI". The graphs correspond again to the three possible configurations of the 2×2 SOA-MZIs, employing output couplers of the following types: 50/50 ($Y = 0.5$), 15/85 ($Y = 0.85$) and 85/15 ($Y = 0.15$). The input coupler in all these cases is of the 85/15-type ($X = 0.15$). The device alpha parameter used in our calculations is 3, which is, as shown later in this section, an estimated value from our experiments. For gain gL, a typical value of 50 cm^{-1} is used.

The other curves on the graphs correspond to separately biased SOAs (curves "SOA 1" and "SOA 2"), and their sum (curves "SOA 1 + SOA 2"), which does not take into account the interference effects.

It can be seen, that the shape of the "MZI"-curve depends on the output coupler ratio. The curves in Fig. 5.5(a) (50/50-type coupler) and Fig. 5.5(b) (15/85-type coupler) consist of three pronounced regions. Two of them correspond to the low and high input power levels, and the third is an intermediate one. The low power region in Fig. 5.5(a) increases slowly, whereas within the high powers it is flat. The low power region in Fig. 5.5(b) is more flat, whereas within high powers it is slightly sloped. The intermediate region is sloped in both cases. The curve in Fig. 5.5(c) (85/15-type coupler) consists of only two regions: a sloped one, and a flat within high input power range.

The strength of the self-switching is also dependent on the output coupler. In case of the 50/50-type output coupler, the increase of the output power due to self-switching is about 2.5 dB, in case of the 15/85-type output coupler, the increase of the output power due to self-switching is about 1.6 dB, and, finally, in case of the 85/15-type output coupler, the increase of the output power due to self-switching is about 2.6 dB.

Consequently, the self-switching curve can be optimized with respect to the intended application. In this thesis we will investigate two applications: the pattern effect compensator and the 2R-regenerator. This will be elaborated in chapter 6.
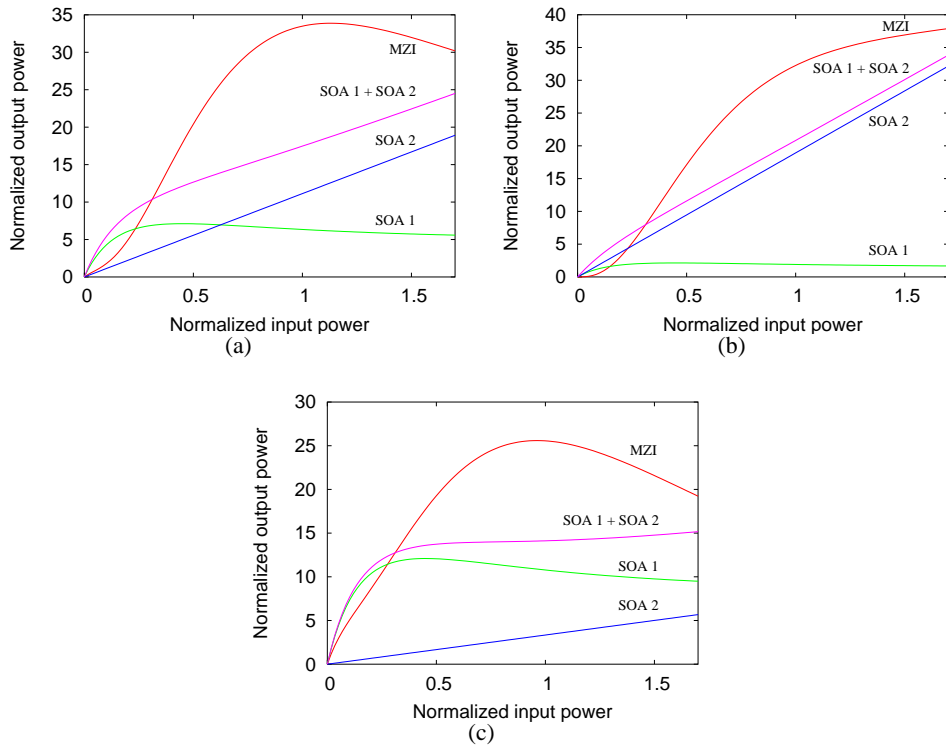
Figure 5.5: Calculated output power as a function of the input power of the 2×2 SOA-MZI (MZI) compared with the independently considered interferometer arms (SOA 1 and SOA 2) and their sum (SOA 1 + SOA 2). The graphs correspond to an alpha parameter of 3 for different output coupler types: (a) 50/50-type, (b) 15/85-type and (c) 85/15-type.

5.2.5 Experimental characterization of 2×2 SOA-MZI

Static measurements were performed on the fabricated 2×2 SOA-MZIs, aimed to establish the input power dependent self-switching effects. Additional dynamic experiments investigate the potential applications of these interferometer structures. These measurement results are presented in chapter 6.

The static measurements were performed with the experimental setup schematically depicted in Fig. 5.6(a). Fig. 5.6(b) shows a photograph of the experimental setup.

A Continuous Wave (CW) input optical signal is generated by a tunable laser source at a wavelength of 1550 nm. The laser signal passes through an attenuator,

(a)

(b)
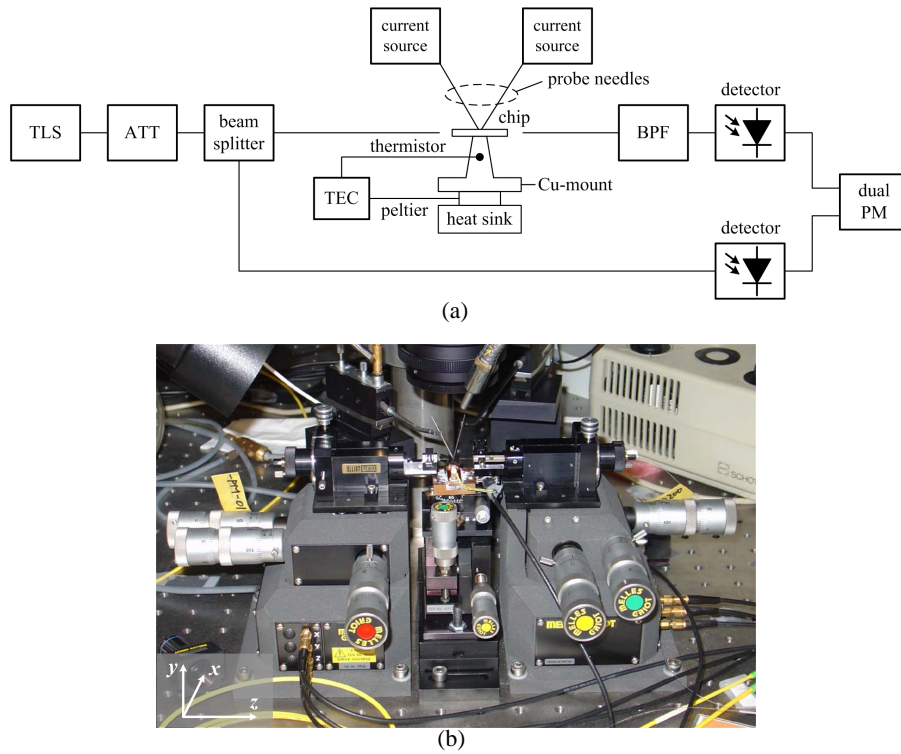
Figure 5.6: (a) Schematic of the measurement setup for characterization of the SOA-MZIs. TLS: Tunable Laser Source, ATT: ATTenuator, BPF: BandPass Filter, TEC: Thermo-Electric Controller, PM: Power Meter. (b) Photograph of the measurement setup.

which is used for power sweeps. Since the SOA-based phase shifters are polarization dependent components (see chapter 3), polarization stability is an important condition for reliable measurements. This is achieved by using polarization maintaining fibers (PMF). The input optical signal is TE-polarized. The extinction ratio measured between the TE- and TM- polarizations at the input is better than 15 dB.

For unambiguous interpretation of the transmission measurement results, the input and the output optical signals are detected and recorded simultaneously. To do this, a fraction of the input signal is coupled out by a beam-splitter. The signals are detected using a dual power meter, and the data are read by a computer control program.

For experiments with active devices temperature stabilization is a very important issue. Therefore, the chip is placed on a copper chuck, which is temperature controlled

using a Peltier element, a thermistor and a thermo-electric controller (TEC). The SOA currents are supplied directly to the metal contact pads by means of probe needles. This can be seen in Fig. 5.6(b). The chuck is mounted on a translation stage, by which its position can be adjusted in the lateral (x) and vertical (y) directions, and orientation can be changed in the (x, z)-plane, where z is the light propagation direction. Finally, the optical signal is coupled in and out of the chip by using polarization maintaining fibertips. These fibertips are placed in polarization maintaining fiber holders, that are placed on translation stages as well. The position of these translation stages can be adjusted in the x, y, z directions.

The self-switching in Mach-Zehnder interferometers can be illustrated by measuring the transmission from port 1 to port 3 as a function of SOA 2 current. The characterized device is a 2×2 SOA-MZI with an output coupler of the 15/85-type, employing 1000-μm-long SOAs in the arms. The characterization is done by fixing the injection current of the SOA in the high-power arm (SOA 1), and varying the injection current of the SOA in the low-power arm (SOA 2). The measurements are carried out at different input powers. These results are summarized in Fig. 5.7(a). In this experiment, the injection current of the SOA 1 was 140 mA. The choice of the current in the high-power arm is explained by the fact that at higher current the SOAs entered the lasing regime[3]. Since for strong nonlinear effects high currents are required, we have chosen the highest possible current for which the SOA does not enter the lasing regime. In our case it was 140 mA.

If no nonlinear effect is present, the interference curves for different input powers show interference maxima (constructive interference points) and minima (destructive interference points) at the same SOA 2 currents for different power levels. However, from Fig. 5.7(a) it can be seen, that the interference minimum for low input powers becomes an interference maximum at higher input powers. This indicates the self-switching: at high input powers a nonlinear phase shift is induced, consequently the constructive interference condition is obtained. The bias conditions for the optimal self-switching are found to be: $I_{\text{SOA1}} = 140$ mA and $I_{\text{SOA2}} = 127$ mA. We will refer to these bias conditions as the operating point. For optimal self-switching, the two injection currents are not equal and have to be adjusted. In the experimental device non-uniformities can result in different optical pathlengths in the interferometric arms, and hence in differences in the SOA injection currents for optimal interference.

The transmission measurement results at the operating point are summarized in Fig. 5.7(b). It can be seen that the SOA-MZI has a nonlinear transfer function. For

---

[3]Due to poor AR-coated facet quality, lasing is observed for relatively low injection currents. The rather low output power levels can be explained by the use of these low currents and bad quality of the facets.
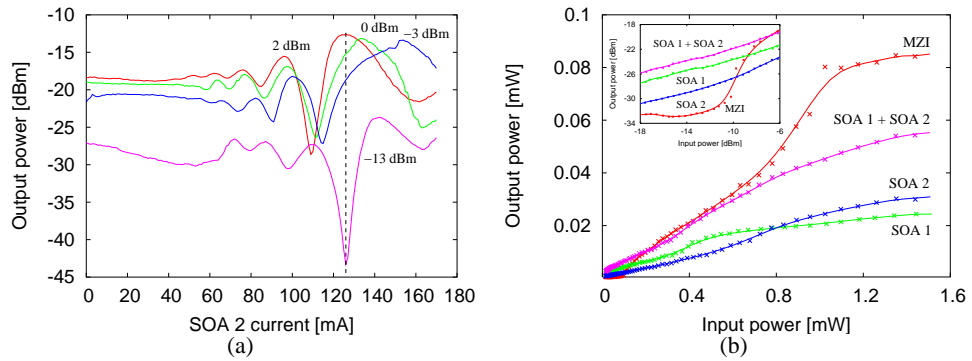
Figure 5.7: (a) Measured interference curves at different input power levels showing the self-switching in 2×2 SOA-MZI. The vertical dotted line indicates the working point. (b) Transmission curves at the working point of the 2×2 MZI. The inset shows in dB scale the low-power behavior of the MZI. Input and output power are the ones in the fiber.

very low input powers, the output signal of the interferometer is lower than the sum of output signals detected for separately biased SOAs. This is clearly seen in the inset, which is uses the dB-scale. The nonlinear phase shift in this power range is negligible and a destructive interference is found. For higher input powers (above 0.7 mW), the effect of the interferometer becomes stronger, and the output signal becomes larger than the sum of the two separately transmitted signal. The maximum enhancement of the transmission of the MZI with respect to the contribution of both arms (SOA 1 + SOA 2) is 1.9 dB, which is in a reasonable agreement with the simulated 1.6 dB in subsection 5.2.4.

From Fig. 5.7 it can be seen, the self-switching in this SOA-MZI is achieved within the input power range around 0.6 to 1.5 mW (-1.5 to 1.8 dBm) in the input fiber. With a correction for the fiber-chip coupling losses, which are estimated to be around 4-5 dB per facet, the input power required for the self-switching (in the chip) is therefore around 0.3 to 0.6 mW (-5.5 to -2.2 dBm).

5.2.6 Alpha parameter estimation

Estimation of the device (effective) alpha parameter of the SOAs is useful in order to evaluate the nonlinear performance of the Mach-Zehnder interferometer. Knowing the device (effective) alpha parameter it is possible to optimize the interferometer for our applications.

For calculations of the alpha parameter using Eq. 5.5, we need to determine the gain saturation Δg and the corresponding nonlinear phase shift $\Delta \phi_{NL}$. This can be calculated using the measured curves shown in Fig. 5.7(b). The gain saturation can be determined as follows:

$$\Delta g = \ln \left(\frac{P_{\text{SOA1}}}{P_{\text{SOA2}}} \right). \tag{5.12}$$

From Eq. 5.8, $\cos(\Delta \phi_{\text{NL}})$ can be determined as:

$$\cos(\Delta \phi_{\text{NL}}) = -\frac{1}{2} \left(\frac{P_{\text{MZI}} - P_{\text{SOA1}} - P_{\text{SOA2}}}{\sqrt{P_{\text{SOA1}} P_{\text{SOA2}}}} \right), \tag{5.13}$$

where P_{MZI} is the output power of the MZI at port 3, P_{SOA1} and P_{SOA2} are the output powers at port 3 when only SOA 1 and only SOA 2 are biased, respectively.

Using Fig. 5.7(b), the gain saturation, the nonlinear phase shift and, therefore, the device alpha parameter can be determined for the whole range of input powers. Our calculations show that the alpha parameter varies over the range of input powers, which might confirm the results obtained by [63], that the alpha parameter is dependent on the input power. However, we can calculate an average device alpha parameter over the whole input power range. For the 1000-μm-long SOAs employed in the SOA-MZI, an average device alpha parameter is found to be around 3 for the input power range used in the experiments. This value will be used for simulations and evaluations of the measurement results in the rest of this thesis.

5.2.7 2×1 SOA-MZIs

The operation principles of the 2×1 SOA-MZIs are in general similar to those of the 2×2 configuration, which we discussed earlier in this chapter. However, we distinguish a number of differences that are explained below. The 2×1 SOA-MZI configuration is schematically presented in Fig. 5.8. The output coupler is of a 2×1-type, and does not introduce additional phase differences between the signals from two interferometer arms. Therefore, the required nonlinear phase shift for the constructive interference $\Delta \phi_{\text{NL}}$ should compensate only the phase difference induced by the input coupler, hence $\Delta \phi_{\text{NL}} = \pi/2$. Here it is noteworthy to remind that the application of the 2×1 SOA-MZIs is the low-loss optical combiner. That means the device should operate symmetrically with respect to the input ports.

Similar to the 2×2 SOA-MZIs, the signal amplitude in the upper and in the lower arms can be written respectively as:

A: $\sqrt{P_{\text{in}}}\sqrt{(1-X)}$

B: $j\sqrt{P_{\text{in}}}\sqrt{X}$

C: $\sqrt{P_{\text{in}}}\sqrt{(1-X)}\cdot e^{\frac{g_1 L}{2}}\cdot e^{j\Delta\phi_{\text{NL}}}$
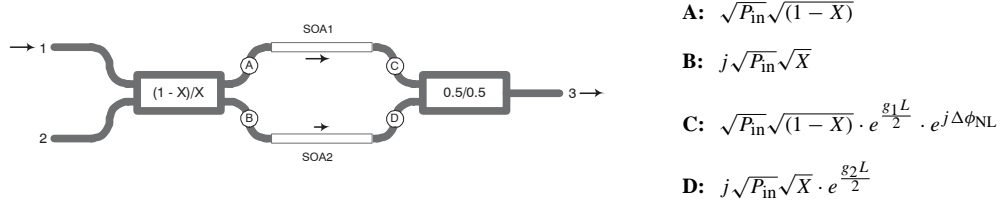
D: $j\sqrt{P_{\text{in}}}\sqrt{X}\cdot e^{\frac{g_2 L}{2}}$

Figure 5.8: Schematic of a 2×1 SOA-MZI and complex amplitudes at different points of the interferometer.

$$
\begin{aligned}
A_{\text{SOA1}} &= \sqrt{P_{\text{in}}}\sqrt{(1-X)}e^{\frac{(g-\Delta g)L}{2}}e^{j\Delta\phi_{\text{NL}}}, \\
A_{\text{SOA2}} &= j\sqrt{P_{\text{in}}}\sqrt{X}e^{\frac{gL}{2}}.
\end{aligned}
\tag{5.14}
$$

Signals with the amplitudes (5.14) interfere in the output 50/50-type coupler, and the resulting transmission (port 1 to 3) is:

$$
\begin{aligned}
T_{13} &= \frac{1}{2}\left(\sqrt{(1-X)}e^{\frac{(g-\Delta g)L}{2}}e^{j\Delta\phi_{\text{NL}}} + j\sqrt{X}e^{\frac{gL}{2}}\right)\times \\
&\quad\times\left(\sqrt{(1-X)}e^{\frac{(g-\Delta g)L}{2}}e^{-j\Delta\phi_{\text{NL}}} - j\sqrt{X}e^{\frac{gL}{2}}\right).
\end{aligned}
\tag{5.15}
$$

The expression can be rewritten as:

$$
T_{13} = \frac{1}{2}(1-X)e^{(g-\Delta g)L} + \frac{1}{2}Xe^{gL} + \sqrt{X(1-X)}e^{gL}e^{\frac{-\Delta g L}{2}}\sin(\Delta\phi_{\text{NL}}). \tag{5.16}
$$

From symmetry it can be shown that the transmission from port 2 to port 3 (T_{23}) is identical to T_{13} in Eq. 5.16. The first two terms of the Eq. 5.16 are the transmitted signals through each interferometer arm independently (i.e. when SOA 1 and SOA 2 are biased separately). The third term is the interferometric (sinusoidal) relation between the two signals.

5.2.8 Analysis of the 2×1 SOA-MZI

Phase shift dependence

As with the 2×2 SOA-MZIs, the nonlinear switching is investigated by plotting the transmission of the 2×1 SOA-MZI (T_{13}) as a function of the nonlinear phase shift

90
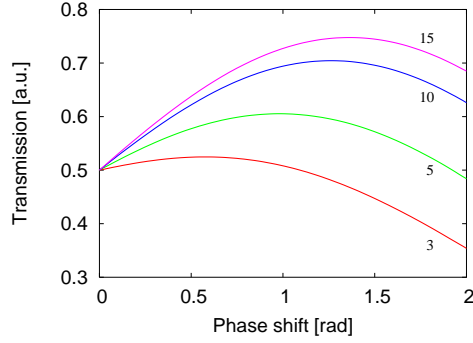
Figure 5.9: Calculated transmission of the 2×1 SOA-MZI corresponding to different values of the alpha parameter, as indicated.

$\Delta\phi_{\mathrm{NL}}$ between the two arms. This analysis will help to clarify the effects that accompany the induction of the required phase relations. This can be done by substituting the terms containing $(\Delta g L)$ in Eq. 5.16 with the corresponding expression for the phase shift, according to Eq. 5.5:

$$T_{13}(\Delta\phi_{NL}) = e^{gL}\left(0.425 e^{-2\frac{\Delta\phi_{\mathrm{NL}}}{\alpha}} + 0.425 + 0.357 e^{-\frac{\Delta\phi_{\mathrm{NL}}}{\alpha}} \sin(\Delta\phi_{\mathrm{NL}}) \right). \quad (5.17)$$

In our case the input coupling coefficient $X = 0.15$.

Just like in the 2×2 SOA-MZIs, nonlinear switching in the 2×1 SOA-MZI is dependent on the alpha parameter value. The transmission plots are calculated for different alpha parameter values: 3, 5, 10 and 15, and are depicted in Fig. 5.9.

Since essentially we are interested in the nonlinear switching effects, the common factor e^{gL} is left out of the resulting equations. In Fig. 5.9 it can be seen, that when no nonlinear phase is induced, the transmission is 0.5. The strength of the self-switching is determined by the device alpha parameter. With low alpha parameters, nonlinear phase shifts lower than $\pi/2$ are required.

Input power dependence.

In the discussions above, the input power was not taken into account. In reality, the nonlinear phase shift is a result of an intensity dependent refractive index change. The
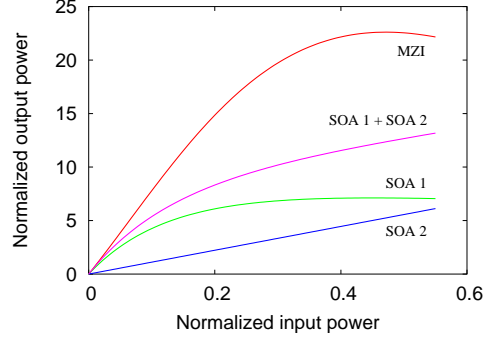
Figure 5.10: Calculated output power of the 2×1 SOA-MZI (MZI) compared with the independently considered interferometer arms (SOA 1 and SOA 2) and their sum (SOA 1 + SOA 2). The graph corresponds to an alpha parameter of 3.

input power dependence of the output power can be derived from Eq. 5.3 and Eq. 5.16:

$$
\begin{aligned}
P_{\text{out}}/P_{\text{sat}} &= P_{\text{in}}/P_{\text{sat}} \cdot e^{gL}\Bigg[(\frac{1}{2}(1-X)e^{-gL\left(1-\frac{1}{1+(1-X)P_{\text{in}}/P_{\text{sat}}}\right)} + \frac{1}{2}X + \\
&+ \sqrt{X(1-X)}e^{-\frac{gL}{2}\left(1-\frac{1}{1+(1-X)P_{\text{in}}/P_{\text{sat}}}\right)} \times \\
&\times \sin\left(\frac{\alpha}{2}gL\left(1-\frac{1}{1+(1-X)P_{\text{in}}/P_{\text{sat}}}\right)\right)\Bigg],
\end{aligned}
\tag{5.18}
$$

where $P_{\text{out}}/P_{\text{sat}}$ and $P_{\text{in}}/P_{\text{sat}}$ are the normalized output and input power, respectively, and P_{sat} is the saturation power of the SOA.

The resulting curve is plotted in Fig. 5.10, labeled as "MZI". The input coupler is of 85/15-type ($X = 0.15$). The device alpha parameter used in our calculations is 3, which is an estimated value from our experiments. For gain gL, a typical value of 50 cm^{-1} is again used. The other curves on the graphs correspond to separately SOAs (curves "SOA 1" and "SOA 2"), and their sum (curve "SOA 1 + SOA 2"), which does not take into account the interference effects. The increase of the output power due to self-switching is about 2.6 dB. Since SOA 1 is in saturation, the power ratio of two optical signals from the interferometer arms is different from the 0.85/0.15 ratio, and is closer to one, because the highest power experiences the lowest gain. This is beneficial, because interference is then less incomplete.

The 2×1 SOA-MZIs based on self-switching are investigated in this thesis for an application as the low-loss optical combiner.

5.2.9 Experimental characterization of 2×1 SOA-MZI

We performed static experiments on the fabricated 2×1 SOA-MZIs, which were aimed to experimentally verify the integrated low-loss optical combiner application, and are described in chapter 7. Since the intention of this chapter is to study the self-switching effects in 2×1 SOA-MZIs, we show here only characteristic results that explain the major difference between the 2×1 and 2×2 MZI configurations, while an more detailed characterization of the combiner application is presented in chapter 7.

The static measurements of the 2×1 SOA-MZI are carried out using the experimental setup shown in Fig. 5.6(a). The measurement procedure is described in details in subsection 5.2.5. The length of the SOAs is 1000 μm. The interference curves (Fig. 5.11(a)) are obtained by fixing the current of the SOA in the high-power arm (with input port 2, this is SOA 2), and varying the current of the SOA in the low-power arm (SOA 1). The injection current of SOA 2 is 120 mA. The measurements are carried out at different input powers.

The choice of the current in the high-power arm is explained by the fact that at higher current the SOAs entered lasing regime. It can be seen, that the major difference of these interference curves is that for symmetric (with respect to the input ports) operation of the interferometer, required for the combiner application, the "starting" point of the interferometer (low power range) is between the destructive and constructive interference points. This has determined the choice of the injection current for SOA 1. The bias conditions for the optimal self-switching are found to be: $I_{\mathrm{SOA2}} =$
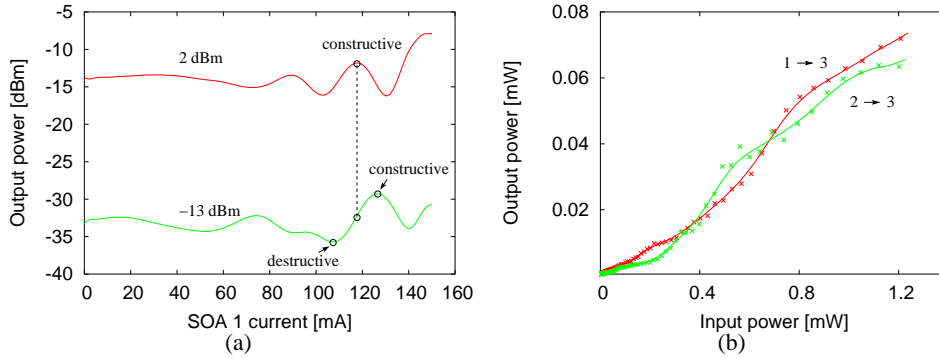
Figure 5.11: (a) Measured interference curves at two different input power levels showing the self-switching in 2×1 SOA-MZI. The vertical dotted line indicates the working point. (b) Transmission curves at the working point. Input and output power are the ones in the fiber.

120 mA and $I_{SOA1} = 117$ mA.

The transmission measurement results at the interference operating point (port 1 to 3 and port 2 to 3) are summarized in Fig. 5.11(b). It can be seen that at this operating point the interferometer works in balance. The experimental result agree qualitatively with the calculation results presented earlier in this chapter.

5.3 Passive semiconductor waveguides as nonlinear phase shifters

Thus far all-optical switching was provided by semiconductor optical amplifiers. The applicability of the SOAs for self-switching in MZIs was shown in the previous section. In these phase shifters, the intensity dependent nonlinear refractive index change originates from the intensity induced carrier depletion and gain saturation effects. However, the SOA-based phase shifters require electrical power. For applications like e.g. the low-loss optical combiner, the preferred phase shifting mechanism is a passive one: combination of optical signals is generally a passive function. An essential restriction put on the nonlinear material is that large refractive index changes should be accompanied with a small absorption, which results in low waveguide losses. Taking into account the application of the passive phase shifters in the integrated low-loss optical combiner, we can formulate the following requirements for the phase shifters:

1. The maximum phase shifter length is in the order of 1000 μm, since longer devices would make the integrated combiner unpractically large.

2. The refractive index change required to induce a nonlinear phase shift of $\pi/2$ is according to Eq. 5.1 about $1.55 \cdot 10^{-3}$.

3. The maximum optical power is limited to 10 mW, since higher powers would not be compatible with the power budgets in optical network.

4. The absorption (propagation losses) in the phase shifter should not exceed 0.5 dB, or 1.15 cm^{-1} for a 1000-μm-long phase shifter, in order to compete with a passive 3-dB combiner. Therefore, the switching power should not exceed 10% of the total input power.

In order to investigate the absorption coefficient and the refractive index change in the nonlinear phase shifters, a simple two-band model can be useful for predictions of the intensity and the frequency dependence of the potential nonlinear materials.

5.3.1 Model for optical nonlinearities in semiconductors

The interaction of light with a semiconductor medium can often be modeled in terms of electronic transitions between a valence and a conduction band. In a direct bandgap semiconductor, due to the momentum conservation, each interband optical transition relates two states in the conduction band and the valence band with the same wavevector, which can be regarded as a two-level system. The macroscopic polarization of semiconductors can then be obtained by a suitable averaging procedure over the ensemble of two level systems. Intraband interactions can be described through relaxation. Following [65], the absorption coefficient and the corresponding change in the refractive index are:

$$\alpha(\omega, I) = \frac{2e^2}{\hbar c \varepsilon_0 V} \sum_{\bar{k}} \frac{\omega \tau_{\text{in}} |\mu_{\text{cv}}|^2 (1 - f_{\text{h}} - f_{\text{e}})}{1 + \left[\omega_{\text{cv}}(\bar{k}) - \omega\right]^2 \tau_{\text{in}}^2 + I/I_{\text{s}}} \tag{5.19}$$

and

$$\Delta n(\omega, I) = \frac{e^2 c \tau_{\text{in}}}{n_0 \hbar c \varepsilon_0 V} \sum_{\bar{k}} \frac{\left[\omega_{\text{cv}}(\bar{k}) - \omega\right] \tau_{\text{in}} |\mu_{\text{cv}}|^2 (1 - f_{\text{h}} - f_{\text{e}})}{1 + \left[\omega_{\text{cv}}(\bar{k}) - \omega\right]^2 \tau_{\text{in}}^2 + I/I_{\text{s}}}, \tag{5.20}$$

where τ_{in} is the intraband relaxation time, I is the intensity, n_0 is the linear refractive index, ε_0 is the vacuum dielectric constant, $\hbar$ is the Planck's constant, μ_{cv} is the dipole transition moment between the conduction and the valence band, f_{e} and f_{h} are the population probability of electrons and holes, respectively, V is the volume of semiconductor. The characteristic intensity I_{s} is defined as:

$$I_{\text{s}} \equiv \frac{\hbar^2 c \varepsilon_0 n_0}{2e^2 |\mu_{\text{cv}}|^2 \tau_{\text{in}} \tau_0}, \tag{5.21}$$

where τ_0 is the depopulation time. In fact, the optically induced change in the refractive index should be defined by $\Delta n_{\text{NL}}(\omega, I) = \Delta n(\omega, I) - \Delta n(\omega, I = 0)$.

An important conclusion drawn from equations (5.19) and (5.20) is that the absorption coefficient and index change depend not only on the frequency of the optical field, but also on its intensity. On the other hand, it can be seen that the intensity dependent optical nonlinearities are scaled by the characteristic intensity I_{s}. If the intensity I is much less than I_{s}, the optical nonlinearities can be neglected. Only if I is comparable or larger than the characteristic intensity I_{s} the nonlinear absorption and the change of the refractive index become notable.

95
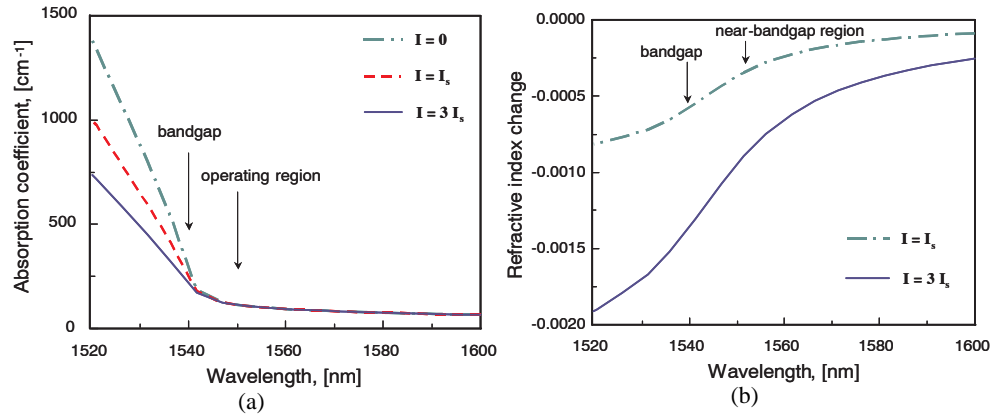
Figure 5.12: (a) Calculated absorption coefficient and (b) change in refractive index of Q(1.54) as a function of photon energy (wavelength).

Using Eq. 5.19 and Eq. 5.20, the absorption coefficient and the refractive index change of Q(1.54) material as a function of photon energy (wavelength) can be calculated[4] for different signal intensities. These plots are given in Fig. 5.12.

It can be seen that the absorption edge locates at the bandgap. The absorption coefficient is smallest in the transparent region away from the absorption edge, such as at 1550 nm. On the other hand, the change of the refractive index is large only near the absorption edge. The optimum trade-off minimizing absorption and maximizing index change is, therefore, achieved at optical frequencies (wavelengths) in the transparent region, but as close as possible to the absorption edge. It is potentially possible to get an optimization of the absorption edge by designing the semiconductor bandgap so that the required operating wavelength (1550 nm) is in that range.

In Fig. 5.13 the change of refractive index as a function of intensity is plotted for three different wavelengths.

From Fig. 5.13 it can be seen, that in the absorption region ($\lambda = 1500$ nm) there is a large change of refractive index (which is, however, accompanied with the large absorption). In the transparency region ($\lambda = 1600$ nm), the refractive index change increases with intensity in an almost linear way. The intensity dependent index change is sizable in the band-edge region ($\lambda = 1550$ nm).

However, it can be concluded that the requirements stated earlier in this section can not be obeyed in bulk materials. The absorption in the transparent region is still high to meet the requirements for our applications. The refractive index changes in

---

[4]See [65] for more detailed explanation.
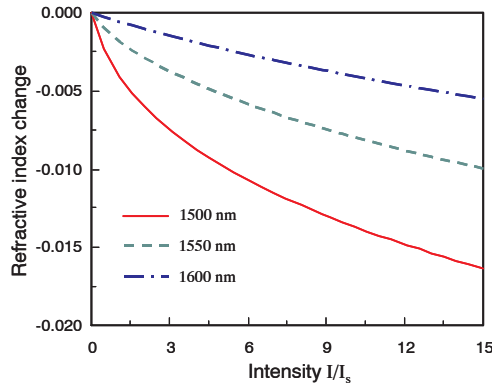
Figure 5.13: Calculated intensity dependent change of refractive index for Q(1.54) material at different operating wavelengths.

these materials are accompanied with considerably high absorption, which is not suitable for the low-loss optical combiner.

More sizable optical nonlinearities are usually attributed to the quantum structures, which are discussed below.

5.3.2 Optical switching in (multi-) quantum well structures

Quantum well structures are very promising for all-optical switching due to a number of inherent nonlinearities. QW materials offer degrees of freedom that can conveniently be used to tailor the optical properties [66]. For nonlinear phase shifting as required in this thesis, the most relevant class of nonlinear effects is related to saturation of optical absorption near to the bandgap energy. As the light is absorbed, a significant population of electrons and holes is generated either creating excitons, or free carriers. Excitons are electron-hole pairs in bound hydrogenic states[5]. An exciton can be created with an energy lower then that required to create a free electron-hole pair. By absorbing directly into the exciton absorption peaks, excitons are generated,

---

[5]An exciton is a bound state of an electron and a mathematically useful imaginary particle called an electron hole pair in a semiconductor. This is a Coulomb correlated electron-hole pair. A vivid picture of exciton formation is as follows: a photon enters a semiconductor, exciting an electron from the valence band into the conduction band. The missing electron in the valence band leaves a hole behind, of opposite electric charge, to which it is attracted by the Coulomb force. The exciton results from the binding of the electron with its hole; as a result, the exciton has slightly less energy than the unbound electron and hole. The wavefunction of the bound state is hydrogenic.

whereas by absorbing at higher photon energies, free carriers are generated. For steady state effects at room temperature with continuous wave light sources it makes little difference which we generate, since the excitons are rapidly ionized, and in thermal equilibrium there are basically only free carriers.

High intensity input optical signals create a high free carrier density. In presence of a high free carrier density the exciton absorption peaks become saturated [67, 68]. A simple explanation for this is that as a number of excitons increases, we start running out of space to create more. Consequently, the probability of creating new excitons reduces, and the optical absorption associated with creating them decreases. Therefore, the exciton absorption line saturates. In reality, this is related to the Pauli principle according to which the free carriers (if they are "cold" enough to be in the states near the band center from which the exciton is comprised), can prevent creation of more excitons.

The changes in the absorption according to the Kramers-Krönig relations lead to intensity dependent changes in the refractive index. The saturation effects associated with the exciton peak in QWs are relatively sensitive. For enhancing the nonlinearities, not a single, but Multi-Quantum Well (MQW) structures are often employed. However, even with the additional contribution of the strong quantum well excitons, these nonlinear effects are not large enough [66] to make low enough energy devices. The effect could be applied e.g. in electroasorptive switches, which are, however, outside of the scope of this thesis.

5.3.3 Optical switching in quantum dot structures

The opto-optic switching in the configurations mentioned above, requires too high switching energies to be used for all-optical switching. Semiconductor Quantum Dots (QDs) are a better candidate for passive nonlinear phase shifters. In a quantum dot a single electron-hole pair is capable to block further interband transitions, resulting in optical transparency of the ground state transition. Such a large absorption change due to state-filling with a single electron-hole pair results in a large refractive index change.

The first evidence of the quantum dot applicability for passive nonlinear phase shifters was shown in the following experiment [69]. A Mach-Zehnder interferometer in QD material was made according to the fabrication technology described in chapter 3. In the material used in this experiment, a single QD layer is embedded into a 370-nm-thick Q(1.25) layer. The room temperature PL of the used sample shows two peaks: one at 1300 nm, corresponding to the film layer, and one at 1500 nm, corresponding to the QDs. One of the arms of the MZI was (externally) illuminated by a
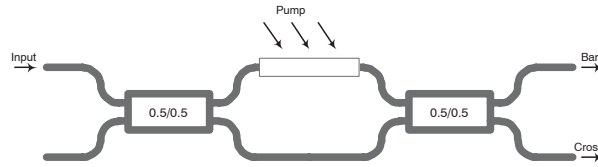
Figure 5.14: Schematic of the all-optical switching setup using a pump beam from the top to excite the QDs in the upper arm of the MZI.

pump signal[6]. This is schematically shown in Fig. 5.14.

The pump beam excites one of the two arms of the MZI from top, i.e. perpendicular to the substrate. The excited surface area is approximately 600×25 μm^2 around the upper interferometer arm. The pump beam ($\lambda > 1350$ nm) excites carriers directly into the InAs/InP QDs, without exciting the bulk InGaAsP waveguide film or the InP cladding layer. The resulting state-filling in the QDs leads to bleaching of the QD absorption. In accordance with the Kramers-Krönig relations, the absorption bleaching causes changes in the refractive index.

The switching is probed by a CW tunable laser source (operating window 1530-1570 nm). The TM-polarized probe beam is coupled into the MZI by microscope objectives. In order to spatially separate the two outputs of the MZI, the probe output is focused onto a slit. The measurement results are presented in Fig. 5.15, where the probe transmission at both output ports is plotted as a function of the pump power. The observed switching originates from the refractive index nonlinearity, since the output signals for the two outputs of the MZI are of similar magnitude and opposite sign, as expected for an induced phase shift. If only bleaching took place, it would result in increased probe transmission for both output ports [69]. Besides, at a shorter pump wavelength (1150 nm), when also the film layer is excited, switching between the two ports could be observed by an infrared camera. In this case, the switching is predominantly due to QD state-filling, and a small part might be due to InGaAsP bandfilling.

In [69] the switching efficiency of this MZI switch is estimated. A phase shift of 4.2 rad/mW of incident power is found. With a correction for the estimated $8 \cdot 10^{-4}$ absorption strength [70] of a single QD layer, a maximum switching efficiency of 5 rad/(μm of absorbed power).

In conclusion, an efficient all-optical switching is obtained from a 600-μm-long

---

[6]This work has been carried out in the close collaboration with the Semiconductor Physics group, COBRA, where the QD material was grown and the optical measurements were done.
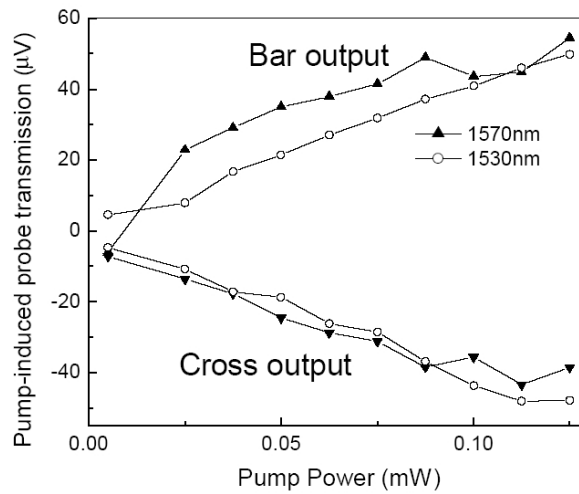
Figure 5.15: Changes of transmission of the probe signal as a function of the pump power, showing all-optical switching at a pump wavelength of 1450 nm and at probe wavelengths indicated on the plot [69].

phase shifter with a single QD-layer, where the nonlinear phase shift between the interferometer arms resulted from the excitation of quantum dots by an additional pump optical signal. For the low-loss optical combiner application, a self-phase modulation effect is required. In this case, the QDs are excited while the signal propagates through the phase shifter waveguide, avoiding passing through the layers above the quantum dots. Such a geometry is expected to be more advantageous for all-optical switching.

Modeling of optical nonlinearities in QDs

In self-switching MZI, no additional pump signal is available. Here, excitation of the QDs should occur at a signal wavelength. In this section, a (simple) model is developed, which can be used for prediction of the wavelength dependence of QDs. This will help in interpreting of the measurement results presented in chapter 7.

In a first approximation, a quantum dot can be described by a two-level model. A photon hitting the QD is absorbed, leaving the QD in an excited state. However, this takes place only if the photon has an energy exactly corresponding to the transition. After the excitation, the QD is transparent, i.e. the next photons passing along will not be absorbed until the QD relaxes back into its ground state. A change in refractive index related to this change in absorption can be calculated using the Kramers-Krönig

relations.

The absorption of light by the quantum dot is described with a Lorentz function [26]:

$$\Delta\alpha(\omega) \propto \frac{\omega_{\text{QD}}^2 \cdot \Gamma/4}{(\omega - \omega_{\text{QD}})^2 + (\Gamma/4)^2}, \tag{5.22}$$

where ω_{QD} is the angular frequency corresponding to the QD transition, and Γ is the Lorentzian linewidth. The Kramers-Krönig relation for the refractive index change is:

$$\Delta n(\omega) \propto \int_0^\infty \frac{\Delta\alpha(\omega')}{\omega'^2 - \omega^2} d\omega'. \tag{5.23}$$

The solution to this integral expression is known from classical theory of a damped harmonic oscillator [26]. Assuming that the refractive index change is relatively small it can be derived that for a single quantum dot:

$$\Delta n(\omega) \propto \frac{\omega_{\text{QD}}^2 - \omega^2}{(\omega_{\text{QD}}^2 - \omega^2)^2 + \omega^2\Gamma^2}. \tag{5.24}$$

This solution can also be expressed in terms of a wavelength as:

$$\Delta n(\lambda) \propto \frac{\lambda_{\text{QD}}^2 \left(1 - \left(\lambda_{\text{QD}}/\lambda\right)^2\right)}{\left(1 - \left(\lambda_{\text{QD}}/\lambda\right)^2\right)^2 + \left(\Delta\lambda_{\text{QD}}/\lambda\right)^2}. \tag{5.25}$$

The subscript "QD" refer to peak and width of the transition of a single quantum dot. There are two complications that should be taken into account when considering self-switching effects in real structures. First, the Gaussian-like curve in the PL spectrum implies a certain distribution of the QD size, as shown in chapter 3. Second, only those QDs transitions should be taken into account, which fall within the linewidth of the optical signal (e.g. the laser, used as an optical input). Because the laser linewidth is much narrower (typically $\ll 0.1$ nm) than the linewidth of a quantum dot (typically ~ 15 nm at the room temperature) and the width of the QD-distribution (typically ~ 100 nm), the laser linewidth can be approximated with a delta function. Integrating over the QD distribution gives the wavelength dependence of the refractive index change due to QD-absorption:

$$\Delta n(\lambda) \propto \int \frac{\lambda_{\text{QD}}^2 \left(1 - \left(\lambda_{\text{QD}}/\lambda\right)^2\right)}{\left(1 - \left(\lambda_{\text{QD}}/\lambda\right)^2\right)^2 + \left(\Delta\lambda_{\text{QD}}/\lambda\right)^2} \exp\left(-\left(\frac{\lambda_{\text{Distr}} - \lambda_{\text{QD}}}{\Delta\lambda_{\text{Distr}}}\right)^2\right) d\lambda_{\text{QD}}. \tag{5.26}$$

101
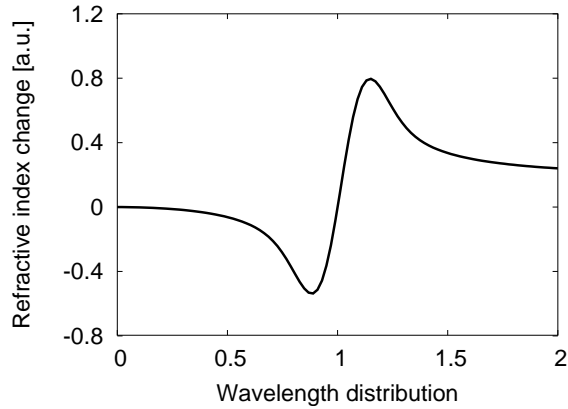
Figure 5.16: Calculated refractive index change (a.u.) as a function of the wavelength distribution.

It can be seen that the largest refractive index changes can be expected in case the wavelength is longer than the photoluminescence peak of the quantum dot distribution (see Fig. 3.5). At the PL-peak, however, it is predicted that no nonlinear effects will occur. This is because $\Delta n(\lambda)$ is an asymmetric function, so that positive and negative contribution from different QDs cancel out. At the flanks of the QD-distribution this does not occur, as the number of QDs with higher and lower transition peak wavelengths are not equal anymore.

5.4   Conclusions

In this chapter, self-switching effects in Mach-Zehnder interferometers were investigated. The required nonlinear phase shift originates from an intensity dependent refractive index change. Therefore an essential component of the Mach-Zehnder interferometers is the nonlinear phase shifter. One of the phase shifters investigated in this thesis is the semiconductor optical amplifier. In SOAs, the intensity dependent refractive index change results from carrier depletion, which occurs at high optical powers. It was shown, that in principle longer SOAs operating at high injection currents can provide higher optical nonlinearities. An important parameter in evaluating the intensity dependent phase shift effects is the alpha parameter, which relates the phase changes with the gain saturation. Experimentally it was found that this parameter changes with input power, but that an average value of 3 reasonably describes our SOAs in the power

range used. In all cases, high alpha parameters of the SOAs are preferred. Two config-urations of SOA-MZIs were treated: 2×2 and 2×1. The 2×2 SOA-MZIs can be used as pattern effect compensators and 2R-regenerators. Their nonlinear behavior and, therefore, possible applications can be engineered by choosing an appropriate output coupler ratio. These applications will be discussed in chapter 6. The 2×1 SOA-MZIs can be used as the low-loss optical combiner. This application will be discussed in chapter 7. The self-switching in this SOA-MZI is achieved within the input power range around 0.6 to 1.5 mW (-1.5 to 1.8 dBm) in the input fiber. With a correction for the fiber-chip coupling losses, which is estimated to be around 4-5 dB per facet, the input power required for the self-switching (in the chip) is therefore around 0.3 to 0.6 mW (-5.5 to -2.2 dBm).

The second type of the phase shifters investigated in this thesis is based on all-optical nonlinearities in passive waveguides. The InP material system offers a number of possibilities to achieve nonlinear phase shifts without an external source. From our calculations it follows that large refractive index changes are accompanied with high absorption, and therefore a trade-off is needed. Bulk materials can not be used for the low-loss combiner application, as required phase shifts result in high losses. Multi-quantum well structures are characterized by stronger nonlinearities. But even with the additional contribution of the strong quantum well excitons, these nonlinear effects are not large enough to make low enough energy devices possible.

Finally, quantum dot structures are expected to provide very strong all-optical nonlinearities, since even a single electron-hole pair is able to induce transparency of the ground state transition. In an experiment with a pump signal exciting the quantum dots from top, all-optical switching in a Mach-Zehnder interferometer is demonstrated. The modeling predicts the largest nonlinear effects at wavelengths longer than the photoluminescence peak.

The pattern effect compensator and the 2R-regenerator are realized based on semiconductor optical amplifier phase shifters, while the low-loss optical combiner is realized with both amplifiers and quantum dot based phase shifters. The next two chapters report on these applications.

Chapter 6

Optical signal regeneration

In this chapter, two novel applications of self-switching in SOA-MZIs are presented. The first one, a pattern effect compensator, reduces unwanted pulse form distortions, the so-called pattern effect, which is a consequence of the amplification of optical signals in SOAs. This component can be used as a pattern-free optical amplifier with an extended input power dynamic range, and a gain comparable to a SOA. The second application, a 2R-regenerator, is improving the noise characteristics of an optical signal.

6.1   Introduction

Due to fiber losses and limited power budgets there is a need to use amplifiers for increasing the scalability of optical networks. Traditionally, the amplification is achieved by first converting the optical signal into an electrical one. In this way amplification, pulse reshaping and retiming take place in the electric domain. Subsequently, the signal is converted back into the optical form. This procedure is well suited for moderate-speed single wavelength operations, but becomes rather expensive and complex for high speed multiwavelength systems [16].

An alternative way to compensate the fiber losses is to use an optical amplifier, which amplifies the optical data stream directly without requiring conversion of the signal into the electrical domain. Optical amplifiers are especially useful for multi-channel systems as they are capable of amplification of all channels simultaneously. Optical signal re-amplification is also referred to as 1R-regeneration. The two main optical amplifier types are the Erbium Doped-Fiber Amplifier (EDFA) [71] and the semiconductor optical amplifier.

Optical amplification can cause a number of problems in optical networks. If the amplifier does not provide the same gain for all the data bits, patterning effects occur and the quality of the optical data signal is degraded. Furthermore, optical amplifiers add ASE noise to the signal, and signal degradation accumulates over multiple amplification stages [16]. This results in bit errors. Using so-called 2R-regenerators, it is possible to reduce the effect of noise in an optical way.

In this chapter two novel applications of SOA-MZIs based on self-switching are presented: the pattern effect compensator and the 2R-regenerator, which are aimed to solve the aforementioned problems.

6.2   Pattern effect compensator

6.2.1   Introduction

In future optical access networks, where the number of required amplifiers is expected to be very high, it will be advantageous to use SOAs because of the low production costs as compared to those of EDFAs. SOAs share many of the features that have made semiconductor lasers the dominant light source for optical communications, making them very attractive candidates for all-optical signal amplification and processing [72]. These features include small size, simple electrical pumping and low power consumption, broad spectral range and opportunities for integration[1]. The SOAs have a gain response time in the order of 1 ps - 0.1 ns. This is faster than that of the EDFAs, which have response times in the millisecond range. This results in both advantages and limitations. The advantage is that SOAs can be used for switching and signal processing in optical networks. The limitation is that the rapid carrier response causes the gain of a SOA to fluctuate with the signal rate for bitrates up to several gigabits per second (Gb/s), whereas EDFAs are operating in the regime of mean saturation. The gain saturation effect is a serious restriction on the linear operation of the SOAs. If the amplifier does not provide approximately the same gain for all the data bits, patterning effects occur and the quality of the optical data signal is significantly degraded.

Obviously, the pulse form distortion depends on the bit pattern. If the input level switches from state "zero" to "one" after a long sequence of "zeros", the leading part of the pulse is amplified with unsaturated gain, whereas the output of the trailing part decreases as the SOA gain saturates. This situation is schematically illustrated in Fig. 6.1(a). However, if the input level changes from state "one" to "zero" and then back to "one" with a short duration of "zero", the amplifier gain does not return to the

---

[1]More on integration of SOAs can be found in chapter 3.
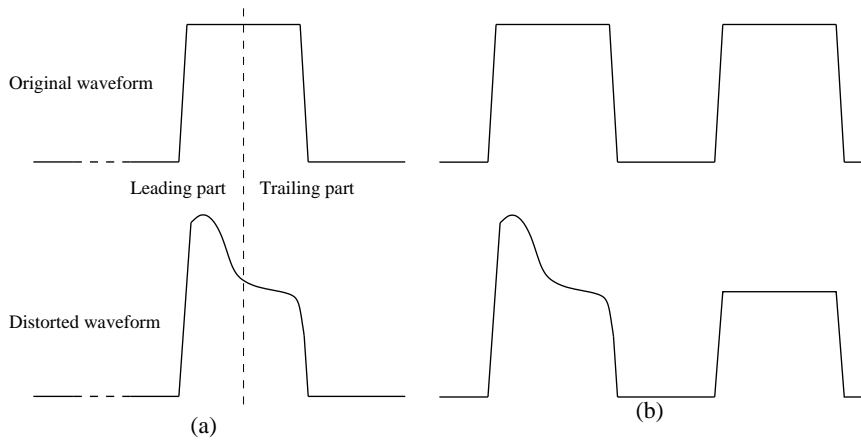
Figure 6.1: The bit pattern dependent pulse distortion. (a) The pulse after a long sequence of "zeros". (b) The first pulse after a long sequence of "zeros", the second pulse after a short duration of "zeros", amplified with saturated gain.

unsaturated value and even the leading part of the following pulse is amplified with a (partially) saturated gain, as schematically illustrated in Fig. 6.1(b).

One of the ways to avoid the pulse form distortion is to choose a sufficiently small magnitude of gain saturation. In this case, however, the Input Power Dynamic Range (IPDR) of the SOA is reduced. Alternatively, the amplifier dynamics must be such that transient gain changes do not affect the neighboring bits, which results in limitations of the maximum allowed bitrates. A more flexible approach to reduce the pulse form distortions is to use one of the compensation methods explained below.

6.2.2 Overview of the pattern effect compensators

A number of methods aimed to reduce pulse form distortions is proposed in the literature. They are summarized below.

One of the methods was proposed by J.A. Constable *et al.* in [73]. It is based on bias current feedback, which is reducing the depth of modulation of the carrier density caused by the modulated input signal. The technique involves detecting and amplifying the fluctuations in the SOA forward voltage, and feeding them back into the DC bias of the device. In this method, the gain changes of the SOA can be reduced, however at the expense of the average gain.

In another approach, proposed by G. Soulage *et al.* in [74] and by L. Lablonde *et al.* in [75], Gain-Clamped SOAs (GC-SOAs) were used. In a GC-SOA, the gain is

clamped by a laser oscillation inside the amplifier. Such an oscillation fixes population inversion and thus the gain. Therefore, no carrier depletion occurs until sufficiently high input powers, leading to a high saturation input power and a large power dynamic range. Based on the static investigations of the GC-SOAs, they allow about 8 dB higher input power levels before saturation and have noise figures only 2-3 dB higher as compared to the conventional SOA. However, dynamic calculations carried out for 10 Gb/s operation, presented by D. Wolfson *et al.* in [76], are indicating that the laser operation of the GC-SOAs leads to a pulse distortion causing pattern effects. These pulse distortions are due to the dynamic changes of the carriers and photon distribution on a time scale given by the relaxation frequency of the GC-SOAs. The distortions lead to a more severe extinction ratio degradation than predicted from the static measurements. This results in lower allowed input powers for the GC-SOAs. Considering the noise figures as well as the acceptable input power level, the GC-SOAs show only about 0.5 dB improvement of the dynamic range compared to the conventional SOA, indicating that the use of GC-SOAs is not providing much improvements.

The techniques listed above are not well suited for use in optical networks as they are causing speed limitations, or large gain reduction.

The first interferometric approach was proposed by Q. Xu *et al.* in [77]. The authors propose to compensate the gain changes in saturation by the phase change effects in a nonsymmetrical interferometric structure, schematically depicted in Fig. 6.2(a). One arm of the interferometer consists of an SOA, which gives the phase shifted optical signal with gain, and the other arm is passive, which gives the unshifted one for compensation. By properly adjusting the two arms of the interferometer, the two optical signals can undergo destructive interference when the gain of the SOA is high, and constructive interference, when the gain is saturated. In this way the pulse form distortion can be compensated.

For increasing the overall gain of the interferometer, a preamplifier can be added to each arm, as it is depicted in Fig. 6.2(b). Since the interferometer uses two 2×1 50/50-type couplers, an initial phase shift of π should always be induced in order create the conditions for the destructive interference. In that configuration, the asymmetry in the interferometer arms is created by the difference in amplifier lengths.

Q. Xu *et al.* have reported the verification of the interferometric suppression of the pattern effect based on a commercially available all-active Mach-Zehnder interferometer. In that device, the SOAs in the two arms had equal lengths. In order to create the asymmetry in the operation of the interferometer, the two arms of the MZI are biased with different currents. These different injection currents result in different saturation powers and carrier lifetimes in the two arms, making it difficult to achieve complete compensation. The good compensation capabilities of the interferometric
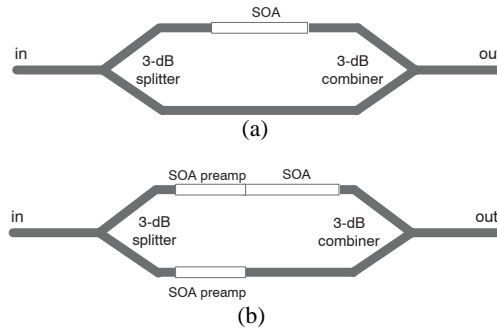
Figure 6.2: (a) Schematic of a MZI with a SOA in one arm and the second passive arm for compensation. (b) Schematic of a MZI with two preamplifiers amplifiers for higher overall gain.
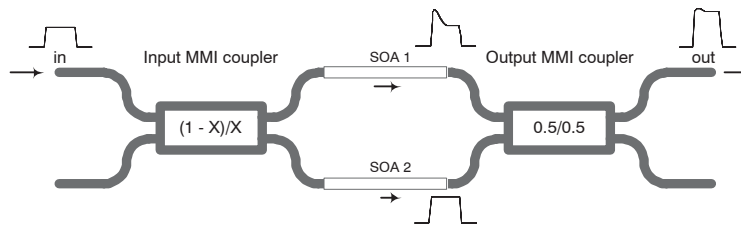
Figure 6.3: Schematic of the proposed interferometric pattern effect compensator based on self-switching.

approach were however shown.

6.2.3 Pattern effect compensator based on self-switching in a SOA-MZI

In this thesis we propose a novel interferometric solution for the compensation of the pattern effect. Such a pattern effect compensator has two identical semiconductor optical amplifiers in the interferometer arms. The advantage of this approach is that the interferometer can be operated closer to the balance (i.e. bias conditions and optical pathlengths are comparable in both arms) making the operation more stable and less wavelength dependent (i.e. more broadband). The pattern effect compensator based on self-switching is shown schematically in Fig. 6.3.

An unequal distribution of the input optical signal is achieved by using a 2×2 MMI coupler with a coupling ratio of 0.85/0.15. The output coupler used in the circuit is a 2×2 MMI 50/50-type coupler. Furthermore, a phase difference of $\pi/2$ is induced

between the two signals by the input MMI coupler. Ideally, SOA 2 is working in the unsaturated regime and does not induce any nonlinear phase shift. Similarly, the leading part of the optical pulse injected into the SOA 1 is amplified with the unsaturated gain. Thus, the total phase difference across the leading part is equal to π at the output, since also the output MMI coupler induces an additional phase difference of $\pi/2$. As a result, destructive interference for the output signal is obtained.

After the amplification of the leading part of the pulse, SOA 1 enters the saturation regime. Therefore, pulse form distortion, and also a nonlinear phase shift caused by change in the refractive index in SOA 1, will take place. If the induced nonlinear phase shift is equal to π, the two signals from the interferometric arms in the trailing part of the pulse will constructively interfere in the output coupler.

The net effect is as follows. The leading part of the distorted pulse experiences a lower transmittance, since no nonlinear phase shift is induced and destructive interference takes place. However, the destructive interference is incomplete because the power levels at the output coupler are unequal and some signal is still present at the output of the interferometer. The trailing part of the pulse experiences a higher transmittance, since a nonlinear phase shift π is induced due to the carrier depletion, resulting in constructive interference. In this way, the pulse distortion is compensated.

6.2.4 Modeling

In order to evaluate the performance of the pattern effect compensator, we use Eq. 5.8, which describes the behavior of a 2×2 SOA-MZI. We assume an ideal interferometer with two identical arms, i.e. there is no optical path difference between the two arms. Consider a single pulse. During the leading part of the pulse, both SOA 1 and SOA 2 are working in the unsaturated regime, which is characterized by the gain values g_1 and g_2, respectively. The nonlinear phase shift between the signals from the two arms is $\Delta\phi_{\text{NL}} = 0$. During the trailing part of the pulse, SOA 1 enters the saturation regime characterized by the gain $g_1 - \Delta g$, while SOA 2 is still operating in the unsaturated regime with the gain g_2. The phase shift between the two signals is assumed to be $\Delta\phi_{\text{NL}} = \pi$.

The expressions for the output power (at output port 3) corresponding to the leading and trailing parts of the pulse can be written as:

$$P_{\text{outL}} = P_{\text{in}} \cdot \left((1-X)(1-Y)e^{g_1 L} + XY e^{g_2 L} - 2\sqrt{X(1-X)Y(1-Y)}e^{\frac{(g_1+g_2)L}{2}} \right) \quad (6.1)$$

and

$$P_{\text{outT}} = P_{\text{in}} \cdot \left((1-X)(1-Y)e^{(g_1-\Delta g)L} + XY e^{g_2 L} + 2\sqrt{X(1-X)Y(1-Y)}e^{\frac{(g_1-\Delta g)L}{2}}e^{\frac{g_2 L}{2}} \right), \quad (6.2)$$

where P_{in} is the input power, and X and Y are the coupling coefficients of the input and output coupler, respectively. For the optimal compensation of the pulse form distortion, the output power of the leading part of the pulse should be equal to the output power of the trailing part of the pulse: $P_{outL} = P_{outT}$.

Output coupler choice

Obviously, the compensation capabilities of the pattern effect compensator depend on both the nonlinear behavior of the SOAs and the interference taking place at the output coupler of the interferometer. The depth of the interference (i.e. complete, or incomplete) is determined by the coupling coupling coefficient Y, which in general might not necessarily be 0.5. The required nonlinear behavior of a SOA can be evaluated in terms of the device alpha parameter, introduced in chapter 5. Therefore, for the optimal interference the right hand sides of Eq. 6.1 and Eq. 6.2 should be equal. After applying some mathematics, the following equation can be derived:

$$\sqrt{\frac{(1-X)(1-Y)}{XY}} \cdot e^{\frac{(g_1-g_2)L}{2}} = 2 \cdot \frac{1+e^{-\frac{\Delta gL}{2}}}{1-e^{-\Delta gL}}. \tag{6.3}$$

The gain saturation Δg according to Eq. 5.5 can be expressed in terms of the alpha parameter. Our pattern effect compensator should preferably operate in balance, which means $g_1 - g_2 = 0$. Eq. 6.3 can then be rewritten as:

$$\sqrt{\frac{1-Y}{Y}} = 2 \cdot \sqrt{\frac{X}{1-X}} \cdot \frac{1+e^{-\frac{\pi}{\alpha}}}{1-e^{-\frac{2\pi}{\alpha}}}. \tag{6.4}$$

Eq. 6.4 offers a possibility to estimate the best output coupling coefficient Y as a function of the alpha parameter. In Fig. 6.4 the optimal coupling coefficient Y of the output coupler is plotted as a function of the alpha parameter for output port 3.

In chapter 5 the effective (device) alpha parameter of our integrated 1000-μm-long SOAs used in the 2×2 SOA-MZIs was estimated to be around 3 (with an injection current of 140 mA, at a wavelength of 1550 nm). For the pattern effect compensator based on these SOAs, from Fig. 6.4 the optimal coupling ratio of the output coupler is 0.4. Therefore, the 50/50-type coupler is found to be the best from the limited number of coupling ratios, which can be provided by MMI couplers.

In practice, the alpha parameter and the available coupling ratio might not be fully matched. In that case, a coupling ratio as close to the ideal one as possible can be combined with a small unbalance (difference in injection currents) between the SOAs. In this way, a relatively stable and broadband operation is still obtained.
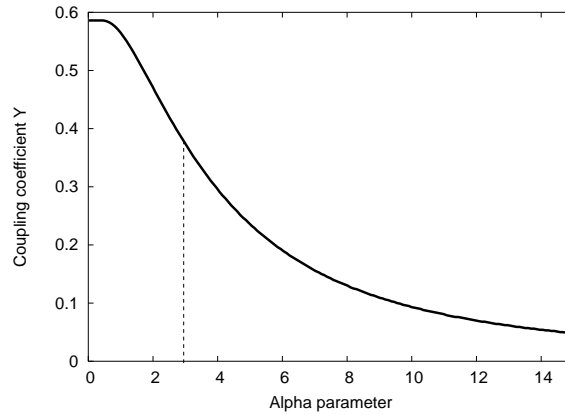
Figure 6.4: Calculated optimal coupling ratio of the output coupler of the pattern effect compensator as a function of the alpha parameter of the SOAs.

Pulse form distortion compensation

The compensation capabilities of the device are investigated using a SOA model developed by M. Heck in [78]. It uses rate equations based on [79]. This model describes the pulse propagation through a SOA. This pulse propagation is calculated by solving a set of rate equations [78] with a finite difference method. In this model, a SOA is divided in a number of sections. In every section, the gain and the refractive index are constant, and depend on the input to that section. In practice, propagation of optical signal in long SOAs results in a carrier density (and consequently the gain), which is not constant over the amplifier length. The pulse propagation through each section is calculated, and the resulting gain g of that section is determined and stored for the next pulse passage. The pulse itself enters the next section with power and phase resulting from the propagation.

The calculated normalized pulse at the input, distorted pulse at the output of SOA 1 and the induced nonlinear phase shift are shown in Fig. 6.5. The parameters of the model were optimized in order to illustrate the compensation effect. It can be seen, that SOA 1 introduces pulse form distortion and that a phase shift of about π is induced during the trailing part of the pulse. In SOA 2 the pulse form remains unchanged; there a negligible phase shift is induced.

The calculated compensated pulse form is shown in Fig. 6.6. The pulse shape is almost fully restored to that of the original pulse. This shows that it is indeed feasible to compensate the pulse distortion due to the pattern effect.

112
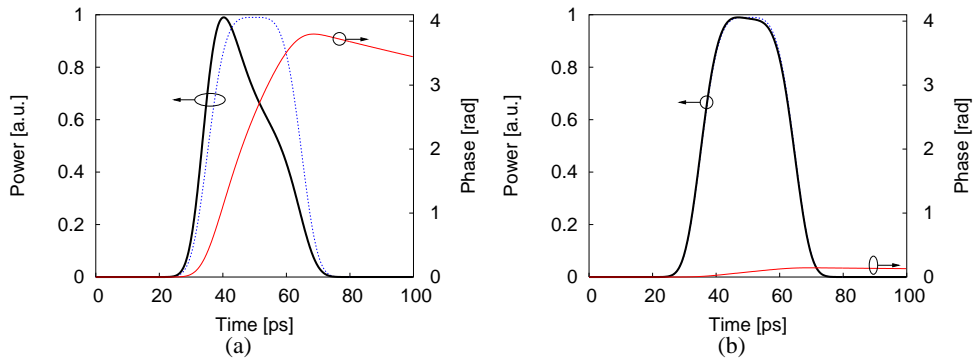
Figure 6.5: Calculated normalized pulses at the input (dashed line) and output (solid thick line) of the (a) SOA 1 and (b) SOA 2, and the corresponding phase changes.
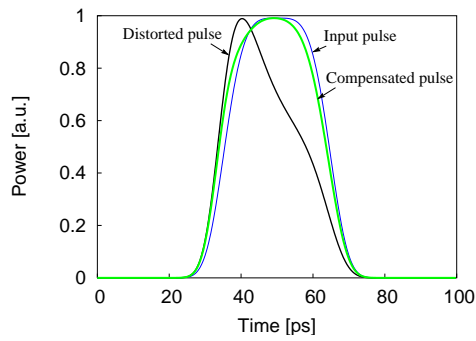
Figure 6.6: Calculated normalized pulses at the input of the SOA-MZI (Input pulse), at the output of a single SOA (Distorted pulse) and a compensated pulse at the output of the SOA-MZI (Compensated pulse).

6.2.5   Fiber-based pattern effect compensator

The pattern effect compensator concept described above was initially verified using a fiber-based Mach-Zehnder interferometer structure. The Mach-Zehnder interferometer consists of two JDS-Uniphase SOAs (type CQF 872) with a measured alpha parameter of 7.2 [80]. The input coupler is a 90/10-type fiber coupler, and the output coupler is a 50/50-type fiber coupler.

113
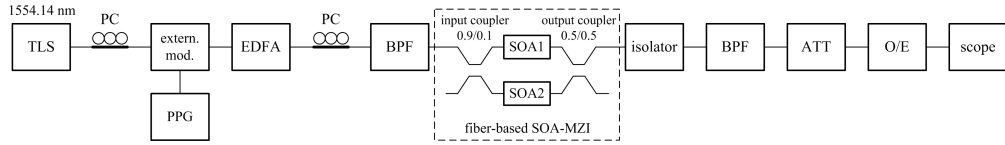
Figure 6.7: Schematic of the measurement setup for characterization of the fiber-based SOA-MZI. TLS: Tunable Laser Source, PPG: Pulse Pattern Generator, EDFA: Erbium Doped-Fiber Amplifier, PC: Polarization Controller, BPF: BandPass Filter, ATT: ATTenuator, O/E: OptoElectronic converter.

The experimental setup[2] is schematically depicted in Fig. 6.7. The input optical signal is generated by the tunable laser source in combination with a pulse pattern generator and a modulator. The wavelength[3] is 1554.14 nm. The emitted Non Return-to-Zero (NRZ) bit sequence at a chosen bitrate passes through an EDFA and an optical bandpass filter to eliminate the ASE. An attenuator is used to avoid saturation of the detector. Detection is done with home-made optoelectronic converters. The electrical output signal from the receiver is displayed on a sampling oscilloscope to show the pulse shapes.

The measurements were performed for single SOA and SOA-MZI configurations. The SOAs are biased with an injection current of 200 mA. In order to compensate for the length difference between the interferometer arms, a pattern 1010..10 at a bitrate of 1.4 Gb/s was used in the experiments [81]. The stability of the experimental setup was one of the main problems. The phase shift resulting from the length difference drifted during the experiment because of changes in environmental conditions. Therefore the conditions for destructive and constructive interference at the output coupler were not always satisfied. This resulted in slow changes of the pattern amplitude. The measurement results are presented in Fig. 6.8. The compensated pulse forms correspond to the optimal interference condition, when compensation occurred.

In Fig. 6.8(a) and Fig. 6.8(b), the distorted pulses at the output of the single SOA configuration are shown, corresponding to input powers of -0.54 and 1 dBm, respectively. In Fig. 6.8(c) and Fig. 6.8(d), the corresponding compensated pulse forms at the output of the pattern effect compensator are shown. The pulse shapes are clearly restored by the interferometric effect.

The fiber-based self-switching 2×2 SOA-MZI has shown the capabilities for the

---

[2]The experimental setup and the measurements were done in cooperation with the Electro-Optical Communication group, COBRA Research Institute, Technische Universiteit Eindhoven.

[3]Wavelength from the International Telecommunication Union (ITU) grid.
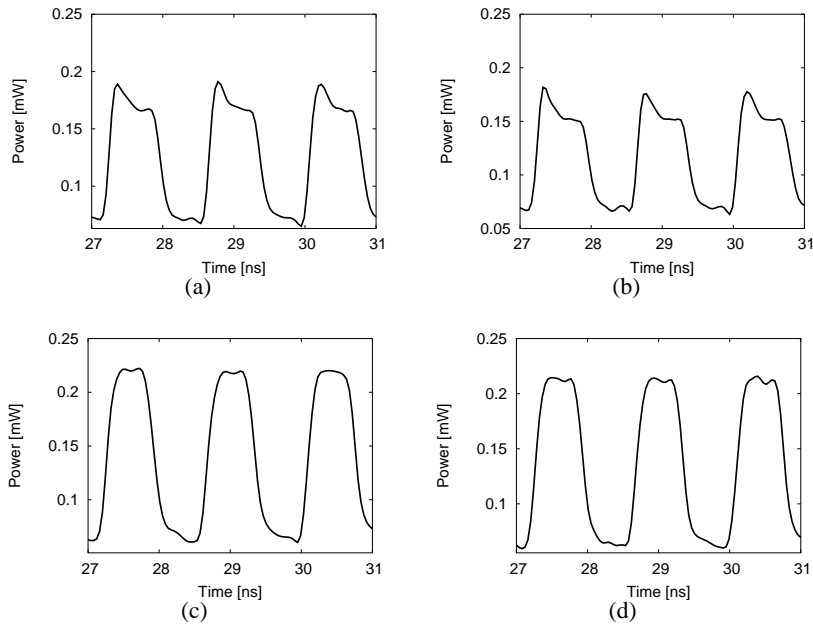
Figure 6.8: Measured pattern effect compensation of the fiber-based SOA-MZI. (a),(b) Distorted pulses with a power of -0.54 and 1 dBm, respectively. (c),(d) Corresponding compensated pulses.

pattern effect compensation. The major problem of the fiber-based device is the instable operation, which can be solved by integrating the pattern effect compensator on a chip. In that way the effect of environmental conditions is avoided, because temperature, humidity, etc are very uniform over the small chip surface.

6.2.6   Integration of the pattern effect compensator

We have designed and fabricated three types of 2×2 SOA-MZI configurations. In each of them the input MMI coupler has a coupling ratio of 0.85/0.15. The difference is in the output MMI coupler, with three possible coupling ratios: 0.5/0.5, 0.15/0.85 and 0.85/0.15. This is in order to investigate the effect of the output coupler and compare it with the modeling.

The pattern effect compensator is based on the active-passive integration technique in InGaAsP/InP. For that, the Low Pressure Metal Organic Vapor Phase Epitaxy (LP-MOVPE) technique using butt-joint coupled active and passive waveguides was

115

used. The SOAs are integrated together with passive waveguides at both sides. These waveguides have a width of 3 μm, and are 100 nm etched into the film layer. The geometry of the passive waveguides is optimized as a trade-off between low propagation losses and low radiation losses in the bends. The MMI couplers are 10-μm-wide, with access waveguides connected with an offset of 2.69 μm. The lengths of 85/15, 50/50 and 15/85 couplers are 724 μm, 489 μm and 234 μm, respectively. The SOA waveguides are optimized for high photon density in order to enter the nonlinear regime at low optical powers. The SOAs are 2-μm-wide, 1000-μm-long waveguides etched 100 nm into the quaternary layer. A layer of a 50-nm-thick PECVD-SiN$_x$ is used as masking material. Both passive and SOA-waveguides are defined simultaneously in a SiN$_x$-layer by a lithographic process in a positive photoresist, followed by the selective etch of the SiN$_x$ layer by RIE employing a CHF$_3$ process. A contact layer required for operation of a SOA causes unwanted propagation losses in passive waveguides. Therefore, it is selectively removed everywhere except for the SOAs. This is achieved in a two-step etching procedure: first, all the waveguides are etched partly to a certain depth (the first etch), second, after removing the SiN$_x$ mask from the passive waveguides, all waveguides are etched to their target depth of 100 nm depth into the film layer (the second etch), also etching away the InGaAs contact layer. The ridge waveguides were etched employing an optimized CH$_4$/H$_2$-RIE technique alternated with an O$_2$-descum process to remove polymer depositions. After that, the SiN$_x$ mask layer was removed, and a new 300-μm-thick layer of PECVD SiN$_x$ for isolation purposes was deposited. Subsequently, the openings on the top of the SOAs were created for electrical contacts. The metal contacts on the p-side were defined using a lift-off process, the metal layers were deposited using a sputtering process. The contact on the n-side was deposited. Both contacts were annealed in order to reduce the contact resistance and make the contacts Ohmic. Finally, the chip was cleaved and AR-coated. The detailed process scheme for fabrication of the active MZIs is presented in subsection 3.4.1.

A photograph of the fabricated chip containing a number of SOA-MZIs with different output couplers is shown in Fig. 6.9.

6.2.7 Measurement results of the integrated pattern effect compensator

Experimental setup

The compensation capabilities of the integrated pattern effect compensator are investigated at three different bitrates: 1.25, 2.5 and 10 Gb/s. The experimental setup used
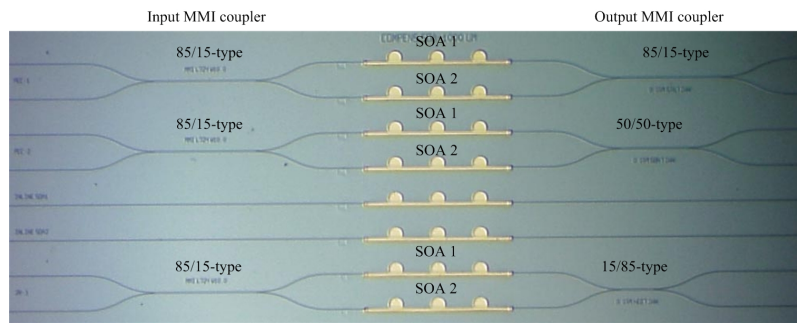
Figure 6.9: Photograph of the fabricated SOA-MZI chip with different interferometer configurations. Two inline SOA are made as test structures.

for the dynamic measurements[4] is shown in Fig. 6.10.

The optical transmitter Tx consists of an external cavity laser at a wavelength of 1550 nm and a modulator driven by a 10 Gb/s pulse pattern generator. The emitted NRZ bit sequence passes through an EDFA, an optical bandpass filter and a variable attenuator. The purpose of this cascade is to provide a strong signal (in the order of 0-12 dBm), whose power level can easily be adjusted. The required input power levels are high due to fiber-chip coupling losses, the need to enter the saturation regime and the requirement to detect enough power at the output port. The chip is mounted on a copper chuck, whose temperature is controlled by a Peltier element. The optical signal is coupled in and out of the chip using fibertips, which were, however, not optimized for coupling to this type of waveguides. This contributed significantly to the high fiber-chip coupling losses. The output signal is detected in a pre-amplified receiver. For assessing the pattern effect and the compensation capabilities of the MZI, the electrical output signal from the receiver is displayed on a sampling oscilloscope in the form of an eye diagram.

Compensation capabilities

In these experiments we investigate the configuration of the pattern effect compensator employing the 50/50-type output MMI coupler, which according to our estimations is the optimal configuration for SOAs with an alpha parameter of 3. In fact, the pattern effect compensator is aimed to be used as a (pattern-free) optical amplifier, for which

---

[4]The measurements are carried out within the ePIXnet Network of Excellence with the Research Center COM, Technical University of Denmark.
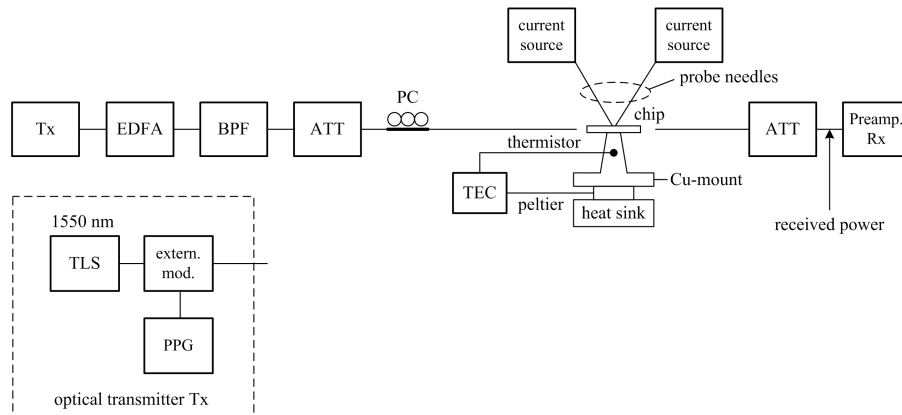
Figure 6.10: Schematic of the measurement setup for characterization of the integrated pattern effect compensator.

the alpha parameter should be as low as possible in order to avoid chirping of the optical signal. An alpha parameter of 3 is high enough to provide the self-switching (see subsection 5.2.4), and low enough for an amplifier.

The pattern effect caused by a single SOA was investigated as follows. If only SOA 1 (the SOA in the high-power arm) is biased, the circuit behaves as an in-line SOA. The injection current was 130 mA (this choice was determined by the bad quality of the facet coatings, which resulted in lasing at higher injection currents). The eye diagrams of the distorted pulse forms corresponding to the three bitrates, 1.25, 2.5 and 10 Gb/s, are shown in Fig. 6.11(a), Fig. 6.11(d) and Fig. 6.11(g), respectively. It can be seen that for higher bitrates, the overshoot becomes smaller. This is because at higher bitrates the gain of SOA 1 does not recover (completely), and even the leading part of the pulse is amplified with a (partly) saturated gain.

The operating point of the pattern effect compensator was chosen by fixing the current of SOA 1 at 130 mA, and choosing the current of SOA 2 by optimizing the eye diagram. The eye diagrams of the compensated pulse forms are recorded for two bias conditions (operating points), which correspond to different constructive interference peaks of the interferometer. Operating point 1 (Fig. 6.11(b), Fig. 6.11(e) and Fig. 6.11(h)) corresponds to bias conditions: I_{SOA1} = 130 mA, I_{SOA2} = 90-93 mA. Operating point 2 (Fig. 6.11(c), Fig. 6.11(f) and Fig. 6.11(i)) corresponds to the bias conditions: I_{SOA1} = 130 mA, I_{SOA2} = 121-123 mA. From the eye diagrams it can be seen that the compensation seems to be better at operating point 1. This could be explained by the more optimal signal strength and phase relations at these bias condi-

118

(a) 1.25 Gb/s: 130 mA, 0 mA   (b) 1.25 Gb/s: 130 mA, 91 mA   (c) 1.25 Gb/s: 130 mA, 122 mA

(d) 2.5 Gb/s: 130 mA, 0 mA   (e) 2.5 Gb/s: 130 mA, 92 mA   (f) 2.5 Gb/s: 130 mA, 121 mA

(g) 10 Gb/s: 130 mA, 0 mA   (h) 10 Gb/s: 130 mA, 90 mA   (i) 10 Gb/s: 130 mA, 123 mA
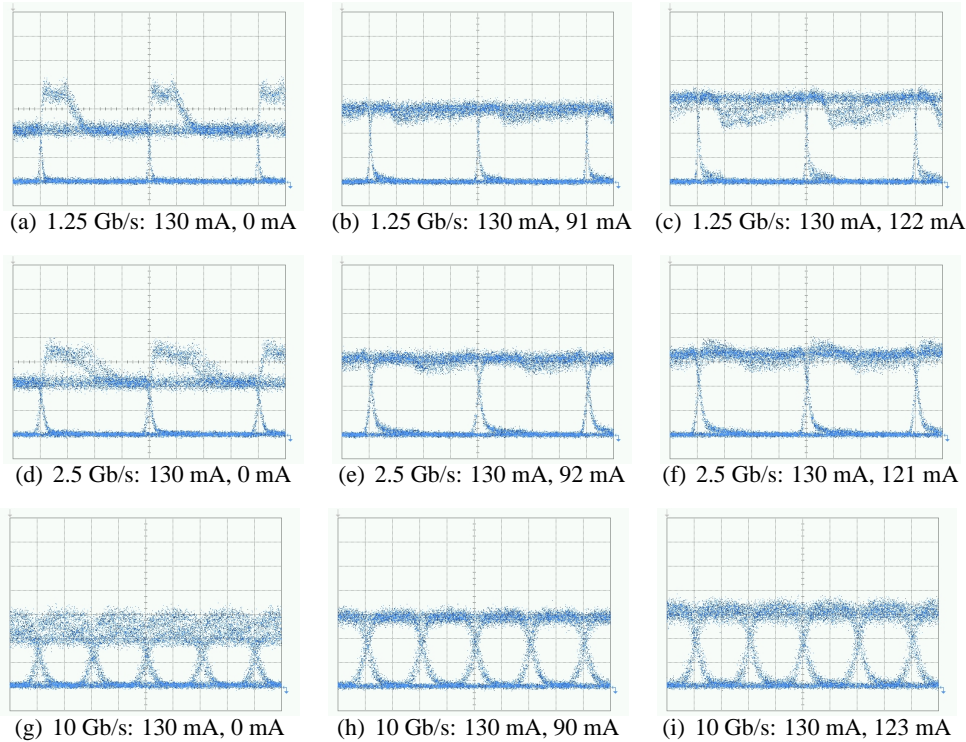
Figure 6.11: Measured eye diagrams of the pattern effect compensator at three bitrates: 1.25, 2.5 and 10 Gb/s. (a),(d),(g) Distorted pulse forms. (b),(e),(h) and (c),(f),(i) Compensated pulse forms. The two series of compensated pulse forms correspond to two operating points, indicated by SOA 1 and SOA 2 currents. The input power (in the fiber) $P_{in} = 6$ dBm.

tions. On the other hand, operating point 2 has an advantage to be more broadband, since the injection currents of the SOAs are closer to each other. The operating points are determined with an input power (measured from the input fiber) of 6 dBm.

It can be seen, that in both cases for optimal compensation the two injection currents are not equal. This can be caused by a number of reasons. First, if SOA 2 starts entering saturation, it should be corrected by decreasing the injection current. Furthermore, we do not have a perfectly matching output coupling ratio to the alpha parameter 3 of the SOAs. Finally, due to technological reasons the two interferometer arms might not be exactly identical, which could result in an additional phase mismatch between the two signals.

As can be seen from the eye diagrams, there is a clear improvement of the optical pulse form at the output of the pattern effect compensator compared to the distorted pulse form at the output of a SOA. From the eye diagrams presented in Fig. 6.11 we can conclude that despite the gain saturation in a single SOA the compensated pulse forms at all three bitrates are nearly equal.

Bitrate limitations

The dynamic operation of the pattern effect compensator based on self-switching has been shown for bitrates up to 10 Gb/s. The question is whether there are any bitrate limitations for this device. As shown previously, the pattern effect caused by an optical amplifier is bitrate dependent. At bit durations longer than the recovery time of an amplifier, the leading part of the pulse is amplified with unsaturated gain, whereas the trailing part of the pulse is amplified with saturated gain. At higher bitrates, however, the gain of SOA 1 does not recover and the entire pulse is amplified with saturated gain. In the first case, the pulse form is compensated by suppressing the overshoot as a result of the (incomplete) destructive interference on one hand, and by enhancing the trailing part of the pulse as a result of the constructive interference on the other hand. In the second case, the SOA-MZI is only operating in saturation and, therefore, in the constructive interference regime. This results in the enhancement of the entire pulse. This can be seen when the overshoot on the eye diagrams of the deteriorated signals at 10 Gb/s is compared with that at the lower bitrates. This also means, that even the "zero" levels of the two signals from the arms of the interferometer interfere constructively. However, since the power of the "zero" level is low, this does not contribute to the output signal significantly, and at the output port of the pattern effect compensator the "zero" is still detected as such. Yet, a slight deterioration of the "zero" level can be observed, when comparing the eye diagrams of the distorted and compensated pulse forms. In case of the pattern effect compensator, the ASE noise added by the SOAs in the interferometer arm is not coherent, thus does not take part in the interference processes. Therefore, no extra noise accumulation as compared to an in-line SOA is expected.

In order to investigate the bitrate independent operation, dynamic measurements were carried out at a bitrate of 20 Gb/s. The corresponding eye diagrams are presented in Fig. 6.12. The results suggest that at this bitrate the gain of the SOA does not recover, and in case the signal passes through a single SOA is amplified with a very low gain. When the signal has passed through the pattern effect compensator, the pulse form is recovered.

These results can be understood by realizing that both the gain compression, lead-

120
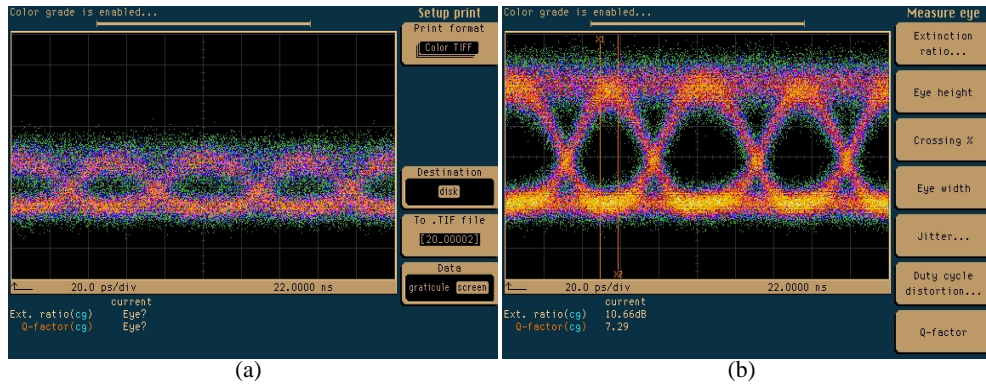
Figure 6.12: Measured eye diagrams of the pattern effect compensator at 20 Gb/s. (a) Distorted pulse forms. (b) Compensated pulse forms.

ing to pattern effects, and the compensation effect in the interferometer are caused by the same effect: carrier depletion. Up to high bitrates (40 Gb/s and more) this close link will hold, and compensation will work. Only if bit periods become comparable with faster effects (interband processes), this breaks down.

Pattern effect compensator as pattern-free amplifier

The pattern effect compensator has an additional advantage with respect to a regular SOA because it, apart from reducing the unwanted pulse distortion, also increases the input power dynamic range. This allows the device to be used as a pattern-free amplifier even at higher input power levels, providing a gain there, comparable to that of a single SOA at low powers. The gain can be compared by measuring the output power of SOA 1 and that of the pattern effect compensator at the same input power level. The output power of the pattern effect compensator is -21.1 dBm, which is 4.3 dB higher than measured at the output of the SOA (in both measurements, the power in the input fiber was 6 dBm). However, this is not a fair comparison, as a normal SOA would not by supplied with the input and output couplers. Therefore, the output power of the single SOA should be corrected for the additional losses caused by the MMI couplers. We estimate the excess loss of an MMI to be around 1 dB (which is in a good agreement with the measurement results presented in subsection 4.3.2). Taking into account coupling ratios, the total loss caused by both MMI couplers is 5.7 dB for the path through SOA 1. With this correction, the pattern effect compensator has a 1.4 dB lower output power. With lower loss MMIs, this small deficit would disappear. Thus,
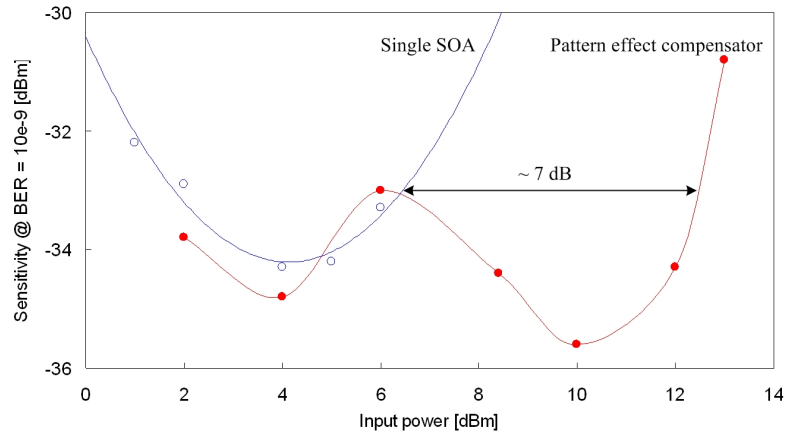
Figure 6.13: Measured receiver sensitivity at BER $= 10^9$ as a function of the input power at 10 Gb/s.

the proposed integrated pattern effect compensator has a gain comparable to the single SOA.

To quantify the performance of the pattern effect compensator, the receiver sensitivity at a bit error-rate (BER) of 10^{-9} is measured for the distorted signal (only SOA 1 is biased) and the compensated signal at the output of the MZI (both SOAs are biased). Operating point 1 of the pattern effect compensator was chosen ($I_{SOA1} = 130$ mA, $I_{SOA2} = 92$ mA). The measurements were performed at a bitrate of 10 Gb/s. The results are shown in Fig. 6.13. It can be seen, that the IPDR of a single SOA is limited. At low input powers, this is caused by spontaneous emission, while at high input powers by the degradation of the extinction ratio due the gain saturation. From this graph it can be seen that the IPDR of the pattern effect compensator is extended by about 7 dB with respect to the single SOA. The reason for this is that the effect of the gain compression, which limits the single SOA, is compensated by the interferometric effect. An important point to make here, is that the curve for the pattern effect compensator in Fig. 6.13 is taken with fixed current settings. This illustrates the stability of the device operation over a wide range of input powers.

Pattern effect compensator with a different output coupler

In order to verify our model for choosing an output coupler for optimal compensation, the compensation capabilities of the SOA-MZI configuration with a 50/50-type

122

(a) 130 mA, 0 mA   (b) 130 mA, 148 mA

(c) 130 mA, 0 mA   (d) 130 mA, 148 mA
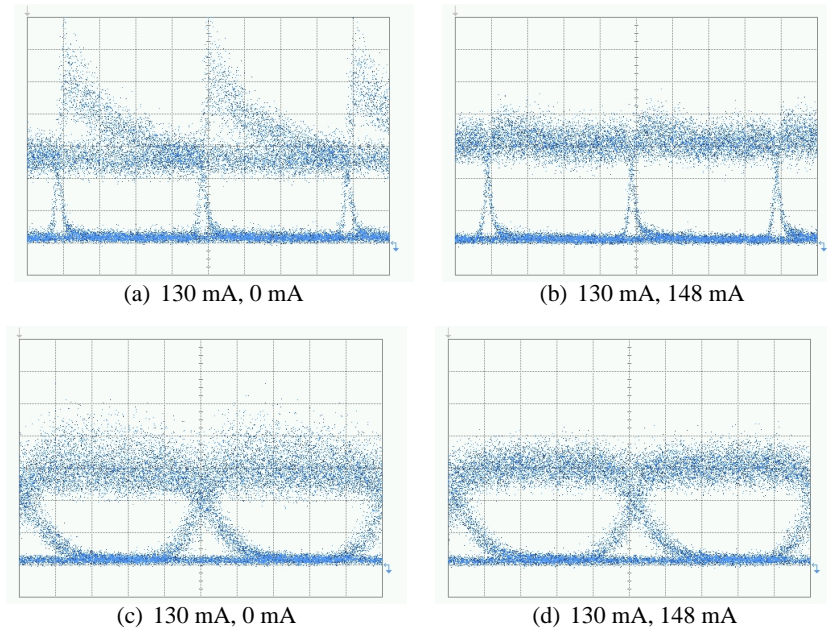
Figure 6.14: Measured eye diagrams of the pattern effect compensator with a different output coupler at two bitrates: 2.5 and 10 Gb/s. (a),(c) Distorted pulse forms. (b),(d) Compensated pulse forms. The input power (in the fiber) P_{in} = 11.4 dBm. The operating points are indicated by SOA 1 and SOA 2 currents.

output coupler are compared with those of a device employing a 85/15-type output coupler (as follows from our model, the configuration using a 15/85-type coupler is not suitable for the compensation with symmetric bias conditions). The experiments were carried out at two bitrates: 2.5 and 10 Gb/s. The eye diagrams for a single SOA and this SOA-MZI are shown in Fig. 6.14. The eye diagrams of the distorted pulse forms corresponding to the bitrates 2.5 and 10 Gb/s, are shown in Fig. 6.14(a) and Fig. 6.14(c), respectively. The corresponding eye diagrams of the compensated pulse forms are shown in Fig. 6.14(b) and Fig. 6.14(d). The input power (measured from the input fiber) was 11.4 dBm. From Fig. 6.14 it can be seen that the compensation is achieved with more asymmetry in the bias conditions than in case the 50/50-type output coupler is used. This is in agreement with our analysis.

123

6.2.8 Conclusions

A pattern effect compensator, based on a Mach-Zehnder interferometer with unequal distribution of the input optical signal, is presented. Its operation principle uses the fact that the leading part of the pulse is attenuated by destructive interference, while the trailing part of the pulse experiences a higher transmittance, due to nonlinear phase shift caused by carrier depletion. In this way the device compensates the pulse distortion. This has the advantage of using two identical SOAs, operating close to balance, which implies stable and broadband operation. The realization of the pattern effect compensator is based on the active-passive integration technique. The integrated pattern effect compensator has shown its compensation capabilities for bitrates of up to 20 Gb/s, and in principle does not depend on the bitrate. Furthermore, the input power dynamic range of the device at 10 Gb/s, compared to a single SOA, is extended by about 7 dB. It provides a gain that is comparable to a single SOA. Therefore, the integrated pattern effect compensator can be used as a pattern effect free optical amplifier with the extended input power dynamic range.

6.3 Optical 2R-regenerator

6.3.1 Introduction

Optical signal amplification in long distance optical links, required in order to compensate for fiber losses, is usually realized using erbium-doped fiber amplifiers. Optical amplifiers add ASE noise to the signal, and signal degradation accumulates over multiple amplification stages [16]. Therefore, after it has been amplified a certain number of times, the optical signal has to be regenerated. Because of cost and transparency considerations, it is preferable to implement the regeneration in an all-optical way, avoiding O-E-O conversions. This can be achieved by passing the optical signal through an optical gate with a nonlinear transfer function [82]. The task of this optical gate is to redistribute the logic signal levels and thereby suppress the ASE noise, added at the amplification stages. In this way, the accumulation of bit errors can be reduced. This process is known as 2R-regeneration, implying both re-amplification and re-shaping.

6.3.2 Optical 2R-regenerators overview

Several 2R-regenerations schemes are proposed in the literature. 2R-regeneration usually employs semiconductor optical amplifiers. It can be performed both with and without wavelength conversion [83]. In most SOA-based regeneration schemes using an interferometer, wavelength conversion to a CW or clock signal is an inherent

property [82]. Such configurations show a large optical signal-to-noise ratio (OSNR) improvement due to the fact that the noisy input signal is wavelength converted to a "clean" optical carrier. However, if the wavelength conversion is not wanted, an additional wavelength converter is required to return the regenerated signal to the original input wavelength. An alternative configuration is possible, where the input signal does not interact with additional signals. In this way, the complexity of the integration can be drastically reduced. This kind of regenerator is referred to as a pass-through regenerator.

Pass-through 2R-regenerator based on a MMI-SOA

A pass-through regenerator configurations based on a 2×2 MMI-SOA is proposed in [84], see Fig. 6.15. The input signal enters one of the input ports (in Fig. 6.15 input port "in") and, in accordance with the MMI theory explained in subsection 2.3.2, excites a number of modes, supported by the MMI waveguide. The propagation constants of these modes depend on the carrier density profile, which is influenced by the input power. The MMI length is chosen in such a way, that for input powers below the SOA saturation, the image at the output is mirrored, implying no signal at the bar-output port. With increasing input power, the MMI-SOA enters the saturation regime, and the output image changes gradually from the mirrored to the non-mirrored, implying that output signal is present at the bar-output port. In this way, a nonlinear S-form transfer function is obtained.

Dynamic measurements are reported in [82] for 10 Gb/s bitrate with a 550-μm-long MMI-SOA. The measurements show suppression of the zero-level, and, therefore, significant extinction ratio improvements.

Figure 6.15: Schematic of the 2R-regenerator based on the 2×2 MMI-SOA.

Pass-through 2R-regenerator based on a SOA-MZI

Most of the SOA-based interferometric switches have a nonlinear transfer function. Therefore, it is possible to employ them for signal regeneration.

MZI with two SOAs

A pass-through 2R-regenerator configuration based on a SOA-MZI is reported in [85]. In this configuration, the 2R-regenerator is an all-active Mach-Zehnder interferometer with 1200-μm-long interferometer arms. The input signal splits equally over the arms and recombines at the output either constructively or destructively, depending on the phase difference between the two signals from the arms. The phase difference is introduced by asymmetrically biasing the interferometer arms. This scheme shows a S-form transfer function, which is close to that of a decision gate. The authors report the regeneration capabilities at 40 Gb/s over an input power dynamic range of about 16 dB.

MZI with a single SOA

A different version of a pass-through 2R-regenerator based on a SOA-MZI configuration is reported in [86]. It is schematically depicted in Fig. 6.16. This 2R-regenerator is based on a Mach-Zehnder interferometer with one arm containing a SOA and one transparent arm. In this way the asymmetry between the two arms is created not by choosing unequal injection currents, but by using only one SOA. An attenuator in the active arm is used in order to equalize the gain and thus make the interference more efficient. The static transmission measurements of this configuration show a S-form regeneration curve. The dynamic measurements at 10 Gb/s show an extinction ratio improvement of 13 dB, and noise suppression.
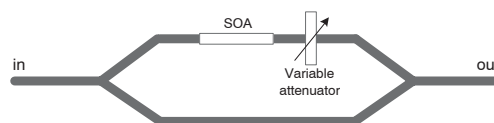
Figure 6.16: Schematic of the 2R-regenerator based on a MZI-configuration with a single SOA.
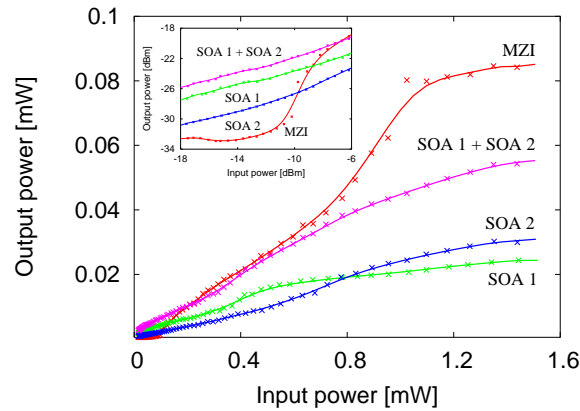
Figure 6.17: Measured transmission curves of the 2×2 SOA-MZI. Input and output power are the ones in the fiber. The inset shows in dB scale the low-power behavior of the MZI.

6.3.3 Pass-through 2R-regenerator based on self-switching in a SOA-MZI

In this thesis we propose an alternative pass-through 2R-regeneration technique. This technique employs a Mach-Zehnder interferometer based on self-switching. Essentially, such a 2R-regenerator has the same structure as the pattern effect compensator, which we investigated in the previous section.

As static measurements results described in chapter 5 suggest, a SOA-MZI based on self-switching has a nonlinear S-form transfer function, see Fig. 6.17. The effect of this nonlinear transfer function is to redistribute the logic signal levels and the ASE noise added to the signals by EDFAs.

The advantages of this approach are a certain flexibility in obtaining a required S-form transfer function by choosing an appropriate output coupler ratio, and a possibility of combining the signal regeneration with the compensation of the pattern effect.

For regeneration, a transfer function is required that consists of three main regimes. Two of them, corresponding to the "zero" and "one" level of the input signal, should be as flat as possible in order to suppress the noise at the corresponding levels, while the slope (third regime) is related to the extinction ratio improvement that can be achieved by the 2R-regenerator.

The nonlinear transfer functions of the 2×2 SOA-MZI of three different configurations were calculated based on the model explained in subsection 5.2.4 for a device
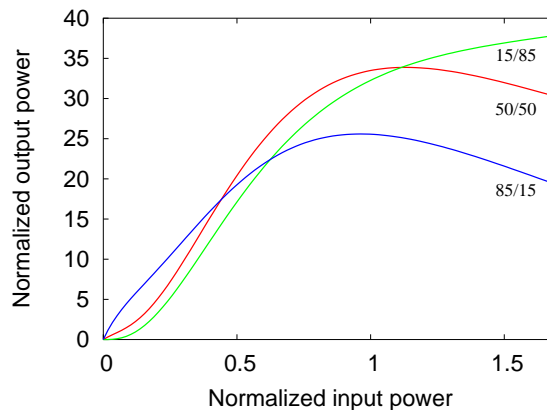
Figure 6.18: Calculated output power of the 2×2 SOA-MZIs with different types of output coupler.

alpha parameter of 3, and are compared in Fig. 6.18.

It can be seen, that the SOA-MZI with the 85/15-type output coupler is not suited for the 2R-regenerator circuit: it does not provide noise suppression around the "zero" level. With the remaining two configurations, suppression of both the "zero" and the "one" levels can be expected. For the SOA-MZI configuration based on the 15/85-type output coupler, the regime corresponding to the "one" level is not completely flat. This has to do with the assumption we have made in the model, that SOA 2 is essentially not saturated. However, if at higher input powers SOA 2 starts entering the saturation, the regime around the "one" level becomes more flat.

6.3.4 Modeling

The regeneration capabilities are investigated using a rate equation based SOA model presented by M. Heck in [78], which describes pulse propagation through a SOA. Some noise is added to the input signal. The calculated normalized pulse at the input, the distorted pulse at the output of SOA 1 with the corresponding nonlinear phase shift, and the regenerated pulse are shown in Fig. 6.19 for different input power levels.

The compensation capabilities of the device can be seen by comparing the noise bands around the "zero" and the "one" levels of the input and output pulses. It should be noticed, that the difference in noise around the "zero" level before and after the pulse can be explained by SOA gain saturation. It can be seen, that the noise around the "zero" level is always suppressed, due to the destructive interference. The noise around
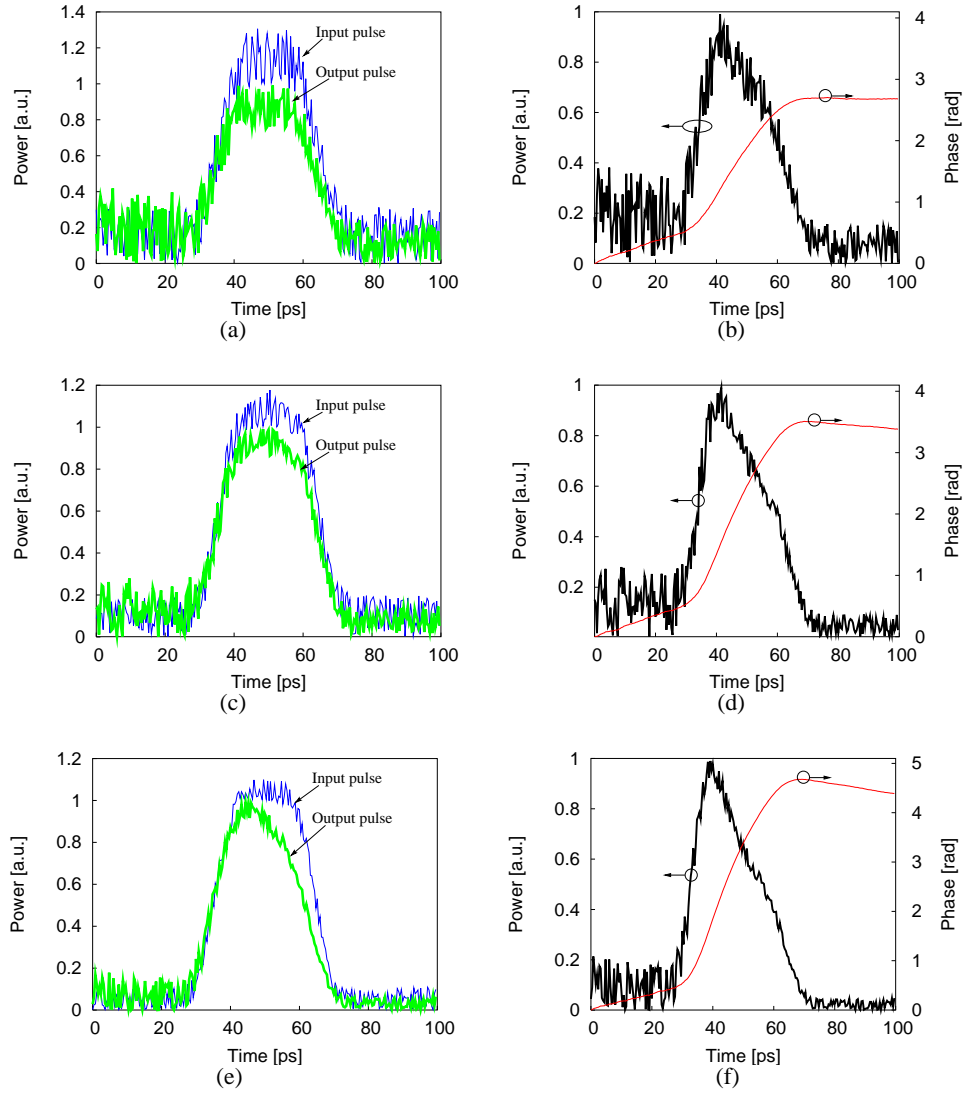
Figure 6.19: (a),(c),(e),(g) Calculated normalized pulses at the input (Input pulse) and output (Output pulse) of the 2R-regenerator at different input power levels. (b),(d),(f),(h) Calculated normalized pulse at the output of SOA 1 and the corresponding induced nonlinear phase shift.

the "one" level is also suppressed. However, at higher input powers, a strong pattern effect in SOA 1 takes place, and it starts dominating (see Fig. 6.19(e)). Therefore, the regeneration is distorted by this not completely compensated pattern effect in SOA 1, deteriorating the "one" level.

It is essential to choose a correct input power for the interferometer. In that case, both 2R-regeneration and pattern-free amplification can be achieved.

6.3.5 Measurement results of the integrated 2R-regenerator

The regeneration capabilities of the integrated 2R-regenerator are experimentally investigated at a bitrate of 2.5 Gb/s. The experimental setup used for the dynamic measurements[5] is schematically depicted in Fig. 6.20. Noise is added to the input signal with an additional EDFA (the out-of-band noise is eliminated by a tunable bandpass filter, while the in-band noise is added to the signal). The input OSNR can be adjusted by controlling the attenuation of the EDFA signal. The remaining part of the measurement setup is identical to the one used for the characterization of the pattern effect compensator. Its complete description can be found in subsection 6.2.7.

current source · current source · probe needles · chip · PC · Tx · EDFA · BPF · ATT · thermistor · ATT · Preamp. Rx · TEC · peltier · Cu-mount · heat sink · received power · EDFA · ATT · noise source
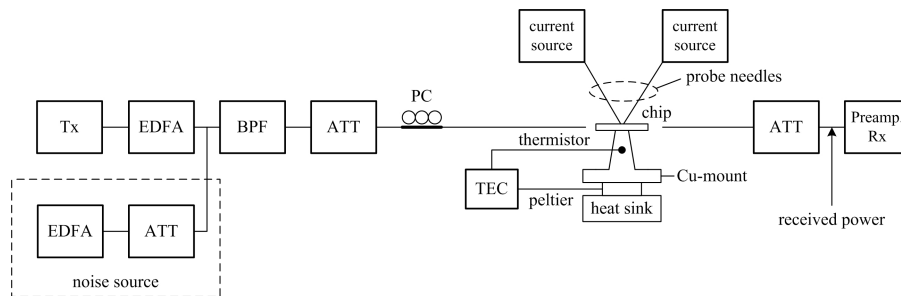
Figure 6.20: Schematic of the measurement setup for characterization of the integrated 2R-regenerator.

The eye diagrams of the input signal (i.e. signal with noise) and the output signal of the 2R-regenerator are shown in Fig. 6.21. The operation point has been chosen by adjusting the injection current of SOA 2 with the fixed injection current of SOA 1, and optimizing opening of the eye pattern. The operating point of the interferometer has the following bias conditions: $I_{SOA1} = 130$ mA, $I_{SOA2} = 82$ mA. The power into the detection system was -20 dBm.

---

[5]The measurements are carried out within the ePIXnet Network of Excellence with the Research Center COM, Technical University of Denmark.
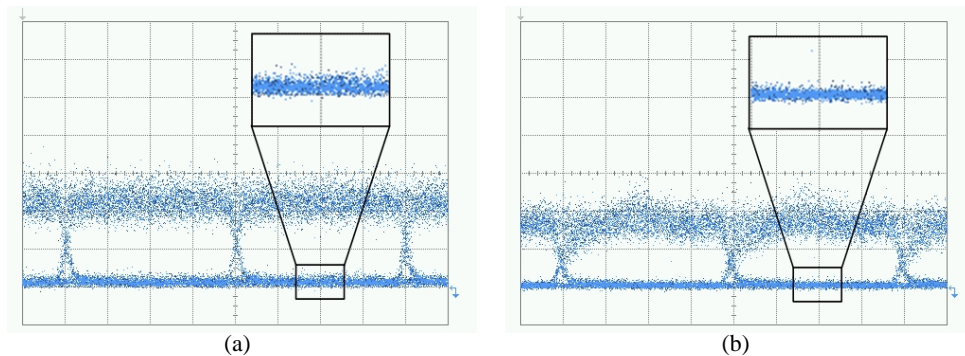
Figure 6.21: Measured eye diagrams of the 2R-regenerator at a bitrate of 2.5 Gb/s. (a) Input signal with noise. (b) Regenerated output signal. The input power (in the fiber) P_{in} = 11 dBm. Scales are identical in both graphs.

In Fig. 6.21 it can be seen, that redistribution of logical levels and reduction of the ASE noise take place. As a result, the noise band around the "zero" level is significantly suppressed. At the same time, the "one" level remains nearly unchanged. The power level is presumably too low to achieve the flat region for the "one" level. The redistribution of the logical levels and noise and, therefore, the regeneration capabilities can be quantified using the receiver sensitivity. This can be measured for the not-regenerated and regenerated signals as a function of the input OSNR. The results are shown in Fig. 6.22.

The receiver sensitivity improvement is negligible for high OSNR input signals. As the OSNR gets smaller, the sensitivity improvement becomes sizable. It can be seen that for an OSNR of 17 dB, an improvement of 2.5 dB is obtained. This is a relatively modest regeneration capability, which can be explained by the not optimally chosen pulse amplitude, resulting in suppression of only the noise around the "zero" logical level. Due to the limited availability of the experimental setup this has not been verified. Furthermore, as simulation results for different input optical power levels suggest, the more noisy "one" logical level could also result from the pattern effect (see a small overshoot on the regenerated eye diagram), occurring in SOA 1, and not sufficiently compensated by the low-power arm of the interferometer.

Bitrate limitations

The capabilities of the 2R-regenerator based on self-switching in a SOA-MZI to improve the OSNR have been shown for 2.5 Gb/s. The eye diagram of the regenerated
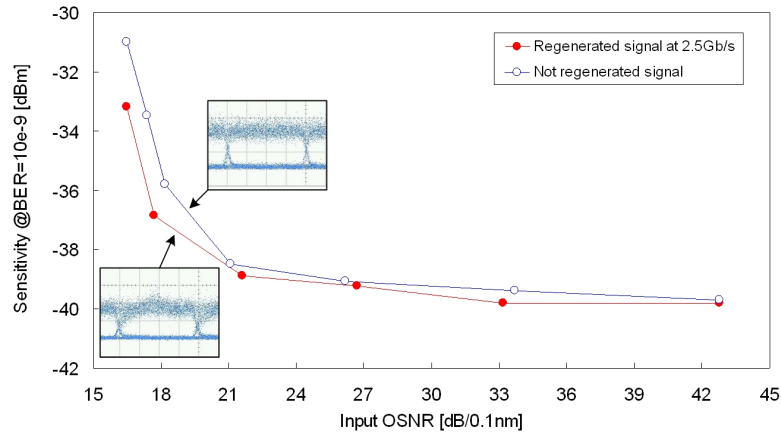
Figure 6.22: Measured receiver sensitivity at BER = 10^9 as a function of the input OSNR at 2.5 Gb/s with and without 2R-regenerator.

signal shows a suppression of noise around the "zero" logical level. For higher bitrates, however, the regeneration capabilities are not observed. We have seen, that the pattern effect compensator operates at 10 and 20 Gb/s, and actually does not depend on the bitrate. For the 2R-regenerator, the situation is different. Here, the noise to be redistributed belongs to the input signal; as a consequence it is also distributed unequally over the interferometer arms, and takes part in the interference processes. At bit durations longer than the recovery time of a SOA, the noise around the "zero" level is suppressed as the gain is recovered, and the SOA-MZI is then operating in the destructive interference regime. At higher bitrates, when the gain remains saturated, the interferometer is working in the constructive interference regime. Therefore, the noise around both logical levels is enhanced by taking part in the constructive interference. As a result, the output OSNR deteriorates. Therefore, high bitrate operation of our 2R-regenerator is limited by the recovery time of the semiconductor optical amplifiers used.

6.3.6 Conclusions

A 2R-regenerator based on Mach-Zehnder interferometer with unequal distribution of the input optical signal is presented. Its operation principle is based on the redistribution of the logical levels and noise due to the S-form transition function. The regeneration is demonstrated at 2.5 Gb/s. The regeneration can be seen as a clear suppression

of noise around the "zero" level. As a result, the receiver sensitivity improvement for an OSNR of 17 dB is 2.5 dB, which is a modest improvement. This can be improved by optimizing the settings of the interferometer and by a better choice of the input pulse amplitude. An advantage of the proposed technique is a possibility to combine the regeneration with pattern-free amplification. The maximum bitrate is limited by the recovery time of the amplifiers. It can, therefore, be increased by increasing the SOA-length and the bias current, as was discussed in section 5.2.

6.4   Conclusions

In this chapter, two novel applications of the self-switching SOA-MZI are presented. These applications are the pattern effect compensator and the 2R-regenerator. The realization of both components is based on the active-passive integration technique. The integrated pattern effect compensator has shown its compensation capabilities for bitrates of up to 20 Gb/s, and in principle does not depend on the bitrate until at least 40 Gb/s. Furthermore, the input power dynamic range of this device at 10 Gb/s, compared to a single SOA, is extended by about 7 dB. It provides a gain that is comparable to a single SOA. Therefore, the integrated pattern effect compensator can be used as a pattern effect free optical amplifier with the extended input power dynamic range.

The integrated 2R-regeneration has shown its regeneration capabilities at 2.5 Gb/s. It can be seen as a clear suppression of noise around the "zero" level. The receiver sensitivity improvement for an OSNR of 17 dB is 2.5 dB. The maximum bitrate is limited by the recovery time of the amplifiers. By optimal choosing an operating point, the regeneration in the proposed device can be combined with pattern-free amplification.

Chapter 7

Low-loss optical combiner

In this chapter, a novel application of self-switching in Mach-Zehnder interferometers is presented, the low-loss optical combiner. This device is aimed to avoid the inherent loss of half of the optical power in conventional passive power splitters/combiners. Two realizations of the low-loss optical combiner circuits are described. One of them is based on semiconductor optical amplifiers, which are used as the nonlinear phase shifters. The second is based on quantum dot material, which provides an intensity dependent phase shift in a fully passive way.

7.1   Introduction

An essential function in optical fiber networks is the combining of optical signals. Traditionally, the combiner is a passive function, obtained e.g. with fused fiber couplers or planar Y-junctions. In photonic integrated circuits directional couplers, Y-junctions or MMI couplers can be used for passive combination of two optical signals. An essential disadvantage of these components is an inherent loss of at least half of the optical power, which will further be referred to as a 3 dB loss. The origin of this loss is explained in Fig. 7.1.

In Fig. 7.1, a Y-junction is shown schematically. In the splitting direction (see Fig. 7.1(a)), an optical mode is split into two parts, one in each output waveguide, resulting that only a half of the power is transmitted to each output port. If the Y-junction is used in the combiner direction (see Fig. 7.1(b)), the optical field launched into one of the input waveguides can be described as a combination of two system modes[1], symmetric and asymmetric, in the interaction region. These modes convert to

---

[1]This explanation is based on the system-mode theory, see in chapter 2.

Figure 7.1: Schematic of a waveguide Y-junction. (a) Splits the optical field into to output waveguides. (b) Combines the fields from two input waveguides.
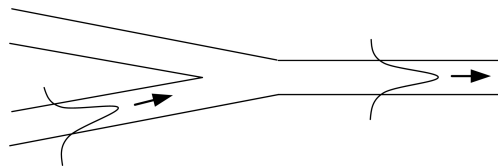
Figure 7.2: Schematic of the nonlinear Y-junction.

the fundamental and the first-order modes, and the first-order mode is usually radiated out. Conversion of the first-order mode to radiation modes makes that at least half of the signal power gets lost. This fundamental 3 dB combiner loss also occurs in other passive couplers, like MMI and directional couplers.

A number of approaches to reduce the unwanted 3 dB loss has previously been proposed. They are summarized below.

7.2 Overview of the low-loss optical combiners

In [87], a symmetric Y-junction for optical signal combining is proposed. This structure, schematically shown in Fig. 7.2, consists of monomode waveguides and exhibits positive Kerr-nonlinearity. In such a nonlinear Y-junction, due to a positive nonlinearity, the refractive index of a mode propagating in one of the arms can be increased. If there is no signal present in the second input port, this is causing an asymmetry of the structure and a large fraction of the optical power will be coupled into the fundamental mode of the output. This configuration requires rather strong nonlinear effects, which is according to simulations difficult to achieve in the InP-based material system (see also chapter 5). It is calculated that the proposed configuration can reduce the loss up to 0.21 dB.

The 3 dB loss can also be avoided using optical switches, but then control func-
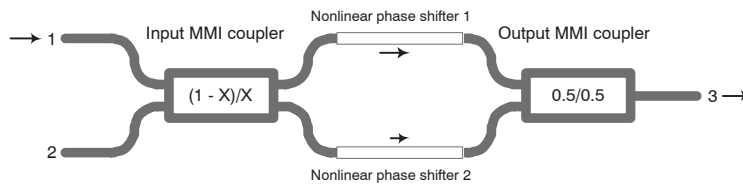
Figure 7.3: Schematic of the proposed low-loss optical combiner.

tions are needed to synchronize the switch with the optical signals. A nonlinear switch, suitable for the combiner function, is proposed in [88]. This device is a Mach-Zehnder interferometer, which has two identical nonlinear interferometer arms and control light ports. The switching principle is based on the push-pull type operation in which one arm is excited shortly after the other. In this way, the optical pathlength of one arm is modified by the first control pulse (leading pulse), due to band-filling nonlinearities. The signal output is consequently switched to the other output port (switch-ON). The signal is gradually switched back to the initial port if the nonlinear waveguide relax to its initial state following the slow carrier recombination. If the other arm is excited by the second control pulse, the nonlinear refractive index change still remaining in the first arm can be canceled by that in the other arm. In this way, a fast switch-OFF can be achieved.

Finally, a semiconductor optical amplifier at the output of the passive optical combiner can be used in order to compensate the 3 dB loss. A drawback of such a configuration is addition of the ASE noise generated by the SOA, which deteriorates the optical signal-to-noise ratio.

In this chapter, a novel application of the MZI based on self-switching is presented, the low-loss optical combiner. This device aims to solve the aforementioned problems.

7.3 Low-loss optical combiner based on self-switching in a MZI

The proposed low-loss optical combiner aims to reduce the unwanted 3 dB loss. It is a 2×1 MZI with unequal distribution of the input optical signal over the interferometer arms. It operates without using any control signals. The device is schematically depicted in Fig. 7.3.

7.3.1 Operation principle

The input optical signal injected in one of the input ports of a 2×1 MZI is distributed unequally over the two interferometer arms by a MMI coupler with a coupling ratio of $(1 - X)/X$. With input port 1 and such an input coupler, the highest power is in the upper arm. A phase difference of $\pi/2$ is induced between the signals in the two arms by the input coupler. In the high-power arm, an intensity dependent phase shift can be induced due to self-phase modulation, while in the low-power arm almost no intensity dependent phase shift is induced. As a result, a nonlinear phase shift $\Delta\phi_{NL}$ can arise between these two optical signals of unequal intensities. However, at low input power levels, the nonlinear phase shift is negligible, and the two signals from the interferometer arms with a phase difference of $\pi/2$ with respect to each other incompletely interfere at the output port of the interferometer. At higher input powers, the phase in the high-power arm changes, and maximum output power (at port 3) can be reached if the nonlinear phase shift compensates the phase differences caused by the input coupler. The two signals from the interferometer arms are then in phase and constructively interfere at the output port. An optimum recombination of the two signals is then observed.

Based on derivations in chapter 5, the combiner transmission can be written as:

$$T_{13} = 0.5 + \sqrt{X(1 - X)} \sin(\Delta\phi_{NL}). \tag{7.1}$$

Using input port 2 instead of 1 mirrors the situation: both the nonlinear and the coupler induced phase shift occurs in the other interferometer arms again, compensating each other. In the opposite direction, the low-loss optical combiner works as a passive 3-dB splitter, since no nonlinear phase shift is induced between two equal optical signals.

Thus, for the operation of the low-loss optical combiner, the optimal nonlinear phase shift is $\pi/2$. If the coupling coefficient X is close to 0.5, the powers in the interferometer arms are nearly equal. In this case the loss of the combiner is minimized, since a complete recombination of optical signals is obtained. However, the length of the nonlinear phase shifter should then be extremely large. On the other hand, if $X = 0$, all power is only injected in one arm, no interference is left, and the loss of a passive optical power combiner is obtained. The dependence of the residual combiner loss on X is shown in Fig. 7.4(a). In our case, with the 85/15-type input coupler ($X = 0.15$), the combiner loss is about 0.7 dB.

The low-loss optical combiner is a power dependent device. The loss in the combiner with an input coupling ratio of 0.85/0.15 is plotted in Fig. 7.4(b). A reduction of power by a factor of 2 from the optimal value results in a loss of -1.2 dB, which is
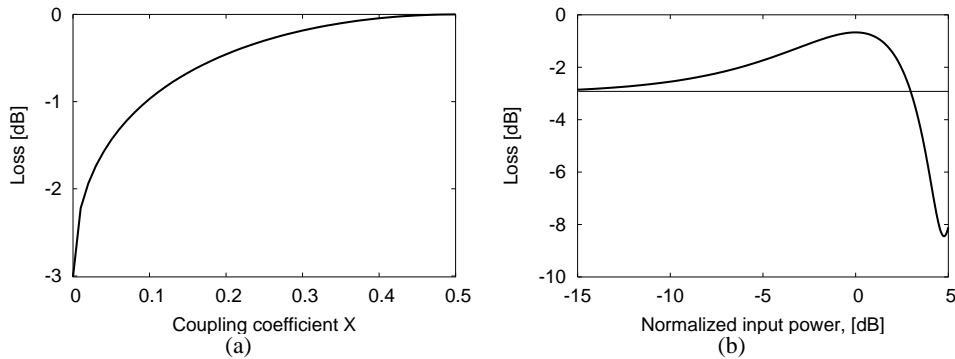
Figure 7.4: Calculated loss of the combiner. (a) Loss as a function of the coupler parameter X. (b) Loss as a function of the input power, with $X=0.15$

still a sizable improvement over a passive combiner. On the other hand, an increase of a factor of 2 results in -3 dB loss. This means that increases in power should be closely controlled. To achieve a high tolerance for power variations, the operational power could be chosen somewhat below the optimum power, e.g. at 40% (-4 dB below the peak transmission). The loss of the combiner is then 1 dB higher at the operational power, but the power range for a loss below that of a passive combiner is in that case approximately 12 dB.

7.3.2   Applications

The low-loss combiner can have a number of applications in optical fiber networks. Some of them are briefly discussed below.

In Passive Optical Networks (PON) [89] users are connected to a local exchange through a fiber tree, as schematically shown in Fig. 7.5. If conventional splitter stages are used, each of the stages introduce a fundamental loss of 3 dB. Because the signal has to be distributed among the subscribers, this loss is unavoidable in the direction towards them. However, in the opposite direction, the situation is different. In this case, optical power is needlessly lost (-3 dB per stage). This requires high-power lasers to be used at the subscriber side. Since the low-loss optical combiner decreases the loss, this leads to using much cheaper lasers. In such optical networks, the access mechanism prevents collision of optical signals. The time scale for switching of the combiners is determined by this access mechanism, with time slots of a few milliseconds.

Like with passive couplers, two signals (of identical wavelength) are not allowed
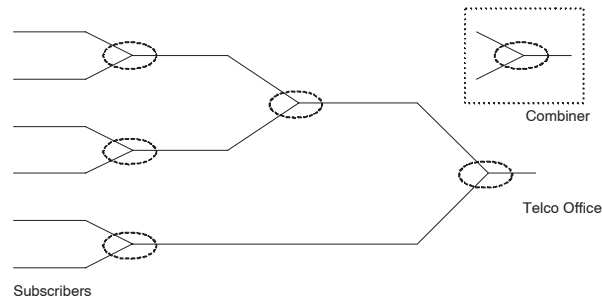
Figure 7.5: Schematic of a passive optical network.

at the same time on the inputs, otherwise the operation is disturbed. Multiple signals will interfere and cause crosstalk, and signal degradation. Applications like PON systems include a time-division access protocol, allowing only one signal at one time, and are therefore suitable for use of the low-loss optical combiner.

In optical fiber networks like SONET/SDH[2], ring configurations are normally used. These are so-called self-healing rings, since the traffic following along a certain path (primary path) can automatically be switched to an alternative path (protection path). An optical protection system is an alternative to this electrical protection (the main advantages are the higher speed and simultaneous operation on many wavelengths). It can be implemented with two optical links, connected at one side to a transmitter with a 1×2 switch, at the other side to a receiver with a combiner. If a fiber breaks the switch selects the intact link. Using the low-loss optical combiner, a 3 dB loss on both links is avoided. The reaction time should be comparable to that of electrical protection (50 ms), so that the nonlinear effects can be slow.

7.3.3 Implementations

As mentioned earlier in this thesis, there are basically two types of nonlinear phase shifters: active and passive. We have used both types to realize low-loss optical combiners. The first one uses semiconductor optical amplifiers as nonlinear phase shifters. The other one uses quantum dot based nonlinear phase shifters. This chapter reports on the realizations of these devices.

---

[2]SONET is short for Synchronous Optical NETwork. SDH is short for Synchronous Digital Hierarchy.
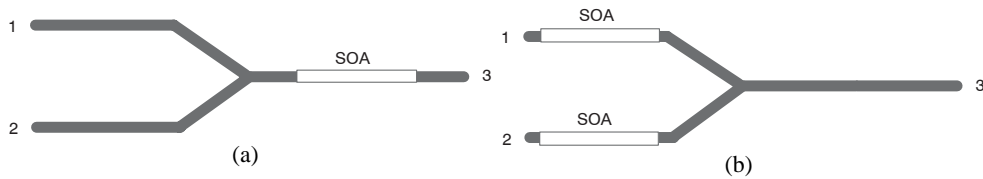
Figure 7.6: Schematic of a passive 3-dB combiner with an in-line SOA. (a) SOA is put in the output port. (b) SOA is put in each input port.
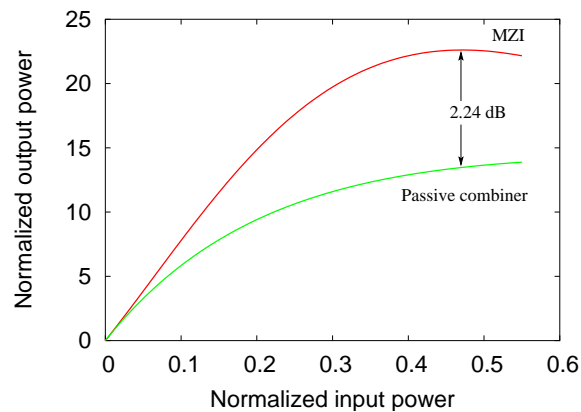
Figure 7.7: Calculated output power of the low-loss optical combiner compared with a passive combiner with an in-line SOA.

7.4   SOA-based low-loss optical combiners

Although combination of optical signals is a passive function, we have first realized it using a SOA-MZI. Since passive combination is often combined with semiconductor optical amplifiers, it is relevant to compare these two implementations with respect to the OSNR. In Fig. 7.6 two configurations of a passive 3-dB combiner with an in-line SOA are shown. The SOA can be placed either in the output port (Fig. 7.6(a)), or in each input port (Fig. 7.6(b)).

In Fig. 7.7 the output power of the passive 3-dB combiner with the SOA in the output port is compared with the output power of the low-loss combiner, which employs the same SOA type. Here, the low-loss combiner uses a 85/15-type input coupler.

From Fig. 7.7 it can be seen that the maximum output power of the low-loss combiner is 2.24 dB higher, implying 2.24 dB lower loss. In case the SOA is placed in
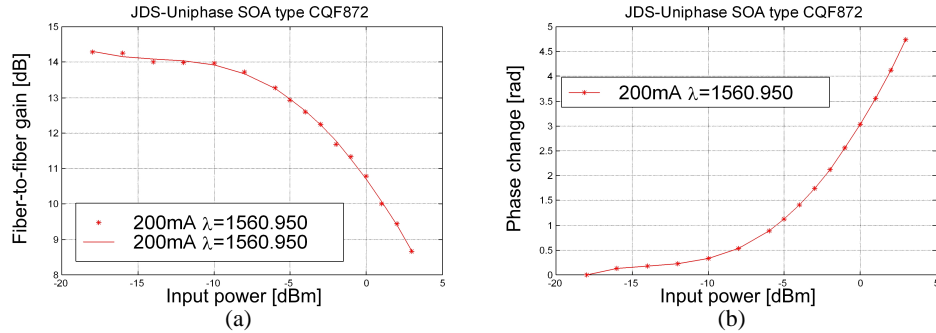
Figure 7.8: (a) Gain saturation and (b) related phase change as a function of the input power measured for a commercial SOA.

the output port, the produced ASE noise is equal to the ASE noise from the two SOAs in the MZI, since the output coupler of the MZI reduces this noise by 3 dB. However, the reduction of the combiner loss by 2.24 dB implies a 2.24 dB increase in OSNR. It is possible to obtain a better OSNR when SOAs are put in each of the input ports of a passive 3-dB combiner with one of the SOAs turned off. But this requires on/off switching of these SOAs according to which input port is used. The low-loss optical combiner should avoid such control requirements.

7.4.1 Fiber-based low-loss optical combiner with SOA phase shifters

Experimental SOA-MZI

The low-loss optical combiner concept described above was initially verified using a fiber-based SOA-MZI structure [80]. The Mach-Zehnder interferometer consists of two JDS-Uniphase SOAs (type CQF 872). From the measured gain saturation curve, shown in Fig. 7.8(a), the phase change in the SOA was derived (see Fig. 7.8(b)) with a measured device alpha parameter of 7.2. For an input power difference of 9.5 dB at the SOAs, as applied in the experiment, $\Delta\phi_{\rm NL} = \pi/2$ is expected for an input power of -1.5 dBm in the SOA-MZI.

The input coupler is a 90/10-type fiber coupler, and the output coupler is a 50/50-type fiber coupler. The fiber-based combiner is schematically shown in Fig. 7.9.

The output powers depend on the two phase shifts: the linear and the nonlinear one. A linear phase shift difference $\Delta\phi_{\rm L}$ is added in order to compensate for the additional phase difference caused by the 2×2 output coupler. The nonlinear phase shift $\Delta\phi_{\rm NL}$ changes sign when changing the input port, as the high-power arm is then
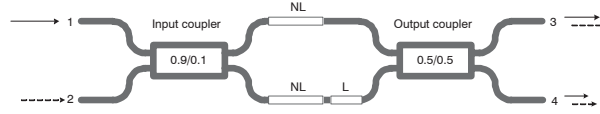
Figure 7.9: Schematic layout of the fiber based combiner. The nonlinear phase shifters in the arms are given as NL, the linear phase difference, resulted from the length difference between the arms, is depicted as L.

the opposite one. In contrast, the linear phase shift $\Delta\phi_L$ is independent of the input port.

The transmissions for the four different paths through the MZI without taking into account the gain effects, can be written as:

$$
\begin{aligned}
T_{13} &= 0.5 - \sqrt{X(1-X)}\cos(\Delta\phi_{NL} + \Delta\phi_L), \\
T_{14} &= 0.5 + \sqrt{X(1-X)}\cos(\Delta\phi_{NL} + \Delta\phi_L), \\
T_{23} &= 0.5 + \sqrt{X(1-X)}\cos(-\Delta\phi_{NL} + \Delta\phi_L), \\
T_{24} &= 0.5 - \sqrt{X(1-X)}\cos(-\Delta\phi_{NL} + \Delta\phi_L).
\end{aligned}
\tag{7.2}
$$

If both $\Delta\phi_{NL}$ and $\Delta\phi_L$ are equal to $\pi/2$, Eq. 7.2 can be reduced to:

$$
\begin{aligned}
T_{13} &= T_{23} = 0.5 + \sqrt{X(1-X)}, \\
T_{14} &= T_{24} = 0.5 - \sqrt{X(1-X)},
\end{aligned}
\tag{7.3}
$$

which is identical to Eq. 7.1, presented earlier.

From Eq. 7.3 the symmetric operation of the combiner is obtained: the output powers are no longer dependent on which input port is used. Both input signals are for the largest part transferred to output port 3. In this way the low-loss optical combiner can be implemented.

Measurements

The experimental setup[3] is schematically depicted in Fig. 7.10.

The input optical signal is generated by a tunable laser source. The wavelength[4] is 1560.95 nm. The emitted optical signal passes through an EDFA, followed by an

---

[3]The experimental setup and the measurements were done in cooperation with the Electro-Optical Communication group, COBRA Research Institute, Technische Universiteit Eindhoven.

[4]Wavelength from the ITU grid.
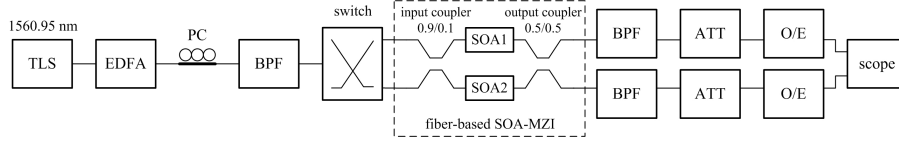
Figure 7.10: Schematic of the measurement setup for characterization of the fiber-based low-loss optical combiner. PC: Polarization Controller. TLS: Tunable Laser Source, BPF: BandPass Filter, ATT: ATTenuator. O/E: OptoElectronic converter.

optical bandpass filter in order to eliminate the ASE. An attenuator is used to avoid saturation of the detector. Detection is done with home-made optoelectronic converters. The electrical output signal from the receiver is displayed on a sampling oscilloscope in the form of pulse shapes.

The SOAs are biased with an injection current of 200 mA. Stability of the measurements was a major issue. Due to environmental influences the value of $\Delta\phi_L$ drifted during the experiment, influencing the output power distribution. Therefore a measurement procedure was developed that determines $\Delta\phi_{NL}$ unambiguously. This was achieved as follows. An optical switch alternated the signal between the input ports, with a frequency (100 Hz) high enough to neglect environmental drift in one switching period. In this way the power difference from the output ports showed a periodic (100 Hz) pattern. This pattern slowly changed in amplitude, due to the environmental drift. For $\Delta\phi_L = 0$ the maximum amplitude A_{max} was obtained, which is according to Eq. 7.2:

$$A_{\max} = T_{13} - T_{14} - T_{23} + T_{24} = 4\sqrt{X(1 - X)}\cos(\Delta\phi_{NL}). \qquad (7.4)$$

The parameter A_{max} was determined by observing the output power distribution. For operation as a combiner (with $\Delta\phi_{NL} = \pi/2$) it becomes zero and the periodic pattern in the output disappears. Switching between the input ports then has no influence. With $\Delta\phi_L = \pi/2$ light from both input ports is primarily guided to port 3.

In Fig. 7.11(a) the A_{max} is shown as a function of the input power into the MZI. A_{max} vanishes at 0.47 mW (-3.3 dBm). At this value the optimal combiner function is found. This verifies that indeed an optically induced phase shift is occurring, and that this phase shift results in the combiner function: both input signals (from either port 1 or 2) are guided to the same output port.

Due to the drift, the combiner operation was only directly observable if $\Delta\phi_{NL}$ is close to $\pi/2$. The output power distribution is given in Fig. 7.11(b) as a function of
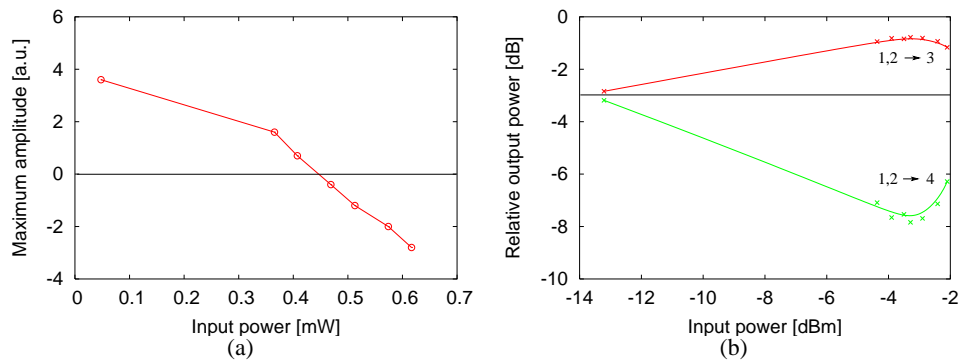
Figure 7.11: Measured fiber-based low-loss optical combiner [80]. (a) Maximum output power difference for the two input ports 1 and 2. For a zero value both signals from port 1 and from port 2 are guided to the same output port. (b) Relative power from the two output ports. A maximum of 85% of the power is guided to port 3, on injection in either of the two input ports. The horizontal line indicates the 3 dB loss of a conventional passive combiner.

the input power. The on-off ratio over the output ports is 7.2 dB. The fraction of the signal from the desired port is 0.85, therefore, the combiner loss is 0.7 dB, which is 2.3 dB improvement over a passive combiner. This improvement is comparable[5] with a simulated value of 2.24 dB in Fig. 7.7.

Conclusions

A self-switching fiber-based SOA-MZI has shown the capabilities for the low-loss optical combiner. It guides 85% of the signal from each of two inputs to the same output port. Nonlinear switching was obtained with carrier depletion in SOAs at an input power of around 0.5 mW (-3 dBm). The fiber-based combiner showed unstable behavior, which can be solved by integrating the low-loss optical combiner on a chip.

---

[5]A remark should be made that the experimental combiner uses an input coupler with a coupling ration of 0.9/0.1, while the calculations are based on the input coupler with a coupling ratio of 0.85/0.15, which might slightly influence the result.

7.4.2   Integrated SOA-based low-loss optical combiners

Design and fabrication of the combiner circuits

The low-loss optical combiner with SOA-phase shifters is realized with the active-passive integration technique in InGaAsP/InP. For that, the Low Pressure Metal Organic Vapor Phase Epitaxy (LP-MOVPE) technique using butt-joint coupled active and passive waveguides was used. The passive waveguides used in the circuits have a width of 3 μm, and are 100 nm etched into the film layer. The geometry of the passive waveguides is optimized as a trade-off between low propagation losses and low radiation losses in the bends. The MMI couplers are 10-μm-wide, with access waveguides connected with an offset of 2.69 μm. The input coupler is of the 85/15-type, with a length of 724 μm. The output MMI coupler is 2×1 50/50-type, with a length of 115 μm.

The SOA waveguides are optimized for high photon density in order to enter the nonlinear regime at low optical powers. The SOAs are 2-μm-wide waveguides etched 100 nm into the quaternary layer. Two generations of the integrated SOA-based low-loss optical combiners have been realized. The first generation was based on the layout of the active regions, as shown in Fig. 3.2(a). Besides, in the first realization the cladding was a 1300-nm-thick InP layer with p = 10^{18} cm^{-3}. The second generation was based on the layout of the active regions, as shown in Fig. 3.2(b). For reducing the propagation losses in the second realization, the p-InP cladding layer was split into two parts: 300-nm-thick InP layer with p = 5×10^{17} cm^{-3} and a 1000-nm-thick InP layer with p = 10^{18} cm^{-3}. In the first realization, the SOA length was 750 μm. The second realization of the combiners includes also longer active regions: 1000, 1250 and 1500 μm. This is in order to investigate the SOA length influence on the nonlinear switching in the combiner circuits. A layer of a 50-nm-thick PECVD-SiN$_x$ is used as masking material. Both passive and SOA-waveguides are defined simultaneously in SiN$_x$-layer by a lithographic process in a positive photoresist, followed by the selective etch of the SiN$_x$ layer by RIE employing a CHF$_3$ process. A contact layer required for operation of a SOA causes unwanted propagation losses in passive waveguides. Therefore, it is selectively removed everywhere except for the SOAs. This is achieved in the two-step etching procedure: first, all the waveguides are etched partly to a certain depth (the first etch), second, after removing the SiN$_x$ mask from the passive waveguides, all waveguides are etched to their target depth of 100 nm depth into the film layer (the second etch), also etching away the InGaAs contact layer. The ridge waveguides were etched employing an optimized CH$_4$/H$_2$-RIE technique alternated with an O$_2$-descum process to remove polymer depositions. After that, the SiN$_x$ mask layer was removed, and a new 300-μm-thick layer of PECVD SiN$_x$ for isolation purposes was deposited.

Figure 7.12: SEM pictures of the active region cross-section. (a) One SOA in one active region. (b) Two SOAs in one active region.

Subsequently, the openings on the top of the SOAs were created for electrical contacts. The metal contacts on the p-side were defined using a lift-off process, the metal layers were deposited using a sputtering process. The contact on the n-side was deposited. Both contacts were annealed in order to reduce the contact resistance and make the contacts Ohmic. Finally, the chip was cleaved and AR-coated. The detailed process scheme for fabrication of the active MZIs was presented in subsection 3.4.1.

We have fabricated two different configurations of the SOA-based low-loss optical combiners. In the first configuration, the SOAs are fabricated in separate active areas, having two contact pads. Therefore, they can be biased independently. The second configuration of combiners has a more compact design, in which both SOAs are placed in one active area, sharing one contact pad. Thus they can be biased simultaneously. Furthermore, a better balance between the interferometer arms is expected, since closely placed SOAs have less problems of non-uniformities introduced by the material and the processing. The cross-sections of these two configurations of SOA-based phase shifters are shown on the SEM pictures in Fig. 7.12. In Fig. 7.12(a) a single SOA configuration is shown, while in Fig. 7.12(b) the cross-section of two SOAs fabricated in one active area is shown.

Measurement results of the integrated low-loss optical combiner

The integrated low-loss optical combiners with SOA-phase shifters were characterized statically. The measurements were performed with an experimental setup, schematically depicted in Fig. 5.6(a), which is detailed described in subsection 5.2.5.
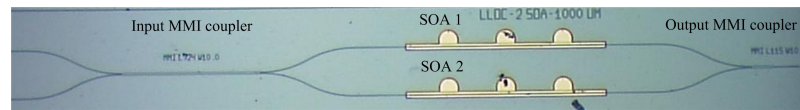
Figure 7.13: Photograph of the fabricated low-loss optical combiner with two independently biased SOAs.

Low-loss combiner with two independently biased SOAs

First, consider the low-loss optical combiner with two independently biased 1000-μm-long SOAs. A feature of this combiner configuration is the possibility to optimize the operating point of the interferometer by adjusting the injection currents of both SOAs independently. However, a major drawback of this configuration is a probability of phase-mismatch due to the optical pathlength difference, since the SOAs are fabricated in separate active areas at a distance of 250 μm from each other. Furthermore, it takes a larger area on the chip. A photograph of the device is shown in Fig. 7.13.

Prior to the transmission measurements, we have determined the operating point of the interferometer. The operating point was determined by fixing the current of the SOA in the high-power arm, varying the injection current of the second SOA and measuring the output power at port 3. The measurements were repeated at different input powers. For the symmetric operation of the low-loss optical combiner with respect to the input ports, the "starting" point of the interferometer (in the low power range) should lie between the destructive and constructive interference points, while at high powers, a constructive interference peak should be obtained. This implies an induced nonlinear phase shift of $\pi/2$, which is required for the combiner operation.

The operating point measurement results (interference curves) for the pair of ports 2 to 3 are presented in Fig. 7.14. The injection current of the SOA in the high-power arm (SOA 2) was fixed at 120 mA (this corresponds to a current density of 0.06 mA/μm^2), and the current of SOA 1 was varied. The measurements were performed at λ = 1550 nm. From Fig. 7.14 it can be seen, that the bias conditions for the optimal self-switching in the low-loss optical combiner are: I_{SOA1} = 117 mA and I_{SOA2} = 120 mA, which is very close to the balance. The injection current in the high-power arm was limited by the fact that at higher current the SOA entered the lasing regime. Since for stronger nonlinear effects high currents are preferred, 120 mA was chosen, being the highest possible current at which SOAs were working in the non-lasing regime.

The output powers corresponding to both optical paths in the interferometric (combiner) direction (port 1 to 3 and port 2 to 3) are plotted in Fig. 7.15(a). For
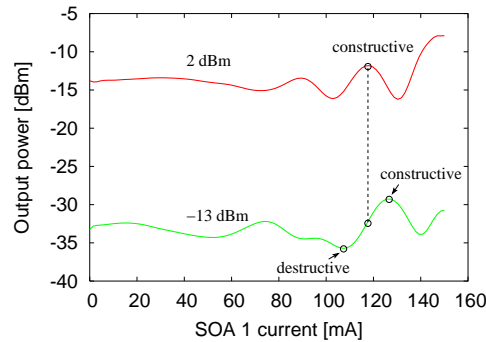
Figure 7.14: Measured interference curves of the combiner at different input power levels. The vertical dotted line indicates the working point.

the low-loss combiner application it is important that it operates symmetrically with respect to both input ports. It can be seen that the operation is indeed very close to symmetry.

In the non-interferometric (splitter) direction (port 3 to 1 and port 3 to 2), the 2×1 SOA-MZI behaves as a passive passive 3-dB splitter with an in-line SOA. Now the optical signal is distributed equally over the interferometer arms. At the input coupler, the two signals are in phase[6], and therefore equal at both port 1 and port 2. These curves are plotted in Fig. 7.15(b). From Fig. 7.15(b) it can be seen that the SOAs in this case are partly saturated by the 50% of the input power in each SOA.

The transmissions measurement results for two opposite directions (combiner versus splitter) are compared in Fig. 7.16. This comparison directly shows the effect of the nonlinear interference, as all linear effects are identical in both directions. Fig. 7.16 shows an improvement of the interferometric direction. From this comparison it follows, that the maximum improvement of the low-loss combiner over the splitter is 1.46 dB (ports 1 and 3), and 2.2 dB (ports 2 and 3). A certain asymmetry in the measurement results can possibly be explained by an additional phase difference between the signals due to a small optical pathlength difference, and possibly different fiber-chip coupling efficiency, due to some facet damages.

We can compare the measured curves with the calculated ones, presented in Fig. 7.7. It can be seen, that the measurements are in the qualitative agreement with the

---

[6]The nonlinear phase shift between two equal signals is not induced. No linear phase difference due to unbalance in the MZI is assumed. In this case the situation is identical to the one illustrated in Fig. 7.7 for a passive combiner with an in-line SOA.
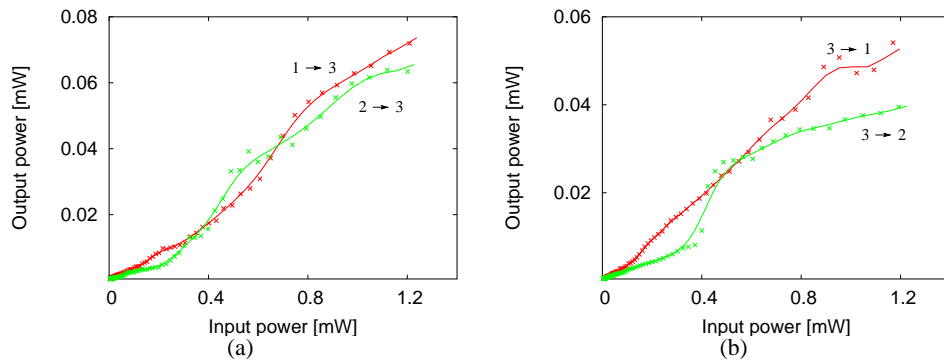
Figure 7.15: Measured transmission curves at the operating point of the low-loss optical combiner. (a) Combiner direction. (b) Splitter direction. Input and output power are the ones in the fiber.
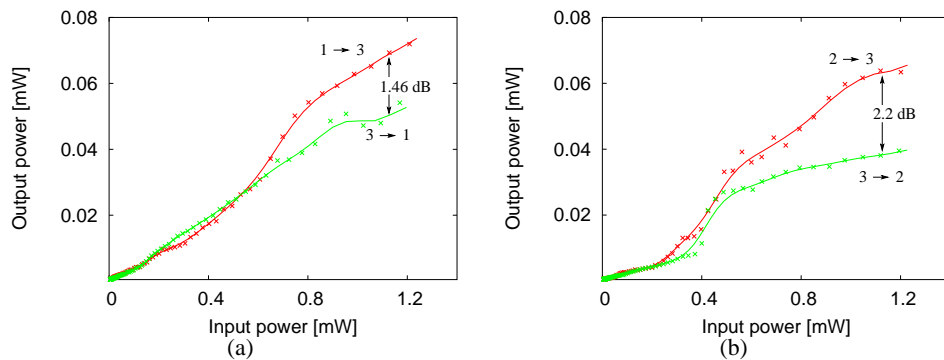
Figure 7.16: Measured transmission curves at the operating point of the low-loss optical combiner. (a) Combiner versus splitter, ports 1 and 3. (b) Combiner versus splitter, ports 2 and 3. Input and output power are the ones in the fiber.

simulations. The kinks in the measured curves can possibly originate from the measurements instabilities. Furthermore, the maximum improvement of the combiner loss with respect to a passive 3-dB splitter with an in-line SOA is 2.2 dB, which is close to the simulated value. The combiner effect is achieved at an input power of around 1.2 mW (0.8 dBm) in the input fiber, which is with the correction for the fiber-chip coupling losses (around 4-5 dB per facet) as low as 0.5 mW (-3.2 dBm).

The low-loss optical combiners with even longer separately biased SOAs (1250

Figure 7.17: Photograph of the fabricated low-loss optical combiner with two simultaneously biased SOAs.

and 1500 μm) have shown poor performance due to severe damages of the facets. Furthermore, the 1500-μm-long SOAs suffered from non-uniform current spreading over the SOA sections. Finally, high ASE power measured at the output of the 1500-μm-long SOAs limited their applicability.

Low-loss combiner with two simultaneously biased SOAs

Consider the low-loss optical combiner with two 1250-μm-long SOAs phase shifters fabricated in one active area, sharing the same metal contact pad. An advantage of this configuration is that both optical pathlengths are hypothetically (almost) equal due to the shorter bends and the more uniform active material within one region. Therefore, the SOA-MZI might operate closer to balance. Furthermore, this configuration requires only one current source and uses less chip area. A photograph of the device is shown in Fig. 7.17.

The total injection current for both SOAs in this experiment is 320 mA. It is assumed, that a current of 160 mA is supplied to each SOA. This corresponds to a current density of 0.064 mA/μm^2.

The two output power curves measured in the interferometric (combiner) direction (port 1 to 3 and port 2 to 3) are compared in Fig. 7.18(a). It can be seen, that the output powers corresponding to both optical paths in the combiner direction are not equal, suggesting not exactly symmetrical operation. The asymmetry of the transmissions in the combiner direction can be observed in Fig. 7.18(a), suggests a linear phase shift between the interferometer arms.

The output powers in the non-interferometric (splitter) direction (port 3 to 1 and port 3 to 2) were also measured. Now the SOAs are partly saturated, since the fraction of power entering the SOA is 50%. The results are shown in Fig. 7.18(b).

The transmissions measurement results for two opposite directions (combiner versus splitter) are compared in Fig. 7.19. This comparison directly shows the effect of the nonlinear interference. Fig. 7.19 shows an improvement of the interferometric direction. From this comparison it follows, that the maximum improvement of the combiner over the splitter is 3.3 dB (ports 1 and 3), and 3.0 dB (ports 2 and 3). This
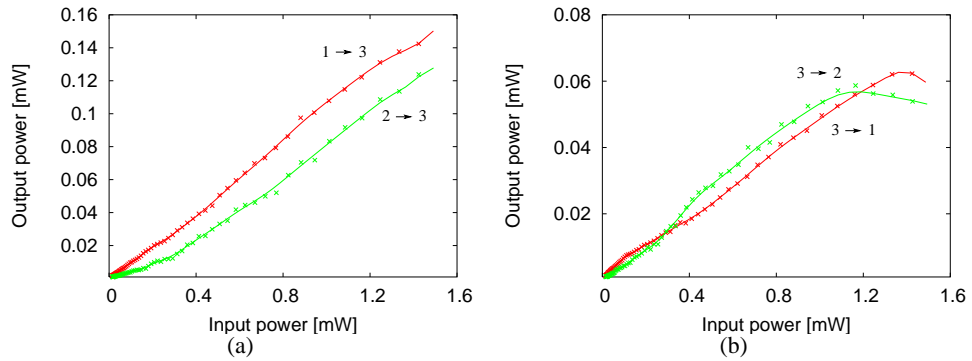
Figure 7.18: Measured transmission curves. (a) Combiner direction. (b) Splitter direction. Input and output power are the ones in the fiber.
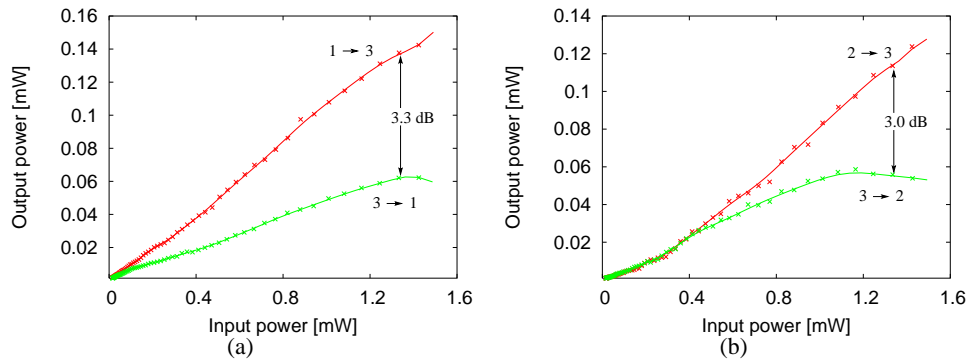
Figure 7.19: Measured transmission curves. (a) Combiner versus splitter, ports 1 and 3. (b) Combiner versus splitter, ports 2 and 3. Input and output power are the ones in the fiber.

can be compared with a predicted value of 2.24 dB in Fig. 7.7. It can be seen, that the measured combiner improvement is higher than the calculated one. An explanation for that might be a coupling between the SOA-waveguides, as they are placed close to each other. Normally, in the interferometric direction the power ratio of two optical signals from the interferometer arms is different from the 0.85/0.15 ratio, and is closer to one, because the highest power experiences the lowest gain. If coupling between the two interferometer arms is taken into account, this ratio becomes even more close to one, which is beneficial, because interference is then even less incomplete, and the

output power becomes higher than the predicted one. Our measurements at different wavelengths showed wavelength dependence of the improvement value, which also points at possible coupling-related effects.

Furthermore, from the comparison of the measured curves with the calculated ones (Fig. 7.7) it can be concluded, that the measured curves representing the output power of the combiner are quite linear, pointing out that the condition of the constructive interference has not been fulfilled yet at the given power levels, and optimum recombination of the optical signals is not obtained. The combiner effect is achieved at an input power of around 1.2 mW (0.8 dBm) in the input fiber, which is with the correction for the fiber-chip coupling losses (around 4-5 dB per facet) as low as 0.5 mW (-3.2 dBm).

An important conclusion is that in case two SOAs are fabricated in one active region sharing the same contact pad, the balance of the interferometer is not perfect, which cannot be improved by adjusting the injection currents. On the other hand, this combiner shows a very good performance for both optical paths.

The bitrate behavior of the combiner has not been tested. In chapter 6 we have shown, that comparable SOA-MZI structures, aimed at pattern effect compensation, can handle bit rates up to 40 Gb/s. Since the combiner function requires only gain saturation (no recovery is needed), it suggests that very high-speed operation of the combiner is, in principle, possible.

Conclusions

A low-loss optical combiner based on a SOA-MZI with unequal distribution of the input optical signal is described. This device aims to compensate for the inherent loss of half of the power in a conventional passive optical power combiner. Our interferometric solution can improve the signal-to-noise ratio compared to a passive power combiner in combination with an in-line SOA. The realization of the low-loss optical combiner is based on the active-passive integration technique. Two configurations of the integrated combiners are discussed. The first employs two independently biased SOAs. An advantage of this configuration is the possibility to optimize the operating point of the interferometer by adjusting the injection currents of both SOAs. A disadvantage is that it takes a larger area on the chip. With 1000-μm-long SOAs, the maximum measured improvement of the combiner with respect to the passive 3-dB splitter with an in-line SOA is 2.2 dB, which is very close to the predicted value. This combiner shows a good symmetry with respect to the input ports. In the second configuration, both SOAs are fabricated in one active area, and share the same contact pad. Consequently, it consumes less chip area and needs only one current source. However,

it was shown that the interferometer is not perfectly balanced in this case. With 1250-μm-long SOAs, the maximum measured improvement of the combiner with respect to the passive 3-dB splitter with an in-line SOA is 3.3 dB, which is higher than a predicted value due to a linear phase shift between the interferometer arms. The combiner effect is achieved at low input power levels: a required input power of around 1.2 mW (0.8 dBm) in the input fiber, which is with the correction for the fiber-chip coupling losses (around 4-5 dB per facet) 0.5 mW (-3.2 dBm). Both configurations have shown stable operation.

7.5 Quantum dot based low-loss optical combiners

In the previous section, we have discussed the low-loss optical combiner based on self-switching in SOA-MZIs. As mentioned before, the combiner is essentially a passive function, whereas SOA-based phase shifters require electrical power. In this section, we will present a novel all-optical switching technique in quantum dots. We apply quantum dot structures to realize a fully passive low-loss optical combiner.

7.5.1 Design and fabrication

The passive low-loss optical combiner is based on material containing quantum dots. A monolayer of InAs quantum dots is embedded in a 500-nm-thick Q(1.29) film layer, which is covered with a 1.3-μm-thick InP cladding. Underneath the QDs, a thin layer of GaAs is inserted for reproducible tuning of the emission wavelength in the 1.55 μm range. Although quantum dots are only needed for the phase shifters, in this realization all the components of the combiners are fabricated in this layer stack.

For fabrication of the QD-based low-loss optical combiners the waveguide mask was used originally designed for the SOA-based devices. Its design overview can be found in the previous section. We have investigated the most compact devices, in which 2-μm-wide phase shifters, etched 100 nm into the quaternary layer, are put at a distance of 15 μm from each other. This was in order to minimize the overall device losses.

The QD-MZIs are made according to the fabrication technology described above. All the waveguides were etched in one step.

7.5.2 Measurement results

Prior to the characterization of the combiner circuit, we have characterized the waveguide losses. These measurement results were discussed in section 4.2. The propaga-
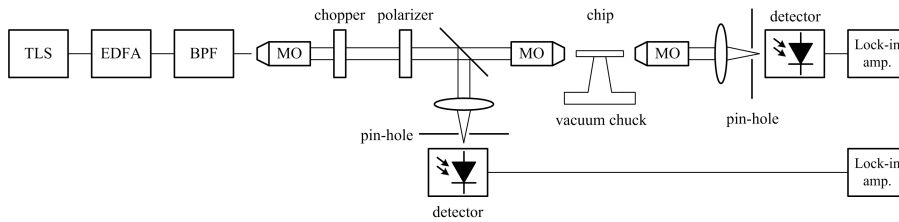
Figure 7.20: Measurement setup for characterization of the switching in QD-MZI. EDFA: Erbium Doped-Fiber Amplifier, MO: Microscope Objective,

tion losses were measured at a wavelength of 1534.8 nm, which is close to the absorption peak of the quantum dots ($\sim$ 1520 nm), see the PL-spectrum in Fig. 3.5. Since the transmission measurements of the MZI will be carried out at higher wavelengths (around 1550 nm), the waveguide losses there are expected to be lower. Therefore, losses in the nonlinear phase shifters fulfill our requirements (see section 5.3).

The experimental setup is schematically depicted in Fig. 7.20. The CW input optical signal is generated by a tunable laser source and EDFA in combination with a tunable bandpass filter. The optical signal passes through an attenuator, which is used for power sweeps. The measurement stability was problematic, because of polarization changes in the fibers in combination with the polarization dependent behavior of the device. For unambiguous interpretation of the transmission measurement results, the input and the output optical signals are detected within a short time interval (less than half a minute) in which changes in polarization in the measurement setup could be neglected. For this reason, a fraction of the input signal is coupled out by a beam-splitter. The light signal is coupled in and out of the chip by two microscope objectives. The light detection system contains a photodetector in combination with optical attenuators (to prevent the saturation of the photodetector) and a lock-in amplifier with a spatial filter (pin-hole) in order to remove the scattered light and light propagating through the film layer outside of the ridge.

The combiner circuit was characterized as follows. First, transmission signals in the interferometric direction (port 1 to 3 and port 2 to 3) were measured as a function of input power. In this direction, the circuit is expected to show switching behavior due to unequal distribution of light over the interferometric arms. Next, transmission signals were measured in the splitter direction (port 3 to 1 and port 3 to 2). In this direction, the device should behave like a splitter because of equal distribution of power over the interferometric arms. By comparing the signals from two opposite directions, all unwanted effects (like e.g. bleaching of the QD absorption) can be excluded.
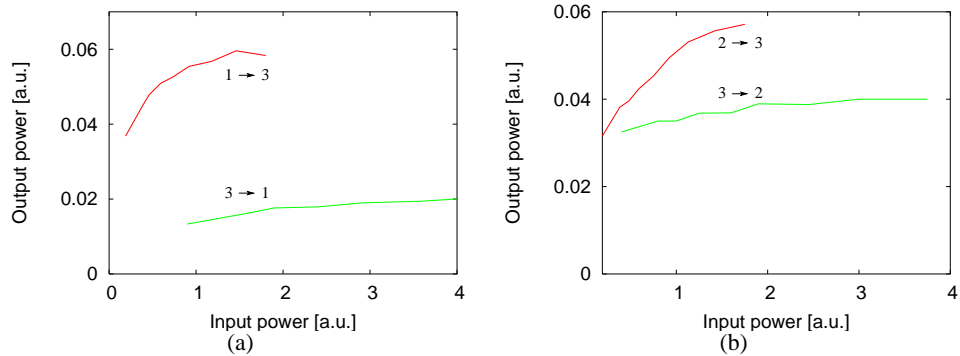
Figure 7.21: Transmission signals as a function of the input power. (a) Ports 1-3, (b) ports 2-3.

Consider a QD-MZI with two 1000-μm-long interferometer arms, placed at a distance of 15 μm from each other. Based on our calculations, presented in section 5.3, the nonlinear switching is expected at the wavelengths longer than the PL peak of the quantum dot distribution ($\sim$ 1520 nm). We have investigated the nonlinear switching at the following three wavelengths: 1530, 1550 and 1570 nm. The wavelengths were chosen to be longer than the absorption peak of the QDs, according to out modeling in subsection 5.3.3. The strongest nonlinear effects were found at a wavelength of 1550 nm.

The measurement results are presented in Fig. 7.21. It can be seen that the transmission curves P_{31} and P_{32} are different. This might possibly be explained by the excitation of the first order mode in the 3-dB output splitter, reported previously in [90], or by a linear phase shift between the interferometer arms due to fabrication imperfections. In the splitter direction, the curves show no sign of interference, but only increase in transmission due bleaching of the QD absorption at higher optical powers, which is also observed for straight waveguides. In the interferometric direction, however, the behavior is quite different. These curves show bending that can only be attributed to a nonlinear switching. In order to single out the interferometric effect, the ratio of the transmission curves measured in opposite directions is shown (Fig. 7.22). These curves are corrected for the optical attenuators.

The graphs in Fig. 7.22 directly show the effect of the nonlinear interference. If the same procedure is applied to a straight waveguide, the result is a horizontal line. This proves that the observed effect is the self-switching.

The maximum improvement of the transmission versus input power is 1.76 dB.
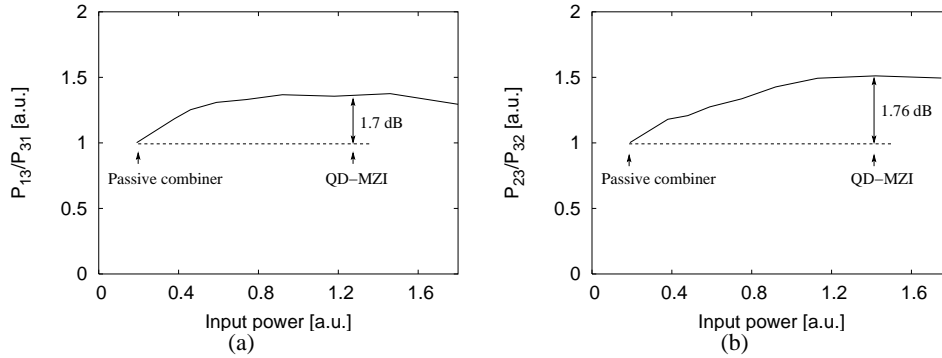
Figure 7.22: Ratios of the transmission signals propagating in the opposite directions. (a) ports 1-3, (b) ports 2-3.

From Fig. 7.22 it is seen that a maximum in the transmission is just reached with the available power. This implies a phase shift between the optical signals from the two arms of more than $\pi/2$ rad. These results are obtained for power levels of a few dBm. This is based on an estimate of coupling losses (3-4 dB) and propagation losses in the chip (3-5 dB).

The QD-MZIs with longer phase shifters have shown poor switching, which could possibly be attributed by the fact that phase shift takes place in the first sections of the phase shifters, and the rest does not contribute to the phase shifting, but only to the absorption.

7.5.3 Conclusions

We have shown a fully passive low-loss optical combiner based on QD-MZI with unequal distribution of the input optical signal. In this device an improvement of up to 1.76 dB is obtained (with respect to a 3 dB-splitter/combiner) in transmission due to all-optical switching. The mechanism of this switching is not yet fully understood. Previous results show that nonlinear effects in InGaAsP or quantum wells (such as the wetting layer in the QD-sample) are much to small to explain the observed effects. Therefore, we attribute the nonlinear switching to the quantum dots. Measurements using signals at two wavelengths, pump-and-probe, will be done in the future to study the dynamics of the non-linear effects in quantum dots. The combiner effect is achieved at input power of a few dBm. The overall losses of the device can be minimized by growing quantum dots selectively only in the phase shifters regions.

7.6 Conclusions

In this chapter, a low-loss optical combiner based on a self-switching Mach-Zehnder interferometer is presented. This device aims to compensate for the inherent loss of the half of the power in a conventional passive power combiner, which is often compensated by using e.g. an in-line SOA. We have realized two types of combiners. The first device uses SOA-based phase shifters, which provide an intensity dependent phase shift. Its realization is based on the active-passive integration technique. The SOA-based combiner provides an improvement of more than 2 dB with respect to a passive combiner, and the measured values are close to the predicted ones. Furthermore, the combiner effect is achieved at low input power levels: a required input power of around 1.2 mW (0.8 dBm) in the input fiber, which is with the correction for the fiber-chip coupling losses (around 4-5 dB per facet) 0.5 mW (-3.2 dBm). Stable operation is obtained. The second device is fully passive, and uses the quantum dot material. An improvement of up to 1.76 dB is obtained at input power of a few dBm. Further investigations are, however, required in order to fully understand the switching mechanisms in quantum dot structures.

Chapter 8

Conclusions and discussion

This chapter summarizes the main conclusions of this thesis. It discusses the future device developments and improvements.

In this thesis we have studied self-switching effects in Mach-Zehnder interferometers. They are based on the unequal distribution of input power over the nonlinear interferometer arms. Switching in these structures is achieved without using control signals. The main conclusions of this thesis are summarized below.

We have shown the applicability of semiconductor optical amplifiers as intensity dependent phase shifters for self-switching, and presented a novel fully passive switching technique based on all-optical nonlinearities in quantum dots. Unlike semiconductor optical amplifiers, the quantum dot based phase shifters cause an intensity dependent phase shift without applying an injection current.

We have developed a fabrication technology and realized a number of applications employing the self-switching effects in Mach-Zehnder interferometers. These applications are: the pattern effect compensator, the 2R-regenerator and the low-loss optical combiner.

The pattern effect compensator and the 2R-regenerator use SOA-based phase shifters. Their realization is based on the active-passive integration technique.

The integrated pattern effect compensator has shown its compensation capabilities for bitrates of up to 20 Gb/s, and in principle does not depend on the bitrate until at least 40 Gb/s. The input power dynamic range of this device at 10 Gb/s is extended by up to 7 dB (with fixed current settings), compared to a single SOA and it provides a gain that is comparable to that of a single SOA. Therefore, the integrated pattern effect compensator can be used as a pattern effect free optical amplifier with an extended input power dynamic range.

The integrated 2R-regenerator has shown its regeneration capabilities for bitrates up to 2.5 Gb/s, which is seen as a noise suppression around the "zero" level. The receiver sensitivity improvement for an input OSNR of 17 dB is 2.5 dB. The maximum bitrate is limited by the recovery time of the amplifiers. By optimally choosing the operating point of the device, the regeneration in the proposed configuration could be combined with pattern-free amplification.

We have developed two types of integrated low-loss optical combiners. In the implementation based on the SOA-phase shifters, an improvement of more than 2 dB with respect to a passive combiner with an in-line SOA is obtained, which is close to the theoretically predicted values. Furthermore, the combiner effect is achieved at low input power levels and shows stable operation. The second implementation is fully passive, and uses the quantum dot material. An improvement of up to 1.76 dB is obtained at input powers of a few dBm. A cascade of low-loss optical combiners can be integrated on one chip (if necessary with other photonic devices) to be used e.g. in passive optical networks, which will have a large improvement of their power budget.

Concluding, we have shown applicability and potential of the self-switching effects in Mach-Zehnder interferometers for optical telecommunication networks. There is, however, room for improvements. First, the Mach-Zehnder interferometers do not provide the output power range (mW-range) required in most applications. This can be improved by further reducing the insertion losses of the device and through optimizing the fiber-chip coupling losses. Furthermore, better quality AR-coated facets will allow to work at higher injection currents, which will result in better nonlinear effects, and higher gain.

Further investigations are required in order to fully understand the switching mechanisms in quantum dots. The overall performance of the passive low-loss optical combiner can be improved by applying the regrowth technique to the quantum dot material, which will allow to grow quantum dots only in the phase shifter sections, reducing the losses in the optical couplers and passive waveguides. Furthermore, QD-based devices should preferably be polarization independent. This could be obtained by optimizing the growth characteristics, or by introducing polarization converting components onto the chip.

Appendix A

Influence of the first-order mode in MMI couplers

The width of the access waveguides of an MMI coupler $w_g = 3$ μm is such that they support not only the zero-, but also higher order modes. The influence of the first-order mode on the performance of the balanced couplers was previously reported in [90]. In this appendix, the influence of the first-order mode on the operation of the unbalanced couplers is discussed.

Based on the general self-imaging properties in MMI couplers, presented in subsection 2.3.2, from Eq. 2.33 for two interfering images with two equal intensities $1/N$ it follows:

$$P_{ij} = \frac{4}{N} \cos^2 \left((N - j)i\frac{\pi}{2N} - b\frac{\pi}{2} \right), \tag{A.1}$$

where i, j are the input and output port numbers[1], $N = 4$ is the number of ports (in a general MMI configuration), $b = 1$ describes symmetrical input field (zero-order mode) and $b = 0$ - asymmetrical input field (first-order mode).

Assuming excitation of only the zero-order mode, the calculated intensity of the resulting image at the 85% output port is 0.854 and at the 15% output port is 0.146 (with input normalized to 1). Excitation of the first-order mode in an access waveguide becomes possible when the input light source is e.g. not centered (displaced) with respect to the access waveguide center. Power fractions in the zero- and first-order modes in this case can be obtained. The influence of each mode can separately be considered.

---

[1]In Eq. A.1, the ports are defined for a general case. Here, $i = 3$ corresponds to the input port, $j = 1$ to the bar-output port, and $j = 3$ - to the cross-output port.

Appendix A. Influence of the first-order mode in MMI couplers

Consider a displacement of 0.9 μm. According to simulations with FIMMWAVE, a power fraction of 0.57 is coupled into the zero-order mode and 0.27 into the first-order mode. Solving Eq. A.1, it can be shown that the total power detected at the 15% output port is higher in the presence of the first-order mode (0.314) as compared to the no-displacement case. Instead, the total power detected at the 85% output port in presence of the both modes, is lower (0.526) as compared to the no-displacement case.

The influence of the first-order mode on the power distribution over the coupler output ports has been qualitatively illustrated using the FIMMWAVE software. In Fig. A.1(a) and Fig. A.1(b) it is shown that a contribution of the first-order mode to the output power detected at the 85% output port is very small and can be neglected. At the 15% output port, however, the first-order mode begins to play a dominant role for input displacement larger than 0.7 μm and reaches its maximum value at a displacement of approximately 1.1 μm.

The total power detected at both output ports is shown in Fig. A.2. Excitation of the first-order mode in access waveguides can thus significantly deteriorate both the coupling ratio of unbalanced MMI couplers. Also the excess losses become higher. Therefore, care should be taken when coupling light into the access waveguides, as well as in the circuit design (when using bends in front of the MMI) to avoid this effect.

In order to verify this theory, the influence of the lateral input displacement and, consequently, of the excitation of the first-order mode on the device performance was measured. It was shown that by increasing the displacement, the total power detected
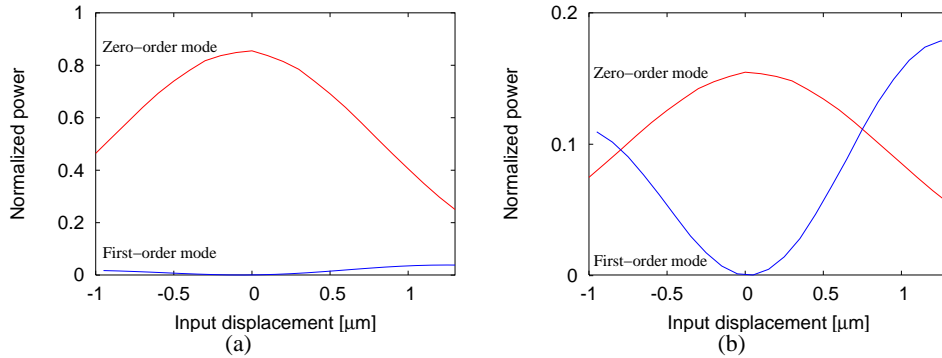
Figure A.1: Power in the zero- and first-order modes as a function of the lateral displacement for the unbalanced MMI coupler. (a) 85% output port, (b) 15% output port.

162
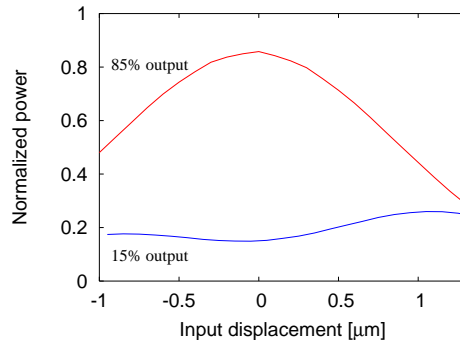
Figure A.2: Total power at each output contained in both modes.

at the 85% output port decreases, whereas the total power detected at the 15% output port increases. Measurements show at approximately 1.1 μm displacement for the 85/15-type MMI coupler, the coupling ratio becomes 0.188 with 1.1 dB excess loss. For the 15/85-type MMI coupler, however, influence of the lateral displacement was less evident. That might be explained by favorable relative phase difference between the zero- and the first-order modes in the access waveguide.

For unbalanced MMI couplers, as suggested by the simulations and confirmed by the measurement results, the correct alignment of the input/output microscope objectives can only be done for the high power output port (in our case 85%). In this case, the maximum power corresponds to the excitation of the zero-order mode in the access waveguides. In the balanced couplers excitation of the first order mode can be avoided by optimizing (equalizing) the output power at both output ports.

Appendix A. Influence of the first-order mode in MMI couplers

Bibliography

[1] Jeff Hecht, *City of Light: The Story of Fiber Optics (Sloan Technology Series)*, Oxford University Press, New York, 1999, ISBN 0-19-510818-3.

[2] P. Nachman, "Mach-Zehnder interferometer as an instructional tool," *American Journal of Physics*, vol. 63, no. 1, pp. 39–43, Jan. 1995.

[3] R.G. Broeke, *A Wavelength Converter Integrated with a Discretely Tunable Laser for Wavelength Division Multiplexing Networks*, Ph.D. thesis, Delft University of Technology, Delft, The Netherlands, 2003.

[4] Juerg Leuthold, Pierre-Andre Besse, Emil Gamper, Marcus Dülk, Stefan Fischer, Georg Guekos, and Hans Melchior, "All-optical Mach-Zehnder interferometer wavelength converters and switches with integrated data- and control-signal separation scheme," *J. Lightwave Technol.*, vol. 17, no. 6, pp. 1056–1065, June 1999.

[5] M.L. Masanovic, E.J. Skogen, J.S. Barton, V. Lal, D.J. Blumenthal, and L.A. Coldren, "Demonstration of monolithically-integrated InP widely-tunable laser and SOA-MZI wavelength converter," in *Proc. IPRM03 conference*, May 12–16 2003, pp. 289–291.

[6] H.P. Zappe, *Introduction to Semiconductor Integrated Optics*, Artech House, London, 1995.

[7] T. Uitterdijk, *Integrated Electro-Optical Switches On InP*, Ph.D. thesis, Delft University of Technology, Delft, The Netherlands, 1997, ISBN 90-9010549-2.

[8] D.H.P. Maat, *InP-based integrated MZI switches for optical communications*, Ph.D. thesis, Delft University of Technology, Delft, The Netherlands, 2001, ISBN 90-9014700-4.

Bibliography

[9] H.G. Bach, J. Krauser, H.P. Nolting, R.A. Logan, and F.K. Reinhart, "Electro-optical light modulation in InGaAsP/InP double heterostructures diodes," *Appl. Phys. Lett.*, vol. 42, no. 8, pp. 692–694, 1983.

[10] R. Prasanth, J.E.M. Haverkort, and J.H. Wolter, "Compact Mach-Zehnder space switch combining bandfilling and the Quantum Confined Stark Effect," in *Proc. IEEE/LEOS Symposium (Benelux Chapter)*. Dec. 2001, Brussels, Belgium.

[11] D.A.B Miller, J.S. Weiner, and D.S. Chemla, "Electric-field dependence of linear optical properties in quantum well structure: Waveguide electroabsorption and sum rules," *IEEE J. Quantum Electron.*, vol. 22, no. 9, pp. 1816–1830, Sept. 1986.

[12] S. Schmitt-Rink, C. Ell, and H. Haug, "Many-body effects in the absorption, gain, and luminescence spectra of semiconductor quantum-well structures," *Phys. Rev. B*, vol. 33, no. 2, pp. 1183–1189, Jan. 1986.

[13] EMIS Datareviews Series No. 6, *Properties of Indium Phosphide*, INSPEC, London and New York, 1991, ISBN 0-85296-491-9.

[14] H. Temkin, V. G. Keramidas, M.A. Pollack, and W.R. Wagner, "Temperature dependence of photoluminescence of n-InGaAsP," *J. Appl. Phys.*, vol. 52, no. 3, pp. 1574–1578, Mar. 1981.

[15] J.J.G.M. van der Tol, "An optical combiner with low loss," in *Proc. IEEE/LEOS Symposium (Benelux Chapter)*. Nov. 1999, pp. 69–72, Mons, Belgium.

[16] G.P. Agrawal, *Fiber-optic communication systems*, Chichester : Wiley-Interscience, 2002.

[17] K. Inoue, "Waveform distortion in a gain-saturated semiconductor optical amplifier for NRZ and Manchester formats," *IEE Proc.-Optoelectron.*, vol. 144, no. 6, pp. 433–437, Dec. 1997.

[18] L. Wosinski, "Silica-on-silicon technology for photonic integrated devices," in *Proc. 6th International Conference on Transparent Optical Networks*, July 2004, pp. 274–279.

[19] G. Beelen, P. Linders, C.G.H. Roeloffzen, A. Driessen, M.B.J. Diemeer, X.J.M. Leijtens, A.F. Bakker, and A.J.T. de Krijger, "First polymer-based reconfigurable add-drop multiplexer," in *Proc. 25th Eur. Conf. on Opt. Comm. (ECOC '99), postdeadline papers*. Sep. 26–30 1999, pp. 58–59, Nice, France.

[20] L. Arizmendi, "Photonic applications of lithium niobate crystals," *Phys. Stat. Sol.*, vol. 201, no. 2, pp. 253–283, Jan. 2004.

[21] P.J. Harmsma, *Integration of Semiconductor Optical Amplifiers in Wavelength Division Multiplexing Photonic Integrated Circuits*, Ph.D. thesis, Delft University of Technology, Delft, The Netherlands, 2000, ISBN 90-9014315-7.

[22] C. Kittel, *Introduction to solid state physics*, Wiley, 1996.

[23] Jr. Peter S. Zory, *Quantum well lasers*, Academic press, London, 1993, ISBN 0-12-781890-1.

[24] D.A.B. Miller, "Optoelectronic applications of quantum wells," *Optics & Photonics News*, vol. 1, no. 2, pp. 7–15, Feb. 1995.

[25] R. Prasanth, *Photonic switching in III/V nanostructures*, Ph.D. thesis, Technische Universiteit Eindhoven, Eindhoven, The Netherlands, 2004, ISBN 90-386-1895-6.

[26] R. Loudon, *The quantum theory of light*, Clarendon Press, Oxford, 1981, ISBN 0-19-851149-3.

[27] F. Fiedler and A. Schlachetzki, "Optical parameters of InP-based waveguides," *Solid State Electron.*, vol. 30, no. 1, pp. 73–83, 1987.

[28] M.S. Stern, P.C. Kendall, R.C. Hewson-Browne, P.N. Robson, and D.A. Quinney, "Scattering loss from rough sidewalls in semiconductor rib waveguides," *Electron. Lett.*, vol. 25, no. 18, pp. 1231–1232, Aug. 1989.

[29] L.H. Spiekman, *Compact Integrated Optical Components for Telecommunication Networks*, Ph.D. thesis, Delft University of Technology, Delft, The Netherlands, 1996, ISBN 90-9009718-X.

[30] H.G. Unger, *Planar optical waveguides and fibres*, Clarendom press, Oxford, 1977.

[31] K.S. Chiang, "Performance of the effective-index method for analysis of dielectric waveguides," *Opt. Lett.*, vol. 16, no. 10, pp. 714–716, Oct. 1991.

[32] J. Buus, "The effective index method and its application to semiconductor lasers," *IEEE J. Quantum Electron.*, vol. 18, no. 7, pp. 1083–1089, July 1982.

[33] L.B. Soldano and E.C.M. Pennings, "Optical multi-mode interference devices based on self-imaging: Principles and applications," *J. Lightwave Technol.*, vol. 13, no. 4, pp. 615–627, Apr. 1995.

[34] P.A. Besse, M. Bachmann, H. Melchior, L.B. Soldano, and M.K. Smit, "Optical bandwidth and fabrication tolerances of multimode interference couplers," *J. Lightwave Technol.*, vol. 12, no. 6, pp. 1004–1009, June 1994.

[35] M. Bachmann, M.K. Smit, P.A. Besse, E. Gini, H. Melchior, and L.B. Soldano, "Polarization-insensitive low-voltage optical waveguide switch using InGaAsP/InP four-port Mach-Zehnder interferometer," in *Techn. Digest Opt. Fiber Comm. (OFC '93), Vol. 4.* Feb. 21–26 1993, pp. 32–33, San Jose, California, USA.

[36] Lucas B. Soldano, Frank B. Veerman, Meint K. Smit, Bastiaan H. Verbeek, Alain H. Dubost, and Erik C.M. Pennings, "Planar monomode optical couplers based on multimode interference effects," *J. Lightwave Technol.*, vol. 10, no. 12, pp. 1843–1849, Dec. 1992.

[37] M. Bachmann, P.A. Besse, and H. Melchior, "General self-imaging properties in $N \times N$ multimode interference couplers including phase relations," *Appl. Opt.*, vol. 33, no. 18, pp. 3905–3911, June 1994.

[38] M. Bachmann, P.A. Besse, and H. Melchior, "Overlapping-image multimode interference couplers with a reduced number of self-images for uniform and nonuniform power splitting," *Appl. Opt.*, vol. 34, no. 30, pp. 6898–6910, Oct. 1995.

[39] B.H. Bransden and C.J. Joachain, ," in *Introduction to quantum mechanics.* 1993, Addison-Wesley Pub Co.

[40] J.J.M. Binsma, P.J.A. Thijs, T. van Dongen, E.J. Jansen, A.A.M. Staring, G.N. van den Hoven, and L.F. Tiemeijer, "Characterization of butt-joint InGaAsP waveguides and their application to 1310 nm DBR-type MQW gain-clamped semiconductor optical amplifiers," *IEICE Trans. Electron.*, vol. E80-C, pp. 675–681, 1997.

[41] J.J.M. Binsma, "Waveguide coupling concepts for InP photonic integrated circuits," in *Proc. 8th Eur. Conf. on Integr. Opt. (ECIO '97).* April 2–4 1997, pp. 522–527, Stockholm, Sweden.

[42] J.J.M. Binsma, M. van Geemert, F. Heinrichsdorff, T. van Dongen, R.G. Broeke, and M.K. Smit, "MOVPE waveguide regrowth in InGaAsP/InP with extremely low butt joint loss," in *Proc. IEEE/LEOS Symposium (Benelux Chapter)*. Dec. 2001, pp. 245–248, Brussels, Belgium.

[43] J.J.M. Binsma, R.G. Broeke, and J.H. den Besten, "InP-based photonic integration technology," in *Technical Digest Integr. Photon. Res. (IPR '04)*. Jun. 30–Jul. 2 2004, p. IFB1, San Francisco, USA, Invited paper.

[44] Y. Barbarin, E.A.J.M. Bente, C. Marquet, E.J.S. Lecère, T. de Vries, P.J. van Veldhoven, Y.S. Oei, R. Nötzel, M.K. Smit, and J.J.M. Binsma, "Butt-joint reflectivity and loss in InGaAsP/InP waveguides," in *Proc. 12th Eur. Conf. on Int. Opt. (ECIO '05)*. April 6–8 2005, pp. 406–409, Grenoble, France.

[45] Q. Gong, R. Nötzel, P.J. van Veldhoven, T.J. Eijkemans, and J.H. Wolter, "Wavelength tuning of InAs quantum dots grown on InP (100) by chemical-beam epitaxy," *Appl. Phys. Lett.*, vol. 84, no. 2, pp. 275–277, Jan. 2004.

[46] J.E.M. Haverkort, R. Prasanth, S. Dilna, E.W. Bogaart, J.J.G.M. van der Tol, E.A. Patent, G. Zhao, Q. Gong, P.J. van Veldhoven, R. Nötzel, and J.H. Wolter, "Photonic switching in InAs/InP quantum dots," in *2004 4th IEEE Conference on Nanotechnology*. Aug. 2004, pp. 86–88, Munich, Germany.

[47] Y.S. Oei, L.H. Spiekman, F.H. Groen, I. Moerman, E.G. Metaal, and J.W. Pedersen, "Novel RIE-process for high quality InP-based waveguide structures," in *Proc. 7th Eur. Conf. on Integr. Opt. (ECIO '95)*. April 3–6 1995, pp. 205–208, Delft, The Netherlands.

[48] U. Niggebrügge, M. Klug, and G. Garus, "A novel process for reactive ion etching on InP, using CH4/H2," in *Inst. Phys. Conf. Ser. No 79*, 1986, pp. 367–372.

[49] T.R. Hayes, M.A. Dreisbach, W.C. Dautremont-Smith P.M. Thomas, and L.A. Heimbrook, "Reactive ion etching of InP using CH_4/H_2 mixtures: Mechanisms of etching and anisotropy," *J. Vac. Sci. Technol. B*, vol. 7, no. 5, pp. 1130–1140, Sept. 1989.

[50] Y.S. Oei, C. van Dam, F.P. van Ham, L.H. Spiekman, B.H. Verbeek, F.H. Groen, E.G. Metaal, and J.W. Pedersen, "Improved RIE technique for controlled roughness and anisotropy in InP based devices," in *Proc. SOTAPOCS XVIII*. May 16–21 1993, pp. 134–141, Honolulu, Hawaii.

Bibliography

[51] J.H. den Besten, *Integration of Multiwavelength Lasers with Fast Electro-Optical Modulators*, Ph.D. thesis, Technische Universiteit Eindhoven, Eindhoven, The Netherlands, 2004, ISBN 90-386-1643-0.

[52] Jan Gerard van Hassel, *Dry processing of GaAs-based MESFETs and pseudo-morphic HFETs*, Ph.D. thesis, Technische Universiteit Eindhoven, Eindhoven, The Netherlands, 1995.

[53] J.J.G.M. van der Tol, M. Silova, F Karouta, R.G. Broeke, H.H. Tan, C. Jagadish, E. Smalbrugge, and B.H. v. Roy, "InP-based waveguides: comparison of ECR plasma etching and wet-chemical etching," in *Proc. IEEE/LEOS Symposium (Benelux Chapter)*. Nov. 2000, pp. 127–130, Delft, the Netherlands.

[54] X.J.M. Leijtens, P. Le Lourec, and M.K. Smit, "S-matrix oriented CAD-tool for simulating complex integrated optical circuits," *J. of Sel. Topics in Quantum Electron.*, vol. 2, no. 2, pp. 257–262, June 1996.

[55] J.J.G.M. van der Tol, R.G. Broeke, and X.J.M.Leijtens, "Low -loss integrated optical combiner based on semiconductor optical amplifiers.," in *Proc. SAFE*, Nov. 2000.

[56] A.Sv. Sudbo, "Film mode matching: a versatile numerical method for vector mode field calculations in dielectric waveguides," *Pure Appl. Opt.*, vol. 2, pp. 211–233, 1993.

[57] S. Adachi, *Physical properties of III-V semiconductor compounds*, John Wiley and Sons, New York, 1992.

[58] L.B. Soldano, *Multimode Interference Couplers. Design and Applications*, Ph.D. thesis, Delft University of Technology, Delft, The Netherlands, 1994, ISBN 90-407-1044-9.

[59] F. Girardin, G. Guekos, and A. Houbavlis., "Gain recovery of bulk semiconductor optical amplifiers," *IEEE Photon. Technol. Lett.*, vol. 10, no. 6, pp. 784–786, June 1998.

[60] Juerg Leuthold, *Advanced Indium-Phosphide waveguide Mach-Zehnder interferometer all-optical switches and wavelength converters*, Hartung-Gorre Verlag, Konstanz, Germany, 1999, ISBN 3-89649-427-9.

[61] G.H.B. Thompson, *Physics of semiconductor Laser Devices*, John Wiley & Sons, 1985, ISBN 0-471-27685-5.

[62] D.C. Hutchings, M. Sheik-Bahae, D.J. Hagan, and E.W. van Stryland, "Kramers-Krönig relations in nonlinear optics," *Opt. and Quantum Electron.*, vol. 24, no. 1, pp. 1–30, Jan. 1992.

[63] Laurent Schares, Colja Schubert, Carsten Schmidt, Hans G. Weber, Lorenzo Occhi, and George Guekos, "Phase dynamics of semiconductor optical amplifiers at 10-40 GHz," *IEEE J. Quantum Electron.*, vol. 39, no. 11, pp. 1394–1408, Nov. 2003.

[64] Lorenzo Occhi, Laurent Schares, and George Guekos, "Phase modeling based on the α-factor in bulk semiconductor optical amplifiers," *IEEE J. Sel. Topics in Quantum Electron.*, vol. 9, no. 3, pp. 788–797, May/June 2003.

[65] G. Zhao, E.A. Patent, and J.J.G.M. van der Tol, "Modeling of optical nonlinearities based on engineering the semiconductor band," *Materials Science in Semiconductor Processing*, vol. 6, no. 1–3, pp. 153–158, Feb.–Jun. 2003.

[66] D.A.B. Miller, *Confined Electronics and Photons*, chapter Quantum well optical switching devices, pp. 675–701, Plenum Press, New York, 1995.

[67] D.S. Chemla, D.A.B. Miller, P.W. Smith, A.C. Gossard, and W. Wiegmann, "Room temperature excitonic nonlinear absorption and refraction in GaAs/AlGaAs multiple quantum well structures," *IEEE J. Quantum Electron.*, vol. 20, no. 3, pp. 265–275, Mar. 1984.

[68] S. Schmitt-Rink, D.S. Chemla, and D.A.B. Miller, "Theory of transient excitonic optical nonlinearities in semiconductor quantum-well structures," *Phys. Rev. B*, vol. 32, no. 10, pp. 6601–6609, Nov. 1985.

[69] R. Prasanth, J.E.M. Haverkort, A. Deepthy, E.W. Bogaart, J.J.G.M. van der Tol, E.A. Patent, G. Zhao, Q. Gong, P.J. van Veldhoven, R. Noetzel, and J.H. Wolter, "All-optical switching due to state filling in quantum dots," *Appl. Phys. Lett.*, vol. 84, no. 20, pp. 4059–4061, May 2004.

[70] D. Birkedal, J. Bloch, J. Shah, L.N. Pfeiffer, and K. West, "Femtosecond dynamics and absorbance of self-organized InAs quantum dots emitting near 1.3 μm at room temperature," *Appl. Phys. Lett.*, vol. 77, no. 14, pp. 2201–2203, Oct. 2000.

[71] G.E. Keiser, *Optical fiber communications*, London : McGraw-Hill, 2000.

[72] Jesper Mørk, Mads L. Nielsen, and Tommy W. Berg, "The dynamics of semiconductor optical amplifiers. modeling and applications," *Optics & Photonics News*, vol. 14, no. 7, pp. 42–48, July 2003.

[73] J.A. Constable, I.H. White, A.N. Coles, and D.G. Cunningham, "Reduction of harmonic distortion and noise in a semiconductor optical amplifier using bias current feedback," *Electron. Lett.*, vol. 29, no. 23, pp. 2042–2044, Nov. 1993.

[74] G. Soulage, P. Doussiere, A. Jourdan, and M. Sotom, "Clamped gain travelling wave semiconductor optical amplifier as a large dynamic range gate," in *Proc. 20th Eur. Conf. on Opt. Comm. (ECOC '94)*, 1994, pp. 451–454.

[75] L. Lablonde, I. Valiente, P. Lamouler, E.D. Delavaque, S. Boj, and C. Simon, "Experimental and theoretical investigation of a gain clamped semiconductor optical amplifier," in *Proc. 20th Eur. Conf. on Opt. Comm. (ECOC '94)*, 1994, pp. 715–718.

[76] D. Wolfson, S.L. Danielsen, C. Joegensen, B. Mikkelsen, and K.E. Stubkjaer, "Detailed theoretical investigation of the input power dynamic range for gain-clamped semiconductor optical amplifier gates at 10Gb/s," *IEEE Photon. Technol. Lett.*, vol. 10, no. 9, pp. 1241–1243, Sept. 1998.

[77] Qianfan Xu, Minyu Yao, Yi Dong, Wenshan Cai, and Jianfeng Zhang, "Experimental demonstration of pattern effect compensation using an asymmetrical Mach-Zehnder interferometer with SOAs," *IEEE Photon. Technol. Lett.*, vol. 13, no. 12, pp. 1325–1327, Dec. 2001.

[78] M.J.R. Heck, E.A.J.M. Bente, Y. Barbarin, D. Lenstra, and M.K. Smit, "Simulation of mode-locked ring lasers including integrated passive components for dispertion compensation," in *Proc. IEEE/LEOS Symposium (Benelux Chapter)*. Dec. 2004, pp. 159–162, Ghent, Belgium.

[79] R.G.M.P. Koumans and R. van Roijen, "Theory for passive mode-locking in semiconductor laser structures including the effects of self-phase modulation, dispersion and pulse collisions," *IEEE J. Quantum Electron.*, vol. 32, no. 3, pp. 478–492, Mar. 1996.

[80] J.J.G.M. van der Tol, H. de Waard, and Y. Liu, "A Mach-Zehnder-Interferometer-based low-loss combiner," *IEEE Photon. Technol. Lett.*, vol. 13, no. 11, pp. 1197–1199, Nov. 2001.

[81] E.A. Patent, J.J.G.M. van der Tol, N. Calabretta, and Y. Liu, "A pattern effect compensator," in *Proc. IEEE/LEOS Symposium (Benelux Chapter)*. Dec. 2001, pp. 233–236, Brussels, Belgium.

[82] Mads L. Nielsen, *Experimental and theoretical investigation of Semiconductor Optical Amplifier (SOA) based all-optical switches*, Ph.D. thesis, DTU, Denmark, 2004, ISBN 87-90974-53-0.

[83] Filip Öhman, Svend Bischoff, Bjarne Tromborg, and Jesper Mørk, "Noise and regeneration in semiconductor waveguides with saturable gain and absorption," *IEEE J. Quantum Electron.*, vol. 40, no. 3, pp. 245–255, Mar. 2004.

[84] J. De Merlier, G. Morthier, T, Van Caenegem, R. Baets, and I. Moerman, "Experimental demonstration of 15 dB extinction ratio improvement in a new 2R optical regenerator based on MMI-SOA," in *Proc. 27th Eur. Conf. on Opt. Comm. (ECOC '01)*. 2001, pp. 574–575, Amsterdam, The Netherlands.

[85] D. Wolfson, A. Kloch, T. Fjelde, C. Janz, B. Dagens, and M. Renaud, "40-Gb/s all-optical wavelength conversion, regeneration, and demultiplexing in an SOA-based all-active Mach-Zehnder interferometer," *IEEE Photon. Technol. Lett.*, vol. 12, no. 3, pp. 332–334, Mar. 2000.

[86] Sam Verspurten, Jan De Merlier, Geert Morthier, Dries Van Thourhout, and Roel Baets, "All-optical SOA-based 2R regeneration at 10 Gb/s in a MZI-configuration with one active arm," in *Proc. of Opt. Ampl. and their Appl.* Jun. 30–Jul. 2 2004, p. JWB13, San Francisco, USA.

[87] G.J.M. Krijnen, H.J.W.M. Hoekstra, P.V. Lambeck, and T.J.A. Popma, "Simulations of low insertion loss nonlinear Y-junction," in *Proc. Sensors and Actuators Symposium*. Nov. 1990, pp. 323–328, Enschede, The Netherlands.

[88] K. Tajima, S. Nakamura, and Y. Ueno, "Femtosecond all-optical switching using efficient incoherent nonlinearity with slow relaxation," *Material Science and Engineering*, vol. B48, no. 1–2, pp. 88–93, Aug. 1997.

[89] I. Van de Voorde, C.M. Martin, J. Vandewege, and X.Z. Qiu, "The superPON demonstrator: and exploration of possible evolution paths for optical access networks," *IEEE Comm. Magazine*, vol. 38, no. 2, pp. 74–82, Feb. 2000.

[90] C. Vazquez, C. Aramburu, J.M. Pena, and Manuel Lopez-Amo, "Accessing guides first order mode influence and optimize tolerances in multimode inter-

ference couplers," *Proc. SPIE International Conference on Applications of Photonic Technology III: Closing the Gap between Theory, Development, and Applications*, vol. 3491, pp. 386–391, Dec. 1998.

List of abbreviations

AFM	Atomic Force Microscopy
AR	Anti Reflection
ASE	Amplified Spontaneous Emission
ATT	ATTenuator
BER	Bit Error-Rate
BPF	BandPass Filter
CBE	Chemical Beam Epitaxy
COBRA	COmmunication technologies, Basic Research and Applications
CW	Continuous Wave
DBR	Distributed Bragg Reflector
DC	Direct Current
ECL	Extended Cavity Laser
ECR	Electron-Cyclotron Resonance
EDFA	Erbium Doped-Fiber Amplifier
FP	Fabry-Pérot
GC-SOA	Gain-Clamped Semiconductor Optical Amplifier
ICP	Inductively Coupled Plasma
IPDR	Input Power Dynamic Range
ITU	International Telecommunication Union
MMI	MultiMode Interference
MO	Microscope Objective
MOCVD	Metal-Organic Vapor-Phase Epitaxy
MZI	Mach-Zehnder Interferometer
NRZ	Non Return-to-Zero
O-E-O	Optical-Electrical-Optical
OSNR	Optical Signal-to-Noise Ratio
OTDM	Optical Time-Division Multiplexing

List of abbreviations

PECVD	Plasma-Enhanced Chemical Vapor Deposition
PIC	Photonic Integrated Circuit
PL	PhotoLuminescence
PMF	Polarization Maintaining Fiber
PON	Passive Optical Network
PPG	Pulse Pattern Generator
QSCE	Quantum Confined Stark Effect
QD	Quantum Dot
QW	Quantum Well
RF	Radio Frequency
RIE	Reactive Ion Etching
SDH	Synchronous Digital Hierarchy
SEM	Scanning Electron Microscope
SOA	Semiconductor Optical Amplifier
SONET	Synchronous Optical NETwork
SPM	Self-Phase Modulation
STW	Stichting voor de Technische Wetenschappen
TE	Transverse Electric
TEC	Thermo-Electric Controller
TLS	Tunable Laser Source
TM	Transverse Magnetic
TU/e	Technische Universiteit Eindhoven
WDM	Wavelength-Division Multiplexing

Summary

OPTICAL SELF-SWITCHING EFFECTS IN MACH-ZEHNDER INTERFEROMETERS

Development of modern optical fiber networks puts an increasing demand on the optical hardware. All-optical signal processing components enable the highest switching rates and allow all-optical regeneration of pulse streams without converting the optical signal into electrical current. The subject of our research is self-switching in a Mach-Zehnder interferometer (MZI) and its applications in optical telecommunication networks. In this device, light injected in one of the input ports is unequally distributed over the two interferometer arms. Due to the intensity dependent refractive index in the interferometer arms, there can be a nonlinear phase shift induced between the optical signals of unequal intensities. The two signals therefore interfere destructively or constructively depending on the input power: in this way we obtain nonlinear self-switching. Two mechanisms of nonlinear phase shifting were considered: active, based on semiconductor optical amplifiers (SOAs), and passive, based on quantum dots (QDs). Interferometers of two types were developed: 2-to-2 (two input ports and two output ports) and 2-to-1 (two input ports and one output port).

The 2-to-2 SOA-MZIs based on self-switching have been investigated for two applications. One of them is the pattern effect compensator. If SOAs are employed for all-optical signal amplification, e.g. in optical access networks, an unwanted pulse distortion (known also as the pattern effect) takes place, as a result of the SOA gain saturation. Our component allows pattern-free amplification of the optical signals at bitrates up to 20 Gb/s. At 10 Gb/s it shows an extended input power range (up to 7 dB improvement) and comparable gain, which makes it suitable to be used as an optical amplifier. Another application of the 2-to-2 SOA-MZI is a 2R-regenerator. Optical amplifiers used in long distance optical links add noise to the optical signal, causing signal degradation. The signal can be regenerated by passing it through an optical gate with a nonlinear transfer function. The 2-to-2 SOA-MZI has such a nonlinear transfer function. The regeneration capabilities were demonstrated at 2.5 Gb/s by an

Summary

improvement of the receiver sensitivity of about 2.5 dB. The dynamic characterization of the chips was carried out in a close cooperation with the research group COM at the Technical University of Denmark within the ePIXnet "network of excellence".

The 2-to-1 MZI based on self-switching can be used as a low-loss optical combiner. An essential function in optical fiber networks is the combining of optical signals. A serious disadvantage of the conventional type of combiners used in the networks is that they let only half of the power (3 dB) through. In order to compensate for this loss, passive optical combiners are often used in combination with an in-line SOA. The first realization of the low-loss optical combiner uses SOAs as active phase shifters. Such an active low-loss combiner shows an improvement of transmission of over 2 dB compared to a conventional combiner with an in-line SOA. It is therefore expected that the output optical signal-to-noise ratio of the self-switching SOA-MZI is more than 2 dB better than that of a conventional combiner with an in-line SOA. While for the pattern effect compensator and the 2R-regenerator SOAs are used not only for inducing the nonlinear phase shift, but also for sufficient amplification, for the low-loss optical combiner the preferred nonlinear effects should be passive: combination of the signal is a passive function. Therefore, the second realization is based on a novel material, quantum dots. QDs provide improved all-optical nonlinearities resulting in a very small switching energy and large refractive index changes. Such a passive 2-to-1 QD-MZI based on self-switching showed an improvement up to 1.7 dB with respect to a conventional combiner. These improvements have a huge effect on e.g. the power budget in passive optical networks, where a large number of splitting stages are required.

The Mach-Zehnder interferometers were realized in the InP/InGaAsP semiconductor material system, which is perfectly suitable for the integration of the photonic integrated circuits for the telecommunication applications. In order to realize both active components (such as e.g. SOAs) and passive components (such as e.g. waveguides, couplers), an active-passive integration technique was applied. This integration was realized in a close cooperation between JDS Uniphase Eindhoven and the COBRA Research Institute. It employs a three-step metal-organic vapor-phase epitaxy regrowth process. The quantum dot material was grown within the COBRA Research Institute. Our MZIs use a ridge waveguide design, for which a reactive ion etching process was developed in the COBRA cleanroom. As a result of photonic integration our integrated Mach-Zehnder interferometers have very small dimensions: less than a square millimeter.

Evgeni Patent.

178

Samenvatting

OPTISCHE ZELF-SCHAKEL EFFECTEN IN MACH-ZEHNDER INTERFEROMETERS

Ontwikkeling van de hedendaagse optische glasvezelnetwerken leidt tot een stijgende behoefte aan optische apparatuur. De optische componenten voor signaalverwerking laten de hoogste schakelsnelheden toe en regeneratie van pulsstromen zonder het optische signaal in een elektrisch om te zetten. Het onderwerp van dit onderzoek is zelfschakeling in een Mach-Zehnder interferometer (MZI) en de toepassingen daarvan in optische telecommunicatienetwerken. In deze component wordt het lichtsignaal ongelijk verdeeld over de twee takken van de interferometer. Wegens de intensiteits-afhankelijke brekingsindex in de interferometertakken kan er een niet-lineaire fase-verschuiving ontstaan tussen de twee optische signalen van ongelijke intensiteit. Deze twee signalen interfereren vervolgens destructief of constructief, afhankelijk van het ingangsvermogen: op deze manier wordt niet-lineaire zelfschakeling verkregen. Twee mechanismen voor de niet-lineaire faseverschuiving zijn onderzocht: actief, gebaseerd op halfgeleider optische versterkers (HOVs) en passief, gebaseerd op quantum doosjes (QDs). Twee types interferometers zijn ontwikkeld: 2-naar-2 (twee ingangs- en twee uitgangspoorten) en 2-naar-1 (twee ingangs- en een uitgangspoort).

De 2-naar-2 HOV-MZIs gebaseerd op zelfschakeling zijn onderzocht voor twee toepassingen. Een daarvan is de patrooneffect-compensator. Wanneer halfgeleider optische versterkers gebruikt worden voor de versterking van optische pulsen, bij-voorbeeld in optische aansluitnetwerken, vindt een ongewenste pulsvervorming (die ook als patrooneffect bekend staat) plaats, als resultaat van de verzadiging van de versterker. Onze component toont patrooneffect-vrije optische versterking bij bitsnel-heden tot 20 Gb/s. Bij een bitsnelheid van 10 Gb/s kan deze component met hogere ingangsvermogens werken (tot 7 dB hoger) zonder ongewenste pulsvervorming, ter-wijl de totale versterking vergelijkbaar is met die van een gewone versterker. Daarom kan de component gebruikt worden als een patrooneffect-vrije versterker. Een andere toepassing van de 2-naar-2 HOV-MZI is een 2R-regenerator. Optische versterkers die

gebruikt worden in optische netwerken op lange afstanden voegen ruis aan het signaal toe. Als gevolg daarvan degradeert het optische signaal. Het signaal kan worden geregenereerd als het door een optische poort gaat met een niet-lineaire overdrachtsfunctie. Onze 2-naar-2 HOV-MZI heeft een dergelijke niet-lineaire overdrachtsfunctie. De potentie voor regeneratie werd aangetoond op 2.5 Gb/s, waarbij de ontvangersgevoeligheid ongeveer 2.5 dB beter werd. De dynamische metingen aan deze componenten zijn gedaan in nauwe samenwerking met de onderzoeksgroep COM binnen het ePIXnet "network of excellence".

De 2-naar-1 MZI gebaseerd op zelfschakeling kan gebruikt worden als een verliesarme optische signaalsamenvoeger. Combinatie van optische signalen in glasvezelnetwerken is een essentiële functie. Een ernstig nadeel van het conventionele type signaalsamenvoeger die in de netwerken wordt gebruikt is dat hij slechts de helft van het vermogen (dus 3 dB) doorlaat. Om dit verlies tegen te gaan wordt een conventionele signaalsamenvoeger vaak gebruikt in combinatie met een in-lijn optische versterker. De eerste realisatie van de verliesarme signaalsamenvoeger gebruikt HOVs als actieve fasedraaiers. Zo'n actieve signaalsamenvoeger toont een verbetering van transmissie met meer dan 2 dB in vergelijking met een conventionele signaalsamenvoeger met een in-lijn versterker. Het is daarom te verwachten dat de signal-ruis verhouding van het uitgangssignaal van de zelfschakelende 2-naar-1 HOV-MZI meer dan 2 dB beter is dan bij een conventionele signaalsamenvoeger in combinatie met een versterker. Terwijl voor een patrooneffect-compensator en een 2R regenerator de versterkers hoofdzakelijk worden gebruikt om niet-lineaire faseverschuiving te introduceren en om het signaal te versterken, wordt voor de verliesarme optische signaalsamenvoeger bij voorkeur een passieve faseverschuivingmechanisme gebruikt: signaalsamenvoeging is namelijk een passieve functie. De tweede realisatie is daarom gebaseerd op het nieuwe materiaal, quantum doosjes. QD's vertonen betere optische niet-lineaire eigenschappen resulterend in een zeer kleine schakelenergie en grote brekingsindexveranderingen. De passieve 2-naar-1 zelfschakelende QD-MZI toont een verbetering van 1.7 dB in vergelijking met een passieve samenvoeger. Deze verbeteringen hebben een groot effect op bijvoorbeeld het vermogensbudget in passieve optische netwerken, waar een groot aantal signaalsamenvoegers wordt vereist.

Al deze Mach-Zehnder interferometers zijn gemaakt in het InP/InGaAsP halfgeleider-materiaalsysteem, dat voor de integratie van fotonisch geïntegreerde circuits voor telecommunicatietoepassingen uitstekend geschikt is. Om zowel actieve componenten (zoals b.v. HOVs) als passieve componenten (zoals b.v. golfgeleiders, koppelaars) op een chip te realiseren, werd een actief-passieve integratietechniek toegepast. Deze integratie werd gerealiseerd in nauwe samenwerking tussen JDS Uniphase Eindhoven en het onderzoeksinstituut COBRA. Het maakt gebruik van een driestaps her-

groeiproces m.b.v. metaal-organisch dampfase epitaxie. Het quantumdoosjesmateriaal werd gegroeid binnen het onderzoeksinstituut COBRA. De kanaalgolfgeleiders in onze MZIs zijn gerealiseerd met een reactief ionenetsproces ontwikkeld in de COBRA-stofarme ruimte. Als resultaat van de fotonische integratie hebben onze geïntegreerde Mach-Zehnder interferometers zeer kleine afmetingen: slechts enkele vierkante millimeters.

Evgeni Patent.

Dankwoord

Na vier jaar promotieonderzoek en het schrijven van dit proefschrift ben ik heel blij om uiteindelijk dit dankwoord te kunnen schrijven. Wanneer u op deze pagina bent gearriveerd na eerst alle voorgaande te hebben gelezen zult u begrijpen dat ik nooit zover had kunnen komen zonder de hulp en inspiratie van anderen, die ik hieronder dan ook van harte wil bedanken.

Allereerst is het mij een genoegen en een voorrecht om mijn eerste promotor, Meint Smit, te mogen bedanken voor zijn wetenschappelijke begeleiding, hulp en, uiteraard, voor de mogelijkheid om dit onderzoek te mogen en kunnen verrichten. Uiteraard heeft mijn dagelijkse begeleider en copromotor Jos van der Tol een indrukwekkende bijdrage geleverd aan het tot stand komen van dit proefschrift. Jos, jouw ideeën, enthousiasme en fundamentele steun bij dit onderzoek hebben ervoor gezorgd dat ik uiteindelijk in staat ben geweest om te promoveren. Ook je inzet bij de laatste (zware) loodjes mogen hier niet onvermeld blijven. Jouw geduld om alle lidwoordjes op de juiste plaats te zetten is echt indrukwekkend.

Verder wil ik de andere leden van de kerncommissie hartelijk bedanken voor het kritisch nakijken van het concept van dit proefschrift.

Promotieonderzoek kun je niet in je eentje doen. In het Russisch zeggen we wel eens: "alleen ben je geen strijder". Deze uitspraak is zeker van toepassing voor het multidisciplinaire slagveld van de fotonische integratie. Veel mensen hebben de afgelopen jaren naast me gestaan en bijgedragen aan dit onderzoek. Ik denk daarbij met name aan de samenwerkingen bij het ontwerpen, fabriceren en karakteriseren van het onderwerp van dit proefschrift: de optische chip.

Een eerste woord van dank gaat hier dan ook uit naar de cleanroom-ploeg, want de cleanroom is enigszins de wieg van een chip. Fouad Karouta, Barry Smalbrugge, Erik Jan Geluk, Ben van Roy en Kitty Sander in Eindhoven, en Tjibbe de Vries, Siang Oei eerst in Delft en later ook in Eindhoven hebben mij uitstekend les gegeven in het lab. Het was daarbij ook een heel prettige samenwerking. Mede dankzij jullie is het werken in de cleanroom mijn grote passie geworden.

Maar ja, wat kun je doen in de cleanroom zonder een chipontwerp? Eerst is dit een zaak van simulaties draaien en maskers ontwerpen. Daarbij was een zeer behulpzame helpdesk in de persoon van Xaveer Leijtens onontbeerlijk. Xaveer, hartelijk dank voor je zeer waardevolle suggesties.

Zonder (goed) materiaal kan er geen enkel (zelfs) briljant idee worden gerealiseerd. Daarom richt ik nog een "dankjewel" aan de groeiers van (toentertijd) JDS Uniphase in Eindhoven voor de actief-passieve plakken en één aan de groeiers van de Halfgeleiders Fysica groep, die de plakken met quantumdoosjes hebben gegroeid.

Op een gegeven moment ligt zo'n optische chip klaar. Toch kun je dan nog steeds niet zeggen of hij het goed doet, of het überhaupt wel doet. Er moet namelijk veel aan gemeten worden. En wat dit meten betreft wil ik vooral een "dankjewel" geven aan Erwin Bente. Voor het opzetten van het indrukwekkende meetlab OLA in het algemeen, en voor de automatisering van mijn meetopstelling in het bijzonder. Ook bedankt voor het leren om metingen bewust te doen en zó ook de meetresultaten te bekijken. Een aantal belangrijke metingen heb ik uitgevoerd in samenwerking met de onderzoeksgroep COM in Kopenhagen binnen het ePIXnet "network of excellence". Jan Hendrik, bedankt voor het organiseren van mijn "meetreis" naar Denemarken.

Dr. Mads Lønstrup Nielsen and prof. Jesper Mørk, thank you very much for the nice opportunity to carry out the dynamic measurements in your lab. This was really a valuable contribution to this thesis.

Martijn Heck, mijn medestrijder voor de Dr.-titel, wil ik graag bedanken voor het geven van de mogelijkheid om zijn programma toe te passen om sommige meetresultaten te analyseren. Ronald Broeke wil ik graag bedanken voor de gezellige en leerzame samenwerking in Delft. Collega's van HGF en in het bijzonder Jos Haverkort, Richard Nötzel en Prasanth wil ik bedanken voor de grootschalige samenwerking op het gebied van niet-lineaire schakelingen in kleinschalige quantumdoosjes.

Promoveren betekent hard werken, echt waar. Dat weten de meesten ook wel. Maar wat kan het werken nog plezierig maken? Ongetwijfeld een gezellige groep. En de gezelligheid kan niet bestaan zonder leuke collega's, die ook je vrienden zijn. Luc, Els, Martijn, het was altijd heel erg gezellig samen (samenwerken, uiteten, koffiedrinken, of gewoon kletsen) en ik hoop dat het zo door zal gaan. Ik wens jullie heel veel succes met het afronden van jullie promotieonderzoek(en).

I would like to thank all the other AIO-colleagues (Pietro, Yohan, Boudewijn, Mark, Fransisco, Omar, Uzma, Mahmoud and Ling), postdocs (Jan Hendrik, Rabah, Mirvais and Stefano) and the researchers of the OED group for sharing all these years the same photonic floor and for being such a nice company. I wish all of you a lot of success in the continuation of your research, and, for the AIOs, the successful finishing of your PhD-theses.

184

Voor de ondersteuning op het gebied van computers ben ik veel dank verschuldigd aan Hans Moerman. Biesonder wil iech nog eine kier miene kamergezel Luc Augustin bedanke, vuer siene groete inzet aon het oetsien van dit buekske en vuer alle andere wirkskes woe er altied vuer miech kloar schtond um te helpe. Een plezierige sfeer in de groep werd verder gestimuleerd door "ons" Els Gerritsen. Els, ik wil je graag bedanken voor al je zorgen gedurende deze jaren, en het (kritisch) nakijken van bepaalde stukken van dit proefschrift.

En dan wil nog al mijn Philips-collega's bedanken voor hun morele steun en begrip in het zware schrijftijdperk van dit proefschrift.

Promoveren kan niet zonder afwisseling, ontspanning en afleiding. Naast diegenen die meegewerkt hebben aan het project, wil ik ook nog een aantal speciale dankwoorden richten tot mensen die heel speciaal zijn voor mij. Ten eerste is dat mijn Deurnese familie Annie en Frans Nooyen, zonder wie het hele avontuur van het promoveren in Nederland nooit gerealiseerd had kunnen worden. Het was en het is altijd prettig te beseffen dat er mensen zijn die voor mij zo veel betekenen. Annie en Frans, oneindig veel dank voor het thuisgevoel dat ik dankzij jullie in Nederland heb gekregen!

For me, the years of living in Eindhoven besides hard working towards challenging results, will always be highlighted by meeting of a real friend with whom I have the pleasure of sharing the excitements and troubles of the life. Massimo, ti sono molto grato per il tuo costante supporto durante questi anni, nonchè per la piacevole convivenza e la tua sincera e preziosa amicizia. Daarnaast wil ik nog Olga hartelijk bedanken voor haar ondersteuning op deze promotie en voor de vele gesprekken gedurende al deze jaren.

En tot slot. *I would like to finish these acknowledgements with a recognition of the tremendous contribution that my family, my parents Larisa and Arkady, and babushka, has made to my work. Despite the distance that separates us, they are constantly in my thoughts and their love and support has been a major stabilizing force and motivation for me during the past years. Their unquestioning faith in me and my abilities has helped to make all this possible and for that, and everything else, I dedicate this thesis to them.*

Curriculum Vitae

Evgeni Patent was born in Minsk, Belarus, on the 26th of September 1977. He studied microelectronics at the Belarusian State University of Informatics and Radioelectronics in Minsk. After obtaining diploma (M.Sc.) with honors in 1999, he started his post-masters Stan Ackermans Institute program Information and Communication Technology at the Eindhoven University of Technology. In 2002 he obtained the title Professional Doctorate in Engineering (PDEng). In 2001 he started his Ph.D. research on the self-switching effects in Mach-Zehnder interferometers within the Opto-Electronic Devices group at the Eindhoven University of Technology. At present he is working at Philips Research Laboratories in Eindhoven, The Netherlands.

List of publications

Journal publications:

- E.A. Patent, J.J.G.M. van der Tol, J.J.M. Binsma, Y.S. Oei, E.A.J.M. Bente, and M.K. Smit, "Self-switching in Mach-Zehnder Interferometers with SOA phase shifters," accepted for publication in *IEEE Photon. Technol. Lett.,* vol. 17, no. 11, 2005.

- E.A. Patent, J.J.G.M van der Tol, M.L. Nielsen, J.J.M. Binsma, Y.S. Oei, J. Mørk, and M.K. Smit, "Integrated SOA-MZI for pattern-effect-free amplification," *IEE Electron. Lett.,* vol. 41, no. 9, pp. 51-52, 2005.

- E.A. Patent, J.J.G.M. van der Tol, J.J.M Binsma, and M.K. Smit, "Effect of the first order mode in access waveguides on the performance of unbalanced MMI couplers," *IEEE Photon. Technol. Lett.,* vol. 16, no. 8, pp. 1882-1884, 2004.

- E.A. Patent, J.J.G.M. van der Tol, P.R.A. Binetti, Q. Gong, Y.S. Oei, R. Nötzel, J.E.M. Haverkort, P.J. van Veldhoven, J.H. Wolter, and M.K. Smit, "First integrated combiner based on self-switching in quantum dots," *IEEE Photon. Technol. Lett.,* vol. 16, no. 10, pp. 2308-2310, 2004.

- R. Prasanth, J.E.M. Haverkort, A. Deepthy, E.W. Bogaart, J.J.G.M. van der Tol, E.A. Patent, G. Zhao, Q. Gong, P.J. van Veldhoven, R. Nötzel, and J.H. Wolter, "All-optical switching due to state-filling in quantum dots," *Appl. Phys. Lett.,* vol. 84, no. 20, pp. 4059-4061, 2004.

- G. Zhao, Patent, E., Tol, J.J.G.M. van der, "Modeling of optical nonlinearities based on engineering the semiconductor band", *Materials Science in Semiconductor Processing,* vol. 6, no. 1-3, pp. 153-158, 2003.

Contributions to international conferences:

Contributed papers:

- E.A. Patent, J.J.G.M. van der Tol, M.L. Nielsen, J.J.M. Binsma, Y.S. Oei, J. Mørk, and M.K. Smit, "Integrated pattern effect compensator based on self-switching", in *Proc. 11th Eur. Conf. on Integr. Opt. (ECIO '05)* April 6-8 2005, pp. 49-52, Grenoble, France.

- E.A. Patent, J.J.G.M. van der Tol, P.R.A. Binetti, Q. Gong, Y.S. Oei, R. Nötzel, J.E.M. Haverkort, P.J. van Veldhoven, J.H. Wolter, and M.K. Smit, "Integrated combiner based on self-switching in quantum dots", in T*echnical Digest Integr. Photon. Res. (IPR '04),* p. IFF5, San Francisco, USA, Jun. 30-Jul. 2 2004.

- J.E.M. Haverkort, R. Prasanth, S. Dilna, E.W. Bogaart, J.J.G.M. van der Tol, E.A. Patent, G. Zhao, Q. Gong, P.J. van Veldhoven, R. Nötzel, and J.H. Wolter, "Photonic switching in InAs/InP quantum dots", *IEEE-Nano,* Muenchen, 2004.

- E.A. Patent, J.J.G.M. van der Tol, J.J.M. Binsma, and M.K. Smit, "Effect of the first-order mode in access waveguides on the performance of unbalanced MMI couplers," in *Proc. IEEE/LEOS Annual Meeting (LEOS '03).* Oct. 26-30 2003, vol. 1, pp. 354-355, Tucson, Arizona, USA.

- G. Zhao, E.A. Patent, and J.J.G.M. van der Tol, "Modeling of Optical Nonlinearities Based on Engineering the Semiconductor Band," in *Proc. 3rd International Workshop on Challenges in Predictive Process Simulation,* Oct. 13-17 2002, Prague, Czech Republic.

- E.A.Patent, J.J.G.M. van der Tol, N. Calabretta and Y. Liu, "Compensation of the pattern effect in SOAs", in *Proc. 2001 International workshop on Optical Signal Processing,* Nov. 29-30 2001, pp.99-101, Copenhagen, Denmark.

Contributions to IEEE/LEOS Benelux symposia:

- E.A. Patent, J.J.G.M. van der Tol, J.J.M. Binsma, Y.S. Oei, E.A.J.M. Bente, and M.K. Smit, "Self-switching in Mach-Zehnder Interferometers based on SOA phase shifters," in *Proc. IEEE/LEOS Symposium (Benelux Chapter).* Dec. 2004, pp.247-250, Gent, Belgium.

- E.A. Patent, J.J.G.M. van der Tol, J.J.M. Binsma, and M.K. Smit, "Conditions for optimum performance of unbalanced MMI couplers," in *Proc. IEEE/LEOS*

Symposium (Benelux Chapter). Nov. 2003, pp. 89-92, Enschede, The Nether-
lands.

- E.A. Patent, J.J.G.M. van der Tol, R.G. Broeke, and J.J.M. Binsma, "Semi-
conductor Optical Amplifiers in a non-linear Mach-Zehnder Interferometer," in
Proc. IEEE/LEOS Symposium (Benelux Chapter). Dec. 2002, pp. 222-225,
Amsterdam, The Netherlands.

- E.A. Patent, J.J.G.M. van der Tol, and N. Calabretta, "A pattern effect compen-
sator," in *Proc. IEEE/LEOS Symposium (Benelux Chapter).* Dec. 2001, pp.
233-236, Brussels, Belgium.

Reports:

- E.A. Patent, *Low-Loss Optical Combiner Based on Semiconductor Optical Am-
plifiers*, post-masters Stan Ackermans Institute program Information and Com-
munication Technology, Technische Universiteit Eindhoven, Eindhoven, The
Netherlands, 2002, ISBN 90-444-0247-1.